The crystalline silica conundrum: the effect of impurities on the respiratory toxicity of diatomaceous earth and synthetic cristobalite

NATTRASS, CLAIRE

The crystalline silica conundrum: the effect of impurities on the respiratory toxicity of diatomaceous earth and synthetic cristobalite

Claire Nattrass

A thesis submitted in partial fulfilment of the requirements for the degree of

Doctor of Philosophy

One Volume

Department of Earth Sciences

Durham University

2015

Abstract

Crystalline silica, in the form of quartz and cristobalite, can cause respiratory diseases, such as silicosis. However, the observed toxicity and pathogenicity of crystalline silica is highly variable. This has been attributed to a number of inherent and external factors, including the presence of impurities that can react with the silica surface. Substitutions of aluminium (Al) for silicon in volcanic cristobalite, and phases occluding its surface, have been hypothesised to decrease its reactivity.

Diatomaceous earth (DE), an industrial source of cristobalite exposure, is studied to determine if structural substitutions in cristobalite are universal and whether they influence toxicity. Crystalline silica is also synthesised with incremental amounts of Al and sodium (Na) dopants. The effect of impurities on cristobalite toxicity is investigated through the physicochemical characterisation of DE and synthetic crystalline silica, and toxicological studies assessing the biological reactivity of these particles.

The physicochemical properties of DE varied by deposit source and processing technique. In processed DE, substantial quantities of cristobalite were observed. However, crystalline silica content could not be correlated with the potential toxicity of DE and this was attributed, in part, to impurities in the cristobalite structure and low cristobalite abundance at the particle surface.

Al-only doped or co-doped (Al+Na) synthetic cristobalite contained structural substitutions (1-4 oxide wt.% Al+Na). Co-doped samples also contained Al/Na-rich phases, such as albite. Doping reduced toxicity compared to non-doped cristobalite. Al-only doping was more effective at decreasing cristobalite reactivity than Al+Na doping. The reduction in cristobalite toxicity was attributed to structural impurities.

This thesis concludes that impurities can reduce the toxic potency of cristobalite and may explain the low reactivity of cristobalite-rich volcanic ash and DE. Whilst further work is required, to determine if these effects are sustained long-term in the lung, the research has substantial implications for the regulation of crystalline silica exposures.

Table of Contents

Abstract i

Table of Contents ii

List of Tables vii

List of Figures ix

Declaration xiii

Acknowledgements xv

Chapter 1 – Introduction **1**

1.1 Project rationale 1

1.2 Background to project 3

1.3 Aims and hypotheses 4

1.4 Thesis structure 7

References 9

Chapter 2 – Background **12**

2.1 Introduction 12

2.2 Crystalline silica 12

2.2.1 Surface properties of crystalline silica *13*

2.2.2 Impurities in crystalline silica *16*

2.3 Crystalline silica toxicity 17

2.3.1 Diseases caused by exposure to crystalline silica *18*

2.4 Mechanisms of crystalline silica toxicity 20

2.4.1 Inhalation of particles *20*

2.4.2 Fate of inhaled particles *22*

2.5 Variability of crystalline silica toxicity 29

2.5.1 Factors affecting crystalline silica toxicity *31*

2.6 Exposure to crystalline silica 44

2.7 Diatomaceous earth 45

2.7.1 Background *45*

2.7.2 Pathogenicity of diatomaceous earth *51*

References 67

Chapter 3 – Methodologies **75**

3.1 Sample preparation 75

3.1.1 Separation of the fine fraction – diatomaceous earth *76*

3.1.2 Grinding to a fine powder – synthetic crystalline silica *76*

3.2 Physicochemical characterisation 77

3.2.1 Bulk analytical techniques *77*

3.2.2 Surface analytical techniques *84*

3.3 In vitro toxicology 90

3.3.1 Haemolysis *90*

3.3.2 Cell culture *91*

3.3.3 Cell treatment *92*

3.3.4 Cytotoxicity *93*

3.3.5 Sub-lethal assays *96*

3.3.6 Cell imaging *99*

3.4 Statistical analysis 99

References 99

Chapter 4 - Global variability of the physicochemical characteristics of diatomaceous earth **101**

4.1 Introduction 101

4.2 Methods 103

4.2.1 Mineralogy and chemical analyses *105*

4.2.2 Physical properties *106*

4.2.3 Statistical analysis *106*

4.3 Results 107

4.3.1 Bulk chemical composition *107*

4.3.2 Crystalline silica *109*

4.3.3 Contaminant phases *115*

4.3.4 Iron release *116*

4.3.5 Surface structure *118*

4.3.6 Physical properties *121*

4.4 Discussion 122

4.4.1 The variability of crystalline silica in DE *123*

4.4.2 The variability of contaminants in DE *126*
4.4.3 Surface structure *128*
4.4.4 The variability of physical properties of DE *129*
4.5 Conclusion 130
References 131

Chapter 5 - Global variability of the potential toxicity of diatomaceous earth **134**
5.1 Introduction 134
5.2 Methods 135
5.2.1 Separation of the fine fraction *135*
5.2.2 In vitro toxicology *136*
5.2.3 Free radical release *137*
5.2.4 Statistical analysis *138*
5.3 Results 138
5.3.1 Haemolysis *139*
5.3.2 Cytotoxicity *141*
5.3.3 Cytokine release *142*
5.3.4 Cell imaging *145*
5.3.5 Free radical release *146*
5.4 Discussion 150
5.4.1 The variability of diatomaceous earth toxicity *150*
5.4.2 Factors affecting the potential toxicity of DE *151*
5.5 Conclusion 163
References 164

Chapter 6 - The effect of Al and Na doping on crystalline silica structure and chemistry **169**
6.1 Introduction 169
6.2 Methods 171
6.2.1 Crystalline silica synthesis *171*
6.2.2 Crystal phases and crystal structure *174*
6.2.3 Elemental composition *175*
6.3 Results 175
6.3.1 Cristobalite formation and abundance *175*
6.3.2 Cristobalite chemistry and structure *189*

6.3.3 Formation of other phases *190*
6.4 Discussion 194
6.4.1 Production of non-doped α-cristobalite *194*
6.4.2 Production of impure α-cristobalite *195*
6.4.3 Crystallisation of other phases *199*
6.4.4 Crystal polymorph, abundance and crystallisation kinetics *202*
6.5 Conclusion 205
References 206

Chapter 7 - The effect of impurities on the potential toxicity of crystalline silica **209**
7.1 Introduction 209
7.2 Materials and methods 211
7.2.1 Samples *211*
7.2.2 Particle characterisation *213*
7.2.3 Free radical generation *214*
7.2.4 In vitro toxicology *214*
7.2.5 Statistical analyses *215*
7.3 Results 216
7.3.1 Particle characterisation *216*
7.3.2 Free radical release *223*
7.3.3 Haemolysis *227*
7.3.4 Cytotoxicity *230*
7.3.5 TNF-α release and NF-κB activation *233*
7.3.6 Particle uptake *235*
7.4 Discussion 237
7.4.1 Particle characterisation *237*
7.4.2 Effect of dopants on the potential toxicity of crystalline silica *239*
7.4.3 Effect of crystallinity on the haemolytic potential of non-doped crystalline silica *245*
7.4.4 Mechanism of toxicity *245*
7.5 Conclusion 247
References 249

Chapter 8 – Implications and Conclusions **253**
8.1 Introduction 253

8.2 Implications for the biological reactivity of volcanic and DE cristobalite 254
8.3 Implications for crystalline silica regulation and hazard management 255
8.4 Implications for the DE hazard and regulations 258
8.5 Future work 259
8.6 Concluding remarks 264
References 264

Appendix 1 - Referenced studies and data 267
Appendix 2 - Raw data 279
Appendix 3 – Publications 280

List of Tables

Chapter 2 – Background

Table 2.1: Summary of toxicology studies with aluminium-treated quartz, and PVNO-treated quartz. 36

Table 2.2: Summary of toxicology studies with iron-treated quartz. 40

Table 2.3: Global production of DE in 2013. 46

Table 2.4: Chemical composition of DE used in a number of studies and from industrial websites. 48

Table 2.5: Crystalline silica content of DE used in different studies. 51

Table 2.6: Epidemiological and clinical studies on DE exposed workers. 55

Table 2.7: *in vivo* studies using DE. 60

Table 2.8: *in vitro* studies of DE. 64

Chapter 4 - Global variability of the physicochemical characteristics of diatomaceous earth

Table 4.1: Sample information for DE chosen for analysis, including sample source, process and grade. 104

Table 4.2: Information for diatomaceous earth samples, including: particle size distribution, surface area and chemical composition. 108

Table 4.3: Total Fe release from DE samples post 8-days incubation as a per cent of total bulk Fe as measured by XRF. 117

Chapter 5 - Global variability of the potential toxicity of diatomaceous earth

Table 5.1: Particle size measured by SEM image analysis. 139

Table 5.2: Cytokine release from J774 macrophages exposed to the separated fine fractions of DE for 24h. 144

Chapter 6 - The effect of Al and Na doping on crystalline silica structure and chemistry

Table 6.1: Chemical composition of dried silica sol as determined by XRF given in wt.%. 172

Table 6.2: A list of samples produced including treatment temperature, time, dopant concentrations, and analyses performed on each sample. 173

Table 6.3: FWHM (indicator of degree of crystallinity), peak area and intensity (indicators of crystal abundance) and peak position (indicator of crystal structure) measurements of the primary cristobalite peak in XRD patterns of samples. 177

Table 6.4: Comparison of experimental and calculated IR frequencies for cristobalite from previous studies and the current study. 181

Table 6.5: Comparison of Raman spectroscopy signal frequencies of cristobalite from previous studies and the current study. 183

Table 6.6: Elemental composition of cristobalite in non-doped and doped samples. 189

Chapter 7 - The effect of impurities on the potential toxicity of crystalline silica

Table 7.1: List of samples used for each analysis method. 212

Table 7.2: Particle size (laser diffraction), surface area (BET) and surface charge in complete medium (RPMI + 10 % foetal bovine serum + antibiotics; zeta potential) for non-doped and doped samples, starting material and standards. 217

Chapter 8 – Implications and Conclusions

Table 8.1: OELs for respirable inert dust, quartz, cristobalite, tridymite, DE and amorphous silica in European countries and the USA. 256

Appendix 1 - Referenced studies and data

Table A1: Summary of crystalline silica synthesis studies and the phases formed at different treatment temperatures, durations and dopant concentrations added. 267

Table A2: Mean particle diameter, particle size distribution (cumulative volume (c.v.) %) and BET surface area of 1600_4 and 2Al+Na_1100_24 ground by cryogenic milling or by hand with agate mortar and pestle. 272

List of Figures

Chapter 2 – Background

Figure 2.1: Different types of surface silanol commonly seen at the surface of crystalline silica. 14

Figure 2.2: Hydrophilic silica surface comprising of silanols that converts to a hydrophobic surface mainly consisting of siloxanes upon dehydration. 15

Figure 2.3: Cleavage of the Si-O bond. 16

Figure 2.4: Some key components of the respiratory tract. 21

Figure 2.5: Processing procedure of DE. 47

Chapter 3 – Methodologies

Figure 3.1: Schematic of the dry-resuspension method used to separate the fine fraction of DE. 76

Figure 3.2: The reduction of resozurin (low fluorescence) to resorufin, which is highly fluorescent. 93

Figure 3.3: The conversion of WST-1 to red formazan by reactions with viable cells 94

Figure 3.4: The conversion of lactate to pyruvate mediated by LDH used to measure cell membrane damage. 95

Chapter 4 - Global variability of the physicochemical characteristics of diatomaceous earth

Figure 4.1: XRD patterns of unprocessed, calcined and flux-calcined DE 109

Figure 4.2: Backscatter image and EDS spectra of flux-calcined DE particle 110

Figure 4.3: Backscatter images of rarely observed pure crystalline silica 111

Figure 4.4: The concentration of Na, Al, ca and Fe impurities in unaltered diatom frustules (those which retained their original morphology), cristobalite patches, and in the amorphous matrices in cristobalite-bearing particles. 112

Figure 4.5: concentrations of Na, Al, Ca and Fe impurities in cristobalite patches by DE source. 113

Figure 4.6: concentrations of Na, Al, Ca and Fe impurities in the amorphous matrices of cristobalite-bearing particles by DE source. 114

Figure 4.7: Backscatter images of contaminant phases in DE**.** 116

Figure 4.8: Total iron release from unprocessed, calcined, and flux-calcined DE over 8 days. 117
Figure 4.9: Total Fe release and speciation of Fe released from DE 118
Figure 4.10: IR spectra of unprocessed DE from Spain and France, and calcined DE from Mexico. 120
Figure 4.11: SEM images of examples of DE morphologies. 122
Figure 4.12: Median particle size of unprocessed, calcined and flux-calcined DE against specific surface area. 129

Chapter 5 - Global variability of the potential toxicity of diatomaceous earth

Figure 5.1: Haemolytic potential of DE samples. 140
Figure 5.2: Cell viability of J774 macrophages exposed to DE. 141
Figure 5.3: Lactate dehydrogenase release from J774 macrophages treated with DE. 142
Figure 5.4: TNF-α production by macrophages exposed to the fine fractions of DE. 143
Figure 5.5: Frustrated phagocytosis in macrophages treated with DE. 145
Figure 5.6: $HO^{\bullet}$ release after 10, 30 and 60 minutes exposure to H_2O_2 from unprocessed (DE_11) and flux-calcined (DE_12) Spanish DE. 147
Figure 5.7: $HO^{\bullet}$ release after 10, 30 and 60 minutes exposure to H_2O_2 from unprocessed (DE_15), calcined (DE_16) and flux-calcined (DE_14) French DE. 148
Figure 5.8: $HO^{\bullet}$ release after 10, 30 and 60 minutes exposure to H_2O_2 from calcined DE from USA-1 (DE_22), calcined DE from Mexico (DE_24), and flux-calcined DE from Mexico (DE_10). 149
Figure 5.9: Relationship between crystalline silica content and reactivity *in vitro.* 152
Figure 5.10: Correlation between bulk Al oxide content and haemolysis post-exposure to 1 mg/ml bulk DE, and cell viability post-exposure to 500 µg/ml bulk DE. 156
Figure 5.11: Relationships between bulk and available Fe and *in vitro* reactivity of DE. 158
Figure 5.12: Relationship between BET surface area and DE reactivity *in vitro.* 161
Figure 5.13: Relationship between particle size and DE reactivity *in vitro.* 162

Chapter 6 - The effect of Al and Na doping on crystalline silica structure and chemistry

Figure 6.1: Schematic of the crystalline silica synthesis method. 172
Figure 6.2: XRD patterns for synthetic samples heated for 12 h at 800, 900, 1000 and 1100 °C. 176

Figure 6.3: XRD pattern of non-doped samples treated at 1500 °C for 12 h or at 1600 °C for 4, 8, or 12 h. 178
Figure 6.4: XRD patterns of doped cristobalite samples treated at 1100 °C for 24 h. 179
Figure 6.5: IR spectra from 400-1600 cm^{-1} of non-doped tridymite (1100_24), non-doped cristobalite (1600_4), Al+Na doped cristobalite (5Al+Na_1100_24), and Al-only doped cristobalite (3Al_1100_24). 180
Figure 6.6: Raman spectra for non-doped (1600_12) and doped cristobalite. 182
Figure 6.7: Raman spectra for non-doped 1100_24. 184
Figure 6.8: Band contrast image showing grain boundaries and phase map showing only cristobalite is present from EBSD analyses of 1600_12. 184
Figure 6.9: Section images, elemental maps and CL images of 1600_12. 185
Figure 6.10: Section images, elemental maps and CL images of 2Al+Na_1100_24. 186
Figure 6.11: Section images, elemental maps and CL images of 3Al+Na_1100_24. 187
Figure 6.12: Section images, elemental maps and CL images of 5Al+Na_1100_24. 188
Figure 6.13: Long scan time XRD patterns of non-doped samples, and doped samples. 191
Figure 6.14: Electron microprobe maps for Si, Al, Na and S (wt.%) for 5Al+Na_1100_24. 192
Figure 6.15: Long scan time XRD patterns from 18-26° 2θ for doped samples treated at 1100 °C for 24 h. 193
Figure 6.16: The cristobalite to nepheline phase diagram, showing the conditions at which albite forms. 200

Chapter 7 - The effect of impurities on the potential toxicity of crystalline silica

Figure 7.1: Particle size distribution of non-doped and doped crystalline silica ground cryogenically 218
Figure 7.2: Representative scanning electron microscopy images of particles used in cytotoxicity assays. 219
Figure 7.3: Zeta potential measurements for non-doped tridymite (1100_24), non-doped cristobalite (1600_4) and doped cristobalite (5Al+Na_1100_24 and 3Al_1100_24) over pH range of 0.5-8.5 in water. 220
Figure 7.4: EPR spectra of non-doped cristobalite (1600_4) and Al+Na doped cristobalite (5Al+Na_1100_24) at 10 mW and 77 K over 6000 G. 222
Figure 7.5: EPR spectra of non-doped cristobalite (1600_4) and Al+Na doped 224

cristobalite (5Al+Na_1100_24) at 77 K over 200 G at microwave powers of 20, 10, 1, 0.1, 0.01 and 0.001 mW.

Figure 7.6: Release of hydroxyl radicals (EPR) from the surface of synthetic crystalline silica samples. 225

Figure 7.7: Release of carboxyl radicals (EPR) from the surface of synthetic crystalline silica samples. 226

Figure 7.8: Haemolytic potential of crystalline silica samples. 228

Figure 7.9: Haemolytic potential of starting materials. 230

Figure 7.10: Cell viability of J774 macrophages treated with crystalline silica samples measured by the alamarBlue® assay 231

Figure 7.11: Cytotoxicity of crystalline silica samples to J774 macrophages measured by the LDH assay. 232

Figure 7.12: Cell viability of J774 macrophages treated with crystalline silica samples measured by the WST-1 assay. 233

Figure 7.13: TNF-α production by J774 macrophages exposed to concentrations of 16-125 µg/ml sample suspensions. 234

Figure 7.14: Ratio of NF-κB measured in the nucleus and the cytoplasm of J774 macrophages treated with crystalline silica for 4 h. 235

Figure 7.15: Light microscopy images of J774 macrophages post-24 h treatment with 500 µg/ml. 236

Appendix 1 - Referenced studies and data

Figure A1: Particle size distributions of 1600_4 and 2Al+Na_1100_24 ground by cryogenic grinding for 30 minutes (red) or 1 h (green), or ground by hand with agate mortar and pestle. 273

Figure A2: Haemolytic potential of the bulk and fine fractions of DE samples. 275

Figure A3: Haemolytic potential of leachates of DE samples. 276

Figure A4: Cell viability of J774 macrophages exposed to DE leachates, measured by the alamarBlue® assay. 276

Declaration

I declare that this thesis, submitted for the degree of Doctor of Philosophy at Durham University, is my own work and not substantially the same as any which has been previously submitted at this or any other university. Where appropriate, I have clearly indicated the contributions of colleagues to fully acknowledge all collaborative work.

Claire Nattrass

Durham University

July 2015

Thank you to my supervisors:

Claire Horwell

Vicki Stone

Ed Llewellin

This work was supported by Durham University and Industrial Minerals Association (IMA) Europe.

Acknowledgements

There are so many people that have supported me throughout the duration of this project that it is not possible to thank them all here by name, so for those not mentioned, thank you – I hope you know who you are! First and foremost I thank IMA-Europe and Durham University for funding the project, and my supervisors. Claire, thank you for taking a chance on me to work on this project, for always having faith that I would succeed throughout, and for all your input to this work. Vicki, I thank you for taking me in at the last moment, for your input to the project, and encouraging me to try new techniques and to become a toxicologist (one day maybe). Ed, thanks for initial discussions of experimental set-up. Thanks also to the research group; a huge thanks to David, a guiding light full of knowledge throughout, this would not have been possible without you and your responses to my never ending emails; Sabina, thanks for always checking in on me, it is always appreciated; and Ines for taking over the reins.

Scientific support throughout this project has been rife both at Durham University and elsewhere and would not have been possible without the kind heartedness of people willing to teach me new things and always taking the time to explain when I didn't understand. Thanks to Gary Oswald and David Johnson (Department of Chemistry) for XRD and BET training respectively. Thanks to Frank Davies for use of the Geography laboratories and to Kathryn Melvin, Amanda Hayton and Alison George (Department of Geography) for training on the LS Coulter and uniaxial press. Thank you to Professor Damian Hampshire and Mark Raine (Department of Physics) for the use of the high temperature furnace and discussions of experimental set-up. A huge thank you to Ian Chaplin (Department of Earth Sciences) for the preparation of sample sections. You always met me with a smile, even though you knew I would bring you a challenge! Thank you to Leon Bowen for training in the SEM, EDS, CL analyses, and for performing EBSD (on tricky samples!), and for occasionally getting it wrong and making me feel clever (ok once, but I will hold it over you forever!).

At Heriot Watt University, I thank David Brown for his patience and belief in me, for performing flow cytometry and training me in many of the methods and always being willing to flick the supernatant from the plate when I was too scared. Thanks to Ali Kermanizadeh for training in all the cytotoxicity methods, for flow cytometry measurements and for not laughing when watching me try and use a multi-channel pipette for the first time. Thank you to Helinor Johnston for training in the NF-κB

method and thanks to all the NanoSafety Group for their support and the lunch time chats. At Università degli Studi di Torino, thank you to Professor Bice Fubini for her support and input to the project. Thank you Cristina Pavan for training in zeta potential, Fe release, and EPR analyses, for performing zeta potential measurements, and analysing EPR of the solid data, amongst everything else. Thanks to Professor Gianmario Martra for the use of his lab and his input to IR measurements. Thank you to Marco Fabbiani for training and running IR measurements (with the most impossible samples!). Thank you also Chiara Gionco for training and running EPR of the solid. At Ludwig Maximilian University of Munich, thanks to David Damby for EMPA work and Danilo Di Genova for performing Raman spectroscopy analyses. Thanks also to Nick Marsh (University of Leicester) for performing XRF analyses, Mike Walter (University of Bristol) for helping with initial synthesis experiments, and Tim Jones (Cardiff University) for use of your particle separator.

Most of these people, and many others, have also helped outside of the laboratory, helping to keep me sane(ish) throughout the project. Friends in the Department, all your support and pub ventures are what made the time in Durham so great. A special thanks to Suzie and Helen for all the fun times, for all the dance moves (from badger to moorhen), and for keeping me well fed; to BJ, Tim, Baker and Clay for including me as 'one of the lads'; to Jing for your wiliness to try everything; to Iza for being with me at the write-up stage; to Iona for proving a non-geologist can do it; and to Izzy et al. for welcoming me when I first arrived. Thanks also to my housemates throughout the years. Pete, there really are no words, so thanks! Rach, sorry for the mess, and congratulations on finishing. Thanks Mark for putting up with my endless rants and explaining what life is like in the real world, Bob for introducing me to Bring It On and for the many cups of tea, and Jordan for providing all the salad a person could ever want! Thanks also to Louise and Mel, and Sara and Rob for being great housemates during my stays in Edinburgh. I can't thank you guys enough.

Thanks to everyone at staff badminton for providing a stress release when most needed and especially Kieran, Joe and Rebecca for helping me improve in some immense doubles matches. Thanks to Cristina, Marco, Chiara, Simone, Yuriy and everyone else in Turin for making my visit there so enjoyable, for showing me how to cook pasta the right way and introducing me to white port! Also, thanks to Karina, Ali, Helinor, Nicola, and the guys for some great nights out in Edinburgh.

Finally, thanks to my family, to my parents for endless provisions of food parcels and "are you done yet"s; Stuart for paving the way; and most of all Steve for his endless patience, belief in me, and being there in the good and bad times – now on to the next chapter!

Chapter 1

Introduction

1.1 Project rationale

Crystalline silica, in the form of quartz and cristobalite, is a known carcinogen and can causes diseases, such as silicosis (Greenberg et al., 2007, IARC, 1997, IARC, 2012, Leung et al., 2012). However, crystalline silica-rich dusts show a range of observed toxicities and it is noted that crystalline silica toxicity is a variable entity (Donaldson and Borm, 1998) termed here as the 'crystalline silica conundrum'. The pathways by which silica causes toxicity are still not fully understood, however, current research suggests that surface properties of silica dusts, including the distribution of silanol populations and surface siloxyl radicals are important in determining silica toxicity (e.g. Pavan et al., 2013). Surface modifications, by mechanical grinding or the addition of impurities, have been shown to alter silica toxicity (e.g. Duffin et al., 2001, Fubini et al., 1995, Vallyathan et al., 1988). In mixed dusts, the presence of other minerals and amorphous phases have also been implicated in affecting crystalline silica toxicity (e.g. Ghiazza et al., 2009, Horwell et al., 2012, Tourmann and Kaufmann, 1994).

Quartz is the most abundant crystalline silica polymorph and is stable at ambient temperature and pressure (Heaney et al., 1994). Therefore, as exposure to quartz is most common, most studies have focused on quartz toxicity. However, cristobalite, a high temperature polymorph of crystalline silica, is found metastably in volcanic domes and in the diatomaceous earth (referred to as DE throughout

this thesis) and ceramics industries, and has also been categorised as carcinogenic (IARC, 1997, IARC, 2012). As cristobalite has a less dense structure than quartz, allowing cations to substitute into the crystal lattice, and volcanic cristobalite has been shown to contain up to 4 oxide wt.% aluminium (Al) and sodium (Na) (Horwell et al., 2012). It is hypothesised that these impurities dampen the toxicity of volcanic cristobalite (Horwell et al., 2012). However, confounding factors such as the presence of other minerals, different chemistries and different particle size and morphologies in volcanic ash have, until now, prevented conclusive evidence that structural impurities can alter volcanogenic cristobalite toxicity.

This transdisciplinary study, involving physicochemical and mineralogical analyses and toxicological assays, examines the effect of external and inherent impurities on crystalline silica structure and toxicity, specifically focussing on the effect of structural impurities within cristobalite. DE provides an occupational case study, where the form and purity of crystalline silica within samples from around the world, which have undergone different processing techniques, can be studied. This provides a second exposure source that can be used alongside volcanic ash to try to understand factors affecting cristobalite toxicity. To date, the DE hazard, and how this varies globally and within the same quarries/plants, has not been adequately addressed as most of the epidemiology studies have been carried out at a single location (California) (e.g. Checkoway et al., 1993, Cooper and Sargent, 1984, Rice et al., 2001) and toxicology studies use few samples and rarely state their source. Whilst crystalline silica content in DE is used to determine crystalline silica exposure limits (Collins et al., 2005, IARC, 1997, Mossman and Glenn, 2013), there is little evidence that crystalline silica content alone is a good indicator of the potential toxicity of these dusts. Therefore, this study of DE provides an opportunity to examine the role of crystalline silica and the effect of other physicochemical components of DE on its reactivity.

Whilst DE provides a unique case study of occupational cristobalite exposure, the same confounding factors observed in volcanic ash apply and it cannot be conclusively determined if cristobalite structural impurities play a role in DE toxicity. Here, in a separate study, the use of synthetically produced cristobalite, with and without the presence of impurities, overcomes these confounding factors. This allows the effect of structural impurities on toxicity to be assessed and characterisation of these samples can implicate *how* these impurities alter the silica surface to control toxicity. Although the ability of Al to decrease quartz toxicity is well established (Duffin et al., 2001, Knaapen et al., 2002, Schins et al., 2002), the mechanisms by which Al dilutes the toxicity of the silica surface are still poorly understood. It is also not known if cristobalite follows the same toxic pathways as quartz, as the mechanisms of crystalline silica induced toxicity are still not fully understood. Therefore, this study provides a unique opportunity to assess the pathways of both non-doped and doped cristobalite in inducing toxicity to further the current understanding of crystalline silica toxicity.

1.2 Background to project

This project stems from the work of Dr Claire Horwell and Dr David Damby on volcanic cristobalite and its potential toxicity. The field of volcanic ash toxicity developed after the 1980 eruption of Mt St Helens, when analysis of the ash showed it to contain crystalline silica in the form of cristobalite (Dollberg et al., 1986). As crystalline silica was known to be involved in diseases such as silicosis, the presence of cristobalite was of primary concern. Since then, the long-term eruption of Soufrière Hills volcano (SHV), Montserrat in 1995, with ash containing high quantities of cristobalite (Baxter et al., 1999, Horwell et al., 2014), has led to a number of studies assessing ash toxicity. These studies of SHV ash have shown low toxicity compared to quartz or cristobalite standards (Cullen et al., 2002, Housley et al., 2002, Wilson et al., 2000), an inability to produce fibrosis in the lung, although

delayed inflammation and enlargement of the lymph nodes was seen (Lee and Richards, 2004), and an inability to bind tightly to lung components, even though these samples contain up to 30 wt.% crystalline silica (Jones and BéruBé, 2011). Some evidence suggested the potential for silicosis to develop over a prolonged exposure (>10 years), however, little exposure data were available (Horwell and Baxter, 2006). More recently, Damby (2012) showed that volcanic ash from a range of dome-forming volcanoes was much less toxic *in vitro* than expected given the high quantities of cristobalite. Horwell et al. have also produced a number of studies of rapid ash analysis for the determination of potential health hazard for both recent and ancient eruptions including quantification of crystalline silica content (e.g. Damby et al., 2013, Horwell et al., 2010a, Horwell et al., 2013, Horwell et al., 2010b, Hillman et al., 2012, Le Blond et al., 2010).

Whilst attempting to understand why cristobalite-rich volcanic ash is mostly inert in toxicological studies, structural studies of volcanic cristobalite showed Al and Na impurities within the crystalline structure and that these substitutions are common to all volcanic cristobalite studied (Damby, 2012, Horwell et al., 2012). It was hypothesised that these impurities could dampen the cristobalite toxicity (Horwell et al., 2012). However, Horwell's study could not test this using cellular or animal models, as it was not possible to separate the volcanic cristobalite from the rest of the ash (which is composed of tens of mineral types) without altering its surface and, hence, toxicological properties.

1.3 Aims and hypotheses

The key aims of this thesis were to determine i) whether structural substitutions within cristobalite are a global phenomenon (i.e. from different natural and synthetic sources) and ii) if the presence of impurities, specifically Al and Na, within the cristobalite crystalline silica structure can alter its toxic potential.

These principal aims will be met by the following objectives specific to each hypothesis:

Hypothesis 1: As with volcanic silica, cristobalite in diatomaceous earth contains structural substitutions.

- To determine whether DE cristobalite contains impurities within its structure
- To determine whether the quantity and type of impurity varies by source and processing technique.

Hypothesis 2: The physicochemical properties of diatomaceous earth vary globally and by processing type.

- To determine the variability of crystalline silica content of DE by source and processing technique.
- To determine the form and polymorph of crystalline silica in DE.
- To determine the range of mineral impurities present in DE from different sources.
- To determine the variability of physical properties, such as surface area, and particle size and shape, of DE powders.

Hypothesis 3: Diatomaceous earth toxicity varies with source and processing technique

and

Hypothesis 4: Diatomaceous earth toxicity is related to crystalline silica content

- To determine if the toxic potential of DE varies with source or processing technique using a suite of *in vitro* assays and acellular assays.
- To determine if the presence of impurities in DE cristobalite control DE toxicity.

- To determine the contribution of other mineral and amorphous phases in DE reactivity.

Hypothesis 5: The structure of crystalline silica is altered by the addition of Al and Na dopants pre-crystallisation

- To produce a suite of cristobalite samples with different levels of added Al and Na.
- To determine if Al and Na impurities are integrated into the crystalline silica structure during sintering of doped amorphous silica and if this is dependent on the initial quantity of dopants added.
- To determine if the incorporation of impurities alters the structure or polymorph of crystalline silica produced.
- To determine the effect of sintering temperature on the polymorph of silica produced.

Hypothesis 6: The toxic potential of crystalline silica is altered by the addition of Al and Na dopants pre-crystallisation

- To determine if the presence of structural impurities alone can affect the toxic potential of cristobalite.
- To determine the effect of structural impurities and external impurities on the toxic potential of crystalline silica.

These aims and objectives will be met using a number of methods to fully characterise DE powders and synthetic crystalline silica samples. *In vitro* toxicological assays will also be used to assess the toxic potential of these dusts.

1.4 Thesis structure

This thesis is constructed to meet the key aims expressed above, in an attempt to solve 'the crystalline silica conundrum' with a focus on cristobalite. First, a case study addressing the variability in the physicochemical characteristic of crystalline silica-containing DE and how these properties may affect its potential toxicity will be presented. Then, a full characterisation of synthetic, doped crystalline silica will be described, and its potential toxicity explored, to determine the role of impurities in crystalline silica toxicity.

Following this Introduction, the thesis will be separated into seven further Chapters:

Chapter 2: Background. This chapter provides background on crystalline silica and the effect of dopants on crystal structure, silica-related disease and mechanisms of toxicity, alongside factors affecting particle toxicity, allowing the reader to navigate the following research chapters and will also give a literature review of known DE characteristics, toxicity and pathogenicity.

Chapter 3: Methodologies. This chapter provides a detailed overview of all the methods used throughout this project, including methods for physicochemical characterisation of bulk samples and surface parameters, and *in vitro* toxicological assays. A number of the methods are used throughout the thesis and, therefore, this chapter acts as a reference for these and is referred to in the subsequent chapters.

Chapter 4: Global variability of the physicochemical characteristics of diatomaceous earth. Here, globally sourced DE was characterised by measuring physicochemical parameters that may control the potential toxicity of these dusts. In particular the form and purity of crystalline silica and how

this varies by source and processing technique is assessed. The variability of other parameters, such as mineral impurities and particle size, shape and surface area are also assessed.

Chapter 5: Global variability of the potential toxicity of diatomaceous earth. The toxic potential of DE samples characterised in Chapter 4 is assessed using an *in vitro* toxicology study. Current regulation of DE exposure is based on few studies from few locations and assumes crystalline silica is the cause of disease. Here, samples with a range of crystalline silica contents and mineral impurities are analysed for their toxic potential, to assess if crystalline silica content is a determining factor of DE reactivity and the potential role of other phases on DE toxicity.

Chapter 6: The effect of Al and Na doping on crystalline silica structure and chemistry. The method developed to produce doped and non-doped crystalline silica under varying treatment conditions (time and temperature) is described here. The samples produced are characterised using a number of techniques to assess the crystalline silica polymorph, the crystal structure and crystal chemistry. This in-depth characterisation allows determination of the parameters altered by doping amorphous silica with Al and Na, and, therefore, parameters which may alter the reactivity of the crystalline silica surface.

Chapter 7: The effect of impurities on the potential toxicity of crystalline silica. A suite of synthetic cristobalite samples (Chapter 6) is used in cellular studies to determine if doping with Al and Na impurities can alter the toxic potency of crystalline silica. Particles are characterised for their size, surface properties and surface reactivity, and used in *in vitro* toxicological assays. The analysis of doped and non-doped crystalline silica samples, including cristobalite and some tridymite-containing samples, allows an investigation into the effect of impurities and crystal polymorph on crystalline silica toxicity.

Chapter 8. Implications and Conclusions. This chapter provides an interpretation of the key findings from the thesis, relating these to the key aims of the project and also to previous studies of volcanic ash. This chapter also addressed the wider implications of key findings for hazard assessment and regulation of exposure to crystalline silica-bearing dusts.

Appendices

Appendix 1. Referenced studies and data: Tabulated and graphical presentation of some key studies and data referenced throughout the thesis.

Appendix 2. Raw data: The raw data obtained and referenced throughout the thesis. Available on CD with the thesis hard copy. Please contact the author for a digital version.

Appendix 3. Publications: Publications published or submitted throughout the course of the thesis.

References

BAXTER, P. J., BONADONNA, C., DUPREE, R., HARDS, V. L., KOHN, S. C., MURPHY, M. D., NICHOLS, A., NICHOLSON, R. A., NORTON, G., SEARL, A., SPARKS, R. S. J. & VICKERS, B. P. 1999. Cristobalite in Volcanic Ash of the Soufriere Hills Volcano, Montserrat, British West Indies. *Science,* 283**,** 1142-1145.

CHECKOWAY, H., HEYER, N. J., DEMERS, P. A. & BRESLOW, N. E. 1993. Mortality among workers in the diatomaceous earth industry. *British Journal of Industrial Medicine,* 50**,** 586-597.

COLLINS, J. F., SALMON, A. G., BROWN, J. P., MARTY, M. A. & ALEXEEFF, G. V. 2005. Development of a chronic inhalation reference level for respirable crystalline silica. *Regulatory Toxicology and Pharmacology,* 43**,** 292-300.

COOPER, W. C. & SARGENT, E. N. 1984. A 26-Year Radiographic Follow-Up of Workers in a Diatomite Mine and Mill. *Journal of Occupational and Environmental Medicine,* 26**,** 456-460.

CULLEN, R. T., JONES, A. D., MILLER, B. G., TRAN, C. L., DAVIS, J. M. G., DONALDSON, K., WILSON, M., STONE, V. & MRGAN, A. 2002. Toxicity of volcanic ash from Montserrat. Edinburgh: Institute of Occupational Medicine. IOM TM/02/01

DAMBY, D., HORWELL, C., BAXTER, P., DELMELLE, P., DONALDSON, K., DUNSTER, C., FUBINI, B., MURPHY, F., NATTRASS, C. & SWEENEY, S. 2013. The respiratory health hazard of tephra from the 2010 Centennial eruption of Merapi with implications for occupational mining of deposits. *Journal of Volcanology and Geothermal Research,* 261**,** 376-387.

DAMBY, D. E. 2012. *From Dome to Disease: The Respiratory Toxicity of Volcanic Cristobalite.* Durham theses, Durham University.

DOLLBERG, D. D., BOLYARD, M. L. & SMITH, D. L. 1986. Chapter 6: Evaluation of Physical Health Effects Due to Volcanic Hazards: Crystalline Silica in Mount St. Helens Volcanic Ash. *American Journal of Public Health,* 76**,** 53-58.

DONALDSON, K. & BORM, P. J. A. 1998. The Quartz Hazard: A Variable Entity. *Annals of Occupational Hygiene,* 42**,** 287-294.

DUFFIN, R., GILMOUR, P. S., SCHINS, R. P. F., CLOUTER, A., GUY, K., BROWN, D. M., MACNEE, W., BORM, P. J., DONALDSON, K. & STONE, V. 2001. Aluminium Lactate Treatment of DQ12 Quartz Inhibits Its Ability to Cause Inflammation, Chemokine Expression, and Nuclear Factor-κB Activation. *Toxicology and Applied Pharmacology,* 176**,** 10-17.

FUBINI, B., BOLIS, V., CAVENAGO, A. & VOLANTE, M. 1995. Physicochemical properties of crystalline silica dusts and their possible implication in various biological responses. *Scandinavian Journal of Work, Environment and Health,* 21 suppl 2**,** 9-14.

GHIAZZA, M., GAZZANO, E., BONELLI, B., FENOGLIO, I., POLIMENI, M., GHIGO, D., GARRONE, E. & FUBINI, B. 2009. Formation of a Vitreous Phase at the Surface of Some Commercial Diatomaceous Earth Prevents the Onset of Oxidative Stress Effects. *Chemical Research in Toxicology,* 22**,** 136-145.

GREENBERG, M. I., WAKSMAN, J. & CURTIS, J. 2007. Silicosis: a review. *Dis Mon,* 53**,** 394-416.

HEANEY, P. J., PREWITT, C. T. & GIBBS, G. V. 1994. *Silica: Physical Behavior, Geochemistry and Materials Applications,* Washington D.C., Mineralogical Society of America.

HILLMAN, S., HORWELL, C., DENSMORE, A., DAMBY, D., FUBINI, B., ISHIMINE, Y. & TOMATIS, M. 2012. Sakurajima volcano: a physico-chemical study of the health consequences of long-term exposure to volcanic ash. *Bulletin of Volcanology,* 74**,** 913-930.

HORWELL, C. & BAXTER, P. 2006. The respiratory health hazards of volcanic ash: a review for volcanic risk mitigation. *Bulletin of Volcanology,* 69**,** 1-24.

HORWELL, C., LE BLOND, J., MICHNOWICZ, S. & CRESSEY, G. 2010a. Cristobalite in a rhyolitic lava dome: evolution of ash hazard. *Bulletin of Volcanology,* 72**,** 249-253.

HORWELL, C., WILLIAMSON, B., DONALDSON, K., LE BLOND, J., DAMBY, D. & BOWEN, L. 2012. The structure of volcanic cristobalite in relation to its toxicity; relevance for the variable crystalline silica hazard. *Particle and Fibre Toxicology,* 9**,** 44.

HORWELL, C. J., BAXTER, P. J., HILLMAN, S. E., CALKINS, J. A., DAMBY, D. E., DELMELLE, P., DONALDSON, K., DUNSTER, C., FUBINI, B., KELLY, F. J., LE BLOND, J. S., LIVI, K. J. T., MURPHY, F., NATTRASS, C., SWEENEY, S., TETLEY, T. D., THORDARSON, T. & TOMATIS, M. 2013. Physicochemical and toxicological profiling of ash from the 2010 and 2011 eruptions of Eyjafjallajökull and Grímsvötn volcanoes, Iceland using a rapid respiratory hazard assessment protocol. *Environmental Research,* 127**,** 63-73.

HORWELL, C. J., HILLMAN, S. E., COLE, P. D., LOUGHLIN, S. C., LLEWELLIN, E. W., DAMBY, D. E. & CHRISTOPHER, T. E. 2014. Chapter 21 Controls on variations in cristobalite abundance in ash generated by the Soufrière Hills Volcano, Montserrat in the period 1997 to 2010. *Geological Society, London, Memoirs,* 39**,** 399-406.

HORWELL, C. J., STANNETT, G. W., ANDRONICO, D., BERTAGNINI, A., FENOGLIO, I., FUBINI, B., LE BLOND, J. S. & WILLIAMSON, B. J. 2010b. A physico-chemical assessment of the health hazard of Mt. Vesuvius volcanic ash. *Journal of Volcanology and Geothermal Research,* 191**,** 222-232.

HOUSLEY, D. G., BERUBE, K. A., JONES, T. P., ANDERSON, S., POOLEY, F. D. & RICHARDS, R. J. 2002. Pulmonary epithelial response in the rat lung to instilled Montserrat respirable dusts and their major mineral components. *Occup Environ Med,* 59**,** 466-72.

IARC 1997. Silica, some silicates, coal dust and para-aramid fibrils. . Lyon: International Agency for Research on Cancer.

IARC 2012. Arsenic, Metals, Fibres, and Dusts. International Agency for Research on Cancer.

JONES, T. & BÉRUBÉ, K. 2011. The bioreactivity of the sub-10µm component of volcanic ash: Soufrière Hills volcano, Montserrat. *Journal of Hazardous Materials,* 194**,** 128-134.

KNAAPEN, A. M., ALBRECHT, C., BECKER, A., HÖHR, D., WINZER, A., HAENEN, G. R., BORM, P. J. A. & SCHINS, R. P. F. 2002. DNA damage in lung epithelial cells isolated from rats exposed to quartz: role of surface reactivity and neutrophilic inflammation. *Carcinogenesis,* 23**,** 1111-1120.

LE BLOND, J., HORWELL, C., BAXTER, P., MICHNOWICZ, S., TOMATIS, M., FUBINI, B., DELMELLE, P., DUNSTER, C. & PATIA, H. 2010. Mineralogical analyses and in vitro screening tests for the rapid evaluation of the health hazard of volcanic ash at Rabaul volcano, Papua New Guinea. *Bulletin of Volcanology,* 72**,** 1077-1092.

LEE, S. H. & RICHARDS, R. J. 2004. Montserrat volcanic ash induces lymph node granuloma and delayed lung inflammation. *Toxicology,* 195**,** 155-165.

LEUNG, C. C., YU, I. T. S. & CHEN, W. 2012. Silicosis. *The Lancet,* 379**,** 2008-2018.

MOSSMAN, B. T. & GLENN, R. E. 2013. Bioreactivity of the crystalline silica polymorphs, quartz and cristobalite, and implications for occupational exposure limits (OELs). *Critical Reviews in Toxicology,* 43**,** 632-660.

PAVAN, C., TOMATIS, M., GHIAZZA, M., RABOLLI, V., BOLIS, V., LISON, D. & FUBINI, B. 2013. In Search of the Chemical Basis of the Hemolytic Potential of Silicas. *Chemical Research in Toxicology,* 26**,** 1188-1198.

RICE, F. L., PARK, R., STAYNER, L., SMITH, R., GILBERT, S. & CHECKOWAY, H. 2001. Crystalline silica exposure and lung cancer mortality in diatomaceous earth industry workers: a quantitative risk assessment. *Occupational and Environmental Medicine,* 58**,** 38-45.

SCHINS, R. P. F., DUFFIN, R., HÖHR, D., KNAAPEN, A. M., SHI, T., WEISHAUPT, C., STONE, V., DONALDSON, K. & BORM, P. J. A. 2002. Surface Modification of Quartz Inhibits Toxicity, Particle Uptake, and Oxidative DNA Damage in Human Lung Epithelial Cells. *Chemical Research in Toxicology,* 15**,** 1166-1173.

TOURMANN, J. L. & KAUFMANN, R. 1994. Biopersistence of the mineral matter of coal mine dusts in silicotic human lungs: is there a preferential release of iron? *Environ Health Perspect,* 102 Suppl 5**,** 265-8.

VALLYATHAN, V., SCHWEGLER, D., REASOR, M., STETTLER, L., CLERE, J. & GREEN, F. H. Y. 1988. Comparative In Vitro Cytotoxicity and Relative Pathogenicity of Mineral Dusts. *Annals of Occupational Hygiene,* 32**,** 279-289.

WILSON, M. R., STONE, V., CULLEN, R. T., SEARL, A., MAYNARD, R. L. & DONALDSON, K. 2000. In vitro toxicology of respirable Montserrat volcanic ash. *Occup Environ Med,* 57**,** 727-33.

Chapter 2

Background

2.1 Introduction

The focus of this thesis is the variable toxicity of crystalline silica and potential factors, specifically impurities, which may control its toxicity. Here, a background is provided, to define crystalline silica and assess the effect of impurities on its structure. This is followed by in-depth discussion of the potential diseases caused by crystalline silica exposure and the most recent understanding of the mechanisms of silica-induced pathogenicity. Evidence of the 'crystalline silica conundrum' - that crystalline silica has variable toxicity dependent of inherent characteristics of the silica itself and the influence of external factors - is presented, followed by discussion of the factors that may cause this observed variability. Finally, a brief introduction to exposure sources with a focus on cristobalite is provided, and there is a thorough examination of diatomaceous earth (DE) toxicity.

2.2 Crystalline silica

Silica is the most abundant compound in the Earth's crust and comes in a number of forms, including amorphous and crystalline. Silica has the chemical composition SiO_2 and consists of tetrahedra comprised of one silicon atom and four oxygen atoms ($[SiO_4]$), where two of the oxygen atoms are shared with neighbouring tetrahedra. The arrangement of these tetrahedra determine the form that

silica takes: in amorphous silica the tetrahedra are unordered, whereas in crystalline silica the tetrahedra are ordered and stacked or rotated in different ways to produce different polymorphs. There are five stable polymorphs of crystalline silica; quartz, tridymite, cristobalite, coesite and stishovite. Coesite and stishovite are both high temperature and pressure polymorphs and are not considered further here. Quartz is the most abundant polymorph as it is stable at surface temperature and pressure. Tridymite and cristobalite are low pressure but high temperature polymorphs with stability fields of 867-1470 °C and 1470-1727 °C respectively (Heaney et al., 1994). Transformations among these polymorphs can occur but are reconstructive and require energy and time. Therefore, cristobalite or tridymite often do not transform to quartz upon cooling, and are found metastably in ambient conditions, such as in volcanic settings, and the DE and ceramics industry.

Each polymorph also has two modifications based upon temperature; low (α) and high (β). Transitions between α and β forms are not reconstructive and do not require breaking of bonds, and occur immediately upon crossing a threshold temperature (i.e. it is a displacive transition). For quartz, this transition temperature is well-defined and occurs at 573 °C (Heaney et al., 1994), whereas, for cristobalite, the transition can occur between 170-270 °C (Frondel, 1962). The transition temperature is altered by structural imperfections such as the presence of impurities or the crystallisation temperature or annealing history as shown in synthetic and natural samples and is discussed below (Damby et al., 2014, Stevens et al., 1997). In this thesis, the primary focus is on cristobalite, however, the other polymorphs are also observed and discussed in Chapters 4 and 6.

2.2.1 Surface properties of crystalline silica

The silica structure composed of [SiO_4], as described above, is an ideal structure for an infinite solid. In reality, these tetrahedra terminate at the silica surface producing a number of surface features.

Two main functional groups present themselves at the surface of crystalline silica: siloxane links (Si-O-Si) or silanol groups (SiOH) due to the reaction with water in most environments (Rimola et al., 2013, Fubini et al., 1995). Surface silanols can be single silanols, whereby three Si-O bonds attach to the bulk, and the Si binds to O, which is bonded with H (Figure 2.1). Geminal silanols can also form, where only two Si-O bonds attach to the bulk. This means Si bonds with two O, which are each bonded to one H (Figure 2.1). Due to the orientation of the O-H bonds, the two H atoms in a geminal silanol cannot bond with each other (Rimola et al., 2013).

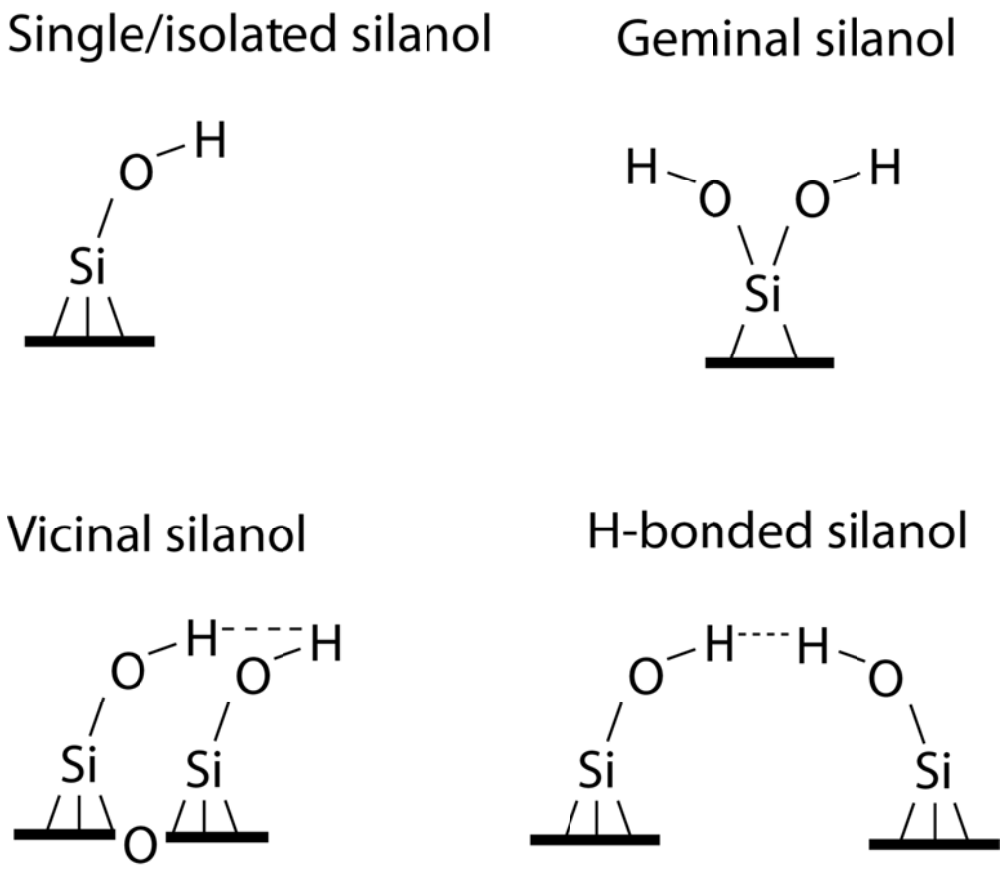

Figure 2.1: Different types of surface silanol commonly seen at the surface of crystalline silica. Adapted and simplified from 3D images in Rimola et al. (2013).

These different silanols can interact in different ways leading to a variety of different silanol group populations at the surface of the crystalline silica. Isolated silanols occur when a single silanol is >3.3 Å away from another silanol, and, therefore, H bonding or interaction cannot occur (Rimola et al.,

2013). This means the H is free for interaction with external components as both a H-bond donor and receptor. Paired silanols give rise to vicinal or H-bonded silanols (Figure 2.1). Vicinal silanols are characterised by a weak interaction between the H of two silanol groups, where the Si atoms are separated by one O atom (Figure 2.1) (Rimola et al., 2013). Therefore, the distance between silanols is <3 Å and H can interact. However, H bonding cannot occur due to the underlying structure in the bulk silica. This interaction can occur between single or geminal silanols so long as they are close enough to each other. H-bonded silanols can also occur between both single and geminal silanols, where strong H-bonds form between H atoms from two silanols that are closer together than 3 Å but do not belong to directly connected tetrahedral (Figure 2.1) (Rimola et al., 2013).

The distribution and extent of these silanol populations can be altered. Dehydration by heating anneals silanols into siloxanes (Figure 2.2) (Fubini et al., 1995, Fubini et al., 1999), or surface reconstruction after grinding can also produce distorted siloxanes or peroxide bridges (Si-$(O)_n$-Si) (Fubini et al., 1995, Fubini et al., 1990). Other surface features can also form through cleavage of the Si-O bond, producing either surface radicals by homolytic cleavage (Figure 2.3a), or a charged surface by heterolytic cleavage (Figure 2.3b) (Fubini et al., 1995). Radicals (where there are unpaired electrons in the atom), can from as $Si^{\bullet}$ or $SiO^{\bullet}$ (Figure 2.3a). The importance of these radical species and the distribution of silanols in relation to the silica surface bioreactivity are discussed in Sections 2.4.2.4 and 2.5.1 below.

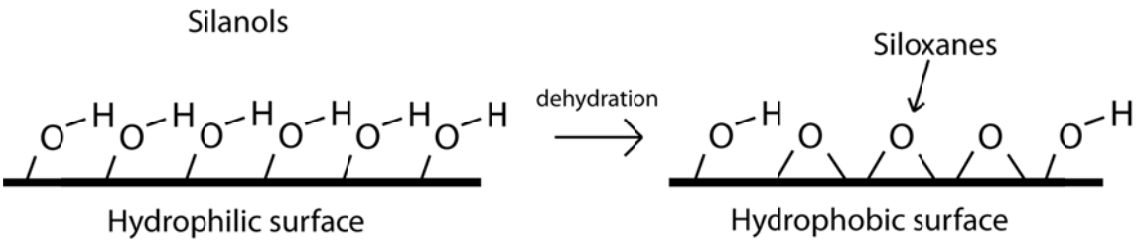

Figure 2.2: Hydrophilic silica surface comprising of silanols that converts to a hydrophobic surface mainly consisting of siloxanes upon dehydration. Redrawn from Fubini et al. (1995).

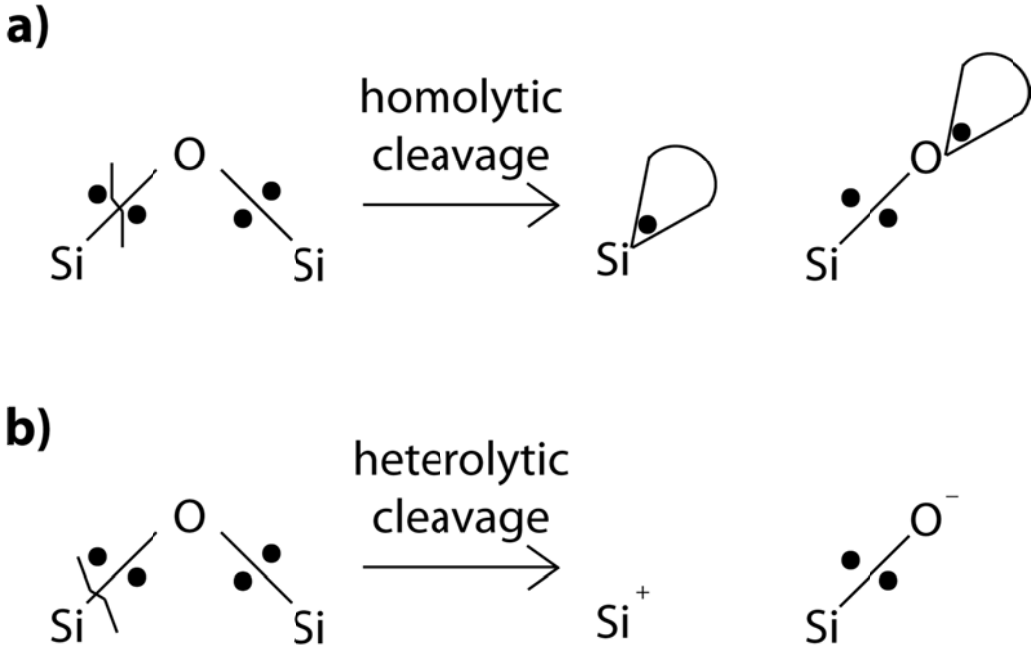

Figure 2.3: Cleavage of the Si-O bond can produce **a)** silica surface radicals by homolytic cleavage, or **b)** charged silyl cations (Si^{+}) or siloxy anions ($Si\text{-}O^{-}$). Redrawn from Fubini et al. (1995).

2.2.2 Impurities in crystalline silica

Although the chemical composition of silica is SiO_2, Al or Fe ions can substitute for silicon in the silica tetrahedron due to their similar charge and atomic radius. As these cations have a lower positive charge (3+ compared to 4+ for silicon), interstitial cations (e.g. Na^{+}, Li^{+}, Ca^{2+}) are required to balance the charge (Deer et al., 2013). These substitutions are more common in cristobalite and tridymite than quartz, as their structure allows more ready substitution of impurities than denser quartz (Shackelford and Doremus, 2008).

Treatment of amorphous silica with impurities pre-crystallisation, either by the incipient wetness method or by sol/gel techniques, has been shown to alter the crystallisation temperature and polymorph produced (Table A1 in Appendix 1). Cristobalite is the polymorph most often formed over a range of temperatures and impurities in these experiments, however, quartz may form at low temperature and dopant concentrations (Saltzberg et al., 1992, Şan and Özgür, 2009) and tridymite is sometimes observed (Chao and Lu, 2002, Thomas et al., 1994, Venezia et al., 2001). If dopant concentrations are high, other mineral phases often form, such as mullite or anorthite, after Al and Na doping or Al and Ca doping, respectively (Perrotta et al., 1989, Saltzberg et al., 1992). Doping with impurities can also decrease the α-β transition temperature of cristobalite (Alcalá et al., 1996), and also, if dopant concentrations are high enough, to completely inhibit the transition, producing chemically stabilised β-cristobalite (e.g. Alcalá et al., 1996, Chao and Lu, 2002, Perrotta et al., 1989, Saltzberg et al., 1992). As doping is shown to result in Al or Fe in tetrahedral coordination when co-doping with Na or Ca (Gai-Boyes et al., 1993, Zhang et al., 1998), it is hypothesised that the interstitial cations prevent the decrease in volume needed to convert β-cristobalite to α-cristobalite upon cooling and, therefore, a β-cristobalite structure remains, often called chemically stabilised cristobalite (CSC) (Saltzberg et al., 1992). The incorporation of structural impurities has also been shown to increase the lattice spacing size in α-cristobalite when dopant concentrations are not high enough to stabilise β-cristobalite (Chao and Lu, 2002). The silica sol/gel method is applied in Chapter 6 to produce cristobalite with Al and Na in its structure. Low dopant concentrations were chosen with an aim to produce impure α-cristobalite (the form seen in volcanic ash, (Damby et al., 2014)), rather than to stabilise β-cristobalite.

2.3 Crystalline silica toxicity

Crystalline silica has the potential to cause respiratory disease and cancer (see below). However, it is well known that the toxic potential of crystalline silica is variable, and exposure to silica does not

cause disease or cancer in all circumstances (e.g. IARC, 1997). Here, the adverse health effects from exposure to crystalline silica are described and the possible mechanistic pathways involved in silica pathogenicity discussed.

2.3.1 Diseases caused by exposure to crystalline silica

2.3.1.1 Silicosis

Silicosis is an untreatable disease specific to silica exposure. It is a fibrotic pulmonary disease that is still of concern worldwide today, predominantly due to occupational exposures, and presents itself in three forms; acute silicosis, accelerated silicosis, and chronic silicosis (Greenberg et al., 2007, Leung et al., 2012). Acute silicosis can occur after exposure to high concentrations of silica over a short period of time (<5 years) (NIOSH, 2002). Acute silicosis is often referred to as silicoproteinosis, as it is characterised by similar pathological characteristics as alveolar proteinosis, where silica induces the production of excessive amounts of proteinaceous material and surfactant protein from cells lining the alveoli (Leung et al., 2012, NIOSH, 2002). Accelerated silicosis has a latency period of 5-10 years from first exposure to the onset of disease (NIOSH, 2002). This is characterised by similar pathogenic properties as the more common chronic silicosis but which develop more rapidly. Chronic silicosis occurs due to exposure to low concentrations of silica over >10 years (Ding et al., 2002, Greenberg et al., 2007, NIOSH, 2002). Chronic silicosis is characterised by silicotic nodules, which form from silica-containing macrophages (a type of white blood cell which is part of the body's immune system) and reticulin (collagen fibre in connective tissue). Histologically, these appear as 'histologic tornadoes', with a hyaline centre, and reticulin arranged concentrically around this, with inflammatory cells at the periphery (Greenberg et al., 2007). When these nodules are <1 cm it is termed simple silicosis. However, this can develop into complicated silicosis, also known as

progressive mass fibrosis (PMF), when nodules coalesce into pulmonary masses >1 cm (Leung et al., 2012, Ding et al., 2002). It is possible that secondary diseases and infections can develop at this stage. Silicosis development often leads to secondary mycobacterial or fungal infections, such as tuberculosis, and chronic obstructive pulmonary disease (COPD) (Leung et al., 2012, NIOSH, 2002). Autoimmune diseases, such as scleroderma, lupus, progressive systematic sclerosis, rheumatoid arthritis and autoimmune haemolytic anemia may also be associated with workers exposed to respirable crystalline silica (Leung et al., 2012, NIOSH, 2002).

2.3.1.2 Cancers

Crystalline silica in the form of quartz and cristobalite has been classified as a Group 1 carcinogen (IARC, 1997), meaning that there is sufficient evidence to support the hypothesis that crystalline silica is carcinogenic to humans. Carcinogenic risk to humans has been considered for a number of industrial exposures including ore mining, granite quarrying, ceramic, pottery and DE industries, and foundry workers. However, there is still controversy as to the link between silicosis and cancer, as many of the studies used did not account for confounding factors, such as exposure to other occupational carcinogens or smoking.

The mechanism of silica-induced cancer is also not fully understood. A review by Borm et al. (2011) considered the mechanisms of primary genotoxicity or secondary genotoxicity. Primary genotoxicity involves direct interaction of particles with DNA, or particle interaction with cells causing increased reactive oxygen species (see below for discussion) and depletion of antioxidants and occurs in the absence of inflammation. Secondary genotoxicity involves chronic inflammation, with the recruitment of inflammatory cells to particle deposition sites. Secondary genotoxicity was the most likely mechanism at low doses of crystalline silica exposure, whereas primary genotoxicity may only occur at extremely high exposure conditions.

2.4 Mechanisms of crystalline silica toxicity

The mechanisms by which crystalline silica cause disease are still not fully understood. Due to the number of different diseases and adverse effects that silica can cause in the respiratory tract, it is probably that a number of different mechanisms play a role in silica pathology. Particle deposition, particle retention and particle clearance from the lung are important factors in determining particle toxicity. Once deposited in the lung, a number of pathways might ensue, causing inflammation, oxidative stress and, ultimately, leading to silicosis or cancer. The latest understanding of these potential pathways is discussed below.

2.4.1 Inhalation of particles

In order for crystalline silica to cause the above diseases, it must be able to enter into the body. The primary pathway is by inhalation, whereby particles suspended in the atmosphere enter through the nasal or oral cavities, and travel down the trachea into the bronchioles and alveoli (Figure 2.4). How far particles can penetrate into the lung is determined by particle size and shape, as airway diameters decrease further into the body and particle deposition is affected, as described below. Particles <100 µm aerodynamic diameter are deemed inhalable but cannot penetrate deep into the lung and remain in the upper regions of the respiratory tract, where they are easily removed and are, therefore, not likely to cause adverse health effects (Quality of Urban Air Review Group, 1996). However, the thoracic fraction (<10 µm aerodynamic diameter) and the respirable fraction (<4 µm aerodynamic diameter) can penetrate into the tracheobronchiolar region and alveolar region respectively (Quality of Urban Air Review Group, 1996), where adverse health effects may occur.

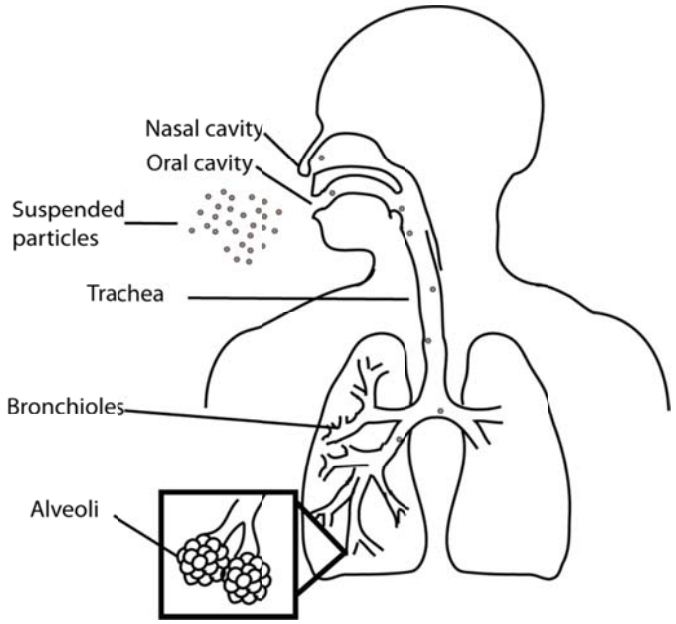

Figure 2.4: Some key components of the respiratory tract. Adapted from Ogele (2014).

Particle size and mass is important in particle inhalation, deposition and clearance (see below) and warrants further discussion here. Particle size can be measured in a number of different ways. Geometric particle diameter can refer to the equivalent spherical diameter (based on particle volume) or be measured directly by image analysis of particles. Alternatively, the aerodynamic diameter can be measured. The aerodynamic particle diameter is the diameter of a unit density sphere having the same terminal settling velocity as the sampled particle, regardless of the particle's shape and density (McClellan, 2000, Quality of Urban Air Review Group, 1996) and is more useful in determining the likelihood of particles being deposited and retained in the lung. Classifications of the inhalable, thoracic and respirable fractions above are based on aerodynamic particle diameter.

Measurements of particle size in this thesis are based on geometric diameter and have been measured by laser diffraction and image analysis. This provides data in volume % or number %, respectively. Measurements of volume % are heavily mass biased, i.e. larger particles of greater mass account for a high percentage of the total % (McClellan, 2000). Therefore, this mass median

diameter calculated for a sample analysed by laser diffraction will be greater than the count median diameter calculated for samples analysed by image analysis and are not directly comparable. These are also not comparable to the aerodynamic diameter. However, the <4 and <10 μm fractions are used as an indicator of material able to be deposited in the lung. The importance of particle size in particle deposition and in toxicity once deposited is discussed in detail below.

2.4.2 Fate of inhaled particles

2.4.2.1 Deposition of particles in the lung

Deposition of particles can occur by five different mechanisms: sedimentation, impaction, diffusion, interception and electrostatic precipitation. Sedimentation, impaction and diffusion are governed by particle size (Schulz et al., 2000). Diffusion is important for particles <0.5 μm diameter. As the distance a particle can travel increases with time and decreased particle diameter, it is more likely that smaller particles that can travel further will hit airspace surfaces and be deposited. Therefore, deposition by diffusion is dominant in the small airways in the lung periphery (Schulz et al., 2000). Sedimentation is important for particles >0.5 μm in diameter. As particles are impacted upon by gravitational forces, and this is greater on particles with increased mass, larger, denser particles are more likely to be deposited by sedimentation. This often occurs in the small conducting airways and alveoli (Schulz et al., 2000). Impaction occurs when particles continue on their projected path, rather than following the airstream through the airways, due to particle inertia, and become deposited on airway walls. Impaction is also affected by particle mass and size, as larger particles have a greater stopping distance (Schulz et al., 2000). However, unlike diffusion and sedimentation, impaction is highly reliant upon the airflow velocity. Therefore, deposition by impaction is most likely to occur in

the larger conducting and extrathoracic airways where airflow velocity is high and there are rapid changes in airflow direction (Schulz et al., 2000).

Interception and electrostatic forces are also causes of particle deposition but are much rarer. Interception occurs when the edge of a particle contacts the airway surface and is an important form of deposition for particle fibres (i.e. particles with aspect ratio >3, long axis >5 µm and diameter <3 µm (WHO, 1985)). As most ambient particles have a neutral charge due to interaction with air ions before entering the lung, electrostatic deposition is more commonly associated with freshly fractured particles, where the surface charge may vary substantially. Therefore, this is likely to be important in occupational settings, such as sand blasting, where exposure to freshly fractured crystalline silica is common (IARC, 1997, Leung et al., 2012). Although total deposition is important, particles deposited in the extrathoracic region (inhalable fraction – thoracic fraction) are less likely to cause adverse health effects than particles deposited in the tracheobronchiolar region (thoracic fraction – respirable fraction) and alveolar region (respirable fraction).

2.4.2.2 Particle clearance and retention in the lung

Once a particle is deposited in the lung it can either be cleared or retained. Clearance can occur by mechanistically or biologically mediated particle transport or by absorption of dissolved materials (Kreyling and Scheuch, 2000). As crystalline silica is insoluble, only clearance by particle transport is discussed here. Particle clearance is dependent on where in the lung particles are deposited. Particles deposited in the thoracic region are mainly cleared by mucociliary transport, which occurs when cilia, small hairs between 5-50 µm in length, beat to move the overlying mucus layer (Kreyling and Scheuch, 2000). As deposited particles can interact immediately with macrophages (defensive phagocytic cells) and be engulfed (phagocytosis, see below), both free particles and those engulfed by macrophages can be transported up the mucociliary escalator to the pharynx where they are

swallowed or expectorated. This process is rapid and occurs over a timescale of hours. However, some particles deposited in this region are cleared more slowly with half-times between 5 and 30 days (Kreyling and Scheuch, 2000).

If particles are deposited in the alveolar region, particle transport is much slower requiring long-term clearance pathways. These include, but are not limited to, free particle transport along the epithelium (cells lining the airway walls) towards ciliated airways where mucociliary clearance can occur, or through the epithelium into interstitial spaces or towards the lymphatic system (Kreyling and Scheuch, 2000). Phagocyte mediated particle clearance also occurs where particles engulfed by macrophages are moved to the same regions as free particles but via chemotactic forces, chemokinetic or random movement (Kreyling and Scheuch, 2000). Phagocytic cells are vital in the particle clearance pathway and specifically alveolar macrophages. Some particles that are taken up by phagocytes are dissolved in low pH lysosomal fluids within compartments of the cell. However, due to crystalline silica's low solubility, breakdown does not occur and the toxic effect of silica on cells (see below) means clearance is low and, therefore, particle retention in the lung leads to the activation of a number of pathways which may eventually conclude in disease. The role of macrophages in silica-induced disease pathways is discussed in detail below.

2.4.2.3 Activation of macrophages

As silica particles do not release chemical signals, it is likely that macrophages come into contact with particles accidentally once deposited in the respiratory tract or by epithelial cell signalling. Binding of the particle to the cell then occurs which may or may not lead to phagocytosis (Gilberti et al., 2008). Particle uptake by macrophages is not fully understood. However, it is hypothesised that scavenger receptors are partially responsible for binding with silica particles, as blocking of these receptors causes a reduction in binding and toxicity (Gilberti et al., 2008, Hamilton et al., 2008). It is

not known if internalisation of the particle is necessary for silica-induced toxicity, or if external binding can also cause toxicity (Gilberti et al., 2008).

Internalised particles can be cleared from the lung as discussed above. Alternatively, particle clearance may fail. Particle uptake involves the internalisation of particles into lysosomal compartments, which have low pH, in order to try to break down the particle. However, as crystalline silica is insoluble, a failure to break down the particle can lead to oxidative stress, a loss of membrane integrity and apoptosis, programmed cell death (Ghiazza et al., 2011, Gozal et al., 2002, Thibodeau et al., 2004). This can lead to the recruitment of more phagocytic cells to remove the dead cell material and the newly exposed particle. These in turn may die leading to the recruitment of more phagocytic cells and a cascade of signalling pathways, which can lead to inflammation or cancer.

Cell signalling involves a number of transcription factors that can be activated by exposure of cells to silica. Activator protein 1 (AP-1), has been implicated in the pathway to apoptosis, and can be stimulated by the mitogen-activated protein kinase (MAPK) pathways (Ding et al., 2002). Activation of nuclear factor κB (NF-κB), another transcription factor, can also be stimulated in macrophages exposed to silica (Chen et al., 1995, Gozal et al., 2002, Rojanasakul et al., 1999). NF-κB in un-activated cells remains in the cytoplasm, bound to inhibitory proteins. Upon exposure to silica the inhibitory proteins degrade, releasing NF-κB, allowing it to translocate into the nucleus, where it can bind to DNA. This activation can be assessed by fluorescently labelling NF-κB and locating whether this has translocated into the nucleus using fluorescent imaging (see Chapter 3 for detail and Chapter 7 for application). Once activated, NF-κB can play a role in the production of cytokines, which are signalling proteins often involved in inflammation (Chen et al., 1995, Gozal et al., 2002, Rojanasakul et al., 1999).

A number of pro-inflammatory chemokines and cytokines have been implicated in silica-induced diseases, such as interleukins and chemoattractants. Of these, the most studied is TNF-α, which is a pro-inflammatory cytokine implicated in silica-induced inflammation and fibrosis (Piguet et al., 1990). The alveolar macrophage has been identified to play a critical role in cytokine production (Gozal et al., 2002), and silica is able to upregulate TNF-α mRNA expression in macrophages and TNF-α protein production (Chen et al., 1995, Gozal et al., 2002, Rojanasakul et al., 1999). However, different macrophage cell types have different abilities to produce TNF-α or induce NF-κB activation (e.g. silica-exposed RAW 264.7 macrophages enhance these, whereas silica-exposed IC_21 macrophages do not (Gozal et al., 2002)). A number of studies have shown that the inhibition of NF-κB prevents the production of TNF-α protein and, therefore, may prevent silica fibrosis (Chen et al., 1995, Gozal et al., 2002, Rojanasakul et al., 1999). TNF-α production by treated macrophages is assessed in Chapters 5 and 7 to determine the pro-inflammatory response of cells treated with DE or synthetic crystalline silica.

Silica has also been shown to upregulate expression of interleukin-1 (IL-1α and IL-1β) (Chen et al., 1995), another pro-inflammatory cytokine. Silica may also alter anti-inflammatory cytokines, such as IL-10 and other chemoattractants involved in neutrophil and macrophage chemotaxis. Most recently, the role of the inflammosome (a multicomplex protein called NALP3) in crystalline silica-induced toxicity has been shown (Cassel et al., 2008, Peeters et al., 2014). Proteins within the inflammosome can react to form capase-1, which has the ability to produce IL-1β cytokines from their precursor Pro-IL-1β (Cassel et al., 2008, Leung et al., 2012). It has been shown in silica-treated macrophages, epithelial cells and mice that secretion of IL-1β is dependent upon the NALP3 inflammosome, as NALP3 blockers inhibited IL-1β production and inflammation was decreased (Cassel et al., 2008, Peeters et al., 2014).

2.4.2.4 Role of reactive oxygen species and reactive nitrogen species

Reactive oxygen species (ROS) and reactive nitrogen species (RNS) are highly volatile molecules that may be implicated in silica toxicity. ROS can be both particle-derived and cell-derived.

2.4.2.4.1 Particle-derived ROS

Dangling bonds produce surface based silica radicals, as described above (Section 2.2.1). These radicals can react with oxygen to form surface bound ROS, including $SiO^{\bullet}$, $SiO_2^{\bullet}$, $SiO_3^{\bullet}$ and $Si\text{-}O_2^{-\bullet}$ (Fubini and Hubbard, 2003). The surface bound ROS can be the source of reactions to produce free radicals. The pure surface can also produce free radicals in solution (Duffin et al., 2001, Fenoglio et al., 2001, Ghiazza et al., 2011, Schins et al., 2002). The silica surface ROS can react in water to produce hydroxyl free radicals ($HO^{\bullet}$) by the following pathway:

$$SiO^{\bullet} + H_2O \rightarrow SiOH + HO^{\bullet}$$

Or can react with H_2O_2 (endogenously available in the lung) in the following manner to produce $HO^{\bullet}$:

$$SiO_2^{\bullet} + H_2O_2 \rightarrow SiOH + HO^{\bullet} + O_2$$

$$Si^{+}O_2^{-\bullet} + H_2O_2 \rightarrow SiOH + HO^{\bullet} + O_2$$

Iron has also been shown to be important in silica-induced $HO^{\bullet}$ production (Cullen et al., 1997, Fubini and Hubbard, 2003). Only trace amounts of iron are needed to produce $HO^{\bullet}$ via the catalytic Fenton reaction, in the presence of H_2O_2:

$$Fe^{2+} + H_2O_2 \rightarrow Fe^{3+} + OH^{-} + HO^{\bullet}$$

Alternatively Fe^{2+} can react with oxygen to form superoxide ions, which can react further with H_2O to produce H_2O_2 and $HO^{\bullet}$:

$$Fe^{2+} + O_2 \rightarrow Fe^{3+} + O_2^{-\bullet}$$

$$O_2^{-\bullet} + H_2O \rightarrow HO_2^{\bullet} + OH^- \text{ or } O_2^{-\bullet} + 2H^+ + e^- \rightarrow H_2O_2$$

$$O_2^{-\bullet} + H_2O_2 \rightarrow HO^{\bullet} + OH^- + O_2$$

As only Fe^{2+} is involved in catalysing these reactions the redox state of iron is important. However, Fe^{3+} can be reduced to Fe^{2+} in the presence of reductants (e.g. through the Haber Weiss cycle) and therefore total surface iron may be important. Fubini et al. (2001) have shown that both the redox state and coordinative state are important in determining the ability of Fe to produce $HO^{\bullet}$.

2.4.2.4.2 Cell-derived ROS

Exposure of cells to crystalline silica can lead to the 'respiratory burst' where phagocytic cells (macrophages) produce $O^{\bullet-}$, H_2O_2 and increased oxygen consumption (Albrecht et al., 2005, Castranova, 1994, Zhang et al., 2000). An increase in RNS is also observed by increased $NO^{\bullet}$ and reactions of NO and $O_2^{\bullet-}$ to form peroxynitrite (Albrecht et al., 2005, Hamilton et al., 2008).

Albrecht et al. (2005) showed that the concentration of ROS could be correlated with the influx of inflammatory cells into rat lungs treated with quartz, and RNS with the total cell count in the lung. This indicates the importance of ROS/RNS in silica-induced toxicity. The use of ROS scavengers decreased the ability of crystalline silica to induce cytotoxicity or genotoxicity in rats (Zhang et al., 2000). ROS scavengers have also decreased the ability of silica to induce some of the inflammatory pathways described above: silica-induced AP-1 activation was shown to be an ROS-mediated process

(Ding et al., 2002), and H_2O_2 or $HO^{\bullet}$ scavengers can inhibited silica-induced NF-kB and TNF production (Ke et al., 2006, Rojanasakul et al., 1999), also shown in cristobalite-treated macrophages, where the addition of antioxidants decreased the ability of cristobalite to induce TNF-α and MIP-2 (another pro-inflammatory cytokine) (Barrett et al., 1999). ROS is also involved in NF-kB activation in human monocytes treated with ultrafine carbon black (Brown et al., 2004). These studies show the importance of ROS and RNS in inducing key mechanisms in the silica-induced inflammation and fibrosis pathways. ROS/RNS are also implicated in genotoxicity and, therefore, potentially silica-induced cancers. ROS are also important in the inflammosome pathway leading to secretion of pro-inflammatory cytokines (Cassel et al., 2008).

2.5 Variability of crystalline silica toxicity

Although crystalline silica is known to be able to cause the diseases above and there is sufficient evidence to support that it is carcinogenic to humans, it is widely recognized that not all crystalline silica has the same toxic or carcinogenic potency: 'the crystalline silica conundrum'. In the 1997 IARC report, although crystalline silica was classified as carcinogenic to humans (IARC, 1997), it was noted that:

"carcinogenicity to humans was not detected in all industrial circumstances studied. Carcinogenicity may be dependent on inherent characteristics of the crystalline silica or external factors affecting its biological activity or distribution of its polymorphs."

Other studies have also highlighted the variability of crystalline silica carcinogenicity and fibrogenic potency (Borm et al., 2011, Donaldson and Borm, 1998, HSE, 2002, Meldrum and Howden, 2002, Mossman and Glenn, 2013). The variability of crystalline silica toxicity is well established amongst

epidemiology studies (Donaldson and Borm, 1998, IARC, 1997, IARC, 2012), and some animal and *in vitro* studies directly comparing crystalline silica reactivity, including those which aim to determine potential factors affecting crystalline silica toxicity, are discussed below.

A number of studies have compared different quartzes in terms of their toxic potential in animal models to determine the variable toxicity of quartz. Clouter et al. (2001) compared the ability of two workplace quartz samples and DQ12 (a quartz sand of high toxic potency) to cause inflammation after intratracheal instillation in rats. Rats treated with DQ12 exhibited increased inflammation, measured by increased neutrophil numbers, and also had increased protein levels in the bronchoalveolar lavage, whereas both commercial samples did not induce these effects. These differences could not be attributed to particle size, surface area, released iron or $HO^{\bullet}$ production (the importance of which are discussed below). Seiler et al. (2004) considered toxicity of four commercial quartz dusts and DQ12 to rats and showed differences in inflammation, TNF-α production and mutagenicity of these samples. Interestingly, TNF-α measurements for the commercial samples in Seiler et al.'s study were below control levels, suggesting a down-regulation, unlike DQ12 treatment where there was an up-regulation of TNF-α. The inflammatory potency and cytotoxicity of Min-U-Sil quartz (99% mineral quartz powder), fine synthetic quartz and nanoquartz samples in rats differed and was not related to particle size or surface area, but did correlate with haemolytic potential used as an assessment of surface reactivity (Warheit et al., 2007). This suggests that variable surface properties of these different quartzes led to the differences in their toxicity.

In vitro, DQ12 has also been shown to be more cytotoxic to alveolar macrophages and more haemolytic (ability to rupture red blood cell (RBC) membranes, which act as a model cell membrane) than the commercial quartz used by Clouter et al. (2001). A study of 16 quartz samples (Bruch et al., 2004), showed their toxicity to guinea-pig alveolar macrophages to vary from as cytotoxic as DQ12 to inactive at the highest dose tested (120 μg/ 3 x 10^5 cells). TNF-α production by rat alveolar

macrophages also varied substantially amongst these samples (Bruch et al., 2004). Slight differences in the concentrations of DQ12 and commercial quartz needed to cause significant DNA strand breakage have also been observed (Cakmak et al., 2004). Although a number of toxicology studies have used cristobalite and quartz, none have directly compared the toxicities of different cristobalite-only powders. However, studies of cristobalite containing DE powders and volcanic ash have shown these dusts to have variable toxicity, these are discussed in full below.

2.5.1 Factors affecting crystalline silica toxicity

The variable toxicity of crystalline silica highlighted above has been attributed to a number of different particle properties and external factors, including polymorphic form, age of the surface, presence of impurities, and particle size and surface area (Meldrum and Howden, 2002). These factors are discussed in detail here. As it is the insoluble particle surface that biological components react with, factors controlling silica toxicity likely relate to its surface properties, and, in particular, surface silanols and surface radicals, which are implicated in silica induced toxicity. The role of surface radicals leading to oxidative stress is discussed above (Section 2.4.2.4).

The density of silanol populations on the silica surface cannot be correlated with its haemolytic potential (Pavan et al., 2013). However, the distribution of isolated and geminal silanols is considered to determine the ability of silica to rupture RBC membranes (Pavan et al., 2013). Pandurangi et al. (1990) showed a correlation between isolated silanol populations and haemolytic potential. Heating of samples anneals the silanol surface to siloxanes (see Section 2.2.1), causing a decrease in H-bonded or interacting silanols and an increase in isolated silanols and, subsequently, a decrease in the haemolytic potential (Hemenway et al., 1993, Pandurangi et al., 1990). The following factors are likely to affect these surface properties and further support the premise here: that surface silanol populations and radicals are important in crystalline silica toxicity.

2.5.1.1 Crystalline silica polymorph

There are few studies which directly compare the toxicities of the different silica polymorphs. An early study (King et al., 1953) on the effect of intratracheally injected quartz, tridymite or cristobalite into rats showed that quartz and cristobalite had similar fibrogenic potency, although cristobalite produced fibrosis more rapidly. However, tridymite was much more potent, causing more severe fibrosis extremely rapidly. Since then, few studies have compared tridymite with the other polymorphs, however, Marks et al. (1956) showed no difference between cristobalite and tridymite toxicity, which was greater than the toxicity of quartz. More recently, Ghiazza et al. (2011) also indicated that cristobalite was more cytotoxic and inflammatory than quartz samples used as controls, although this was not the focus of their study which assessed DE toxicity and is discussed below. These studies indicate cristobalite and tridymite may have a higher toxic potency than quartz.

However, Elias et al. (2002), indicated that polymorphic form did not control the transforming potency (indicator of genotoxicity) or cytotoxicity of silica, and that surface silanol populations were more important. Also, a review comparing literature of the toxicities of quartz and cristobalite showed no difference in their toxic potential overall (Mossman and Glenn, 2013). This is likely because quartz and cristobalite have similar densities of silanol groups at their surface (Meldrum and Howden, 2002) and, as it is known that silanol groups are important in crystalline silica reactivity (see above), it is unlikely the polymorphic form is important in controlling silica toxicity. The similar structure of cristobalite and tridymite also suggests the polymorph would not control toxicity (Smith, 1998). This, and the variable toxic potency among samples of the same polymorph, suggests that factors affecting surface properties are more important in determining crystalline silica toxicity than the polymorphic form.

2.5.1.2 Freshly fractured vs aged surface

The age of the silica surface has been shown to be important in determining its reactivity. Grinding of silica cleaves Si-O bonds by homolytic or heterolytic cleavage. With homolytic cleavage, dangling bonds form, producing $Si^{\bullet}$ or $SiO^{\bullet}$ surface radicals. Heterolytic cleavage produces a charged surface or Si^{+} and $Si\text{-}O^{-}$ (Fubini et al., 1995, Vallyathan et al., 1988) (Section 2.2.1). These highly reactive species subsequently react with components in the atmosphere to form peroxyradicals ($Si\text{-}O_2^{\bullet}$), superoxide radicals ($Si\text{-}O_2^{\bullet -}$) or CO_2-based radicals ($Si\text{-}CO_2^{\bullet}$) (Fubini et al., 1990). These species can also reform into strained reactive siloxane or peroxide bridges (Si-O-Si, $Si\text{-}(O)_n\text{-}Si$) (Fubini et al., 1995, Fubini et al., 1987, Fubini et al., 1990).

It has been shown that, in air, silica surface radicals diminish with a half-life of ~ 30 h, which is related to a decrease in the generation of $HO^{\bullet}$ in H_2O_2 (Vallyathan et al., 1988). Further, this was linked to the respiratory burst of alveolar macrophages. As the age of the silica surface (stored in air) increased, the haemolytic potency to RBCs, cytotoxicity to alveolar macrophages and release of H_2O_2 and superoxide from macrophages was decreased (Vallyathan et al., 1988). Surface radicals have been shown to persist on the silica surface in aged dusts, however, these do not appear to be involved in silica pathogenicity (Fubini et al., 1995). Freshly fractured surfaces have also been shown to be able to stimulate the AP-1 pathway (described above), showing AP-1 DNA binding and transactivation activity (Ding et al., 2002).

2.5.1.3 Role of impurities

Surface modifications by the addition of impurities such as aluminium lactate and iron in various forms have been shown to alter the toxic potential of silica by altering surface properties of the silica particles or by reacting with ROS.

The effect of Al treatment on crystalline silica toxicity is well established (Table 2.1). Duffin et al. (2001) showed treatment of DQ12 quartz with aluminium lactate (AL) decreased its haemolytic potential, where the effect was more pronounced at low doses than high doses (12-fold decrease at 0.63 mg/ml compared to 2-fold at 5 mg/ml). Other studies have also shown the ability of $AlCl_3$ treatment and treatment with Al-rich clay extracts to decrease the haemolytic potential of quartz (Nolan et al., 1981, Stone et al., 2004). AL treatment of quartz has also been shown to decrease the cytotoxicity to lung macrophages or epithelial cells (Knaapen et al., 2002, Schins et al., 2002, Thibodeau et al., 2004) and reduce quartz-induced DNA damage and particle uptake into epithelial cells *in vitro* (Schins et al., 2002).

The ability of AL to decrease the cytotoxic, and inflammatory potency of quartz *in vivo* by a decrease in inflammatory cells and proteins, has been shown in a number of studies (Albrecht et al., 2005, Cullen et al., 1997, Duffin et al., 2001, Duffin et al., 2002, Duffin et al., 2007, Knaapen et al., 2002). To further assess the potential mechanisms by which AL treatment reduces quartz toxicity, Duffin et al. (2001) measured NF-κB activation, MIP-2 (a pro-inflammatory cytokine) mRNA expression and $HO^{\bullet}$ generation by particles. AL treatment significantly decreased NF-κB DNA binding and MIP-2 mRNA expression compared to saline treated DQ12, and caused a 60% reduction in $HO^{\bullet}$ generation indicating a reduction in pro-inflammatory indicators and oxidative stress. Treatment with AL has also been shown to decrease DNA damage *in vivo* (Knaapen et al., 2002). It is clear from these studies that Al can reduce the toxic potential of quartz. However, the mechanisms by which Al causes this reduction is poorly understood. It is thought that Al bind to silanols, replacing H^+ and thereby preventing adsorption of cell membrane components to the silica surface (Fubini, 1998).

The polymer PVNO can also dampen quartz toxicity and is often more effective than AL (Albrecht et al., 2005, Knaapen et al., 2002, Nolan et al., 1981). The binding of PVNO is known to be independent

of Al, as the presence of Al does not decrease PVNO binding (Nolan et al., 1981). It is known that PVNO binds by a strong H bond with silanol groups on the surface (Fubini, 1998). The alteration of silanol groups by both AL and PVNO and the accompanying decrease in quartz toxicity shows the importance of these groups in silica-induced toxicity, and that both AL and PVNO can decrease toxicity even though they occupy different binding sites, demonstrating that multiple surface sites may be important in silica toxicity.

Table 2.1: Summary of toxicology studies with aluminium-treated quartz, and PVNO-treated quartz.

Study	Crystalline silica	Impurity compound	Animal/ Cell	Type	Key endpoints	Results
Albrecht et al. (2005)	DQ12	AL PVNO	Animal	Rat	Inflammatory cell count β-Glucuronidase and myeloperoxidase cytotoxicity (LDH) Histopathology	AL treatment ↓ inflammatory and cytotoxic indicators PVNO ↓ inflammatory and cytotoxic indicators and was more inhibitory than AL
Cullen et al. (1997)	DQ12	AL	Animal	Rat	Inflammatory cells	AL treatment ↓ inflammatory indicators
		AL	Cell	macrophages	Cytotoxicity (LDH) H_2O_2 superoxide dismutase	AL treatment ↓ superoxide dismutase (involved in oxidant injury)
		AL	acellular		OH generation	No difference to untreated quartz
Duffin et al. (2001)	DQ12	AL	Cell	human RBC	Haemolysis	AL treatment ↓ haemolysis
			Animal	Rat	Inflammatory cell count MIP-2 NF-κB activation	AL treatment ↓ inflammatory indicators and NF-κB activation
			acellular		OH generation	AL treatment ↓ OH generation by quartz
Duffin et al. (2002), (2007)	DQ12	AL	Animal	Rat	MIP-2 Inflammatory cell count	AL ↓ inflammatory indicators

Knaapen et al. (2002)	DQ12	AL	Cell	Rat lung epithelial type II cells	Cytotoxicity (MTT)	AL and PVNO treatment ↓ cytotoxicity
		PVNO		Human neutrophils	superoxide release	AL did not alter superoxide release, PVNO ↓ superoxide release
			Animal	Rat	Total protein Cytotoxicity (LDH) Myeloperoxidase DNA damage	AL and PVNO ↓ inflammatory indicators, cytotoxicity and DNA damage PVNO was more effective at ↓ quartz reactivity than AL
Nolan et al. (1981)	Min-U-Sil	$AlCl_3$ PVNO	Cell	human RBC	Haemolysis	Al treatment ↓ haemolysis PVNO ↓ haemolysis
Thibodeau et al. (2004)	Min-U-Sil	AL	Cell	MH-S	Apoptosis lysosomal damage cytotoxicity (LDH)	AL treatment ↓ apoptosis AL treatment did not ↓ lysosomal leakage but altered lysosomal damage AL treatment ↓ cytotoxicity
Schins et al. (2002)	DQ12	AL PVNO	Cell	A549 human lung epithelial cells	DNA damage Cytotoxicity (LDH, MTT) Particle uptake	AL and PVNO ↓ DNA damage, cytotoxicity, and particle uptake
			acellular		OH generation	AL and PVNO ↓ OH generation
Stone et al. (2004)	DQ12	CMD extract Attapulgite extract Kaolin extract	Cell	sheep RBC	Haemolysis	CMD, attapulgite and kaolin extract ↓ haemolysis, effect could be inhibited with cation chelator

	Montmorillonite extract Hectorite extract				
	CMD extract Kaolin extract Hectorite extract	Animal	Rat	Inflammatory cell count MIP-2 Protein	CMD extract ↓ inflammatory cells, protein in BAL Kaolin and hectorite extracts ↓ inflammatory cells

Silica toxicity can also be altered by Fe impurities (Table 2.2), however, the effect of Fe is less well understood than that of Al or PVNO. Treatment of quartz with $FeCl_3$ decreased its haemolytic potential, however this was to a lesser extent than $AlCl_3$ treatment (Nolan et al., 1981). Cellular studies have shown treatment of quartz with $Fe(NO_3)_3$ can decrease the cytotoxicity and apoptosis to rat alveolar macrophages (Ghiazza et al., 2011), and treatment with ferric or ferrous chloride decrease H_2O_2 production by macrophages (Cullen et al., 1997). Particulate Fe contamination of quartz increased its inflammatory potency *in vivo* (Cullen et al., 1997), and Castranova et al. (1997) showed high levels of particulate Fe contamination could increase damage to the alveolar air-blood barrier, inflammation, macrophage activation and lipid peroxidation. Conversely, treatment of quartz with ferric or ferrous chlorides had no effect on its inflammatory potency in the rat model (Cullen et al., 1997).

A number of studies have shown that Fe in quartz can increase $HO^{\bullet}$ generation (e.g. Daniel et al., 1995, Fubini et al., 1995, Ghiazza et al., 2011). Daniel et al. (1995) showed removal of iron impurities from quartz decreased $HO^{\bullet}$ production and O_2 consumption *in vitro*. Ghiazza et al. (2011) showed that Fe treatment slightly increased $HO^{\bullet}$ generation, yet there was a decrease in toxicity towards macrophages. Fe eliminated $COO^{\bullet}$ production, which mirrored the effects on inflammation markers, suggesting the type of free radical production is important in silica toxicity and can be altered by Fe impurities. However, $HO^{\bullet}$ generation may still contribute to silica toxicity.

Other impurities may also affect quartz toxicity. Carbon may anneal surface radicals (Fubini, 1998) and has been shown to decrease both $HO^{\bullet}$ and $COO^{\bullet}$ production by quartz (Ghiazza et al., 2013). Carbon also decreased quartz cytotoxicity and the ability of quartz to induce oxidative stress and pro-inflammatory cytokines in mouse macrophages (Ghiazza et al., 2013).

Table 2.2: Summary of toxicology studies with iron-treated quartz

Study	Crystalline silica	Impurity compound	Animal/ Cell	Type	Endpoints	Results
Castranova et al. (1997)	Quartz	Fe (from grinding in stainless steel)	Animal	Rat	Inflammatory cell count RBC count Macrophage activation Lipid peroxidisation	High Fe contamination ↑ damage to alveolar air-blood barrier, inflammation, macrophage activation and lipid peroxidation
Cullen et al. (1997)	DQ12	Fe^{2+} and Fe^{3+} chlorides carbonyl iron	Animal	Rat	Inflammatory cells TNF-α	No effect of ferric or ferrous chloride treatments on inflammatory potential of quartz. Particulate iron needed in 12:1 ratio with quartz to decrease inflammation
		Fe^{2+} and Fe^{3+} chlorides	Cell	Macrophages	Cytotoxicity (LDH) H_2O_2 superoxide dismutase	Fe ↓ H2O2 production
		Fe^{2+} and Fe^{3+} chlorides	acellular		OH generation	No difference to untreated quartz
Ghiazza et al. (2011)	Quartz	$Fe(NO_3)_3$	acellular		OH and COO generation	Fe ↑ OH but ↓ COO production
			Cell	rat alveolar macrophages	Cytotoxicity (WST-1) Apoptosis Particle uptake	Fe ↓ cytotoxicity and apoptosis Fe had no effect on particle uptake
Nolan et al. (1981)	Min-U-Sil	$FeCl_3$	Cell	human RBC	Haemolysis	Fe treatment ↓ haemolysis but was less effective than Al

2.5.1.4 Presence of mineral impurities

As exposure to crystalline silica often occurs when the crystalline silica is hosted in a mixed dust, the presence of other minerals may alter its toxicity. Toxicity of the crystalline silica may be dampened by masking of the surface with other minerals, as has been hypothesised for decreasing the toxic potential of volcanic cristobalite (Horwell et al., 2012). The presence of a glass phase masking the crystalline surface has also been suggested to dampen cristobalite toxicity in volcanic ash (Horwell et al., 2012, Housley et al., 2002) and DE (Ghiazza et al., 2009).

The presence of quartz in heterogenous particles (i.e. composed of more than one mineral and/or phase) has also been shown to affect its toxicity in coal mine dusts (Donaldson and Borm, 1998, Tourmann and Kaufmann, 1994). Investigation of coalmine dusts and quartz mixed with coal suggested that the removal of more soluble minerals over time from quartz-containing particles leads to delayed, but comparable, toxicity to pure quartz dusts (Le Bouffant et al., 1982). However, in a later study, protective clay layers were not removed after long exposure of particles in the lung and the per cent of uncoated quartz could not be correlated to silicosis grade (Tourmann and Kaufmann, 1994). Instead, Fe leaching from the dusts was correlated with massive nodular fibrosis (Tourmann and Kaufmann, 1994), likely by the mechanisms described above. Release of other components from the mineral impurities in solution may also react with the silica surface, thereby altering toxicity. Treatment of DQ12 with coalmine dust, kaolin and attapulgite (clay minerals) extracts decreased its haemolytic potential, and coalmine dust, kaolin and hectorite decreased inflammatory markers *in vivo* (Stone et al., 2004). However, treatment with montmorillonite or hectorite extracts did not decrease quartz-induced haemolysis, showing the type of clay is important in determining its effect on quartz reactivity. A cation chelator decreased the inhibitory effect caused by the extracts (Stone et al., 2004), however, the composition of the extracts was not measured so it is unknown which cation caused the inhibitory effect.

2.5.1.5 Particle size and shape

The importance of particle size on deposition and clearance from the lung is discussed above. Here, the effect of particle size on silica toxicity post-deposition is considered. It is known that particle size can affect particle toxicity. A number of rat instillation studies have addressed the effect of particle size on lung inflammation. A study of different sized polystyrene particles demonstrated that 64 nm particles were more able to increase inflammatory indicators in rat lungs than particles of 202 or 535 nm diameter (Brown et al., 2001). More recently, silica nanoparticles of 50 nm were shown to have increased inflammatory and toxic potency compared to silica particles of 200 nm in rat lungs (Brown et al., 2014). This is likely due to the increased surface area associated with finer particles (assuming particles are non-porous and a regular shape). Duffin et al. (2002) showed that surface area dose determined the inflammatory potential of low solubility, low toxicity particles instilled in rat lungs. As the correlation passed through zero it was shown that only the difference in surface area was accountable for the different inflammogenic potency of these dusts. A comparison with DQ12 quartz to these low toxicity dusts showed an expected increased toxicity from the trend line suggesting that, although surface area is likely to play a role in crystalline silica toxicity, other surface functionalities, which were dampened by Al impurities (discussed above), play a role in crystalline silica inflammatory potency (Duffin et al., 2002, Duffin et al., 2007). This was also supported by Il-8 production by human type II epithelial cells exposed to quartz, which increased more with increasing surface area dose than for low solubility, low toxicity particles (Duffin et al., 2007).

Particle size has also been shown to affect particle uptake by J774 macrophages (cells used in this thesis), where uptake of 20 nm polystyrene beads was more rapid and extensive than for 200 nm polystyrene beads (Clift et al., 2008). Particle shape can also have a significant impact on particle phagocytosis and has been shown to be more important than particle size (Champion and

Mitragotri, 2006). Fibres (aspect ratio >3, length>5 µm and diameter <3 µm (WHO, 1985)), in particular, cause frustrated phagocytosis, where macrophages struggle to fully engulf particles (Schinwald and Donaldson, 2012). Frustrated phagocytosis is dependent on the length of the fibre, where silver nanowires >14 µm *in vitro* or >10 µm *in vivo* caused frustrated phagocytosis (Schinwald and Donaldson, 2012).

Although crystalline silica fibres are rare and, therefore, may not be the cause of most crystalline silica toxicity observed throughout different industries, some instances of crystalline silica fibres or fibre-like particles (aspect ratio >3) exist. In volcanic ash, nanofibers of cristobalite were observed (Reich et al., 2009). However, these particles had a diameter of 20-50 nm and a length in the order of hundreds of nm so are not long enough to cause frustrated phagocytosis. Ziemann et al. (2014) presented a unique case of cristobalite fibres crystallised from alkaline earth silicate wools (AES). Samples of AES contained 8-34 wt.% crystalline silica after heat treatment and 12-33 $X10^6$ fibre-like particles/mg or 10-24 $X10^6$ WHO fibres. Crystalline silica content did not determine the biological reactivity of these samples, yet fibre morphology may have played a role. Another possible example of crystalline silica fibres is that of 'fibrous' DE, which was shown to be more toxic than 'non-fibrous' DE (Chamberlain et al., 1982). However, no information was provided as to the quantity of fibres in these samples. Other particle morphologies are also important in particle toxicity: graphene platelets have a low aerodynamic diameter due to their sheet-like structure so are respirable. However, they have a large geometric diameter of up to 25 µm and can cause inflammatory effects *in vitro* and *in vivo* (Schinwald et al., 2012). Particle shape, rather than surface area, was also shown to be more important in inducing pro-inflammatory cytokine production by macrophages treated with sheet-like mica (Holopainen et al., 2004).

2.6 Exposure to crystalline silica

Exposure to quartz can occur in a number of different occupational and ambient settings. Some of the primary sources of occupational exposure to quartz are through sandblasting, granite mining or quarrying activities, ore mining, foundry working, and construction (IARC, 1997, IARC, 2012, NIOSH, 2002). Ambient exposures are from volcanic ash, and crustal dusts (e.g. dust storms) and through environmental exposures to industrially-generated dusts (e.g. construction, agriculture, open-cast mining etc.).

Exposure to cristobalite and tridymite is less common. Tridymite, especially, is of little concern due to the few exposure routes: small amounts in volcanic settings and some DE and ceramics industries. Cristobalite is much more predominant in these settings. In volcanic ash in dome-building settings, cristobalite can comprise up to 30 wt.% of the ash (Jones and BéruBé, 2011, Horwell et al., 2014). However, the toxicity of the ash cannot be related to the cristobalite content, and epidemiology studies are usually short-term and, therefore, not long enough to track the onset of silicosis in exposed populations (Damby, 2012, Horwell and Baxter, 2006). As volcanic eruptions producing the ash are rarely continuous, exposure is often intermittent and sometimes short-term. However, at Soufrière Hills Volcano (SHV), Montserrat, frequent eruption of cristobalite-laden ash occurred for >10 years (Horwell et al., 2014). Still, epidemiological evidence is limited. Clinical and exposure studies at SHV began in 1997, two years after the initial eruption, and follow-up periods allowed production of a risk assessment of the potential for silicosis to develop (Baxter et al., 2014). The risk of silicosis was found to be low. However, preventive measures (evacuation of ash-rich areas and use of masks) and the emigration of large numbers of the population (meaning long-term follow-up was difficult) means assessing the ability of ash to cause silicosis is difficult, although toxicological studies suggest the risk is low (Baxter et al., 2014).

Other cristobalite exposure can occur in the pottery industry. Cherry et al. (1998) showed an increase in lung cancer in pottery workers exposed to cristobalite. However, although this could be related to mean silica exposure it could not be related to cumulative silica exposure. By far the most common and, therefore, most studied, exposure to cristobalite is in the DE industry. As DE is the focus of Chapters 4 and 5 of this thesis a full background of DE characteristics and review of epidemiology, clinical and toxicology studies is provided below.

2.7 Diatomaceous earth

2.7.1 Background

Diatomaceous earth (DE), also referred to as kieselguhr or diatomite, is a sedimentary deposit of highly siliceous diatom frustules. In its raw form, DE is predominantly amorphous, however, during processing crystallisation to predominantly cristobalite occurs (see below). Deposits of DE are also often found in close association with clay minerals, such as smectite and illite. Due to the morphology of the diatom frustules, DE is a highly porous material, with low density and high absorptive capacity. These unique physicochemical properties make DE ideal for many different applications, in particular, DE is used in the filter aid and filler industries.

2.7.1.1 Distribution

The commercial value of DE means that deposits are mined worldwide. The largest mine is located in Lompoc, California, however deposits are found in all continents and the producers of DE are shown in Table 2.3. USA is the greatest producer of DE, followed by China and then Denmark. In Denmark a highly clay-contaminated DE, called Moler, is mined.

Table 2.3: Global production of DE in 2013. Egypt and Iran also though to produce DE but no information is available. *Data from 2012. (British Geological Survey, 2015).

Country	Production in 2013 (tonnes)	Country	Production in 2013 (tonnes)
Czech Republic	49000	**Argentina**	55000
Denmark	128125	**Brazil**	3000
France	85000	**Chile**	27092
Hungary	434	**Peru**	124917
Poland	600		
Spain	53713	**China**	420000
Turkey	85000	**Japan**	100000
		Korea (Rep. of)	34000
Algeria	2124	**Saudi Arabia**	1000
Ethiopia	4000	**Vietnam**	10000
Kenya	1054		
Mozambique	550	**Australia**	21000
		New Zealand	4
Costa Rica	4029*		
Mexico	87463		
USA	770000		
		World total	**2063076**

2.7.1.2 Processing

In order to provide the optimum product for different end uses, DE is processed. The processing procedure is shown in Figure 2.5. First DE is quarried and transported from the mine to the processing plant, where DE deposits of different grades (based on the purity of the deposit) are mixed in varying quantities, dependent upon the required purity of the final product. This mixture is then milled and dried at low temperatures. If further processing is required, calcination can occur. Calcination is a process that involves heating the powder to high temperatures of ~1000 °C, which leads to the decomposition of carbonates and other compounds considered as impurities. This process causes particles to agglomerate into a coarser grained product, more suitable for use in the filter aid industry. Calcination can occur with (flux-calcined) or without (simply-calcined) a fluxing agent, usually sodium carbonate or sodium chloride. The fluxing agent generally produces a white coloured product, preferred for filler industries. Classification of the powder after calcination

separates the coarse and fine particles giving two separate products, suitable for use in the filter aid and filler industries respectively.

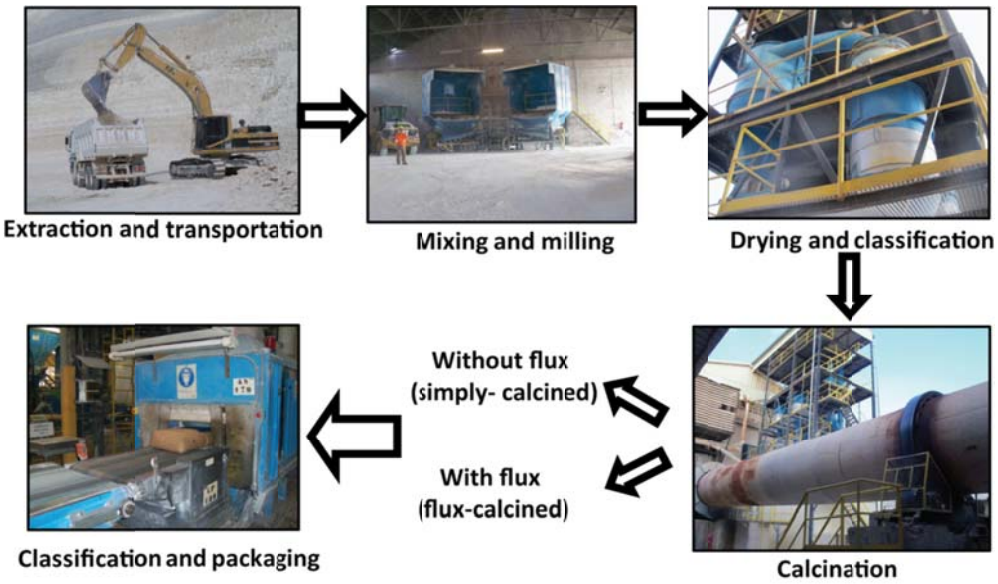

Figure 2.5: Processing procedure of DE. Images taken in a Spanish DE quarry and processing plant.

2.7.1.3 Physicochemical properties of DE

DE deposits are primarily SiO_2 in their bulk chemistry (Table 2.4), ranging from 65-98 oxide wt.%, due to the high silica content of the diatom frustules. However, Al impurities are seen (up to 18 wt.% Turkey and China) and are also high in DE from Thailand (up to 15 wt.%). Fe_2O_3 content ranges from 0.1-6.5 wt.%. Other elements are found in trace quantities in most instances, however, CaO of 9 wt.% is seen in Spanish DE and high MgO is seen (up to 4 wt.%) in Turkish samples. The presence of Na_2O is higher in flux-calcined samples when compared to the calcined or unprocessed alternatives, due to the addition of a sodium-based fluxing agent during the processing of these DE. Calcination and flux-calcination tend to increase the purity of the product (i.e. SiO_2 content), however, there is a large range of impurity concentrations among DE that has undergone the same processing technique and also among DE from the same locations.

Table 2.4: Chemical composition of DE used in a number of studies and from industrial websites. U = unprocessed, C = calcined, FC = flux-calcined.

Reference	Country	Condition	Chemical Composition (oxide wt.%) Si	Al	Fe	Ti	Ca	Mg	Na	K
Mount Sylvia Diatomite Pty Ltd (2015)	Australia	U	90.1	4.6	3.2	0.4	0.6	0.6	0.1	0.1
Qingdao Qiancheng Minerals Co. Ltd. (1990)	China	U	>87	<3	<1.5		<0.3		<0.4	
Shengzhou Huali Diatomite Products Co. Ltd. (2015)	China	U	65.5	16.5	6.5		1.5		2.5	
		U	68.0	17.5	5.5		1.5		2.5	
		C	90.0	4.5	1.8		1.0		1.2	
		C	90.0	4.5	1.8		1.0		3.0	
		FC	89.5	4.2	1.8		1.0		3.0	
		FC	89.5	4.2	1.8		1.0		0.5	
Ghiazza et al. (2009)	European	C	90.4	3.7	2.3	0.1	1.3	0.4	0.0	0.3
		FC	88.0	3.1	2.1	0.5	1.3	0.3	4.4	0.2
		FC	88.8	2.9	2.0	0.5	0.5	0.2	3.7	0.2
Elias et al. (2000)	France	U	97.8	0.9	1.2		0.3	0.2		
		FC	97.9	0.5	0.9	0.2	0.3	0.1		
Imerys Minerals Ltd. (2012)	France	C	89.4	3.5	1.7		0.5	0.4	2.4	
		FC	91.7	2.8	1.8		0.4	0.3	2.5	
Nowak (1976)	Iceland		89.4	2.1	2.3		0.7			0.2
Mahani and Kazemeine (2003)	Iran	U	84.2	4.9	1.5					
			76.4	8.5	2.3					
			90.5	2.3	0.6					
		H_2SO_4 treated	93.9	2.3	0.2					
			85.1	5.2	0.6					
			93.8	2.3	0.2					
Imerys Minerals Ltd. (2012)	Mexico	U	88.0–93.0	2.0–4.5	0.9-2.1		0.4-1.5	0.2-0.4	0.4- 2.0	
		C	91.0-93.2	3.2-4.0	1.4-1.9		0.5-0.8	0.2-0.3	0.6- 1.4	

		FC	90.4-93.5	2.3-2.8	0.8-1.6		0.4-0.6	0.3-0.4	3.1- 3.9	
Imerys Minerals Ltd. (2012)	Spain	U	74.3	0.8	0.4		9.0	0.4	0.1	
		C	91.6	0.7	0.4		3.9	0.4	1.5	
		FC	93.2	0.9	0.4		3.5	0.4	1.5	
Chaisena and Rangsriwatananon (2004)	Thailand	U	71.9	14.6	5.8	0.5	0.2	0.7		
Tsai et al. (2006)	Thailand	C	92.0	3.3	1.3					
Pimraksa and Chindaprasirt (2009)	Thailand	U	77.5	14.2	5.2	0.5	0.0	0.5	0.2	2.1
(Goren et al., 2002)	Turkey	U	74.4	14.6	3.6		1.6	1.4	0.7	2.4
		HCl treated	80.0	14.0	2.8		0.6	0.9	1.5	
(Şan et al., 2009)	Turkey	U	68.1	18.0	3.4	0.3	1.0	4.2	0.7	1.3
		HCl treated	78.7	14.1	2.3	0.3	0.3	1.3	0.6	0.9
Elias et al. (2000)	USA	U	98.3	0.5	0.6	0.1	0.2	0.2		
		FC	98.3	0.5	0.7		0.2	0.2		
Hart and Hesterberg (1998)	USA	U	82.8	3.8	1.3	-	0.7	0.8	0.6	0.7
		FC	87.0	4.3	1.6	-	0.6	0.8	4.4	0.7
Imerys Minerals Ltd. (2012)	USA	U	89.0-93.0	2.0-3.3	1.0-1.4		0.3-0.8	0.5-0.7	1.0- 2.5	
		C	91.1-92.8	3.3-4.0	1.1-1.3		0.2-0.6	0.4-0.6	0.8- 1.2	
		FC	89.6-91.9	3.3-4.0	1.2-1.5		0.5	0.5-0.6	2.1- 3.3	

Due to high silica content of DE, crystalline silica can form during calcination: generally, crystalline silica content is shown to be very low in unprocessed samples (0-4 wt.%), high in calcined samples (>10 wt.%), and highest in flux-calcined samples (>20 wt.%) (Table 2.5). The small amount of

crystalline silica seen in unprocessed samples may be due to contaminants from volcanic material or sands that may be found in the deposits (Hein et al., 1978), as DE deposits are often formed in volcanic lakes or near volcanic vents (Van Eaton et al., 2013), due to the abundance of Si in water around volcanic areas. Alternatively, diagenesis to quartz of the amorphous DE may occur at depth and pressure with burial of the deposit (Hein et al., 1978). To form quartz, amorphous silica follows the diagenetic pathway amorphous silica → opal-CT → quartz (Mizutani, 1977), which may occur in the DE deposits. During diagenesis, opal-CT, a hydrous microcrystalline form of silica, may also be produced in the DE frustules. Although there is some debate as to its structure, most studies indicate that opal-CT is formed by cristobalite and tridymite stacking (Mizutani, 1977). Therefore, identification of cristobalite or tridymite in DE deposits may be due to the misidentification of opal-CT. Regardless, calcination dramatically increases the amount of crystallisation, resulting in crystalline silica contents up to 20% and 80% in calcined and flux-calcined samples respectively, usually with cristobalite the predominant polymorph produced (Table 2.5).

Contaminant minerals, such as clays and carbonates are often seen in DE deposits. Clays such as illite, kaolinite and montmorillonite have been observed in DE deposits (Chaisena and Rangsriwatananon, 2004, Şan et al., 2009, Goren et al., 2002). Calcite and feldspars have also been detected in DE deposits (Goren et al., 2002, Mahani and Kazemeine, 2003, Tsai et al., 2004). These impurities and can alter the efficiency of DE in filtration or absorption and some authors have tried to remove these impurities using acid or heat treatment of DE material to produce a purer product (Goren et al., 2002, Mahani and Kazemeine, 2003, Şan et al., 2009).

Table 2.5: Crystalline silica content of DE used in different studies. U = unprocessed, C = calcined, FC = flux-calcined. C 900 and C 1200 = calcined at 900 and 1200 °C respectively. NQ = observed but not quantified.

Reference	Condition	% crystalline silica		
		Cristobalite	Quartz	Total
(Bye et al., 1984)	U		1-3	1-3
	C	0-11	1-2	2-12
	FC	77-85	<0.5	77-85
Checkoway et al. (1993)	U		0-4	0-4
	C	10-20		10-20
	FC	20-25		20-25
Elias et al. (2006)	U	0	0	0
	C 900	<0.5	1	1
	C 1200	48	1	49
	FC	47-58	0	47-58
Ghiazza et al. (2009)	C	20	NQ	20
	FC	45		45
	FC	45		45
Hart and Hesterberg (1998)	U		4	4
	C	40	2	42
Rafnsson and Gunnarsdóttir (1997)	U		trace	
	FC	>70	<2	>70
Smart and Anderson (1952)	C	1-3		1-3
	FC	30-45		30-45

2.7.2 Pathogenicity of diatomaceous earth

2.7.2.1 Epidemiology and clinical studies

Epidemiology studies of DE are summarised in Table 2.6 and discussed in detail below.

2.7.2.1.1 California

DE has been mined for many years and one of the first studies on the health effects caused by occupational exposure to DE was by Legge and Rosencrantz (1932). This study looked at DE from California, which contained approximately 85 wt.% SiO_2 when dry, and assessed the damage to the lungs of 108 Mexican men using x-ray examinations of the chest. This preliminary study concluded that 68.5% of the workers had pneumoconiosis due to silica. Subsequently, a number of in-depth epidemiological and clinical studies have been performed looking at the exposure to DE in California.

In 1977 a NIOSH health hazard evaluation of Johns-Manville Corporation in Lompoc, California was performed. Dust samples were collected and exposure surveillance showed that 61% of 28 workers were exposed to concentrations greater than the threshold of 0.05 mg/m^3. Examinations of medical records and chest x-rays led to the conclusion that lung cancer and other respiratory diseases were higher than expected in these workers and mortality was also in excess in workers. However this was based on a small cohort and Cooper and Sargent (1984) later showed that only 11/437 (2.5%) workers in the same DE mine and plant were considered with pneumoconiosis after studying chest x-rays from 1974-1979.

The largest cohort study of DE workers was undertaken by Checkoway et al., who were also the first group to study mortality patterns of the workers in DE mines and plants. The initial study (Checkoway et al., 1993) was undertaken in two plants in California and the main cohort consisted of 2570 white men. Cause of death data were determined from the National Death Index (NDI) and death certificates and exposure was determined from personal records, including work history, job assignments, leave of absence and dates of job changes. Standardised mortality ratios (SMRs), calculated by comparing mortality of the cohort to mortality in the US population, showed there was an excess in mortality in both non-malignant respiratory diseases (NMRDs), not including pneumonia

and infectious disease (SMR = 2.59), and lung cancer (SMR = 1.43). This was supported by similar findings in smaller cohorts of black men, white women and white men with previous exposure to asbestos working in the DE mines. Relative risks were also calculated for increasing duration of exposure to dust and cumulative crystalline silica exposure, showing a strong gradient when a latency period of 15 years was used and a relative risk of 2.88 for workers employed over 20 years. Even when a higher asbestos exposure was considered, re-analysis still showed a relationship between crystalline silica exposure and lung cancer (Checkoway et al., 1996).

An extended follow-up of this cohort was performed using new historical exposure data to calculate a more accurate exposure (Seixas et al., 1997) and men exposed to asbestos were included due to a new study allowing asbestos exposure of the cohort to be quantified (Gibbs and Christensen, 1994). Similar results were observed with a mortality excess of NMRD (SMR = 2.01) and lung cancer (SMR = 1.29), although these were both reduced from SMRs calculated in the 1993 study. Further study of this cohort by Hughes et al. (1998), where radiographic evidence was used, determined a strong relationship between exposure-response and the risk of opacities in chest x-rays indicative of radiological silicosis. This study also showed that crystalline silica exposure was more important than dust exposure, a conclusion enabled by the differentiation of exposure to natural and calcined DE dusts. A conclusion could not be reached as to whether silicosis is a co-condition necessary for silica associated lung cancer, as the increased risk of lung cancer in this cohort was not restricted to those with positive chest x-rays showing silicosis (Checkoway et al., 1999). The above studies, although fraught with uncertainties, are the most detailed studies on DE workers and have been used in a numerous reviews of silica toxicity (e.g. Borm et al., 2011, Steenland et al., 2001) and in studies hoping to conclude an acceptable chronic inhalation reference level for crystalline silica (Collins et al., 2005).

Quantitative risk assessments of crystalline silica exposure and lung cancer mortality, and mortality due to lung disease other than cancer (LDOC), have also been performed on a cohort of DE workers in California (Park et al., 2002, Rice et al., 2001). Workers were exposed to a mean concentration of 0.29 mg/m^3 respirable crystalline silica. Rice et al. (2001) concluded that at the current NIOSH recommended exposure limit (REL; 0.05 mg/m^3 respirable crystalline silica) there was a 2% (19/1000) above background risk of a male worker, working for 45 years, suffering from lung cancer. There is an added risk of 75/1000 workers developing silicosis at these recommended exposure levels, and at the higher exposure concentration of 0.29 mg/m^3, which these DE workers are exposed to, 200/1000 lifetime excess deaths would occur due to LDOCs (Park et al., 2002). These studies show that the RELs for crystalline silica set by OSHA and NIOSH may still pose an unacceptably high risk among DE workers.

Further, evidence of DE pathogenicity in California and other US locations is shown by chest x-rays of DE workers. The ability of DE to cause pneumoconiosis was supported by chest x-rays of 20 DE workers, where it was established that processed DE was more potent than unprocessed (Smart and Anderson, 1952). Harber et al. (1998) showed a correlation between exposure and grade of disease, but no correlation between cristobalite exposure and lung function (i.e. spirometric tests) was observed. Dutra (1965) also showed disease similar to acute silicosis in one DE worker, whereas Harber et al. (1998) and Vigliani and Mottura (1948) (Italy) showed opacities that were dissimilar to those typically produced by quartz exposure.

Table 2.6: Epidemiological and clinical studies on DE exposed workers.

Reference	Location	Study details	Key observations	Comments
Beskow (1978)	Sweden	Analysis of the national pneumoconiosis register from 1931-1975	Six cases of silicosis in DE workers were reported. Cases suggested calcined DE was more potent and silicosis could develop in just 2-3 years	Small sample
Checkoway et al. (1993)	California	Records and cause of death information of a cohort of 2570 white men used to calculate exposure and standardised mortality ratios (SMRs), which were compared to the US population	Excess in mortality of non-malignant respiratory disease (SMR=2.59) and lung cancer (SMR=1.43), relative risk showed strong gradient with increased exposure to dust and crystalline silica when 15 year latency period used.	Findings supported by smaller cohorts of black men, white women and white men previously exposed to asbestos
Checkoway et al. (1996)	California	Similar study to Checkoway et al. (1993) but a higher asbestos exposure was imposed.	Still a strong relationship between crystalline silica exposure and lung cancer.	
Checkoway et al. (1999)	California	Analysis of chest x-ray data and lung cancer mortality data from cohort used in Seixas et al. (1997) to determine if silicosis is a necessary or incidental condition for silica induced lung cancer	Increased risk of lung cancer was not restricted to workers with chest x-rays showing silicosis, so no conclusion reached as to whether silicosis is a co-condition necessary for silica associated lung cancer.	
Cooper and Sargent (1984)	California	Examination of chest x-rays from 1974-1979 of 473 workers	2.5% workers had pneumoconiosis and these were mainly workers who had been employed more than 25 years	
Dutra (1965)	California	Case report on 51 year old male worker who had been in the diatomite industry for 26 years.	Chest x-rays indicated far-advanced coalescent pneumoconiosis and maximum breathing capacity was 23% of expected. Post-death lung examination indicated similar disease to acute silicosis.	Only one case examined
Ebina et al. (1952)	Japan	Study of pneumoconiosis in cohort or 106 DE workers	11% showed signs of silicosis and pneumoconiosis observed in workers that had been employed over 15 years	
Harber et al. (1998)	California	Exposure to dust and cristobalite calculated from records and chest x-rays of 492 workers examined and 267 workers underwent spirometry tests	40% workers working >12.5 years had >=0/1 scores. Correlation between exposure and degree of radiographic profusion. Prevalence of abnormality lower than previous era (e.g. Legge and Rosencrantz (1932)). Some lung	smoking questionnaires showed >60% of both radiographic group and spirometry group were current or previous smokers

			opacities not typical of silica, likely total dust mixtures responsible. No relationship between lung function and exposure to dust or cristobalite	
Hughes et al. (1998)	California	Examination of chest x-rays for signs of silicosis from cohort used in Seixas et al. (1997)	Strong relationship between exposure and risk of opacities in chest x-rays indicative of silicosis. Crystalline silica exposure more important than dust exposure.	
Joma et al. (1994)	Netherlands	Investigation of 172 male workers in potato sorting plant for pneumoconiosis and airflow limitation	No increased risk of pneumoconiosis in exposed group compared to control. Airflow limitations in exposed group compared to control.	
Legge and Rosencrantz (1932)	California	Examination of the chest x-rays of 108 DE workers for signs of tuberculosis and silicosis	Pneumoconiosis due to silica was found in 68.5% of workers, disease is slow growing	First study recognising DE induced pneumoconiosis
NIOSH (1977)	California	Collection of dust samples, and exposure data. Examination of chest x-rays.	61% of workers were exposed to concentrations greater than the 0.05 mg/m^3 threshold. Lung cancer, other respiratory diseases and mortality were in excess in DE workers	Based on small cohort of only 28 workers
Park et al. (2002)	California	Quantitative risk assessment of crystalline silica exposure and mortality due to lung diseases other than cancer (LDOC) using DE worker cohort	Addition risk to that found by Rice et al. (2001) of 7.5% workers developing silicosis. At actual exposure concentrations (0.29 mg/m3), 200/1000 lifetime excess deaths would occur due to LDOC.	
Rafnsson and Gunnarsdóttir (1997)	Iceland	Study of 1346 DE workers	Increase in lung cancer for entire cohort and those working in loading was not statistically significant. Increases in cervical, brain and skin cancer. Men working 5 years or 300 hours or more showed increase in all cancers,	Short follow-up period of 5-9 years, so lung cancer may not have time to develop.
Rice et al. (2001)	California	Quantitative risk assessment of crystalline silica exposure and lung cancer mortality using DE worker cohort	At the current NIOSH exposure limit there was a 2% above background risk of a male worker, working 45 years suffering from lung cancer.	
Seixas et al. (1997)	California	Extended study of Checkoway et al. (1993) using new historical data to calculate more accurate exposure, and the inclusion of men	Excess in mortality of non-malignant respiratory disease (SMR=2.01) and lung cancer (SMR=1.29). These are both reduced from the 1993 study.	

		previously exposed to asbestos		
Smart and Anderson (1952)	California, Nevada and Oregon	Examination of 20 chest-x-rays of DE workers	DE can cause pneumoconiosis, with calcined and flux-calcined being more potent. Fresh water DE is less toxic than marine DE even when flux-calcined.	
Vigliani and Mottura (1948)	Italy	Examination of chest x-rays for 20 workers in filter candle factories for signs of silicosis in 1944-1949, and an autopsy of one of the workers whom died during the study	13/20 workers were silicotic, and 7 of these were in the advanced stage with one worker having open tuberculosis. Pathological findings differed from quartz induced silicosis.	Few cases.

2.7.2.1.2 Other diatomaceous earth mines and plants

Other DE plants have also been studied but in much less detail. Studies of a DE plant in Iceland supports findings from those studies performed in California (Rafnsson and Gunnarsdóttir, 1997). The study of a cohort of 1346 DE workers suggested a link between cristobalite and DE exposure and lung cancer when compared to the Icelandic public. This study allowed the discrimination between those workers involved in production and exposed to 0.02-0.5 mg/m^3 respirable cristobalite (but who may have been exposed to other carcinogens in the processing plant), and those involved in ship-loading of the final product, exposed to 0.03-0.7 mg/m^3 respirable cristobalite. An increase in all cancers and lung cancer was observed for the entire cohort and for those men working only in loading. The length of employment was also important, with men working 5 years or more or 300 hours or more showing an increase in all cancers and lung cancer. The modes of action for other cancers are not described and are unlikely to be due to exposure to DE. The increase in lung cancer observed was low and not statistically significant but this may be due to short follow-up period (5-9 years), barely long enough for lung cancer to develop.

Other studies, in Japan and Sweden, considered pneumoconiosis as an endpoint. Ebina et al. (1952) concluded that workers exposed to DE containing 76-86% amorphous silica in a Japanese DE factory were at a higher risk of pneumoconiosis. Of 106 workers, 11% showed signs of silicosis and advanced pneumoconiosis was seen in some workers who had worked there for over 15 years. In the period 1931 to 1975, six cases of silicosis in DE factory workers were reported to the Swedish national pneumoconiosis register (Beskow, 1978). These cases showed that calcined DE was more potent than unprocessed DE and that that silicosis could develop with just 2-3 years exposure. It also showed that cristobalite, but also tridymite, seemed to contribute to silicosis development. This is interesting as little work has been done on the tridymite polymorph as it is mainly cristobalite found in calcined DE.

2.7.2.1.3 Other diatomaceous earth exposure studies

It is not only through the manufacturing of DE that people are exposed. A study of male workers in a potato sorting plant (Joma et al., 1994), where workers were exposed to DE, likely through use of DE as a natural pesticide, showed that there was no increased risk of pneumoconiosis in the exposed group compared to control groups. However, airway obstruction did occur in the exposed group. There was no difference between the effects of total dust and respirable silica, likely due to the DE being in its unprocessed, amorphous form and therefore being considered to have a lower toxic potential. This study highlights the need to assess exposure to DE in other industries where it is used once processed, especially DE that is calcined and therefore the silica is in a crystalline form.

2.7.2.1.4 Confounding factors and uncertainties

There are a number of confounding factors that must be accounted for in these epidemiological studies, including smoking, asbestos exposure and exposure to substances other than DE that could lead to an increased risk of respiratory diseases and other end points being assessed (Hessel, 1999).

Although some studies attempt to address these factors, it is often difficult to separate effects from DE exposure and smoking especially. Epidemiology studies also do not allow easy comparison of the effects of exposure to processed and unprocessed DE, with workers often swapping between mining and processing jobs. Therefore, toxicological studies are employed to look more closely at the mechanisms of DE-induced disease and the different potencies of unprocessed and processed DE. Toxicology can also help to determine the role of crystalline silica in DE toxicity.

2.7.2.2 Toxicological studies

2.7.2.2.1 In vivo studies

In vivo studies of unprocessed, amorphous DE show it has the potential to be pathogenic (Table 2.7), causing acute/sub-acute inflammation in rats 60 days after a single intratracheal injection of 10 mg DE, an effect that decreased with time (Adamis et al., 2000). While inhalation of unprocessed DE (170 million particles per cubic foot (mppcf)) by guinea pigs for 39-44 h/week for 24 months resulted in fibrosis, calcined, cristobalite-rich DE was seen to cause more severe fibrosis more rapidly (Pratt, 1983). Calcined DE was also shown to cause fibrosis in exposed guinea-pigs (Maeda et al., 1986). However, in a separate study, exposure via inhalation to 5-50 mppcf flux-calcined DE, consisting of 61% cristobalite, for 30 h/week up to 30 months caused no body weight loss or pulmonary fibrosis in rats, guinea pigs or dogs (Wagner et al., 1968).

Table 2.7: *in vivo* studies using DE.

Reference	Sample(s)	Assay	Exposure	Animal subject	Dose	Duration	Results	Conclusions
Adamis et al. (2000)	amorphous DE	Bronchoalveolar lavage (BAL)	Injection into trachea	Rat	10 mg/animal	15, 60, 180 days	After 60 days there was an increase in the number of free cells in the BAL and DE slightly enhanced LDH activity and phospholipid content, but was not as potent as quartz	DE can produce acute/sub-acute inflammation. Here, it gradually became more moderate after 60 days
Wagner et al. (1968)	flux-calcined DE	Body weight	Inhalation	Dogs, guinea-pigs, rats	2, 5, 50 mppcf	6 h/day, 5 days/week, for 6, 12, 18, 24, 30 months	Dogs and guinea-pigs showed no decrease in body weight. Rats showed a decrease in body weight at the highest concentration and 5 mppcf exposure compared to controls.	
		Haematology	Inhalation	Dogs		6 h/day, 5 days/week, for 6, 12, 18 months	No change from the controls	
		Cristobalite in the lung	Inhalation	Rats		6 h/day, 5 days/week, for 6, 12, 16.5 months	cumulative deposition of cristobalite	

		Pathology	Inhalation	Dogs, guinea-pigs, rats	2, 5, 50 mppcf	6 h/day, 5 days/week, for 6, 12, 18, 24, 30 months	No pulmonary fibrosis after 16.5-18 months in rats, guinea-pigs and dogs, though fibrotic reactions observed in the lymph nodes of dogs only. Moderate histiocytic and giant cell response even at the lowest exposure	
Maeda et al. (1986)	calcined DE		intratracheally	Guinea-pigs	25 mg/0.5 ml saline	2h, 4h, 1, 2, 3, 4, 5, 6 and 7 days, 5, 6 and15 months	Pronounced neutrophil invasion of bronchioles after 4 h. Number of macrophage and neutrophils were greater than controls up to 7 days post exposure. Mild diffusive fibrosis first observed at 6 months and was present at 15 months. Was confined to areas containing DE.	Calcined DE can cause fibrosis
Pratt (1983)	natural DE, calcined DE	Silica in the lung	Inhalation	Guinea-pigs		7-8 h/day, 5.5 days/week for 21-24 months	Calcined silica caused fibrosis after 15 months and this was severe by 21 months. Natural DE only caused fibrosis at 24 months and was not as severe. This was indicated by changes in dry lung weight.	Calcined DE, in the form of cristobalite, more potent than amorphous DE.

2.7.2.2.2 In vitro studies

Many *in vitro* studies indicate that the cytotoxicity of DE does not correlate with crystalline silica content (Table 2.8), as unprocessed and calcined DE exert a greater cytotoxic effect than cristobalite-rich flux-calcined DE in a number of *in vitro* assays on different cell lines (Bye et al., 1984, Elias et al., 2006, Ghiazza et al., 2009, Hart and Hesterberg, 1998). Bye et al. (1984) showed that DE could cause membrane damage (as an indicator of cytotoxicity) to macrophages. Cytotoxicity could be induced by exposure to unprocessed, calcined and flux-calcined DE. However, flux-calcined samples (>70 wt.% cristobalite) were significantly less cytotoxic than unprocessed samples (amorphous) or calcined samples (<11 wt.%) and no explanation was given as to why. Brown et al. (1980) and Chamberlain et al. (1982) showed that fibrous DE was more reactive *in vitro* than non-fibrous DE, but in each instance the calcined sample was less toxic that the corresponding unprocessed sample (Brown et al., 1980). Hart and Hesterberg (1998) showed treatment with unprocessed or calcined flux-calcined DE could decrease cell proliferation, colony forming efficiency, and cytotoxicity. In all instances unprocessed DE, containing 4 % quartz but mainly amorphous, was more reactive than flux-calcined samples (40 % cristobalite +2 % quartz). Later, Ghiazza et al. (2009) also showed that flux-calcined samples containing ~45 % cristobalite were less cytotoxic, pro-inflammatory and caused less oxidative stress than calcined samples with only 20 % cristobalite content. They attributed the low toxicity of flux-calcined DE to the formation of a vitreous rim during flux-calcination, as acid treatments showed cristobalite resided in the centre of the particle, and infrared spectroscopy showed a lower coverage of silanols in flux-calcined samples than calcined samples.

The studies above indicate that crystalline silica content does not govern the toxicity of DE *in vitro*. However, work by Elias and co-workers has shown that cristobalite-rich DE samples (both flux-calcined and those calcined at high temperature) have increased pro-carcinogenic potential in Syrian

hamster embryos (SHE) compared to unprocessed DE and DE calcined at lower temperature (Elias et al., 2000, Elias et al., 2006). Elias et al. (2006) showed heating of DE in the lab at 900 or 1200 °C, to mimic simple calcination, could increase the ability of DE to generate $HO^{\bullet}$ and $COO^{\bullet}$. However, flux-calcined samples did not produce $COO^{\bullet}$. Commercially heated DE (flux-calcined) and DE heated at 1200 °C inhibited cell proliferation more than unprocessed DE or DE heated at 900 °C, yet both heated DE samples were less cytotoxic and less reactive than unprocessed DE in affecting abnormal cell division. Flux-calcined samples were, however, the most cytotoxic. The morphological transforming potency (an indicator of genotoxicity) was greater for calcined and flux-calcined samples than unprocessed DE and was linked to the increased free radical production from these samples compared to unprocessed DE. Exposure to both unprocessed and flux-calcined DE also resulted in an increase in abnormal nuclei formation (a marker of genotoxicity) in Chinese hamster ovary cells, with the damage caused significantly higher than the quartz and cristobalite standards (Hart and Hesterberg, 1998).

Table 2.8: *in vitro* studies of DE.

Reference	Sample(s)	Assay	Cell line	Dose	Duration	Results	Conclusions
Adamis et al. (2000)	DE powder 90% amorphous	LDH release	Rat peritoneal macrophages	600 µg dust per 4.5 x 10^6 cells	3 h	DE caused very low levels of LDH to be released, lower than TiO2 negative standard.	DE caused high haemolysis but did not damage macrophage membranes.
		Haemolysis	Erythrocytes	2 mg/ml	1 h	DE caused 99% haemolysis.	
Brown et al. (1980)	Natural and calcined DE	Enzyme release (LDH, beta-Glucuronidase)	Macrophages			Both natural and calcined DE II (fibrous) were ranked more reactive than natural or calcined DE I. Calcined DE less reactive than raw DE.	Toxicity not linked to crystalline silica content. V79 and A549 cell assays most selective tests.
		Cell survival	V79 Chinese hamster lung cells		6 days		
		Giant cell formation	A549 Type II alveolar cells	100-200 µg/ml	5 days		
		Haemolysis					
Bye et al. (1984)	Natural, calcined and flux-calcined DE powder	LDH release	Mouse peritoneal macrophages	4, 8, 12, 16, 20 µg dust per 1.2 x 10^6 cells	18 h	LDH release from DE treated macrophages was 11-59% that of DQ12. Natural and calcined DE produced a significantly higher response compared to flux-calcined samples.	Toxicity of these DE samples is not related to the content of crystalline silica.
Chamberlain et al. (1982)	Fibrous and non-fibrous DE	LDH release	Mouse peritoneal macrophages	50, 100, 150 µg/ml	18 h	Non-fibrous DE were cytotoxic to macrophage cells but inert towards A549 and V79 cells.	Non-macrophage cell lines are relatively insensitive to dusts

		Cell survival	V79 Chinese hamster lung cells		6 days	Fibrous DE were cytotoxic to all cell types.	that are only fibrogenic but are very sensitive to fibrous morphology of carcinogenic dusts
		Giant cell formation	A549 Type II alveolar cells	100-200 µg/ml	5 days		
Elias et al. (2000), (2006)	Amorphous and calcined DE	Cell proliferation	Syrian hamster embryo cells	1.82-43.7 µg/cm^2	3 days	Concentration-dependent decrease in cell proliferation after exposure to DE. Flux-calcined DE and DE calcined at 1200 °C more inhibitory than DE and DE calcined at 900 °C	Heating of DE increases transformation potency but blunts cytotoxicity. $OH^{\bullet}$ release correlated to transforming potency, inhibition of cell proliferation and cell division aberrations. Finer fractions more cytotoxic and cause more cell division aberrations and morphological transformations. Likely due to higher abundance of reactive sites and $OH^{\bullet}$ release per m^2 exposed.
		Cell division aberration	Syrian hamster embryo cells	4.5-18 µg/cm^2	24 h	Calcined DE less active than DE	
		Cloning efficiency	Syrian hamster embryo cells	1.9-30.4 µg/cm^2	7 days	DE more cytotoxic than calcined DE, which was not cytotoxic at the highest concentration tested. Commercially flux-calcined DE the most cytotoxic.	
		Transformation assay	Syrian hamster embryo cells	1.9-30.4 µg/cm^2	7 days	DE did not induce transformation while a concentration-dependent increase in transformation frequency induced by calcined and flux-calcined DE. Fine fraction of commercially flux-calcined DE most transforming.	
Ghiazza et al. (2009)	Calcined and flux-calcined DE	LDH release	Murine alveolar macrophages	10-80 µg/cm^2	24 h	Calcined DE exerted a cytotoxic effect, induced NO synthesis and caused lipid peroxidation under	Total amount of cristobalite is not a determinant factor

		Nitric oxide synthesis	Murine alveolar macrophages	10-80 μg/cm^2	24 h	conditions where flux-calcined DE did not have a significant effect	and vitreous phase after flux-calcination could play a key role.
		Thiobarbituric acid-reactive substances (TBARS) assay	Murine alveolar macrophages	80 μg/cm^2	24 h		
Hart and Hesterberg (1998)	Natural and flux-calcined DE	Inhibition of cell proliferation	Chinese hamster ovary cells	0-30 μg/cm^2	3 days	Natural DE inhibited cell proliferation more than flux-calcined DE	Toxicity did not correlate with crystallinity. Natural DE most toxic and amorphous. Tests suggest in vitro toxicity is determined by both number of particles/unit mass and particles having at least one dimension >7.5 μm.
		Colony-forming efficiency	Chinese hamster ovary cells	0-30 μg/cm^2	5 days	Natural DE decreased colony-forming efficiency more than flux-calcined DE. When filtered through 0.22 μm filter no inhibition of cell proliferation was observed	
		Cell viability	Chinese hamster ovary cells	20 μg/cm^2	1-3 days	Cell viability remained >85% for natural DE, and ~90% for flux-calcined DE	
		Abnormal nucleus induction	Chinese hamster ovary cells	0-30 μg/cm^2	2 days	DE induced greater amounts of abnormal nuclei than cristobalite and quartz. Natural and flux-calcined DE-exposed cells both had grossly abnormal nuclear morphology.	

References

ADAMIS, Z., TÁTRAI, E., HONMA, K., SIX, É. & UNGVÁRY, G. 2000. In Vitro and in Vivo Tests for Determination of the Pathogenicity of Quartz, Diatomaceous Earth, Mordenite and Clinoptilolite. *Annals of Occupational Hygiene,* 44**,** 67-74.

ALBRECHT, C., KNAAPEN, A., BECKER, A., HÖHR, D., HABERZETTL, P., VAN SCHOOTEN, F., BORM, P. & SCHINS, R. 2005. The crucial role of particle surface reactivity in respirable quartz-induced reactive oxygen/nitrogen species formation and APE/Ref-1 induction in rat lung. *Respiratory Research,* 6**,** 1-16.

ALCALÁ, M. D., REAL, C. & CRIADO, J. M. 1996. A New "Incipient-Wetness" Method for the Synthesis of Chemically Stabilized β-Cristobalite. *Journal of the American Ceramic Society,* 79**,** 1681-1684.

BARRETT, E. G., JOHNSTON, C., OBERDÖRSTER, G. & FINKELSTEIN, J. N. 1999. Antioxidant Treatment Attenuates Cytokine and Chemokine Levels in Murine Macrophages Following Silica Exposure. *Toxicology and Applied Pharmacology,* 158**,** 211-220.

BAXTER, P. J., SEARL, A. S., COWIE, H. A., JARVIS, D. & HORWELL, C. J. 2014. Chapter 22 Evaluating the respiratory health risks of volcanic ash at the eruption of the Soufrière Hills Volcano, Montserrat, 1995 to 2010. *Geological Society, London, Memoirs,* 39**,** 407-425.

BESKOW, R. 1978. Silicosis in diatomaceous earth factory workers in Sweden. *Scandinavian journal of respiratory diseases,* 59**,** 216-221.

BORM, P. J. A., TRAN, L. & DONALDSON, K. 2011. The carcinogenic action of crystalline silica: A review of the evidence supporting secondary inflammation-driven genotoxicity as a principal mechanism. *Critical Reviews in Toxicology,* 41**,** 756-770.

BRITISH GEOLOGICAL SURVEY 2015. World Mineral Production 2009-2013. Keyworth, Nottingham: British Geological Survey.

BROWN, D. M., DONALDSON, K., BORM, P. J., SCHINS, R. P., DEHNHARDT, M., GILMOUR, P., JIMENEZ, L. A. & STONE, V. 2004. Calcium and ROS-mediated activation of transcription factors and TNF-alpha cytokine gene expression in macrophages exposed to ultrafine particles. *Am J Physiol Lung Cell Mol Physiol,* 286**,** L344-53.

BROWN, D. M., KANASE, N., GAISER, B., JOHNSTON, H. & STONE, V. 2014. Inflammation and gene expression in the rat lung after instillation of silica nanoparticles: Effect of size, dispersion medium and particle surface charge. *Toxicology Letters,* 224**,** 147-156.

BROWN, D. M., WILSON, M. R., MACNEE, W., STONE, V. & DONALDSON, K. 2001. Size-dependent proinflammatory effects of ultrafine polystyrene particles: a role for surface area and oxidative stress in the enhanced activity of ultrafines. *Toxicol Appl Pharmacol,* 175**,** 191-9.

BROWN, R. C., CHAMBERLAIN, M., DAVIES, R., MORGAN, D. M. L., POOLEY, F. D. & RICHARDS, R. J. 1980. A comparison of 4 in vitro systems applied to 21 dusts. *In:* BROWN, R. C. (ed.) *The in Vitro Effects of Mineral Dusts.* London, United Kingdom.: Academic Press.

BRUCH, J., REHN, S., REHN, B., BORM, P. J. A. & FUBINI, B. 2004. Variation of biological responses to different respirable quartz flours determined by a vector model. *International Journal of Hygiene and Environmental Health,* 207**,** 203-216.

BYE, E., DAVIES, R., GRIFFITHS, D. M., GYLSETH, B. & MONCRIEFF, C. B. 1984. In vitro cytotoxicity and quantitative silica analysis of diatomaceous earth products. *British Journal of Industrial Medicine,* 41**,** 228-234.

CAKMAK, G. D., SCHINS, R. P. F., SHI, T., FENOGLIO, I., FUBINI, B. & BORM, P. J. A. 2004. In vitro genotoxicity assessment of commercial quartz flours in comparison to standard DQ12 quartz. *International Journal of Hygiene and Environmental Health,* 207**,** 105-113.

CASSEL, S. L., EISENBARTH, S. C., IYER, S. S., SADLER, J. J., COLEGIO, O. R., TEPHLY, L. A., CARTER, A. B., ROTHMAN, P. B., FLAVELL, R. A. & SUTTERWALA, F. S. 2008. The Nalp3 inflammasome is essential for the development of silicosis. *Proceedings of the National Academy of Sciences of the United States of America,* 105**,** 9035-9040.

CASTRANOVA, V. 1994. Generation of oxygen radicals and mechanisms of injury prevention. *Environ Health Perspect,* 102 Suppl 10**,** 65-8.

CASTRANOVA, V., VALLYATHAN, V., RAMSEY, D. M., MCLAURIN, J. L., PACK, D., LEONARD, S., BARGER, M. W., MA, J. Y., DALAL, N. S. & TEASS, A. 1997. Augmentation of pulmonary reactions to quartz inhalation by trace amounts of iron-containing particles. *Environmental Health Perspectives,* 105**,** 1319-1324.

CHAISENA, A. & RANGSRIWATANANON, K. 2004. EFFECTS OF THERMAL AND ACID TREATMENTS ON SOME PHYSICO-CHEMICAL PROPERTIES OF LAMPANG DIATOMITE. *Suranaree Journal of Science and Technology,* 11**,** 289-299.

CHAMBERLAIN, M., DAVIES, R., BROWN, R. C. & GRIFFITHS, D. M. 1982. In Vitro Tests For The Pathogenicity of Mineral Dusts. *Annals of Occupational Hygiene,* 26**,** 583-592.

CHAMPION, J. A. & MITRAGOTRI, S. 2006. Role of target geometry in phagocytosis. *Proceedings of the National Academy of Sciences of the United States of America,* 103**,** 4930-4934.

CHAO, C. H. & LU, H. Y. 2002. beta-cristobalite stabilization in (Na2O+Al2O3)-added silica. *Metallurgical and Materials Transactions a-Physical Metallurgy and Materials Science,* 33**,** 2703-2711.

CHECKOWAY, H., HEYER, N. J., DEMERS, P. A. & BRESLOW, N. E. 1993. Mortality among workers in the diatomaceous earth industry. *British Journal of Industrial Medicine,* 50**,** 586-597.

CHECKOWAY, H., HEYER, N. J., DEMERS, P. A. & GIBBS, G. W. 1996. Reanalysis of mortality from lung cancer among diatomaceous earth industry workers, with consideration of potential confounding by asbestos exposure. *Occupational and Environmental Medicine,* 53**,** 645-647.

CHECKOWAY, H., HUGHES, J. M., WEILL, H., SEIXAS, N. S. & DEMERS, P. A. 1999. Crystalline silica exposure, radiological silicosis, and lung cancer mortality in diatomaceous earth industry workers. *Thorax,* 54**,** 56-59.

CHEN, F., SUN, S. C., KUH, D. C., GAYDOS, L. J. & DEMERS, L. M. 1995. Essential Role of NF-κB Activation in Silica-Induced Inflammatory Mediator Production in Macrophages. *Biochemical and Biophysical Research Communications,* 214**,** 985-992.

CHERRY, N. M., BURGESS, G. L., TURNER, S. & MCDONALD, J. C. 1998. Crystalline silica and risk of lung cancer in the potteries. *Occupational and Environmental Medicine,* 55**,** 779-785.

CLIFT, M. J. D., ROTHEN-RUTISHAUSER, B., BROWN, D. M., DUFFIN, R., DONALDSON, K., PROUDFOOT, L., GUY, K. & STONE, V. 2008. The impact of different nanoparticle surface chemistry and size on uptake and toxicity in a murine macrophage cell line. *Toxicology and Applied Pharmacology,* 232**,** 418-427.

CLOUTER, A., BROWN, D., HÖHR, D., BORM, P. & DONALDSON, K. 2001. Inflammatory Effects of Respirable Quartz Collected in Workplaces versus Standard DQ12 Quartz: Particle Surface Correlates. *Toxicological Sciences,* 63**,** 90-98.

COLLINS, J. F., SALMON, A. G., BROWN, J. P., MARTY, M. A. & ALEXEEFF, G. V. 2005. Development of a chronic inhalation reference level for respirable crystalline silica. *Regulatory Toxicology and Pharmacology,* 43**,** 292-300.

COOPER, W. C. & SARGENT, E. N. 1984. A 26-Year Radiographic Follow-Up of Workers in a Diatomite Mine and Mill. *Journal of Occupational and Environmental Medicine,* 26**,** 456-460.

CULLEN, R. T., VALLYATHAN, V., HAGEN, S. & DONALDSON, K. 1997. Protection by Iron Against the Toxic Effects of Quartz. *Annals of Occupational Hygiene,* 41**,** 420-425.

DAMBY, D. E. 2012. *From Dome to Disease: The Respiratory Toxicity of Volcanic Cristobalite.* Durham theses, Durham University.

DAMBY, D. E., LLEWELLIN, E. W., HORWELL, C. J., WILLIAMSON, B. J., NAJORKA, J., CRESSEY, G. & CARPENTER, M. 2014. The [alpha]-[beta] phase transition in volcanic cristobalite. *Journal of Applied Crystallography,* 47.

DANIEL, L. N., MAO, Y., WANG, T. C. L., MARKEY, C. J., MARKEY, S. P., SHI, X. L. & SAFFIOTTI, U. 1995. DNA Strand Breakage, Thymine Glycol Production, and Hydroxyl Radical Generation Induced by Different Samples of Crystalline Silica in Vitro. *Environmental Research,* 71**,** 60-73.

DEER, W. A., HOWIE, R. A. & ZUSSMAN, J. 2013. *An Introduction to the Rock-forming Minerals*, Mineralogical Society of Great Britain & Ireland.

DING, M., CHEN, F., SHI, X., YUCESOY, B., MOSSMAN, B. & VALLYATHAN, V. 2002. Diseases caused by silica: mechanisms of injury and disease development. *International Immunopharmacology,* 2**,** 173-182.

DONALDSON, K. & BORM, P. J. A. 1998. The Quartz Hazard: A Variable Entity. *Annals of Occupational Hygiene,* 42**,** 287-294.

DUFFIN, R., GILMOUR, P. S., SCHINS, R. P. F., CLOUTER, A., GUY, K., BROWN, D. M., MACNEE, W., BORM, P. J., DONALDSON, K. & STONE, V. 2001. Aluminium Lactate Treatment of DQ12 Quartz Inhibits Its Ability to Cause Inflammation, Chemokine Expression, and Nuclear Factor-κB Activation. *Toxicology and Applied Pharmacology,* 176**,** 10-17.

DUFFIN, R., TRAN, C. L., CLOUTER, A., BROWN, D. M., MACNEE, W., STONE, V. & DONALDSON, K. 2002. The Importance of Surface Area and Specific Reactivity in the Acute Pulmonary Inflammatory Response to Particles. *Annals of Occupational Hygiene,* 46**,** 242-245.

DUFFIN, R., TRAN, L., BROWN, D., STONE, V. & DONALDSON, K. 2007. Proinflammogenic effects of low-toxicity and metal nanoparticles in vivo and in vitro: highlighting the role of particle surface area and surface reactivity. *Inhal Toxicol,* 19**,** 849-56.

DUTRA, F. R. 1965. Diatomaceous earth pneumoconiosis. *Archives of environmental health,* 11**,** 613-619.

EBINA, T., TAKASE, Y., INASAWA, Y. & HORIE, K. 1952. Silicosis in the diatomaceous earth factories. *The Tohoku journal of experimental medicine,* 56**,** 214.

ELIAS, Z., POIROT, O., DANIÈRE, M. C., TERZETTI, F., BÉNA, F., FENOGLIO, I. & FUBINI, B. 2002. Role of Iron and Surface Free Radical Activity of Silica in the Induction of Morphological Transformation of Syrian Hamster Embryo Cells. *Annals of Occupational Hygiene,* 46**,** 53-57.

ELIAS, Z., POIROT, O., DANIÈRE, M. C., TERZETTI, F., MARANDE, A. M., DZWIGAJ, S., PEZERAT, H., FENOGLIO, I. & FUBINI, B. 2000. Cytotoxic and transforming effects of silica particles with different surface properties in Syrian hamster embryo (SHE) cells. *Toxicology in Vitro,* 14**,** 409-422.

ELIAS, Z., POIROT, O., FENOGLIO, I., GHIAZZA, M., DANIÈRE, M. C., TERZETTI, F., DARNE, C., COULAIS, C., MATEKOVITS, I. & FUBINI, B. 2006. Surface Reactivity, Cytotoxic, and Morphological Transforming Effects of Diatomaceous Earth Products in Syrian Hamster Embryo Cells. *Toxicological Sciences,* 91**,** 510-520.

FENOGLIO, I., PRANDI, L., TOMATIS, M. & FUBINI, B. 2001. Free radical generation in the toxicity of inhaled mineral particles: the role of iron speciation at the surface of asbestos and silica. *Redox Report,* 6**,** 235-241.

FRONDEL, C. 1962. *The system of mineralogy, Vol. III The silica minerals,* New York, J. Wiley and Sons.

FUBINI, B. 1998. Surface Chemistery and Quartz Hazard. *Annals of Occupational Hygiene,* 42**,** 521-530.

FUBINI, B., BOLIS, V., CAVENAGO, A. & VOLANTE, M. 1995. Physicochemical properties of crystalline silica dusts and their possible implication in various biological responses. *Scandinavian Journal of Work, Environment and Health,* 21 suppl 2**,** 9-14.

FUBINI, B., BOLIS, V. & GIAMELLO, E. 1987. The surface chemistry of crushed quartz dust in relation to its pathogenicity. *Inorganica Chimica Acta,* 138**,** 193-197.

FUBINI, B., FENOGLIO, I., ELIAS, Z. & POIROT, O. 2001. Variability of biological responses to silicas: effect of origin, crystallinity, and state of surface on generation of reactive oxygen species and morphological transformation of mammalian cells. *J Environ Pathol Toxicol Oncol,* 20 Suppl 1**,** 95-108.

FUBINI, B., GIAMELLO, E., VOLANTE, M. & BOLIS, V. 1990. Chemical functionalities at the silica surface determining its reactivity when inhaled. Formation and reactivity of surface radicals. *Toxicol Ind Health,* 6**,** 571-98.

FUBINI, B. & HUBBARD, A. 2003. Reactive oxygen species (ROS) and reactive nitrogen species (RNS) generation by silica in inflammation and fibrosis. *Free Radical Biology and Medicine,* 34**,** 1507-1516.

FUBINI, B., ZANETTI, G., ALTILIA, S., TIOZZO, R., LISON, D. & SAFFIOTTI, U. 1999. Relationship between Surface Properties and Cellular Responses to Crystalline Silica: Studies with Heat-Treated Cristobalite. *Chemical Research in Toxicology,* 12**,** 737-745.

GAI-BOYES, P. L., SALTZBERG, M. A. & VEGA, A. 1993. Structures and Stabilization Mechanisms in Chemically Stabilized Ceramics. *Journal of Solid State Chemistry,* 106**,** 35-47.

GHIAZZA, M., GAZZANO, E., BONELLI, B., FENOGLIO, I., POLIMENI, M., GHIGO, D., GARRONE, E. & FUBINI, B. 2009. Formation of a Vitreous Phase at the Surface of Some Commercial Diatomaceous Earth Prevents the Onset of Oxidative Stress Effects. *Chemical Research in Toxicology,* 22**,** 136-145.

GHIAZZA, M., SCHERBART, A. M., FENOGLIO, I., GRENDENE, F., TURCI, F., MARTRA, G., ALBRECHT, C., SCHINS, R. P. F. & FUBINI, B. 2011. Surface Iron Inhibits Quartz-Induced Cytotoxic and Inflammatory Responses in Alveolar Macrophages. *Chemical Research in Toxicology,* 24**,** 99-110.

GHIAZZA, M., TOMATIS, M., DOUBLIER, S., GRENDENE, F., GAZZANO, E., GHIGO, D. & FUBINI, B. 2013. Carbon in intimate contact with quartz reduces the biological activity of crystalline silica dusts. *Chem Res Toxicol,* 26**,** 46-54.

GIBBS, G. W. & CHRISTENSEN, D. R. 1994. The asbestos exposure of workers in the Manville diatomaceous earth plant, Final report to the International Diatomite Producers Association. Lompoc, California. *In:* ASSOCIATION, I. D. P. (ed.).

GILBERTI, R. M., JOSHI, G. N. & KNECHT, D. A. 2008. The phagocytosis of crystalline silica particles by macrophages. *Am J Respir Cell Mol Biol,* 39**,** 619-27.

GOREN, R., BAYKARA, T. & MARSOGLU, M. 2002. A study on the purification of diatomite in hydrochloric acid. *Scandinavian Journal of Metallurgy,* 31**,** 115-119.

GOZAL, E., ORTIZ, L. A., ZOU, X., BUROW, M. E., LASKY, J. A. & FRIEDMAN, M. 2002. Silica-induced apoptosis in murine macrophage: involvement of tumor necrosis factor-alpha and nuclear factor-kappaB activation. *Am J Respir Cell Mol Biol,* 27**,** 91-8.

GREENBERG, M. I., WAKSMAN, J. & CURTIS, J. 2007. Silicosis: a review. *Dis Mon,* 53**,** 394-416.

HAMILTON, J., RAYMOND F., THAKUR, S. A. & HOLIAN, A. 2008. Silica binding and toxicity in alveolar macrophages. *Free Radical Biology and Medicine,* 44**,** 1246-1258.

HARBER, P., DAHLGREN, J., BUNN, W., LOCKEY, J. & CHASE, G. 1998. Radiographic and Spirometric Findings in Diatomaceous Earth Workers. *Journal of Occupational and Environmental Medicine,* 40**,** 22-28.

HART, G. A. & HESTERBERG, T. M. 1998. *In vitro toxicity of respirable-size particles of diatomaceous earth and crystalline silica compared with asbestos and titanium dioxide,* Hagerstown, MD, ETATS-UNIS, Lippincott Williams & Wilkins.

HEANEY, P. J., PREWITT, C. T. & GIBBS, G. V. 1994. *Silica: Physical Behavior, Geochemistry and Materials Applications,* Washington D.C., Mineralogical Society of America.

HEIN, J. R., SCHOLL, D. W., BARRON, J. A., JONES, M. G. & MILLER, J. 1978. Diagenesis of late Cenozoic diatomaceous deposits and formation of the bottom simulating reflector in the southern Bering Sea*. *Sedimentology,* 25**,** 155-181.

HEMENWAY, D. R., ABSHER, M. P., FUBINI, B. & BOLIS, V. 1993. What is the relationship between hemolytic potential and fibrogenicity of mineral dusts? *Arch Environ Health,* 48**,** 343-7.

HESSEL, P. A. 1999. Methodological Issues Related to Studies of Workers in the Diatomaceous Earth Industry. *Indoor and Built Environment,* 8**,** 127-131.

HOLOPAINEN, M., HIRVONEN, M.-R., KOMULAINEN, H. & KLOCKARS, M. 2004. Effect of the shape of mica particles on the production of tumor necrosis factor alpha in mouse macrophages. *Scandinavian Journal of Work, Environment & Health,* 30**,** 91-98.

HORWELL, C. & BAXTER, P. 2006. The respiratory health hazards of volcanic ash: a review for volcanic risk mitigation. *Bulletin of Volcanology,* 69**,** 1-24.

HORWELL, C., WILLIAMSON, B., DONALDSON, K., LE BLOND, J., DAMBY, D. & BOWEN, L. 2012. The structure of volcanic cristobalite in relation to its toxicity; relevance for the variable crystalline silica hazard. *Particle and Fibre Toxicology,* 9**,** 44.

HORWELL, C. J., HILLMAN, S. E., COLE, P. D., LOUGHLIN, S. C., LLEWELLIN, E. W., DAMBY, D. E. & CHRISTOPHER, T. E. 2014. Chapter 21 Controls on variations in cristobalite abundance in ash generated by the Soufrière Hills Volcano, Montserrat in the period 1997 to 2010. *Geological Society, London, Memoirs,* 39**,** 399-406.

HOUSLEY, D. G., BERUBE, K. A., JONES, T. P., ANDERSON, S., POOLEY, F. D. & RICHARDS, R. J. 2002. Pulmonary epithelial response in the rat lung to instilled Montserrat respirable dusts and their major mineral components. *Occup Environ Med,* 59**,** 466-72.

HSE, H. A. S. E. 2002. *Respirable crystalline silica - Phase 1. Variability in fibrogenic potency and exposure-response relationships for silicosis,* Richmond, Surrey, HSE Books (available at: www.hse.gov.uk/pUbns/priced/eh75-4).

HUGHES, J., WEILL, H., CHECKOWAY, H., JONES, R., HENRY, M., HEYER, N., SEIXAS, N. & DEMERS, P. 1998. Radiographic Evidence of Silicosis Risk in the Diatomaceous Earth Industry. *American Journal of Respiratory and Critical Care Medicine,* 158**,** 807-814.

IARC 1997. Silica, some silicates, coal dust and para-aramid fibrils. . Lyon: International Agency for Research on Cancer.

IARC 2012. Arsenic, Metals, Fibres, and Dusts. International Agency for Research on Cancer.

IMERYS MINERALS LTD. 2012. *Diatomite Product List* [Online]. http://www.imerys-perfmins.com/diatomite/eu/diatomite-products.htm. [Accessed 11/06/2015 2015].

JOMA, T. H. J. M., BORM, P. J. A., KOITER, K. D., SLANGEN, J. J. M., HENDERSON, P. T. & WOUTERS, E. F. M. 1994. Respiratory effects and serum type III procollagen in potato sorters exposed to diatomaceous earth. *International Archives of Occupational and Environmental Health,* 66**,** 217-222.

JONES, T. & BÉRUBÉ, K. 2011. The bioreactivity of the sub-10µm component of volcanic ash: Soufrière Hills volcano, Montserrat. *Journal of Hazardous Materials,* 194**,** 128-134.

KE, Q., LI, J., DING, J., DING, M., WANG, L., LIU, B., COSTA, M. & HUANG, C. 2006. Essential role of ROS-mediated NFAT activation in TNF-alpha induction by crystalline silica exposure. *Am J Physiol Lung Cell Mol Physiol,* 291**,** L257-64.

KING, E. J., MOHANTY, G. P., HARRISON, C. V. & NAGELSCHMIDT, G. 1953. The Action of Different Forms of Pure Silica on the Lungs of Rats. *British Journal of Industrial Medicine,* 10**,** 9-17.

KNAAPEN, A. M., ALBRECHT, C., BECKER, A., HÖHR, D., WINZER, A., HAENEN, G. R., BORM, P. J. A. & SCHINS, R. P. F. 2002. DNA damage in lung epithelial cells isolated from rats exposed to quartz: role of surface reactivity and neutrophilic inflammation. *Carcinogenesis,* 23**,** 1111-1120.

KREYLING, W. G. & SCHEUCH, G. 2000. Clearance of Particles Deposited in the Lungs. *In:* GEHR, P. & HEYDER, J. (eds.) *Particle-Lung Interactions.* New York: Marcel Dekker, Inc.

LE BOUFFANT, L., DANIEL, H., MARTIN, J. C. & BRUYERE, S. 1982. Effect of Impurities and Associated Minerals on Quartz Toxicity. *Annals of Occupational Hygiene,* 26**,** 625-634.

LEGGE, R. & ROSENCRANTZ, E. 1932. Observations and Studies on Silicosis by Diatomaceous Silica. *American Journal of Public Health and the Nations Health,* 22**,** 1055-1060.

LEUNG, C. C., YU, I. T. S. & CHEN, W. 2012. Silicosis. *The Lancet,* 379**,** 2008-2018.

MAEDA, H., FORD, J., WILLIAMS JR, M. G. & DODSON, R. F. 1986. An ultrastructural study of acute and long-term lung response to commercial diatomaceous earth. *Journal of Comparative Pathology,* 96**,** 307-317.

MAHANI, H. & KAZEMEINE, M. 2003. Treatment of diatomaceous earth to obtain its catalyst support. *Scientia Iranica,* 10**,** 350-356.

MARKS, J., MASON, M. A. & NAGELSCHMIDT, G. 1956. A Study of Dust Toxicity using a Quantitative Tissue Culture Technique. *British Journal of Industrial Medicine,* 13**,** 38.

MCCLELLAN, R. O. 2000. Particle Interactions with the Respiratory Tract. *In:* GEHR, P. & HEYDER, J. (eds.) *Particle-Lung Interactions.* New York: Marcel Dekker, Inc.

MELDRUM, M. & HOWDEN, P. 2002. Crystalline Silica: Variability in Fibrogenic Potency. *Annals of Occupational Hygiene,* 46**,** 27-30.

MIZUTANI, S. 1977. Progressive ordering of cristobalitic silica in the early stage of diagenesis. *Contributions to Mineralogy and Petrology,* 61**,** 129-140.

MOSSMAN, B. T. & GLENN, R. E. 2013. Bioreactivity of the crystalline silica polymorphs, quartz and cristobalite, and implications for occupational exposure limits (OELs). *Critical Reviews in Toxicology,* 43**,** 632-660.

MOUNT SYLVIA DIATOMITE PTY LTD. 2015. *Mount Sylvia Diatomite Products* [Online]. http://www.mtsylviadiatomite.com.au/diatomite-products/. [Accessed 11/06/2015 2015].

NIOSH 2002. Health Effects of Occupational Exposure to Respirable Crystalline Silica. *In:* SERVICES, D. O. H. A. H. (ed.).

NOLAN, R. P., LANGER, A. M., HARINGTON, J. S., OSTER, G. & SELIKOFF, I. J. 1981. Quartz hemolysis as related to its surface functionalities. *Environmental Research,* 26**,** 503-520.

NOWAK, W. S. 1976. The diatomite industry of Iceland: The Development of a subarctic resource. *Cahiers de géographie du Québec,,* 20**,** 143-162.

OGELE, T. A. 2014. *Anatomy of the Respiratory System* [Online]. http://cnx.org/contents/60ffba05-d8e9-4f25-b02f-e4bf23142dd7@1/Anatomy_of_the_Respiratory_Sys: Creative Commons Attribution License (3.0) [Accessed 20/06/2015 2015].

PANDURANGI, R. S., SEEHRA, M. S., RAZZABONI, B. L. & BOLSAITIS, P. 1990. Surface and bulk infrared modes of crystalline and amorphous silica particles: a study of the relation of surface structure to cytotoxicity of respirable silica. *Environmental Health Perspectives,* 86**,** 327-336.

PARK, R., RICE, F., STAYNER, L., SMITH, R., GILBERT, S. & CHECKOWAY, H. 2002. Exposure to crystalline silica, silicosis, and lung disease other than cancer in diatomaceous earth industry workers: a quantitative risk assessment. *Occupational and Environmental Medicine,* 59**,** 36-43.

PAVAN, C., TOMATIS, M., GHIAZZA, M., RABOLLI, V., BOLIS, V., LISON, D. & FUBINI, B. 2013. In Search of the Chemical Basis of the Hemolytic Potential of Silicas. *Chemical Research in Toxicology,* 26**,** 1188-1198.

PEETERS, P. M., EURLINGS, I. M., PERKINS, T. N., WOUTERS, E. F., SCHINS, R. P., BORM, P. J., DROMMER, W., REYNAERT, N. L. & ALBRECHT, C. 2014. Silica-induced NLRP3 inflammasome activation in vitro and in rat lungs. *Part Fibre Toxicol,* 11**,** 58.

PERROTTA, A. J., GRUBBS, D. K., MARTIN, E. S., DANDO, N. R., MCKINSTRY, H. A. & HUARG, C.-Y. 1989. Chemical Stabilization of β-Cristobalite. *Journal of the American Ceramic Society,* 72**,** 441-447.

PIGUET, P. F., COLLART, M. A., GRAU, G. E., SAPPINO, A.-P. & VASSALLI, P. 1990. Requirement of Tumour Necrosis Factor for Development of Silica-Induced Pulmonary Fibrosis. *Nature,* 344**,** 245.

PIMRAKSA, K. & CHINDAPRASIRT, P. 2009. Lightweight bricks made of diatomaceous earth, lime and gypsum. *Ceramics International,* 35**,** 471-478.

PRATT, P. C. 1983. Lung dust content and response in guinea pigs inhaling three forms of silica. *Archives of environmental health,* 38**,** 197-204.

QINGDAO QIANCHENG MINERALS CO. LTD. 1990. *Qiancheng Minerals* [Online]. http://www.qianchengminerals.com/_d4.htm. [Accessed 11/06/2015 2015].

QUALITY OF URBAN AIR REVIEW GROUP 1996. Airborne particulate matter in the United Kingdom. *In:* DEPARTMENT OF THE ENVIRONMENT (ed.). London, UK.

RAFNSSON, V. & GUNNARSDÓTTIR, H. 1997. Lung cancer incidence among an Icelandic cohort exposed to diatomaceous earth and cristobalite. *Scandinavian Journal of Work, Environment and Health,* 23**,** 187-192.

REICH, M., ZÚÑIGA, A., AMIGO, Á., VARGAS, G., MORATA, D., PALACIOS, C., PARADA, M. Á. & GARREAUD, R. D. 2009. Formation of cristobalite nanofibers during explosive volcanic eruptions. *Geology,* 37**,** 435-438.

RICE, F. L., PARK, R., STAYNER, L., SMITH, R., GILBERT, S. & CHECKOWAY, H. 2001. Crystalline silica exposure and lung cancer mortality in diatomaceous earth industry workers: a quantitative risk assessment. *Occupational and Environmental Medicine,* 58**,** 38-45.

RIMOLA, A., COSTA, D., SODUPE, M., LAMBERT, J.-F. & UGLIENGO, P. 2013. Silica Surface Features and Their Role in the Adsorption of Biomolecules: Computational Modeling and Experiments. *Chemical Reviews,* 113**,** 4216-4313.

ROJANASAKUL, Y., YE, J., CHEN, F., WANG, L., CHENG, N., CASTRANOVA, V., VALLYATHAN, V. & SHI, X. 1999. Dependence of NF-kappaB activation and free radical generation on silica-induced TNF-alpha production in macrophages. *Mol Cell Biochem,* 200**,** 119-25.

SALTZBERG, M. A., BORS, S. L., BERGNA, H. & WINCHESTER, S. C. 1992. Synthesis of Chemically Stabilized Cristobalite. *Journal of the American Ceramic Society,* 75**,** 89-95.

ŞAN, O., GÖREN, R. & ÖZGÜR, C. 2009. Purification of diatomite powder by acid leaching for use in fabrication of porous ceramics. *International Journal of Mineral Processing,* 93**,** 6-10.

ŞAN, O. & ÖZGÜR, C. 2009. Investigation of a high stable β-cristobalite ceramic powder from CaO–Al2O3–SiO2 system. *Journal of the European Ceramic Society,* 29**,** 2945-2949.

SCHINS, R. P. F., DUFFIN, R., HÖHR, D., KNAAPEN, A. M., SHI, T., WEISHAUPT, C., STONE, V., DONALDSON, K. & BORM, P. J. A. 2002. Surface Modification of Quartz Inhibits Toxicity, Particle Uptake, and Oxidative DNA Damage in Human Lung Epithelial Cells. *Chemical Research in Toxicology,* 15**,** 1166-1173.

SCHINWALD, A. & DONALDSON, K. 2012. Use of back-scatter electron signals to visualise cell/nanowires interactions in vitro and in vivo; frustrated phagocytosis of long fibres in macrophages and compartmentalisation in mesothelial cells in vivo. *Particle and Fibre Toxicology,* 9**,** 34.

SCHINWALD, A., MURPHY, F. A., JONES, A., MACNEE, W. & DONALDSON, K. 2012. Graphene-based nanoplatelets: a new risk to the respiratory system as a consequence of their unusual aerodynamic properties. *ACS Nano,* 6**,** 736-46.

SCHULZ, H., BRAND, P. & HEYDER, J. 2000. Particle deposition in the respiratory tract. *In:* GEHR, P. & HEYDER, J. (eds.) *Particle-Lung Interactions.* New York: Marcel Dekker, Inc.

SEILER, F., REHN, B., REHN, S. & BRUCH, J. 2004. Different toxic, fibrogenic and mutagenic effects of four commercial quartz flours in the rat lung. *International Journal of Hygiene and Environmental Health,* 207**,** 115-124.

SEIXAS, N. S., HEYER, N. J., WELP, E. A. E. & CHECKOWAY, H. 1997. Quantification of Historical Dust Exposures in the Diatomaceous Earth Industry. *Annals of Occupational Hygiene,* 41**,** 591-604.

SHACKELFORD, J. F. & DOREMUS, R. I. 2008. *Ceramic and Glass Materials: Structure, Properties and Processing,* New York, Springer Science+Business Media.

SHENGZHOU HUALI DIATOMITE PRODUCTS CO. LTD. 2015. *Products* [Online]. http://www.cndiatomite.com/pages/pro.html. [Accessed 11/06/2015 2015].

SMART, R. H. & ANDERSON, W. M. 1952. Pneumoconiosis due to diatomaceous earth; clinical and x-ray aspects. *Industrial medicine & surgery,* 21**,** 509-518.

SMITH, D. K. 1998. Opal, cristobalite, and tridymite: Noncrystallinity versus crystallinity, nomenclature of the silica minerals and bibliography. *Powder Diffraction,* 13**,** 2-19.

STEENLAND, K., MANNETJE, A., BOFFETTA, P., STAYNER, L., ATTFIELD, M., CHEN, J., DOSEMECI, M., DEKLERK, N., HNIZDO, E., KOSKELA, R. & CHECKOWAY, H. 2001. Pooled exposure–response analyses and risk assessment for lung cancer in 10 cohorts of silica-exposed workers: an IARC multicentre study. *Cancer Causes and Control,* 12**,** 773-784.

STEVENS, S. J., HAND, R. J. & SHARP, J. H. 1997. Temperature dependence of the cristobalite α-β inversion. *Journal of thermal analysis,* 49**,** 1409-1415.

STONE, V., JONES, R., ROLLO, K., DUFFIN, R., DONALDSON, K. & BROWN, D. M. 2004. Effect of coal mine dust and clay extracts on the biological activity of the quartz surface. *Toxicology Letters,* 149**,** 255-259.

THIBODEAU, M. S., GIARDINA, C., KNECHT, D. A., HELBLE, J. & HUBBARD, A. K. 2004. Silica-Induced Apoptosis in Mouse Alveolar Macrophages Is Initiated by Lysosomal Enzyme Activity. *Toxicological Sciences,* 80**,** 34-48.

THOMAS, E. S., THOMPSON, J. G., WITHERS, R. L., STERNS, M., XIAO, Y. & KIRKPATRICK, R. J. 1994. Further Investigation of the Stabilization of β-Cristobalite. *Journal of the American Ceramic Society,* 77**,** 49-56.

TOURMANN, J. L. & KAUFMANN, R. 1994. Biopersistence of the mineral matter of coal mine dusts in silicotic human lungs: is there a preferential release of iron? *Environ Health Perspect,* 102 Suppl 5**,** 265-8.

TSAI, W.-T., HSIEN, K.-J. & LAI, C.-W. 2004. Chemical activation of spent diatomaceous earth by alkaline etching in the preparation of mesoporous adsorbents. *Industrial & Engineering Chemistry Research,* 43**,** 7513-7520.

TSAI, W.-T., LAI, C.-W. & HSIEN, K.-J. 2006. Characterization and adsorption properties of diatomaceous earth modified by hydrofluoric acid etching. *Journal of Colloid and Interface Science,* 297**,** 749-754.

VALLYATHAN, V., SHI, X. L., DALAL, N. S., IRR, W. & CASTRANOVA, V. 1988. Generation of free radicals from freshly fractured silica dust. Potential role in acute silica-induced lung injury. *Am Rev Respir Dis,* 138**,** 1213-9.

VAN EATON, A. R., HARPER, M. A. & WILSON, C. J. N. 2013. High-flying diatoms: Widespread dispersal of microorganisms in an explosive volcanic eruption. *Geology*.

VENEZIA, A. M., LA PAROLA, V., LONGO, A. & MARTORANA, A. 2001. Effect of Alkali Ions on the Amorphous to Crystalline Phase Transition of Silica. *Journal of Solid State Chemistry,* 161**,** 373-378.

VIGLIANI, E. C. & MOTTURA, G. 1948. Diatomaceous Earth Silicosis. *British Journal of Industrial Medicine,* 5**,** 148-160.

WAGNER, W. D., FRASER, D. A., WRIGHT, P. G., DOBROGORSKI, O. J. & STOKINGER, H. E. 1968. Experimental Evaluation of the Threshold Limit of Cristobalite—Calcined Diatomaceous Earth. *American Industrial Hygiene Association Journal,* 29**,** 211-221.

WARHEIT, D. B., WEBB, T. R., COLVIN, V. L., REED, K. L. & SAYES, C. M. 2007. Pulmonary Bioassay Studies with Nanoscale and Fine-Quartz Particles in Rats: Toxicity is Not Dependent upon Particle Size but on Surface Characteristics. *Toxicological Sciences,* 95**,** 270-280.

WHO 1985. Reference methods for measuring airborne man-made mineral fibres. Copenhagen: World Health Organization Regional Office for Europe, (Environmental Health Report No. 4).

ZHANG, H., NIU, J.-Z., KOU, Y., TANAKA, T. & YOSHIDA, S. 1998. Surface Coordinate Geometry of Iron Catalysts: Formation of Tetrahedral/Octahedral Site on Silica Surface with/without Sodium Promoter. *Journal of Solid State Chemistry,* 137**,** 325-331.

ZHANG, Z., SHEN, H.-M., ZHANG, Q.-F. & ONG, C.-N. 2000. Involvement of Oxidative Stress in Crystalline Silica-Induced Cytotoxicity and Genotoxicity in Rat Alveolar Macrophages. *Environmental Research,* 82**,** 245-252.

ZIEMANN, C., HARRISON, P. T., BELLMANN, B., BROWN, R. C., ZOITOS, B. K. & CLASS, P. 2014. Lack of marked cyto- and genotoxicity of cristobalite in devitrified (heated) alkaline earth silicate wools in short-term assays with cultured primary rat alveolar macrophages. *Inhal Toxicol,* 26**,** 113-27.

Chapter 3

Methodologies

A variety of different methods were used in order to fully characterise the samples used throughout this thesis, and to test their toxic potential. Here, these methods are described in detail and will be referred to in future chapters.

Both diatomaceous earth and synthetic crystalline silica samples were used. The samples chosen for analysis are described in detail in the relevant chapters and will not be discussed here. Samples were prepared in various ways for different techniques. As DE samples were provided in a powdered form, all analyses were performed on powders, and the separated fine fraction of these powders. Synthetic crystalline silica samples were produced as pellets (see Chapter 6 for method). Sections of these pellets were used to produce cross sections for imaging and elemental analysis. The remainder of the pellets were ground into a fine powder for further analyses.

3.1 Sample preparation

For toxicological analyses it is important to use particles that are biologically relevant i.e. particles that have the potential to penetrate into the lung. Particles are classified as inhalable, thoracic and respirable, based on the particle size (<100 μm inhalable; <10 μm thoracic; <4 μm respirable (Quality of Urban Air Review Group, 1996)) (see Chapter 2). Therefore, the fine fractions, which were approximately PM10 (50 % <10 μm), were separated or ground for the two different sample types.

3.1.1 Separation of the fine fraction – diatomaceous earth

Separation of the fine fraction of DE powders was performed by a dry re-suspension method previously described by Moreno et al. (2005) and used for the separation of fine fractions of volcanic ash (Jones and BéruBé, 2011). The sample was suspended in a horizontal rotating drum with a baffle (1.5 rpm). Airflow of 6 l/min was passed through this system, which carried suspended particles through a gravitational settling chamber, where coarser particles were deposited, and the fine fraction continued through a Negretti elutriation filter system and was collected on a polycarbonate filter (Figure 3.1). Particles were gently scraped from the filter using a Teflon spatula and particle size assessed by scanning electron microscopy (SEM; see below) imaging.

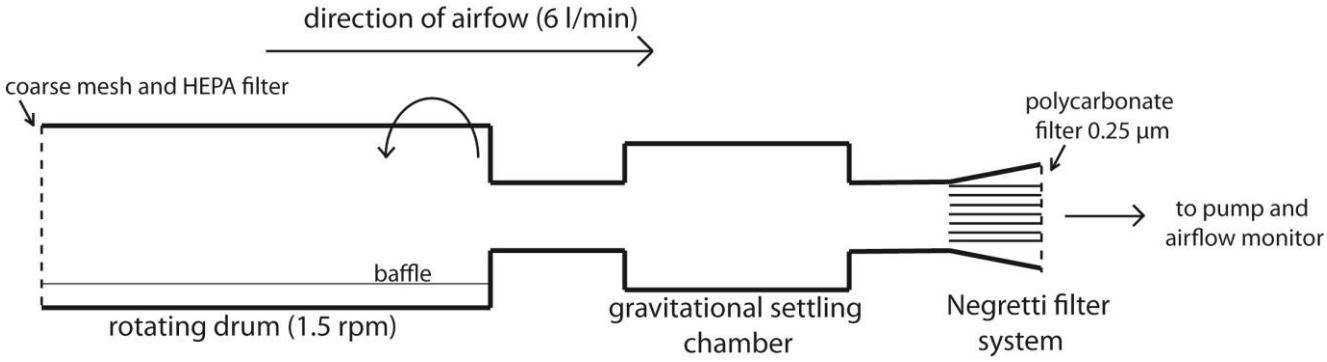

Figure 3.1: Schematic of the dry-resuspension method used to separate the fine fraction of DE.

3.1.2 Grinding to a fine powder – synthetic crystalline silica

Synthetic crystalline silica was produced by heating a silica sol/gel at high temperatures to produce a pellet (see Chapter 6 for detail). To grind this pellet into particles sufficiently small to potentially enter the lung, hand grinding and cryogenic milling were both tested. For hand grinding, samples were ground by hand in air, in an agate mortar and pestle until no large grains could be felt. Cryogenic grinding was performed using a 6870 Freezer/Mill® (SPEX®SamplePrep) within a

polycarbonate tube with polycarbonate coated magnet at 77 K. At this temperature, the sample is brittle and so can be ground more efficiently as the magnet moves (at 12 cycles per second) from side to side. The low temperature also prevents samples and the instrument from being heated during this intense grinding. Samples were ground for 30 minutes with 2 minutes cooling time every 5 minutes to ensure the sample and instrument remained cool. Particle size was then analysed by laser diffraction (see Section 3.2.1.6, below) to determine if a thoracic powder had been produced by either method for use in toxicology studies. Comparison of hand-ground and cryogenically ground particle size distributions is presented in Appendix 1. As cryogenic grinding was more efficient, this method was employed in Chapter 7.

3.2 Physicochemical characterisation

3.2.1 Bulk analytical techniques

3.2.1.1 Electron microscopy based analysis

3.2.1.1.1 Sample preparation

Particulate samples were prepared for imaging by spreading particles across a polycarbonate sheet using an ethanol dipped cotton bud, and sticking the sheet to an aluminium stub using a carbon sticky pad. Samples were sputter coated with gold/palladium to a thickness of ~20 nm to prevent charging of the particles under the beam.

Cross sections of samples were produced in thick resin blocks by Ian Chaplin (Durham University). Powdered samples of DE were prepared by suspending particles in resin which was allowed to set. Synthetic pellets were impregnated in resin and allowed to set. Both sample types were then

diamond polished using UltraPrep diamond discs of 20 and 10 µm. Samples were lapped on a glass plate using silicon carbide powder of 1200 grit. Then, samples were polished using diamond suspensions of 15 µm and perforated TexMet for 3 minutes, and diamond suspensions of 15, 9, 6, 3 and 1 µm on TexMet cloth for 5 minutes each on an EcoMet 300 and AutoMet 300 (Buehler) to produce a smooth surface for analysis. Further polish using colloidal silica was used to prepare samples for electron backscatter diffraction (EBSD) analysis (below).

Imaging and elemental analysis were performed on all samples using a Hitachi SU-70 field emission gun (FEG) scanning electron microscope (SEM) and a FEI Helios Nanolab 600 at the GJ Russell Facility, Durham University. Electron microprobe analyses (EMPA) were performed on a Cameca SX-100 at Ludwig-Maxmilians-Universität München, Germany. A number of different analyses can be performed in conjunction with electron microscopy to give topographic information, qualitative and quantitative elemental composition, and crystallographic information:

3.2.1.1.2 Secondary electron imaging

Secondary electron (SE) imaging was used to image particles of diatomaceous earth and crystalline silica to give topographic and morphological data. SE imaging was also used to check sample preparation, to ensure areas where topography varied were not used in elemental analysis. Samples were analysed at a working distance of 15 mm and an accelerating voltage of 8 kV. The maximum diameter and the length of the axis at 90° to this diameter of up to 2000 imaged particles were measured using ImageJ software to assess their particle size distribution and aspect ratios.

3.2.1.1.3 Backscatter electron imaging

Backscatter electron (BSE) imaging was used to image cross sections of particles and to help identify phases for elemental analysis. As electrons originating from the beam are reflected more by elements with higher atomic number, these appear brighter than low atomic number elements in the image produced. Samples were analysed at a working distance of 15 mm and an accelerating voltage of 15 kV.

3.2.1.1.4 Energy dispersive X-ray spectroscopy

Energy dispersive X-ray spectroscopy (EDS) can be used in conjunction with SEM as a semi-quantitative method to measure the elemental composition of cross sectional samples. As electrons from the beam excite electrons in the atoms of the sample, X-rays are emitted and detected using an INCA x-act LN_2-free analytical Silicon Drift Detector (Oxford Instruments). The data are then analysed using Oxford Instruments' INCA software. Analysis occurs at a working distance of 15 mm at an accelerating voltage of 15 kV. Before each session, the instrument calibration was checked using a cobalt standard under the same analysis conditions. However, the lack of appropriate standards for each element and the lower detection limit of EDS compared to wavelength dispersive spectrometers (WDS) used in the electron microprobe (below) means the data are only semi-quantitative.

3.2.1.1.5 Electron microprobe analysis

Electron probe micro analysis (EPMA) measurements were carried out on a Cameca SX-100 system equipped with a LaB_6 cathode and five vertical crystal wavelength dispersive spectrometers (WDS) detectors by Dr. David Damby (Ludwig-Maxmilians-Universität München, Germany). Samples were analysed for Na, Al, Si, Mg, S, K and Fe using a focused beam. Measurements for Na, Si and Al were performed at an accelerating voltage of 15 keV at a current of 4 nA, and Mg, S, K and Fe at 15 keV

and 40 nA. Sodium was measured first to minimise the effect of sodium drift on the results. Instrument calibration was carried out by analysing the following reference materials of known compositions: Na on albite, Al on Al_2O_3, Si on quartz, Mg on periclase, S on anhydrite, K on orthoclase, Fe on Fe_2O_3. The crystals used for measurements were Sp1 TAP (Na, Mg), Sp2 PET (S, K), Sp3 LLIF (Fe), Sp4 TAP (Al), Sp5 TAP (Si).

3.2.1.1.6 Electron backscatter diffraction

Electron backscattered diffraction (EBSD) was performed by Leon Bowen (Durham University) using an Oxford Nordlys HKL detector on a focussed ion beam (FIB) SEM (FEI Helios Nanolab 600) to determine the crystal polymorph and crystalline structures in synthetic crystalline silica samples. Samples were inserted at a 70° angle and electron beam applied. Some electrons are diffracted and are detected by a phosphor screen, which fluoresces when excited by these electrons, producing an electron backscatter diffraction pattern. As electrons are diffracted according to Bragg's Law (Equation 3.1), the lattice parameters can be determined.

$$n\lambda = 2dsin\theta$$

Equation 3.1

where n is an integer, λ is the wavelength of incident wave, d is the spacing between the planes in the atomic lattice, and θ is the angle between the incident ray and the scattering planes.

3.2.1.1.7 Cathodoluminescence

Cathodoluminescence (CL) was also used to assess the crystallinity of selected areas of some synthetic samples using a Gatan MonoCL cathodoluminescence system and Digiscan II image

processing software (Gatan, Inc., Pleasanton, CA, USA) attached to the Hitachi SU70 FEG-SEM (Durham University). A voltage of 8 kV was applied to cause sample luminescence. Panchromatic scans, and those with a red, green or blue filter, were applied to determine the wavelength of sample luminescence. True colour compositions were produced from the red, green and blue filter greyscale scans to determine the wavelengths emitted from different areas of the sample. This can allow identification of minerals and grain boundaries, as luminescence is affected by both chemistry and crystal structure.

3.2.1.2 X-ray Diffraction

X-ray diffraction (XRD) was used to analyse the crystalline composition of samples and to give relative quantities of crystalline silica polymorphs. All samples were run on a Bruker AXS D8 ADVANCE with DAVINCI design at Durham University. X-rays were emitted from a copper source and these are diffracted by atoms within the sample according to Bragg's Law (Equation 3.1). In crystalline samples, where the atoms are ordered, the angle at which the X-rays are diffracted is always the same and can be used to determine the crystal lattice parameters. This is matched against library standards or theoretically calculated lattice parameters to identify different crystal phases in a sample.

Here, two different techniques were used. First, crystalline phases were identified using a locked coupled scan from 2-90° 2θ, where both the source and the detector move in unison and a rapid scan can be obtained. Samples were prepared by grinding by hand in an agate mortar and pestle and sieving through a 250 µm mesh onto a silicon slide coated with a small quantity of Vaseline. This process ensures random orientation of the crystals. The patterns produced showing crystalline phases were matched to library standards to determine which crystalline phases were present in the samples.

Second, ground samples were compacted into a well of an aluminium holder using the knife-edge of a spatula to ensure random crystal orientation (Batchelder and Cressey, 1998). A run was then performed using a fixed parallel beam (6° θ) and a moving detector to cover the range 18-35° 2θ. The intensity of the primary peak (26.6 7°2θ for quartz and 21.8 °2θ for cristobalite) was used as a proxy to calculate the relative amounts of crystalline silica. To account for the different diffraction intensities of quartz and cristobalite, the peak heights of pure-phase quartz and cristobalite standards, run under the same conditions, were used to normalise the relative peak heights in the samples. This allowed the addition of peak intensities of quartz and cristobalite to give relative total crystalline silica amongst samples.

3.2.1.3 Infrared spectroscopy - bulk

Infrared spectroscopy (IR) was used to assess the crystal lattice parameters of crystalline silica in synthetic samples to assess the effect of impurities on crystal structure. An IR beam is passed through a sample and measuring the amount and different wavelengths absorbed. This absorption can be converted by Fourier Transform to produce spectra for each sample. For bulk analysis, samples were mixed with KBr (which is transparent to IR) in a ratio of 1:40 or 1:160 and pressed into a pellet at 5 tons using a uniaxial press. The sample was analysed in air by Marco Fabbiani using a Bruker IFS88 instrument with DTGS detector (Università degli Studi di Torino, Italy) at wavenumbers of 400-4000 cm^{-1}, but are presented from 400-1600 cm^{-1} which refers to the bulk sample. A resolution of 4 cm^{-1} and 128 scans were used to increase the signal to noise ratio.

3.2.1.4 Raman spectroscopy

Raman spectroscopy can be used to assess to crystal structure of individual crystals. Raman spectra were taken with a confocal micro-Raman spectrometer by Dr. Danilo Di Genova (HORIBA XploRA Raman Microscope; Mineralogical State Collection, Munich). Samples were excited using the 532 nm laser focused with a 100x long-wide-distance objective with a laser spot diameter of 0.7 µm. The beam was transmitted through an optical fibre to the spectrometer using a 50 µm diameter fibre core as a pinhole for the confocal setup. Raman spectra were collected with a 1024 pixel CCD chip detector. For the measurements, a 100 % optical density filter and a 1200 T grating was used; slit 100, hole 300. Exposure time was set to 5 seconds and data collected in a single acquisition. The 638 nm and near-infrared 785 nm lasers were also tested, however, the 532 nm laser provided the best peak resolution.

3.2.1.5 X-ray fluorescence

X-ray fluorescence (XRF) was used to determine the bulk composition of samples and was performed at the Department of Geology, University of Leicester, UK using a PANalytical Axios Advanced PW4400 X-ray fluorescence spectrometer by Dr Nick Marsh. XRF measures the secondary X-rays emitted by a sample exposed to a radiation beam, due to the excitation of electrons. These X-rays can be used to identify and quantify elements in a sample. Fused beads were used to avoid mineralogical orientation and ensure a representative sample.

3.2.1.6 Laser diffraction

Particle size distribution was measured using laser diffraction (Coulter LS 13320, Durham University) and applying the Fraunhofer theory to the results obtained. A random subsample of each powder was taken by inverting the container and allowing fines to settle, as previously used for volcanic ash particles (Horwell, 2007). The subsample was suspended in water to an obscuration of 8-12% and

ran in duplicate for 90 s in the laser diffractometer. A PIDS system was also applied for the analysis of finer fractions, allowing more accurate measurements of particles <200 nm, allowing the whole 0.04-2000 µm range to be analysed. Laser diffraction is based on the diffraction of light from a particle assuming that all particles are spherical. As some samples contained particles with different morphologies (e.g. fibres), SEM image analysis of particle size and morphology was also performed on samples of interest (see above).

To produce the percentage of particles that fall within certain size bins, a model must be applied to the raw data. Here, both Fraunhofer and Mie theories were considered (Appendix 2), however, Fraunhofer theory was chosen for final presentation. While Fraunhofer and Mie theory have been shown to be comparable for larger particles (>50 µm), the Fraunhofer theory underestimates the percentage of fine material compared to Mie theory. However, the Mie theory requires the input of a real refractive index (RI) and imaginary RI, and an accurate imaginary RI could not be found for DE.

3.2.2 Surface analytical techniques

3.2.2.1 Surface area analysis

The specific surface area of particles can be an important determinant of their toxic potential, as a larger surface area has been shown to cause increased toxic potential (Duffin et al., 2002, Duffin et al., 2007). Measurements of nitrogen adsorption at 77 K using a Micromeritics TriStar3000 instrument (Durham University) were used to determine the surface area of samples. Samples were dried in nitrogen gas at 120 °C for at least 2 h to remove water and other adsorbed species from the surface. The moles of nitrogen adsorbed by samples were measured with the sample in a glass BET tube with isothermal jacket at relative pressures (ratio of absolute pressure to saturated vapour pressure (P/Po)) ranging from 0.05-0.3. The Brunauer-Emmett-Teller (BET) theory was applied to the

collected data to determine the specific surface area of the powders. This theory allows for multi-layering of gas molecules on the surface of particles, but contains some assumptions; that gas molecules will adsorb in infinite layers and that these layers do not interact with each other. This method allows comparisons among samples and whether their surface area is related to their toxicity.

3.2.2.2 Infrared spectroscopy - surface

IR was used to study the surface species on both synthetic and DE samples. Pellets of the materials were pressed at <1 tons, transferred to a gold frame and inserted into a cell with a CaF_2 window. Samples were analysed in air, outgassed, rehydrated, and post-isotopic exchange at room temperature. Outgassing removes water in the air and weakly adsorbed water at the surface to provide information on surface silanols. Exchange with D_2O allows available silanol populations at the surface to be identified. Samples were analysed by Marco Fabbiani in the 400-4000 cm^{-1} wavenumber range using a Bruker IFS28 instrument and MCT detector (Università degli Studi di Torino, Italy). A resolution of 4 cm^{-1} and 128 scans were used to increase the signal to noise ratio.

3.2.2.3 Zeta potential

Zeta potential measurements can give information on the surface charge of a particle. If a particle suspension has a negative charge, cations in the suspension will be attracted to the surface. This produces a slipping plane (a plane between strongly bound ions at the surface which will move with the particle through the suspension and ions that will not move with the particle). The potential between this slipping plane and the dispersant is the zeta potential. This can be measured by applying an electric field across the suspension of particles and particles will move to the oppositely charged electrode to their surface. The velocity at which the particles move is proportional to the

zeta potential and therefore can be used to calculate the zeta potential of particles using the Henry Equation (Equation 3.2),

$$U_E = \frac{2\,\varepsilon\,z\,f(\kappa a)}{3\eta}$$

Equation 3.2

where U_E = electrophoretic mobility (velocity), z = zeta potential, ε = dielectric constant, η = viscosity and f(κa) = Henry's function (which is 1.5 when measuring particles suspended in aqueous solution (the Smoluchowski model)).

As the pH of the dispersant is known to affect the zeta potential, the zeta potential of synthetic samples was measured at pH of 0.5 to 8.5. First, 10 ml water was added to 6 mg sample and sonicated for 2 minutes. The pH was adjusted to 8.5 using NaOH and the zeta potential measured by Cristina Pavan using a Malvern Nanosizer, which uses a combination of laser Doppler velocimetry and phase analysis light scattering (PALS), with 5 repeats of each measurement (Università degli Studi di Torino, Italy). The pH was then decreased by adding HCl and the zeta potential measured every 1 pH. Each sample was run in triplicate.

Zeta potential measurements were also made on particles in complete Roswell Park Memorial Institute (RPMI) medium (see below for detail) at a single pH to determine the zeta potential of particles in conditions used in the *in vitro* toxicology studies. Samples at 62.5 µg/ml in complete medium were sonicated for 20 minutes and the zeta potential measured using a Malvern Nanosizer (Heriot Watt University).

3.2.2.4 Solid electron paramagnetic resonance

Solid electron paramagnetic resonance (EPR) was performed by Chiara Gionco and Cristina Pavan used to assess the presence of silica-based surface radicals (Chapter 2) and paramagnetic metal ions in synthetic samples (applied in Chapter 6). This method applies a magnetic field across the sample, which causes unpaired electrons to align either parallel or anti-parallel to the magnetic field, whereby each alignment has a specific energy. The difference between the energy of each alignment (ΔE) is equal to the energy emitted or absorbed by an unpaired electron moving from the upper to the lower energy field or vice versa (hv), and is related to the g-factor (g_e), Bohr magneton (μ_B), and the strength of the magnetic field (B_o) as shown in Equation 3.3.

$$\Delta E = hv = g_e \mu_B B_o$$

Equation 3.3

When the magnetic field strength is increased until the ΔE is equal to the microwave energy, the unpaired electrons can move between the two spin states. This causes a net absorption of energy which can be measured.

Samples (75 μg) were analysed in vacuum at 77 K using a Bruker EMX spectrometer. To determine bulk paramagnetic centres, a large scan range was used (6000 G), to observe Fe and Al based centres and $Si^{\bullet}$. EPR was performed with settings: receiver gain $1x10^4$, microwave power 10 mW, modulation amplitude 2 G, scan time 80 s, 3 scans.

Smaller scan ranges were used at higher resolution (400 G and 200 G), to focus on the area of the spectra showing Si based radicals and Al and Ti paramagnetic centres. At 200 G, focussed on the central part of the spectrum, the microwave power was progressively decreased from 10 mW to

0.001 mW. At 10 mW $Si^{\bullet}$ centres are partially saturated and increase in intensity upon decreasing the microwave power, so that at lower microwave power the $Si^{\bullet}$ are more visible in the spectra.

3.2.2.5 Electron paramagnetic resonance - spin trap

Free radical release, important in silica toxicity (Chapter 2) can be measured by an EPR spin trap method. Radicals produced by the sample surface are highly reactive and, thus, short-lived. DMPO is used as an organic stabiliser (spin trap) forming DMPO-radical complexes allowing the radicals released to be measured. Hydroxyl ($HO^{\bullet}$) and carboxyl ($COO^{\bullet}$) radicals were both considered for synthetic samples and $HO^{\bullet}$ only for DE. $HO^{\bullet}$ are produced by Fenton chemistry in hydrogen peroxide (Chapter 2) but can also be released by silica surface dangling bonds. $COO^{\bullet}$ are formed by the cleavage of C-H bonds in sodium formate (Chapter 2).

HO radicals

First, 250 µl phosphate buffer solution, 125 µl DMPO and 250 µl H_2O_2 were added to 37.5 mg of sample. The suspension was continually stirred in the dark (using a plastic-coated magnet and stirring plate) and aliquots taken at 10, 30 and 60 minutes for analysis using a Miniscope MS100 (Università degli Studi di Torino). The following settings were used: receiver gain 9 x 10^2; microwave power 10 mW; microwave attenuation 10 dB; modulation amplitude 1 G; scan (sweep) time 80s; BO field 3344.15; sweep length 120. The average of two scans were used in each analysis and each sample run in duplicate. For DE, samples were filtered through a 0.25 µm filter before analysis to remove large particles. Synthetic sample were not filtered.

COO radicals

To 37.5 mg of sample, 125 µl of DMPO and 125 µl of 1.36 g sodium formate in 10 ml 0.5 M phosphate buffer solution were added. The samples were stirred continually in the dark and aliquots taken at 10, 30 and 60 minutes for analysis using a Miniscope MS100 and the same settings above.

3.2.2.6 UV-Vis spectrometry

Iron release from the surface of particles over time was analysed by using the Fe^{2+} specific chelator ferrozine. Ferrozine is an organic compound which forms complexes with ferrous iron producing a magenta-coloured solution, which is stable over a wide pH range (Stookey, 1970). Ascorbic acid can be used to reduce Fe^{3+} to Fe^{2+} which can then be measured using ferrozine. The absorption of light at wavelength 562 nm can then be measured spectrophotometrically to determine the quantity of ferrous iron released from the surface of each sample. Therefore, total available iron and available Fe^{2+} can be measured, and the difference between these gives available Fe^{3+}.

Available Fe was measured by weighing 20 mg powder into 50 ml centrifuge tube and adding either 10 ml ferrozine and 10 ml distilled water or 10 ml ferrozine and 10 ml ascorbic acid, to measure Fe^{2+} and total Fe, respectively. Samples were incubated on an orbital shaker at 37 °C. After 2 h, 1 ml of supernatant was removed and centrifuged at 10000 rpm for 15 minutes. The supernatant was transferred to a cuvette and absorbance read at 562 cm^{-1} by UV-Vis spectroscopy (Uvikon spectrophotometer, Università degli Studi di Torino). Afterwards, the supernatant was replaced into the centrifuge tube, which was then incubated. Measurements were made each day over 9 days to observe the progressive release of Fe over time.

3.3 *In vitro* toxicology

3.3.1 Haemolysis

Analysis of the haemolytic potential of samples gives an indication of their reactivity *in vitro* in a quick and affordable way. Haemolysis relies on particle-cell membrane interactions and indicates the particles' ability to rupture cell membranes via physical or chemical interaction (Pavan et al., 2013). Although red blood cells are not likely to be directly exposed to inhaled particles (and not in the lung), they act as a model cell membrane, as red blood cells do not have a nucleus or other organelles. Haemolysis has previously been shown to be a good indicator or crystalline silica's inflammatory potential (Pavan et al., 2014) and is, therefore, employed here for initial screening of particles for further analysis.

Particle preparation

Particles were suspended in saline at 1 mg/ml, sonicated for 20 minutes and serially diluted to give final concentrations of 1000, 500, 250, 125 and 62 µg/ml. DQ12 and TiO_2 controls were prepared in the same way.

To determine if soluble components of DE were haemolytic, two highly haemolytic DE powders (DE_05, DE_11) were leached in saline for one hour at the top treatment concentration (1000 µg/ml) by shaking gently, the suspension was then centrifuged at 5000 rcf for 15 minutes and filtered through a 0.2 µm Nalgene syringe filter, and the collected leachates were used in the haemolysis assay.

Blood preparation

A volume of 1 ml of sheep blood in Alsever's solutions (Oxoid Ltd.) was centrifuged at 5000 rpm for 2 minutes and the supernatant removed. Isolated red blood cells were washed three times with saline and 100 µl of cells were added to 3.6 ml saline.

Haemolysis assay

Particles suspensions (150 µl) were added to a 96 well plate in triplicate, alongside saline (untreated control), 0.5% Triton-X in saline (positive control), DQ12 (positive standard) and TiO_2 (negative standard). Next, 75 µl of the prepared blood was added to each well, and the plate covered and placed on an orbital shaker for 30 minutes (synthetic samples) or 1 hour (DE). Post-exposure, the plate was centrifuged and the supernatant removed to a new plate. Absorbance was measured at 540 nm (SpectraMax M5, Heriot-Watt University) and per cent haemolysis calculated from Equation 3.4.

$$Haemolysis\ (\%) = \left(\frac{Absorption\ of\ sample - absorption\ of\ untreated\ control}{Absorption\ of\ positive\ control - absorption\ of\ untreated\ control}\right) \times 100$$

Equation 3.4

3.3.2 Cell culture

J774 murine macrophages were chosen as the study cell type. J774 cells originate from a female mouse tumour and are frequently used in cell studies. They are semi-adherent and can be cultured easily. Cells were cultured in RPMI medium containing 10 µl/ml L-glutamine, 10 µl/ml penicillin and streptomycin, and 10% bovine foetal serum (complete medium). Cell cultures were maintained at between 3-9 x 10^5 cells/ml by scraping cells every 2-3 days to prevent cells overgrowing and becoming confluent. Cultured cells were incubated at 37 °C in an atmosphere of 5 % CO_2.

Macrophages were chosen for this study as they are phagocytes and are actively involved in particles clearance from the lung (see Chapter 2). Therefore, macrophages represent an effective model for the potential toxicity of inhaled particles for a mono cell culture. Co-cultures or multi-cell cultures are more complex and, although more representative of the lung environment, this makes it difficult to determine mechanistic causes of pathogenicity.

3.3.3 Cell treatment

For cell treatment, cells were scraped from culture flasks and new complete medium added. Viable cells were counted by adding 100 µl trypan blue to 100 µl cells, and pipetting this onto a haemocytometer. Non-viable cells (those with a damaged membrane) allow the trypan blue dye into the cell and therefore appear blue. These cells were not included in the viable cell count. The cells were then diluted to 5 x 10^5 cells/ml.

To treat the cells, 100 µl cells were added to a 96 well plate and incubated at 37 °C in an atmosphere of 5% CO_2 for 24 h to allow cells to adhere to the base of the wells. After this period, the medium was removed and 100 µl of particle suspensions or controls added to each well and the plate incubated for 24-48 h. Post-exposure, a number of assays were performed on the cells and the supernatant to determine cytotoxicity, and sub-lethal indicators of cell damage or distress.

Particle suspensions were prepared in complete RPMI medium at concentrations of 500 µg/ml and sonicated for 20 minutes. The suspensions were then serially diluted to final concentrations of 500, 250, 125, 63, 31, 16 and 8 µg/ml, and 100 µl added to each well in the 96 well plate in triplicate, alongside controls (complete medium (untreated control) and 0.5% Triton-X in complete medium (positive control)). As with haemolysis, DQ12 was used as a positive particle standard and TiO_2 as a negative particle standard. Cells were exposed to treatments for 24 or 48 h at 37°C in 5% CO_2.

Leachates were also produced by preparing particle suspensions of 63 µg/ml in complete medium (in the absence of cells) and leaching these for 24 h at 37°C in 5% CO_2. The suspensions were centrifuged at 5000 rcf for 10 minutes and the collected leachate used to treat the cells. The potential toxicity of the leachates was assessed using the alamarBlue® assay (below).

3.3.4 Cytotoxicity

Post-exposure to treatments, cytotoxicity assays can be used to measure cell viability or cell damage. This gives an indicator of the potential for particles to cause harm, but does not provide information on the mechanisms of cell death. Cell viability or death can be measured in a number of ways:

3.3.4.1 AlamarBlue assay

The alamarBlue assay is based on the ability of metabolising cells to produce a reducing environment. Viable cells can reduce resazurin to resorufin (Figure 3.2), which fluoresces at 560 nm. As the metabolism of damaged or dead cells is much lower than viable cells, the level of fluorescence can be used to determine cell viability.

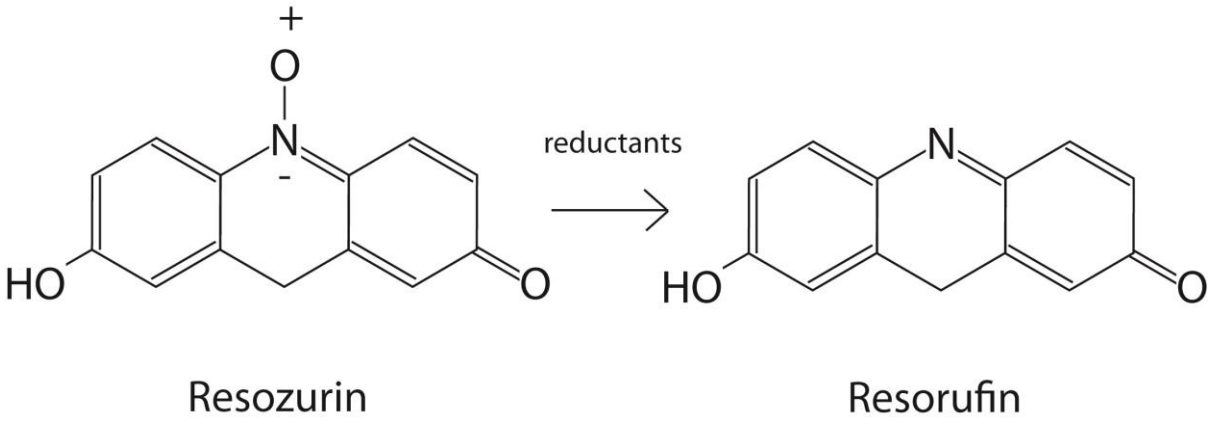

Figure 3.2: The reduction of resozurin (low fluorescence) to resorufin, which is highly fluorescent.

Following exposure, the supernatant was removed from treated cells. A solution of 1 mg/ml alamarBlue® reagent (resazurin sodium salt; Sigma) in saline was diluted 1:10 in complete medium and 100 µl added to the cells. The plate was incubated for 3-4 hours and fluorescence measured at excitation at 560 nm and emission at 590 nm (SpectraMax M5, Heriot-Watt University). Comparison to an untreated control and positive controls allows the per cent viability to be calculated (Equation 3.5).

$$Cell\ viability\ (\%) = \frac{(sample\ reading - \ positive\ control\ reading)}{(untreated\ control\ reading - \ positive\ conrol\ reading)} X\ 100$$

Equation 3.5

3.3.4.2 WST-1 assay

Similar to the alamarBlue assay, the WST-1 assay is based on the metabolism of viable cells. Post-treatment cells are incubated with WST-1, a tetrazolium salt that is cleaved by reactions with viable cells to form soluble formazan dye (red; Figure 3.3). This can be measured spectrophotometrically.

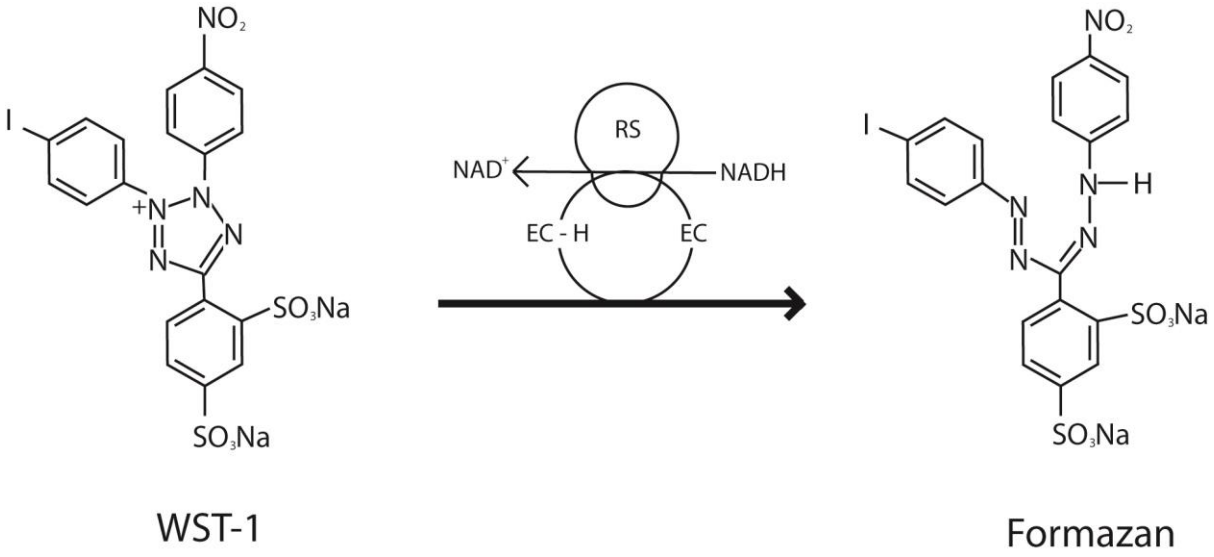

Figure 3.3: The conversion of WST-1 to red formazan by reactions with viable cells (adapted from Roche Diagnostics (2008).

Post-exposure, the supernatant was removed from the cells and 100 µl WST-1, diluted 1:10 in complete medium, was added to each well. Cells were incubated for 3 hours and the absorbance measured at 450 nm. Equation 3.5 was used to calculate per cent cell viability.

3.3.4.3 Lactate dehydrogenase assay

Rather than measuring the cell metabolism, the lactate dehydrogenase (LDH) assay is a measure of cell damage. LDH is released from damaged cells and catalyses the conversion of lactate to pyruvate and vice versa (Figure 3.4). During this reaction a concurrent conversion of NAD^+ to NADH occurs (Figure 3.4). This can be measured spectroscopically using colorimetric indicators.

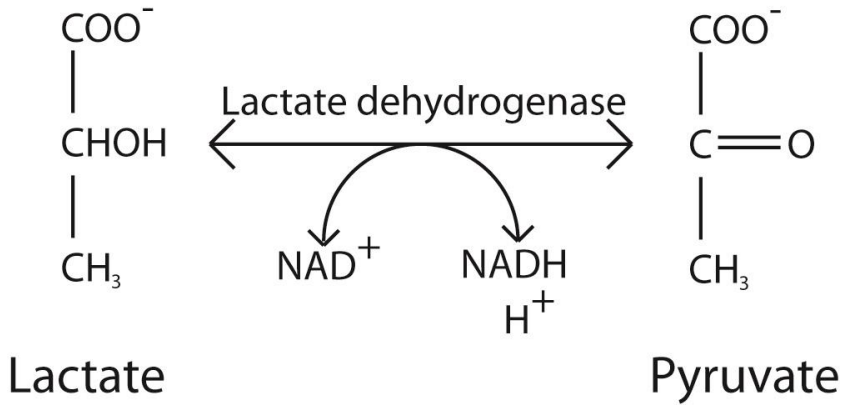

Figure 3.4: The conversion of lactate to pyruvate mediated by LDH used to measure cell membrane damage.

LDH release from macrophages was measured by adding 10 µl of cell supernatant to 50 µl 1 mg/ml Nicotinamide adenine dinucleotide (NADH) in 0.75 mM sodium pyruvate, incubating for 30 minutes at 37 °C in 5% CO_2, and adding 50 µl of 2 mg/ml 2,4-dinitrophenylhydrazine in 1M HCl. This was incubated for 20 minutes at room temperature in the dark, before adding 50 µl 4M sodium hydroxide and measuring the absorbance at 550 nm (MRX Revelation Microplate Reader, Dynex Magellan Biosciences). Comparisons with an untreated and a positive control allow the cytotoxicity to be calculated using Equation 3.6.

$$Cytotoxicity\ (\%) = \frac{(absorbance\ of\ sample - absorption\ of\ positive\ control)}{(absorbance\ of\ untreated\ control - absorption\ of\ positive\ conrol)} X\ 100$$

Equation 3.6

3.3.5 Sub-lethal assays

3.3.5.1 Cytokine release

Cytokines are soluble proteins released by activated macrophages. Exposure to toxins, including silica, leads to the release of pro-inflammatory cytokines, such as interleukin 1β (IL-1β) and tumour necrosis factor alpha (TNF-α) from macrophages, which are associated with silica toxicity (Chapter 2) and are measured in this study. Numerous other cytokines and other mediators are also released by macrophages, which interact causing complex feedback mechanisms. Here, IL-10, an anti-inflammatory cytokine, was considered to provide information on the balance between pro- and anti-inflammatory signalling. Keratinocyte chemoattractant (KC) was also measured, as this is induces macrophage and neutrophil chemotaxis.

Cytokine production was measured using BD™ Cytometric Bead Array cytokine flex sets (bead based immunoassay; BD Biosciences, Heriot-Watt University). The supernatants were removed from cells treated with 125 µg/ml or lower concentrations of samples and stored at -80 °C until needed. Once defrosted, the supernatant was centrifuged at 2500 rpm for 10 minutes and 25 µl of each sample treatment added to a round bottomed 96 well plate in triplicate. Standards were produced by adding 4 ml of assay diluent to the standard beads for each cytokine to be analysed. A serial dilution was performed to give final standard concentrations of 0, 10, 20, 40, 80, 156, 312.5, 625, 1250 and 2500 pg/ml, and 25 µl of each was added to the first ten wells of the plate. Capture beads for each cytokine analysed were vortexed and 50 µl of each capture bead added to capture diluent to give a

total of 2500 µl solution. Then, 25 µl of this solution was added to each well and the plate incubated for 1 h at room temperature. Detection beads were prepared in the same way, diluted in detection bead buffer, 25 µl added to each well, and the plate incubated at room temperature for 1 h in the dark. After incubation, 125 µl of wash buffer was added to each well and the plate centrifuged at 250 rcf for 5 minutes. The supernatant was then removed by quickly inverting the plate and 200 µl wash buffer added to each well. The plate was shaken for 1 minute and read by flow cytometry on BD FacsArray by Dr. Ali Kermanizadeh and Dr. David Brown (Heriot Watt University). Flow cytometry was used to discriminate between different bead populations based on size and fluorescence, according to the manufacturer's instructions.

3.3.5.1 NF-κB activation

NF-κB is a protein which is a primary transcription factor involved in regulation of the immune response. Incorrect regulation can lead to inflammation and cancer. NF-κB can be activated by a number of different stimuli, including reactive oxygen species and cytokines. In unstimulated cells NF-κB resides in the cytoplasm but, once activated, NF-κB translocates to the nucleus of the cell, where it can activate particular genes. Analysis of the movement of NF-κB from the cytoplasm into the nucleus can be measured by the NF-κB assay.

NF-κB activation was measured in treated J774 macrophages. Sterilised coverslips were placed in each well of a 24 well plate, and 5 X 10^5 cells in complete medium were added to each well and the plate incubated for 24 h. Cells were treated with 250 µl particle suspensions in complete medium at concentrations of 125 µg/ml and incubated at 37 °C in 5% CO_2 for 4 h. Cells were then fixed by treatment with 250 µl 3% formaldehyde in PBS for 30 minutes at 5 °C, and the cell membrane permeabilised by treating with 250 µl of 0.2% Triton-X in PBS for 15 minutes at room temperature. Permeabilisation allows the following treatments to enter into the cell. Then, cells were treated with

250 µl of 1 mg/ml BSA in PBS for 1 h to avoid preferential binding by other components in the solution. Cells were treated with 250 µl NF-κB antibody solution (Mouse anti-NFκB (p65) (Life Technologies) diluted 1/200 in PBS with 0.5% BSA) for 1 h, which binds to NF-κB specifically and then 250 µl Alexafluor 488 solution (Goat anti-mouse lgG (Life Technologies) diluted 1/200 in PBS with 0.5% BSA) for 1 h in the dark, which is a fluorescent marker that binds to the NF-κB antibody to allowing NF-κB to be imaged. Cells were treated with 250 µl DAPI (4',6-diamidino-2-phenylindole) solution (0.5 µg/ml DAPI in PBS with 0.5% BSA) for 20 seconds, which stains the cell nuclei by binding with DNA, and the coverslips were mounted on glass microscope slides using Mowoil. Cells were washed with PBS three times between each step.

The treated cells were imaged using fluorescence microscopy (Zeiss Axioscope) at excitation wavelength 488 nm and emission wavelength 519 nm for the NF-κB stain (NF-κB image). Images of the same area were taken by exciting the DAPI stain with UV light and an emission filter (blue) at 416 nm to image the stained nuclei (DAPI image). Images were analysed using the method employed by Noursadeghi et al. (2008) using ImageJ image analysis software. Briefly, a copy of the NF-κB image was made and this and the DAPI image were transformed to binary to give areas of the whole cell and of the nuclei respectively. The binary DAPI image was subtracted from the binary NF-κB image to give the area of the cell cytoplasm. Then, the cell cytoplasm image was merged with the original NF-κB image and a histogram of the intensity produced. Then, the original NF-κB image was merged with the binary DAPI image and a histogram produced. Due to difference in intensity between different images the ratio of the intensity in the nuclei and cytoplasm was calculated. This allowed the analysis of whether NF-κB had been activated and moved into the cell nucleus.

3.3.6 Cell imaging

For DE, cells treated with the five fine fractions were imaged by light microscopy. J774 cells (2.5 x 10^5) were treated with 600 µl of 63 µg/ml DE in a 24 well plate. Cells were scraped from the plate and 50 µl of the cell suspension diluted in 300 µl saline and centrifuged onto a microscope slide at 1160 rcf for 5 minutes. The treated cells were dried and stained with Diff-Quik (Fisher Scientific). Slides were dipped in methanol, then Eosin G in phosphate buffer and Thiazine dye in phosphate buffer, rinsed with H_2O and air dried. For synthetic samples, light microscopy was used to take images of treated cells in a 96 well plate, without dying to observe particle uptake.

3.4 Statistical analysis

Student's t-test and ANOVA general linear model with a Tukey's post-hoc test were performed to determine the significance of differences among two data points and multiple data respectively (Minitab 15). Pearson's correlation test was used to determine significant correlations amongst different physicochemical characteristics and toxicological results (* $p < 0.05$, ** $p < 0.01$, *** $p < 0.001$).

References

BATCHELDER, M. & CRESSEY, G. 1998. Rapid, accurate phase quantification of clay-bearing samples using a position-sensitive X-ray detector. *Clays and Clay Minerals,* 46**,** 183-194.

DUFFIN, R., TRAN, C. L., CLOUTER, A., BROWN, D. M., MACNEE, W., STONE, V. & DONALDSON, K. 2002. The Importance of Surface Area and Specific Reactivity in the Acute Pulmonary Inflammatory Response to Particles. *Annals of Occupational Hygiene,* 46**,** 242-245.

DUFFIN, R., TRAN, L., BROWN, D., STONE, V. & DONALDSON, K. 2007. Proinflammogenic effects of low-toxicity and metal nanoparticles in vivo and in vitro: highlighting the role of particle surface area and surface reactivity. *Inhal Toxicol,* 19**,** 849-56.

HORWELL, C. J. 2007. Grain-size analysis of volcanic ash for the rapid assessment of respiratory health hazard. *Journal of Environmental Monitoring,* 9**,** 1107-1115.

JONES, T. & BÉRUBÉ, K. 2011. The bioreactivity of the sub-10µm component of volcanic ash: Soufrière Hills volcano, Montserrat. *Journal of Hazardous Materials,* 194**,** 128-134.

MORENO, T., HIGUERAS, P., JONES, T., MCDONALD, I. & GIBBONS, W. 2005. Size fractionation in mercury-bearing airborne particles (HgPM10) at Almadén Spain: Implications for inhalation hazards around old mines. . *Atmospheric Environment,* 39**,** 6409–6419.

NOURSADEGHI, M., TSANG, J., HAUSTEIN, T., MILLER, R. F., CHAIN, B. M. & KATZ, D. R. 2008. Quantitative imaging assay for NF-κB nuclear translocation in primary human macrophages. *Journal of Immunological Methods,* 329**,** 194-200.

PAVAN, C., RABOLLI, V., TOMATIS, M., FUBINI, B. & LISON, D. 2014. Why does the hemolytic activity of silica predict its pro-inflammatory activity? *Particle and Fibre Toxicology,* 11**,** 76.

PAVAN, C., TOMATIS, M., GHIAZZA, M., RABOLLI, V., BOLIS, V., LISON, D. & FUBINI, B. 2013. In Search of the Chemical Basis of the Hemolytic Potential of Silicas. *Chemical Research in Toxicology,* 26**,** 1188-1198.

QUALITY OF URBAN AIR REVIEW GROUP 1996. Airborne particulate matter in the United Kingdom. *In:* DEPARTMENT OF THE ENVIRONMENT (ed.). London, UK.

ROCHE DIAGNOSTICS 2008. Apoptosis, Cytotoxicity and Cell Proliferation 4th ed. https://lifescience.roche.com/wcsstore/RASCatalogAssetStore/Articles/05242134001_05.08.pdf.

STOOKEY, L. L. 1970. Ferrozine---a new spectrophotometric reagent for iron. *Analytical Chemistry,* 42**,** 779-781.

Chapter 4

Global variability of the physicochemical characteristics of diatomaceous earth

4.1 Introduction

Diatomaceous earth (DE) is mined globally and may undergo processing by calcination (without flux) or flux-calcination (with a sodium carbonate or sodium chloride fluxing agent) at ~1000 °C (processed samples). During this process, amorphous silica, which comprises most of the diatom deposits (unprocessed DE), is converted to crystalline silica, predominantly in the form of cristobalite (see Chapter 2 for full details). As inhalation of crystalline silica can cause disease or cancer, processed DE has the potential to cause chronic respiratory disease (Chapter 2). However, the variability of crystalline silica toxicity is well known, and can be affected by impurities within the sample, as has previously hypothesised for cristobalite in volcanic ash or quartz in coalmine or workplace dust (Chapter 2) (Donaldson and Borm, 1998, Horwell et al., 2012, Clouter et al., 2001). Yet, how the properties of DE vary with deposit source and processing technique has not been examined in detail and toxicological and epidemiological studies focus on few samples from few locations. Therefore, as the properties of DE may alter its toxicity, the variability of the DE hazard is also not known and this is examined in this chapter.

The form and purity of crystalline silica, and how this is altered during different processing techniques and the effect of the source of the deposit is poorly constrained. Calcination produces DE

containing 1-49% crystalline silica and flux-calcined samples contain between 20 and 85% crystalline silica (Table 2.5, Chapter 2), implying the addition of a flux promotes crystallisation. Elias et al. (2006) showed calcination temperature is important, as increasing the temperature from 900 to 1200 °C increased crystalline silica content from 1-49%. There was also a large difference in the crystalline silica content of two industrially heated samples (57 and 79% crystalline silica) from USA and France respectively (Elias et al., 2000). However, usually the effect of deposit source is not addressed. Cristobalite is the predominant polymorph formed in both calcined and flux-calcined samples, with up to 2% quartz observed in some studies (Bye et al., 1984, Elias et al., 2000, Hart and Hesterberg, 1998), although quartz is not always quantified (Ghiazza et al., 2009).

The chemical composition of DE varies with source and processing, containing between 65-98 wt.% SiO_2 (Table 2.4, Chapter 2). Calcination or flux-calcination generally increases the purity of the DE (all >88 wt.% SiO_2). Amongst studies it can be seen that the quantity and type of impurities vary by source, however, only one study compares the properties of DE from different locations (although this is not the key aim of the study) (Elias et al., 2000). As chemical data presented are usually bulk, there is no information on the form these impurities take, whether they are incorporated into amorphous material or other minerals or, in processed samples, taken into the cristobalite structure. There is some evidence that Fe is important in determining the transforming potency (an indicator of genotoxicity) of DE (Elias et al., 2006). This mechanism is reliant on available Fe at the surface of DE particles in particular coordinative and oxidative states to produce free radicals by Fenton chemistry (Chapter 2). Ghiazza et al. (2009) showed Fe^{3+} in tetrahedra or higher coordination at the surface of flux-calcined and calcined DE and iron oxides at the surface of calcined samples. However, there is no information on how the available surface Fe may vary with source.

Here, a sample-set of DE sourced from seven locations, including unprocessed, calcined and flux-calcined samples is used to address the effect of DE source and processing on its physicochemical

properties. These samples are analysed for the form of crystalline silica, the amount, type and location of impurities, particle size, surface area and particle morphology, which are all known to affect silica-dust toxicity (Chapter 2). The variability of these properties is discussed in relation to the *in vitro* reactivity of DE in Chapter 5, to attempt to understand the variability of the DE hazard globally.

4.2 Methods

Nineteen DE samples were sourced from mines around the world to account for the global variability of DE deposits (Table 4.1). A range of DE products that encompasses the spectrum of compositional characteristics and processing techniques available was selected using geochemical data obtained though the European Industrial Minerals Association (IMA - Europe). The sample set comprised unprocessed, calcined and flux-calcined samples, and included filler and filter aid grades of DE, which are determined by post-calcination size classification. Samples were chosen from a range of source deposits, including those with high Al, Fe or Ca bulk impurities, as possible indicators of clay or carbonate contaminants. Unprocessed samples and the equivalent sample post-processing were sourced where possible in order to directly establish the effects of processing.

Table 4.1: Sample information for DE chosen for analysis, including sample source, process and grade. U= unprocessed, C = calcined, FC = flux-calcined. [#]The fine fractions of these samples were separated for use in toxicology assays. *Samples were sourced from two separate deposits in the USA and so are denoted as USA-1 and USA-2.[1-4] Unprocessed samples and their corresponding processed samples.

Sample information			
Sample ID	**Source**	**Process**	**Grade**
DE_05[#1]	Spain	U	Filler
DE_11[2]	Spain	U	Filler
DE_13[3]	France	U	Filter aid
DE_15[4]	France	U	Filter aid
DE_16[4]	France	C	Filter aid
DE_18	China	C	Filter aid
DE_20[#]	Mexico	C	Filter aid
DE_21	USA-1*	C	Filter aid
DE_22	USA-1	C	Filler
DE_23	USA-1	C	Filter aid
DE_24[#]	Mexico	C	Filter aid
DE_06[1]	Spain	FC	Filler
DE_07	USA-1	FC	Filler
DE_08[#]	USA-2*	FC	Filler
DE_09	Chile	FC	Filler
DE_10[#]	Mexico	FC	Filler
DE_12[2]	Spain	FC	Filler
DE_14[3]	France	FC	Filter aid
DE_17	China	FC	Filter aid

4.2.1 Mineralogy and chemical analyses

All methods used for the physicochemical analysis of DE here are described in detail in Chapter 3. The crystalline silica polymorph and relative crystalline silica contents were measured by X-ray diffraction position sensitive detection (XRD-PSD; Bruker D8 Advance, Durham University) from 5-90° 2θ. The intensity of the primary peak (26.6 °2θ for quartz and 21.8 °2θ for cristobalite) was used as a proxy for the relative amounts of crystalline silica. To account for the different diffraction intensities of quartz and cristobalite, the peak heights of pure-phase quartz and cristobalite standards, run under the same conditions, were used to normalise the relative peak heights in the samples. This allowed the addition of peak intensities of quartz and cristobalite to give relative total crystalline silica contents amongst the samples.

Bulk chemical compositions were measured by X-ray fluorescence (XRF; PANalytical Axi0s Advanced X-ray fluorescence spectrometer, University of Leicester). Particle sections were produced in polished resin blocks, coated with 25 nm carbon, and imaging and elemental analysis were performed by scanning electron microscopy (SEM) and energy dispersive X-ray spectroscopy (EDS) at 15 kV (Hitachi SU-70 FEG SEM, Durham University)**.** The elemental composition of cristobalite in individual particles, and amorphous material in cristobalite-containing particles was measured in samples where these particles were clearly seen. Fe release and speciation was analysed on selected samples to assess the available Fe at the surface of the sample. DE was incubated in ferrozine or ferrozine and ascorbic acid, to measure Fe^{2+} and total Fe, respectively, by reading absorbance at 562 cm^{-1} by UV-Vis spectroscopy (Uvikon spectrophotometer, Università degli Studi di Torino) over 8 days.,

Surface silanol populations were measured by Fourier transform infra-red spectroscopy (FTIR). FTIR with DTGS detector was used to examine the DE surface silanols (Vector 22, Università degli Studi di

Torino). The absorbance of IR by pelleted samples in a cell with CaF_2 windows was recorded at wavenumbers 400-4000 cm^{-1}. The sample was analysed outgassed, rehydrated, post-isotopic exchange (D_2O), and finally exchanged with H_2O.

4.2.2 Physical properties

Particle size distributions were analysed by laser diffraction using a Coulter LS analyser (Durham University), with polarization intensity differentiation scattering (PIDS) to analyse particles in the range of 0.04-2000 µm diameter (all samples fell within this range). Data are presented as cumulative volume % and are an average of two 90 second measurements, analysed by Fraunhofer theory.

Qualitative analysis of dominant diatom morphology was performed on all samples by mounting particles on polycarbonate discs, which were adhered to aluminium stubs by carbon pads. These were coated with 25 nm gold/palladium and imaged at 8 kV by SEM (Durham University).

Surface area was analysed by nitrogen adsorption measurements at 77 K using a TriStar 3000 instrument (Durham University). Samples were dried in nitrogen gas at 120 °C overnight. The Brunauer-Emmett-Teller (BET) theory was applied to measurements at relative pressures of 0.05-0.24, and the results are the mean of three repeated measurements.

4.2.3 Statistical analysis

Student's t-test was performed to determine the significance of differences among the physicochemical characteristics of DE samples.

4.3 Results

4.3.1 Bulk chemical composition

The bulk chemical composition was variable across deposit sources and processing technique (Table 4.2). All samples were predominantly SiO_2, which ranged from 87-94 wt.%. Samples contained up to 7 wt.% and 4 wt.% Al_2O_3 and Fe_2O_3, respectively. Fe_2O_3 content was highest in French samples and Al_2O_3 contents were lower in Spanish samples compared to other locations. Samples from Spain had CaO contents up to 9 wt.%, substantially higher than from all other locations. CaO was also slightly elevated in the Chilean flux-calcined sample compared to other samples. On average, flux-calcined samples contained significantly more Na_2O than unprocessed and calcined samples from all locations ($p < 0.001$), and contained less Al_2O_3 than calcined samples. Other elements comprised <1 wt.% in all samples.

Table 4.2: Information for diatomaceous earth samples, including: particle size distribution, surface area and chemical composition. Table sorted by process: U=unprocessed; C=calcined; FC=flux-calcined. s.d. = standard deviation (n=3). #The fine fractions of these samples were separated for use in toxicology assays. *Samples were sourced from two separate deposits in the USA and so are denoted as USA-1 and USA-2.[1-4] Unprocessed samples and their corresponding processed samples.

Sample information				Particle size distribution (c.v. %)		BET surface area (m^2/g)		Chemical composition (wt.%)							
Sample ID	**Source**	**Process**	**Grade**	**<4 µm**	**<10 µm**	**Mean**	**s.d.**	**SiO_2**	**TiO_2**	**Al_2O_3**	**Fe_2O_3**	**MgO**	**CaO**	**Na_2O**	**K_2O**
DE_05[#1]	Spain	U	Filler	11.3	38.8	7.5	0.7	90.47	0.05	0.91	0.38	0.34	6.96	0.65	0.14
DE_11[2]	Spain	U	Filler	12.4	47.3	6.3	0.4	87.26	0.05	1.40	0.42	0.49	8.96	1.04	0.17
DE_13[3]	France	U	Filter aid	7.8	28.0	22.9	0.2	89.02	0.64	4.42	3.22	0.36	0.66	0.38	0.35
DE_15[4]	France	U	Filter aid	7.9	28.5	23.8	0.3	87.40	0.70	4.73	3.99	0.49	0.74	0.19	0.34
DE_16[4]	France	C	Filter aid	6.7	25.0	3.8	0.1	88.03	0.66	4.50	3.86	0.39	0.66	0.17	0.33
DE_18	China	C	Filter aid	7.3	28.1	3.1	0.1	93.49	0.15	3.71	1.67	0.35	0.08	-0.04	0.50
DE_20[#]	Mexico	C	Filter aid	6.8	25.3	4.0	0.1	92.00	0.24	5.07	1.95	0.34	0.30	-0.13	0.20
DE_21	USA-1*	C	Filter aid	6.2	21.7	5.7	0.2	87.83	0.32	6.57	1.81	1.02	0.54	0.51	1.02
DE_22	USA-1	C	Filler	25.4	71.5	10.6	0.2	93.24	0.17	3.82	1.15	0.65	0.17	0.03	0.59
DE_23	USA-1	C	Filter aid	21.8	65.5	6.8	0.2	93.88	0.15	3.03	1.05	0.69	0.30	0.21	0.47
DE_24[#]	Mexico	C	Filter aid	12.1	45.0	5.9	0.2	93.63	0.19	3.89	1.49	0.33	0.22	0.01	0.18
DE_06[1]	Spain	FC	Filler	8.5	34.4	1.1	0.1	91.27	0.03	0.67	0.35	0.27	6.25	1.00	0.09
DE_07	USA-1	FC	Filler	10.6	31.6	1.3	0.0	91.67	0.15	3.00	1.07	0.53	0.29	2.69	0.48
DE_08[#]	USA-2*	FC	Filler	9.2	28.7	1.3	0.1	93.07	0.06	1.12	1.99	0.51	0.30	2.89	0.03
DE_09	Chile	FC	Filler	9.8	33.4	1.5	0.1	93.04	0.10	1.82	0.95	0.23	1.29	2.15	0.34
DE_10[#]	Mexico	FC	Filler	8.7	35.3	1.7	0.1	93.64	0.10	2.05	0.80	0.14	0.32	2.59	0.12
DE_12[2]	Spain	FC	Filler	8.5	33.4	1.0	0.1	90.67	0.03	1.12	0.35	0.31	6.64	0.69	0.10
DE_14[3]	France	FC	Filter aid	6.4	17.0	1.1	0.1	87.36	0.58	4.10	2.61	0.40	0.62	3.17	0.39
DE_17	China	FC	Filter aid	4.6	11.4	1.0	0.0	91.68	0.13	3.12	1.44	0.27	0.11	2.22	0.51

4.3.2 Crystalline silica

Crystalline silica was the dominant mineral phase in flux-calcined and calcined samples (Figure 4.1). Flux-calcined samples were predominantly cristobalite; though, samples from China and USA also contained small quantities of quartz (Figure 4.1c). Conversely, calcined samples contained cristobalite as well as quartz, with the exception of cristobalite-only Mexican samples DE_20 and DE_24 (Figure 4.1b). Quartz was the dominant crystalline silica polymorph in calcined samples DE_16 and DE_21, whereas cristobalite was the dominant phase in the other calcined samples. Mean cristobalite peak intensity was three times higher in flux-calcined samples than in calcined samples, as calcined samples retained more amorphous material and a proportion of the crystalline silica was quartz. These differences in abundance were substantiated by qualitative SEM imaging (cristobalite presented as patches as discussed below). Unprocessed samples were predominantly amorphous and only contained small amounts of cristobalite (Figure 4.1a) or, rarely, quartz was observed in all four unprocessed samples.

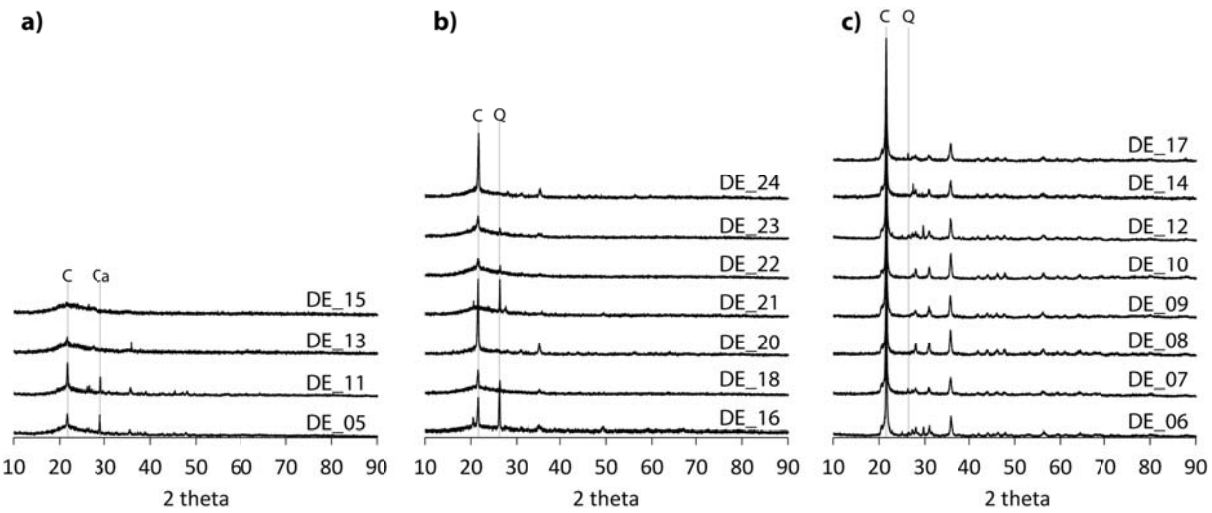

Figure 4.1: XRD patterns of **a)** unprocessed, **b)** calcined and **c)** flux-calcined DE. C = cristobalite, Q = quartz, Ca = calcite. Only primary peaks are labelled for clarity. Quartz was not detected in unprocessed samples by XRD.

By backscatter SEM, crystalline silica appeared as dark grey patches within lighter grey matrices of amorphous material (Figure 4.2). In samples that contained both quartz and cristobalite, cristobalite could often be identified by characteristic 'fish-scale' cracking, indicative of the particle having undergone the transition from the high-temperature beta form to the low-temperature alpha form (Carpenter et al., 1998). By EDS analysis on cristobalite-only samples and 'fish-scale' patches in samples containing both polymorphs, Na, Al, Fe and Ca were detected in the cristobalite (Figure 4.2). The amorphous matrix was enriched in impurities compared to the cristobalite, containing Na, Al, Fe, Ca, Mg, K, Ti and P and Mn (Figure 4.2).

Crystalline silica particles, with a different morphology to the patches described above, were also observed, both as pure SiO_2 particles, or pure SiO_2 with other phases or amorphous material surrounding it (Figure 4.3). However, these particles were rare.

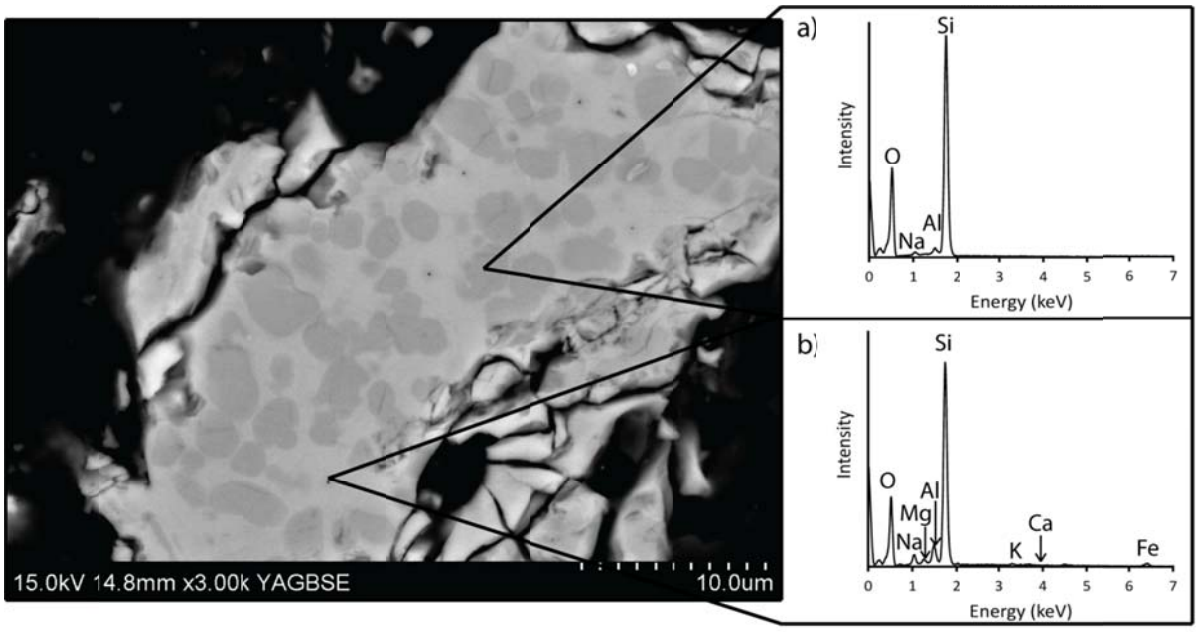

Figure 4.2: Backscatter image and EDS spectra of flux-calcined DE particle. Backscatter image of DE particle in a flux-calcined sample with cristobalite patches (dark grey; identified by cracking and cristobalite is the only crystalline phase in this sample by XRD) surrounded by an amorphous matrix (light grey). EDS spectra of **a)** cristobalite patches showing Al and Na impurities and **b)** amorphous matrix containing Na, Mg, Al, Ca, K and Fe impurities. These are representative spectra from ~800 spot analyses of cristobalite patches and amorphous matrices (400 of each). Some cristobalite patches also contained Ca and Fe, and some amorphous material also contained Ti and P.

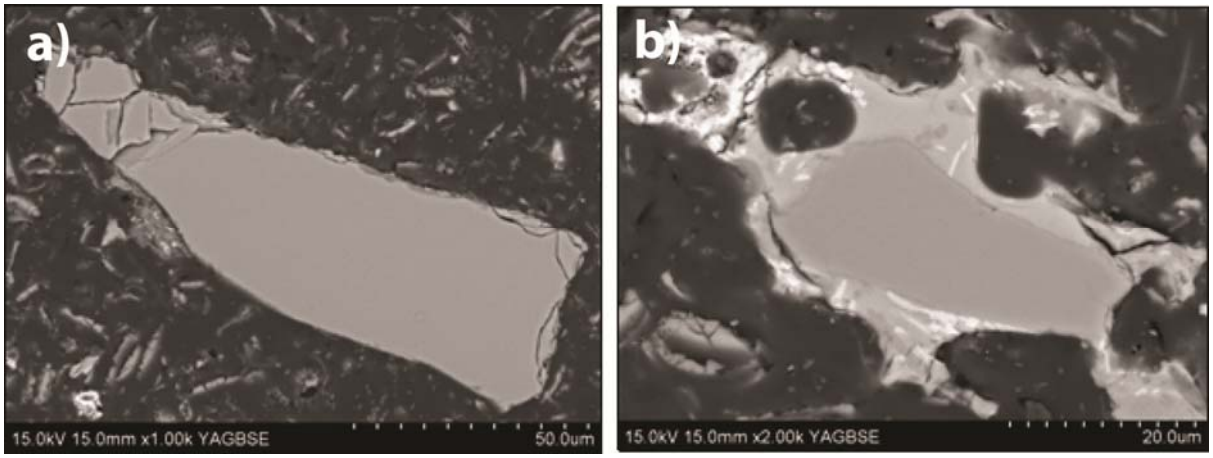

Figure 4.3: Backscatter images of rarely observed pure crystalline silica as **a)** an individual particle, and **b)** surrounded by other phases.

Quantities of 0.2 to 12.8 oxide wt.% of Al, Na, Fe and Ca were detected in the cristobalite patches of the samples analysed. The same elements comprised 4.8 to 38.8 oxide wt.% in the amorphous matrices. Analysis of diatom skeletons, which did not appear to have undergone any transformation and retained their original morphology, showed them to contain <5 oxide wt.% impurities (Figure 4.4). Na, Al, Ca and Fe accounted for the majority of impurities in all areas analysed, however, in some instances other impurities, such as Ti, K, P, Mg, accounted for up to 20 oxide wt.%. The EDS data are semi-quantitative, and many of the cristobalite areas analysed were small (~3 µm diameter), so these data give an indication of the level of impurities and their distribution throughout these particles.

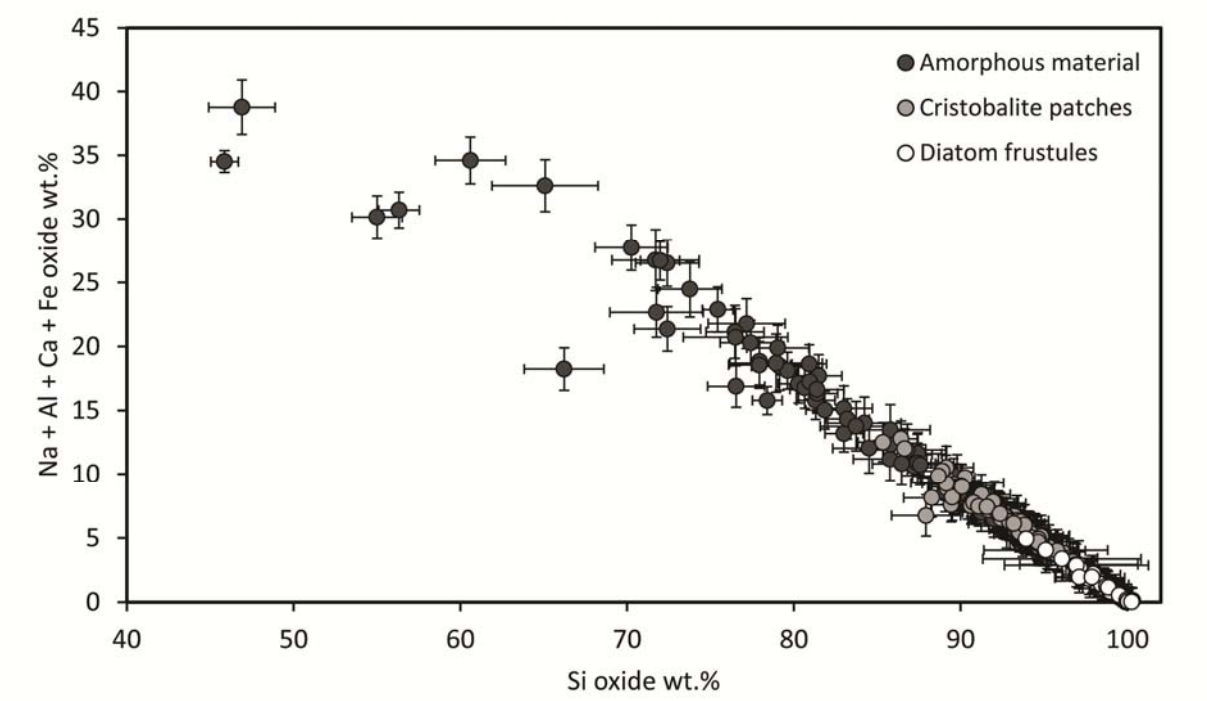

Figure 4.4: The concentration of Na, Al, Ca and Fe impurities in unaltered diatom frustules (those which retained their original morphology), cristobalite patches, and in the amorphous matrices in cristobalite-bearing particles. Error bars represent 1 standard deviation.

The impurities present in cristobalite patches in samples sourced from different locations are shown in Figure 4.5. Only samples where cristobalite patches were clearly visible were analysed so all DE sources could not be assessed. Out of the samples analysed, Mexican samples contained some of the most impure cristobalite (Figure 4.5a), which was mainly due to an excess of Al compared to other samples ($p < 0.01$) (Figure 4.5b). Cristobalite in Spanish samples was enriched in Ca compared to other locations ($p < 0.01$) (Figure 4.5e), whereas cristobalite in French samples was enriched in Fe ($p < 0.01$) (Figure 4.5b).

The same enrichment of elements was observed in the amorphous matrix of cristobalite-bearing particles: Mexican sample were enriched in Al compared to samples from other locations ($p < 0.01$) (Figure 4.6b), French samples were enriched in Fe (Figure 4.6c), and Spanish samples were enriched

in Ca ($p < 0.01$) (Figure 4.6e). However, in the amorphous matrix Spanish samples were also enriched in Na compared to other locations ($p < 0.01$) (Figure 4.6d).

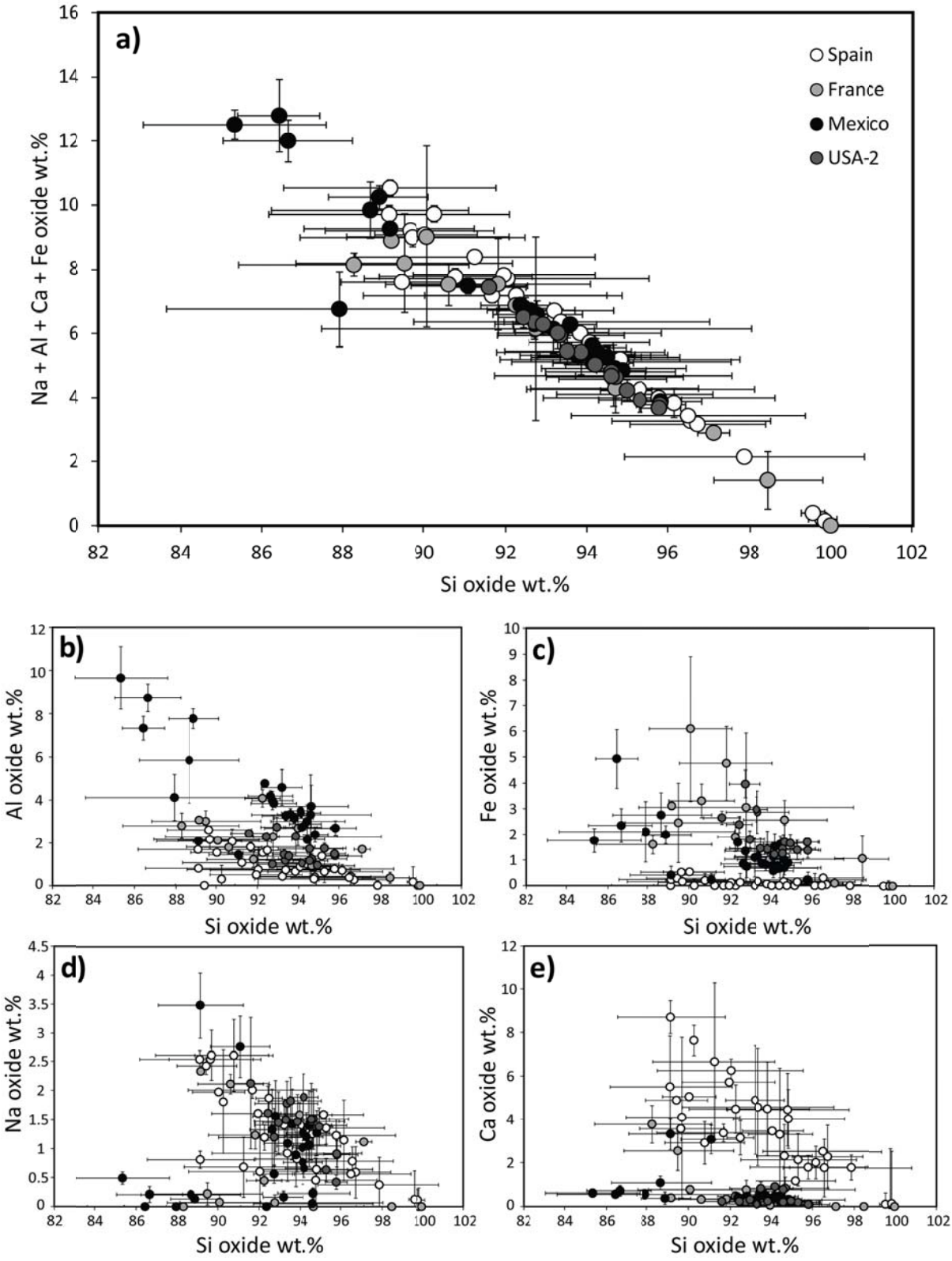

Figure 4.5: concentrations of **a)** Na, Al, Ca and Fe impurities in cristobalite patches by DE source, and the concentration of **b)** Al, **c)** Fe, **d)** Na, and **e)** Ca in cristobalite patches by DE source. Error bars represent 1 standard deviation.

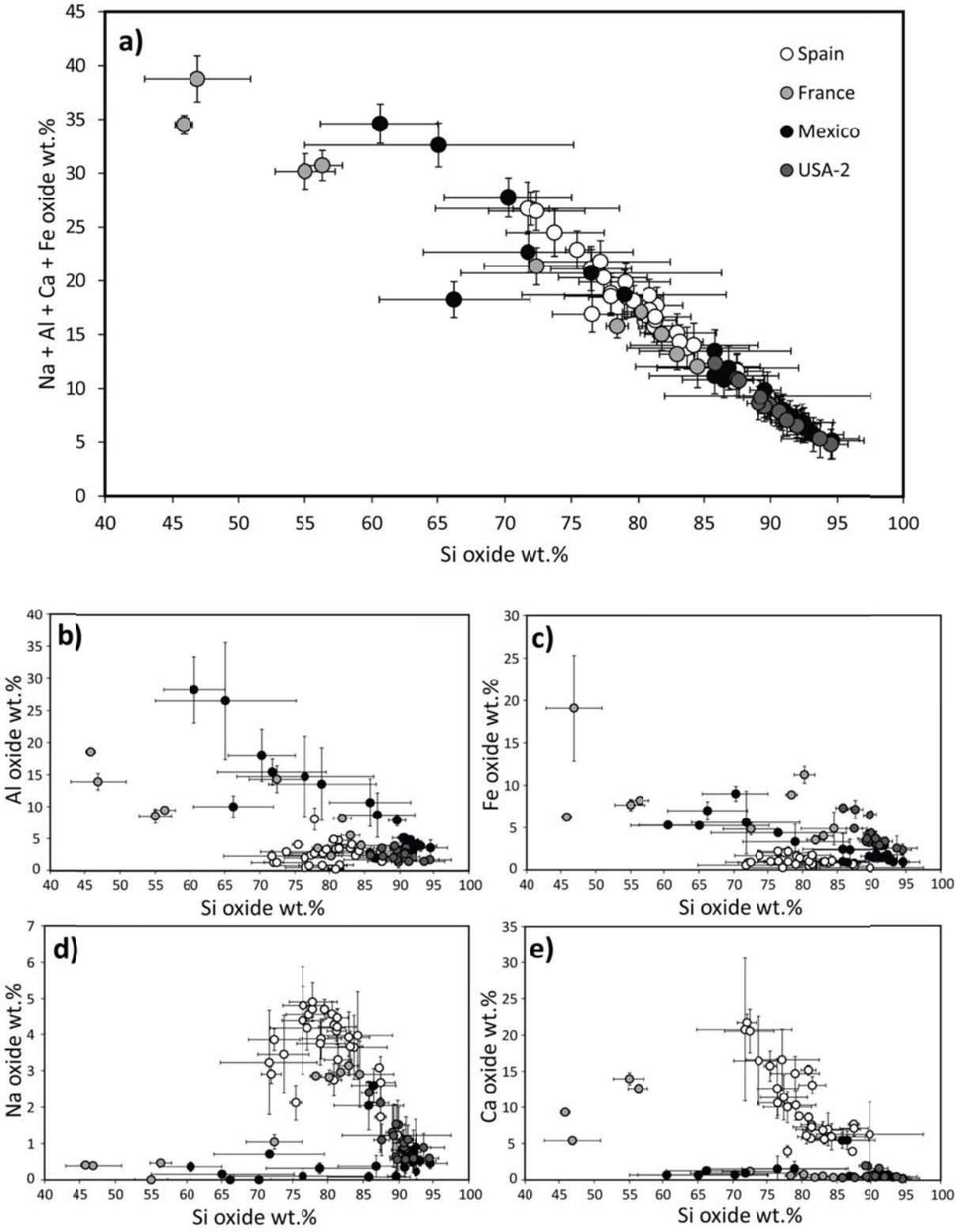

Figure 4.6: concentrations of **a)** Na, Al, Ca and Fe impurities in the amorphous matrices of cristobalite-bearing particles by DE source, and the concentration of **b)** Al, **c)** Fe, **d)** Na, and **e)** Ca in amorphous matrices by DE source. Error bars represent 1 standard deviation.

4.3.3 Contaminant phases

Spanish samples contained calcite (Figure 4.1 and 4.7a); this was most prominent in the unprocessed samples (DE_05, DE_11), with only traces remaining in the corresponding flux-calcined samples (DE_06, DE_12). Calcium silicates were observed in abundance in all Spanish samples (Figure 4.7b). Clays were observed by SEM-EDS (texturally, and by their high Al contents) and were most prevalent in French samples (e.g. Figure 4.7c), but were also observed in samples from USA-1, Mexico and China. Distinct clay phases were not identifiable using textural features or chemical composition, and quantities were too low for detection by XRD.

In the French, unprocessed samples, iron-rich particles of up to 70 µm were observed and these were iron and titanium-rich or iron and phosphorus-rich particles (Figure 4.7d). These larger particles were not observed in the equivalent calcined and flux-calcined samples; instead, small iron-rich patches were seen throughout particles and sometimes in cracks and pore spaces (Figure 4.7e). Some of these deposits were iron and titanium-rich but were mostly iron and silicon. In calcined samples where the corresponding unprocessed samples were not available, iron-rich patches were also seen throughout the particles (Figure 4.7f).

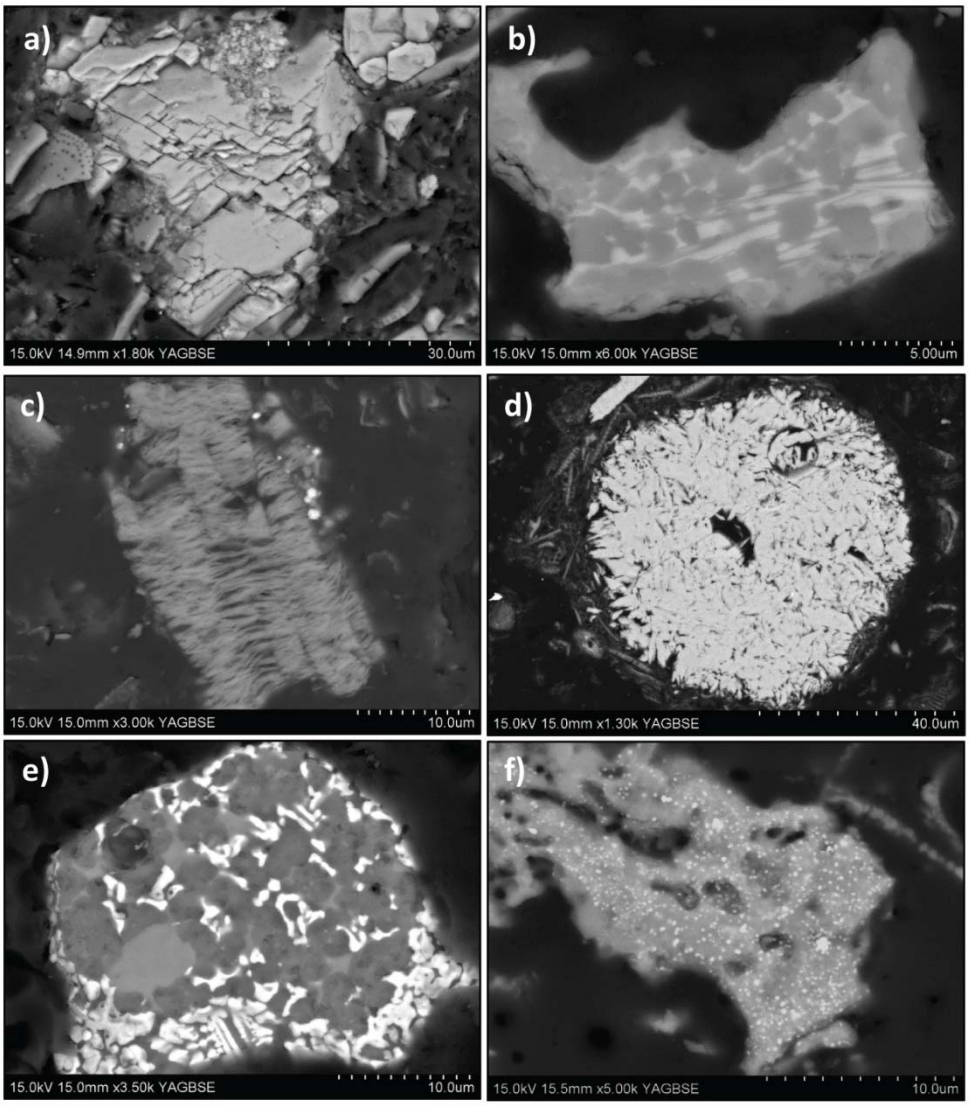

Figure 4.7: Backscatter images of contaminant phases in DE**. a)** a pure calcite particle in unprocessed DE from Spain (DE_05), **b)** a particle containing calcium silicate (very light grey) and cristobalite patches (dark grey) in flux-calcined DE from Spain (DE_06), **c)** a clay mineral particle in an unprocessed sample from France (DE_13), **d)** a large iron phosphate particle in unprocessed DE from France (DE_13), and **e-f)** iron-rich patches within particles in a French (DE_16) and Mexican (DE_24) calcined samples.

4.3.4 Iron release

Total iron release from DE over 9 days is shown in Figure 4.8. Results are presented as release by mass or surface area dose (surface area data are presented in Table 4.2). In both cases, DE_15 (an unprocessed French sample) showed the highest release of Fe, releasing 220 µmol/g or 9 µmol/m^2

after 8 days, followed by DE_16 (calcined French sample), which released 28 µmol/g or 7 µmol/m^2. DE_22 released 19 µmol/g total Fe by mass, whereas all other samples released <7 µmol/g after 8 days (Figure 4.8a). By surface area dose (Figure 4.8b), flux-calcined samples DE_14, DE_12 and DE_10 released 6, 5 and 3 µmol/m^2 respectively by day 8, whereas all other samples released <2 µmol/m^2. Total Fe release post-8 days incubation was 2-44% of the total bulk Fe, as measured by XRF (Table 4.3).

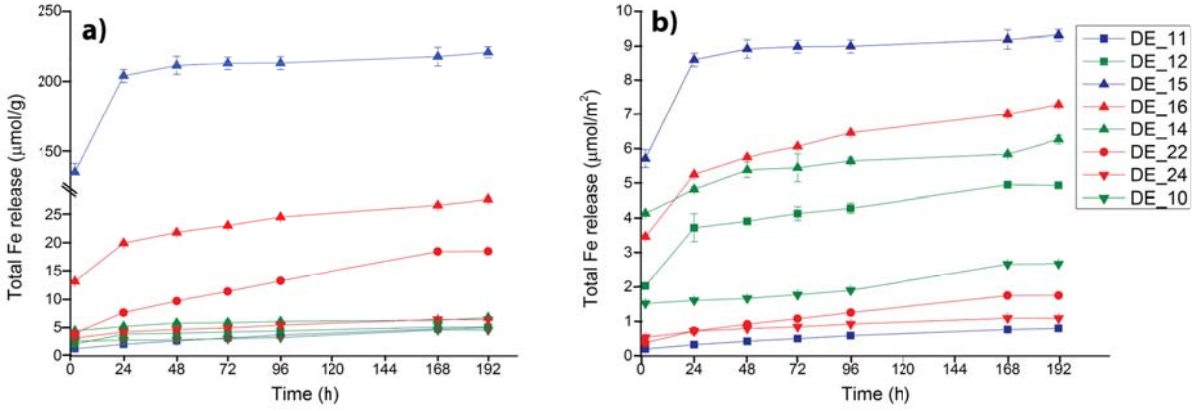

Figure 4.8: Total iron release from unprocessed (blue), calcined (red), and flux-calcined (green) DE over 8 days by **a)** sample mass, and **b)** sample surface area.

Table 4.3: Total Fe release from DE samples post 8-days incubation as a per cent of total bulk Fe as measured by XRF.

Sample	Total Fe (µmol/g)		% available Fe
	Fe release	Bulk Fe (XRF)	
DE_11	5.0	52.5	9.6
DE_12	5.1	43.7	11.6
DE_15	221.0	500.1	44.2
DE_16	27.7	483.2	5.7
DE_14	6.8	326.5	2.1
DE_22	18.5	144.3	12.9
DE_24	6.4	186.0	3.5
DE_10	4.6	100.6	4.6

The speciation of Fe release after 2 h is shown in Figure 4.9a. In Spanish samples, Fe^{2+} was the dominant species of Fe, whereas in all other samples Fe^{3+} was dominant. However, after 8 days of incubation, Fe^{2+} was released in greater quantities than Fe^{3+} in all samples except DE_22 and DE_11 where Fe^{3+} was dominant, and DE_16 where Fe^{2+} and Fe^{3+} release were equal (Figure 4.9b).

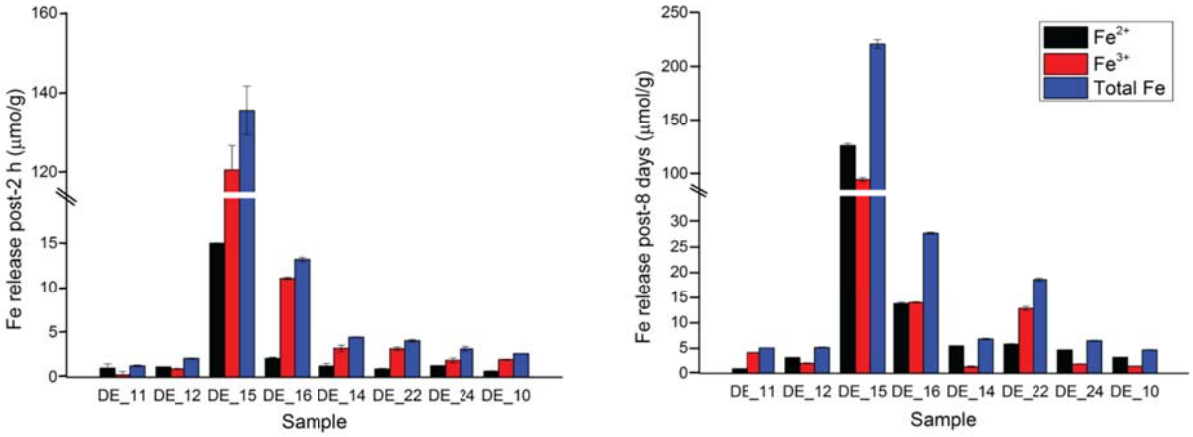

Figure 4.9: Total Fe release and speciation of Fe released from DE **a)** post-2 h incubation, and **b)** post-8 days incubation by sample mass.

4.3.5 Surface structure

IR spectroscopy allowed the identification of some surface features in the three samples analysed (DE_11, DE_15, and DE_24). All spectra showed a broad signal between 3750-2750 cm^{-1} attributed to O-H banding, including H-bonded, interacting silanols (see Chapter 2, Section 2.2.1) and water (Figure 4.10) (Morrow and Gay, 2000). The large signal observed at 1490 cm^{-1} in DE_11 only (Figure 4.10a) is representative of calcite (Gunasekaran et al., 2006, Downs, 2006). Isolated silanols may be present in DE_24, as indicated by a small peak at ~3750 cm^{-1} (Morrow, 2000), although this is difficult to determine. The signals seen clearly in DE_15 between 2950-2830 cm^{-1}, and observed as very small peaks in DE_11 and DE_24 spectra, are indicative of C-H bonding, and may be introduced

from solvents used during sample preparation, or may be due to organic material in the sample. The slope to the spectra is an artefact of particle scattering of the IR beam, and is caused by large particles in the samples.

Outgassing and isotopic exchange had no effect on the spectra of DE_11 or DE_24 (Figure 4.10a and c). For DE_15, there is a large reduction in the intensity of the O-H banding signal once outgassed, compared to in air. After isotopic exchange with D_2O, a further decrease in the O-H banding signal was observed, and an increase in absorbance in the 2750-2250 cm^{-1} region (Figure 4.10b). This indicates that some of the OH exchanged with D_2O.

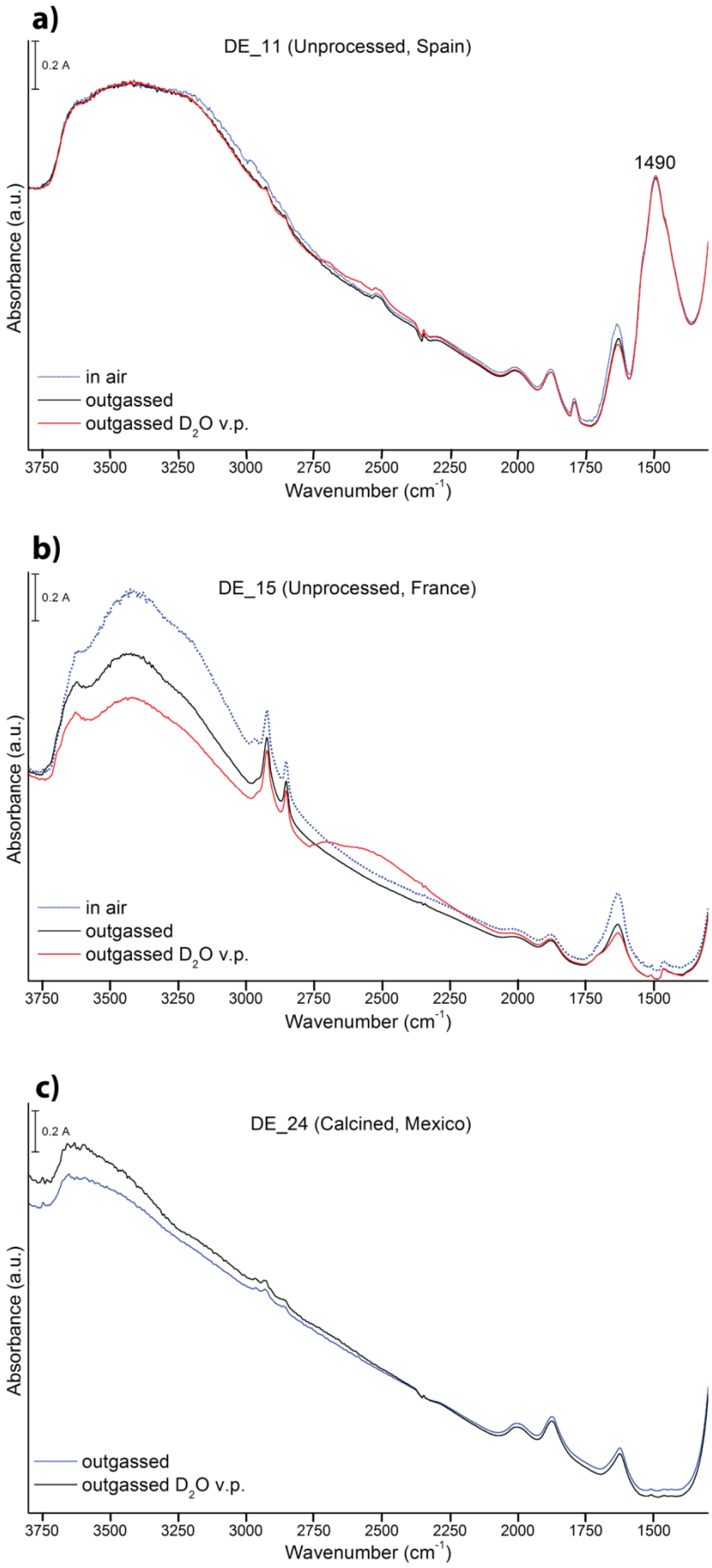

Figure 4.10: IR spectra of unprocessed DE from **a)** Spain and **b)** France, and **c)** calcined DE from Mexico.

4.3.6 Physical properties

Samples contained between 11 and 71 c.v. % particles <10 µm and between 5 and 25 c.v. % particles <4 µm in diameter (Table 4.2), analogous to the thoracic and respirable fractions, respectively (Quality of Urban Air Review Group, 1996). Flux-calcined samples were coarser than unprocessed and calcined samples for both filler and filter aid grade samples. Calcined samples had a wide range of particle size distributions, containing between 22 and 71 c.v. % <10 µm material (Table 4.2).

Particle morphology varied substantially amongst samples as the dominant diatom species varied with sample source. Samples from Chile, China, Mexico and Spain contained predominantly disc-shaped diatoms, whereas samples from USA-2 and France consisted mainly of cylindrical diatoms (Figure 4.11). Samples sourced from USA-1 contained a number of different diatom species and morphologies, including disc-shaped, and long, thin diatoms (Figure 4.11c). Most particles were fragments of diatoms and, therefore, particle morphology varied substantially within individual samples. Processed samples contained some sintered particles and fused pores, and this was most evident in flux-calcined samples, where large agglomerates of diatoms were observed (Figure 4.11d).

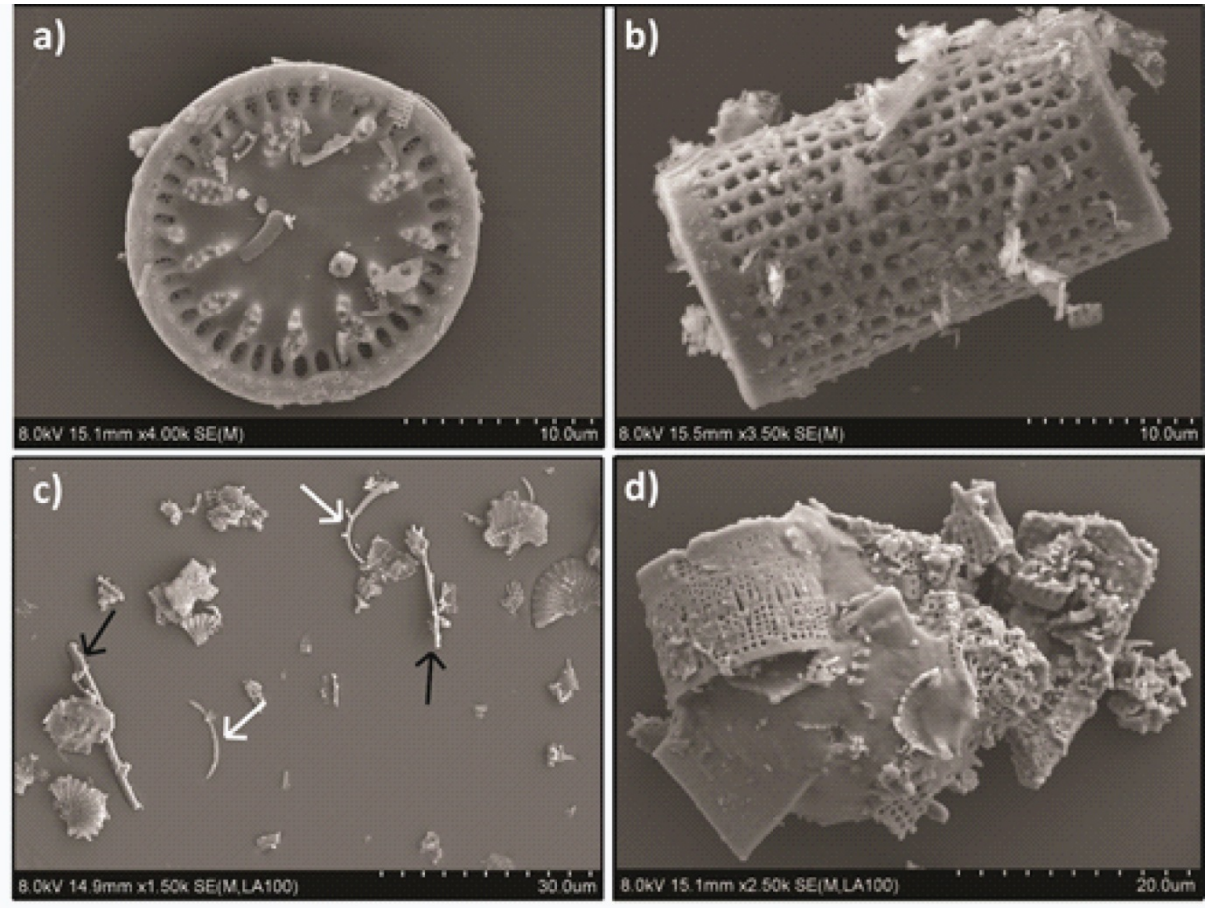

Figure 4.11: SEM images of examples of DE morphologies. **a)** disc-shaped DE found in Chilean, Chinese, Mexican and Spanish samples, **b)** cylindrical diatoms found in French and USA-2 samples, **c)** fibre-like rods (black arrows) and diatom rinds (white arrows), and **d)** a large agglomeration of fused diatoms in a flux-calcined DE sample. See Appendix 2 for catalogue of images.

Surface area did not vary much among flux-calcined samples and was always <1.7 m^2/g. However, in calcined and unprocessed samples, surface area varied substantially, ranging from 3.1 to 10.6 m^2/g in calcined samples and 6.3 to 23.8 m^2/g in unprocessed samples (Table 4.2).

4.4 Discussion

Previously, studies on the DE hazard have looked at few samples, often not stating the source, and epidemiology studies have usually focused on one plant in California (e.g. Checkoway et al., 1993, Park et al., 2002, Rice et al., 2001). Therefore, little is known about how the DE hazard varies

worldwide and by processing. Here, physicochemical properties of DE that may affect its potential toxicity vary considerably among samples which are sourced from different locations and have undergone different types of processing.

4.4.1 The variability of crystalline silica in DE

4.4.1.1 Crystalline silica form

Treatment of DE by calcination is used to optimise the physicochemical properties for use in the filtration and filler industries, during which amorphous silica crystallises (Engh, 2000, Flörke et al., 2000). Crystalline silica is a known carcinogen and can cause silicosis, however, it is well established that crystalline silica toxicity is variable and that its variability is likely dependent on its physicochemical characteristics (Chapter 2). Therefore, it is important to understand both the crystalline silica content and the form that crystalline silica takes in DE. Here, crystalline silica contents and polymorphs varied substantially amongst DE samples from different locations, with processing playing a key role. Flux-calcined samples were the most crystalline silica-rich, where cristobalite was the dominant crystalline silica polymorph. In these samples, cristobalite formed in patches throughout particles, crystallising within a matrix of amorphous material (Figure 4.2). Most calcined samples contained both cristobalite and quartz and there is some evidence that the quartz formed during calcination (based on data from the unprocessed DE_15 and calcined DE_16 samples). This distribution of crystalline silica polymorphs by processing technique has also been observed by Ghiazza et al. (2009) and Elias et al. (2000). The preferential crystallisation of cristobalite in flux-calcined samples is likely due the addition of the fluxing agent: doping of amorphous silica with sodium salts promotes cristobalite crystallisation instead of quartz at the temperatures used for calcination (Chao and Lu, 2000, Venezia et al., 2001).

It is unknown why quartz preferentially forms in some calcined samples, whereas in others only cristobalite is observed (Mexican samples DE_20 and DE_24). No link could be made between bulk impurities (measured by XRF) and the ratio of quartz to cristobalite in calcined samples. It was thought that the presence of impurities in the sample could lead to the preferential crystallisation of cristobalite (or tridymite) over quartz in the two Mexican samples, as impurities may prevent the re-structural transition between these phases and quartz upon cooling through the transition temperature (867 °C (Heaney et al., 1994)). Alternatively, different calcination temperatures may have been used at different processing sites, either intentionally or due to different furnace set-up or duration (which is altered for different products). However, this information was not available from the industry and, even if a temperature <867 °C was used (stability field of quartz), we have shown that as low as 800 °C cristobalite preferentially forms in non-doped silica, or silica remains amorphous when impurities are present (see Chapter 6). It has also been shown that cristobalite forms at these temperatures in volcanic environments (Horwell et al., 2013, Damby, 2012). As unprocessed samples from many of the locations could not be sourced, it is also possible that quartz is in the original material, but this cannot be verified. Thus, why quartz is present in calcined samples from some locations remains unknown.

Unprocessed samples contained trace quantities of cristobalite and quartz; the cristobalite in unprocessed samples likely forms by diagenesis of amorphous silica over time, or is possibly from other sources, such as volcanic deposits (Flörke et al., 2000). By BSE imaging, crystalline silica patches appeared to be similar to those observed in processed samples, suggesting that diagenesis is the most likely source of most of the cristobalite detected in the unprocessed samples. However, individual crystalline silica particles were observed, albeit rarely, in unprocessed samples, or large silica crystals coated with other phases (Figure 4.3). The crystal polymorph of these particles could not be determined, however, EDS analysis showed them to be pure SiO_2, whereas cristobalite patches always contained impurities (Figure 4.4 and 4.5). This, and the different morphology of

these particles, suggests that they were not formed by diagenesis and are possibly quartz and may be from volcanic deposits (Chapter 2). Further analyses, such as Raman spectroscopy, of these particles would be necessary to determine the silica polymorph. However, as these particles were rare, it is unlikely they would have a large impact on DE reactivity.

4.4.1.2 Crystalline silica purity

The cristobalite patches in the samples analysed were impure, containing Al, Na, Ca and Fe (e.g. Figure 4.2). Aluminium and Fe ions can substitute for Si in the silica tetrahedra, but require interstitial cations (e.g., Na or Ca) to charge balance the substitution (Deer et al., 2013), as has been discussed for volcanic cristobalite (Damby et al., 2014, Horwell et al., 2012). Semi-quantitative EDS analysis showed that the amorphous matrix surrounding the cristobalite patches was enriched in impurities compared to the cristobalite itself (Figure 4.4). In some cases, both the cristobalite and surrounding matrix were enriched in impurities that were also high in the bulk sample by XRF: the bulk, cristobalite and amorphous matrices in Spanish samples were enriched in Ca and French samples in Fe. However, Al was not enriched in the bulk of Mexican samples compared to other locations, but was enriched in the cristobalite and amorphous matrix (Figure 4.5). Unfortunately, cristobalite purity in samples from other locations could not be analysed by EDS due to difficulties with sample preparation (particles were often plucked from the resin during polishing and the porosity of the particles made it difficult to produce flat surfaces for analysis).

It is possible that the impurities seen in the cristobalite and amorphous matrix come from phases which are broken down during calcination - Ca-rich phases in Spanish samples and Fe-rich phases in French samples - as these were seen in abundance in the unprocessed samples from these locations (see below). However, the duration of calcination or flux-calcination is normally <2 h, which may not be long enough for phase breakdown and diffusion of these elements into the crystalline silica

structure. Although some impurities were seen in unaltered diatoms, these were depleted in impurities compared to cristobalite (Figure 4.4) so cannot be the only source of impurities observed in cristobalite. Rarely, some particles with similar chemical composition to the amorphous matrices were observed in the unprocessed samples. It is possible that cristobalite formed in these particles during calcination, and that impurities would have become trapped in the structure during crystallisation and not be able to diffuse out. The diffusion of impurities away from the cristobalite patches would also explain why the amorphous matrix in these particles is enriched in impurities compared to the cristobalite. However, the abundance of these amorphous particles in unprocessed samples (with similar chemistry to the cristobalite-bearing particles in processed samples) is too low to account for all the cristobalite formed. Therefore, to fully understand the source of the impurities and how they are incorporated into the crystalline silica structure, a more detailed study is required. More unprocessed samples and more accurate data from better prepared samples and, given the small areas needed to be studied, diffusion profiles away from the cristobalite patches would be needed. This was beyond the scope of this current study, where the main aim was to determine if the cristobalite was impure in DE, but is included here as an interesting aside that should be the focus of future study.

4.4.2 The variability of contaminants in DE

Contaminant phases were observed in all samples. Spanish deposits contained calcite (DE_05, DE_11), determined by XRD, IR and BSE imaging. Calcite would thermally decompose at calcination temperatures (~1000°C) (Rodriguez-Navarro et al., 2009), allowing Ca and Si to form calcium silicates, which were in abundance in flux-calcined samples from Spain. High Ca contents were expected as samples from Spain have been shown to have high Ca content (Table 2.4, Chapter 2). Calcium silicates were also observed in the flux-calcined Chilean sample (DE_09) and slightly

elevated CaO concentrations. Unprocessed samples from Chile were not available to determine if calcite was present pre-processing.

Bulk Fe and Al contents of French samples were higher than those seen in previous studies. Fe contents of 3-4 oxide wt.% were observed compared to 1-2 oxide wt.% previously observed, and Al contents of 4-5 oxide wt.% compared to previously measured 1-4 wt.% (Table 2.4, Chapter 2, (Elias et al., 2000, Ghiazza et al., 2009, Imerys Minerals Ltd., 2012). These impurities were incorporated into clay minerals and iron-rich particles, which are likely to be broken down during calcination as few individual clay mineral particles or large iron-rich particles were seen in processed samples compared to unprocessed samples from France. As with Ca in Spanish samples, this frees Fe ions to react with Si, and precipitate in pores and cracks, which was seen in all calcined samples (Figure 4.7e-f), although some may be incorporated into the cristobalite structure (see above). The addition of a sodium carbonate flux leads to sodium silicate melt binding with Fe (Flörke et al., 2000), which explains the lack of iron-rich particles in flux-calcined samples.

Bulk Fe contents do not necessarily indicate the available Fe at the surface of particles, which is important in free radical release and interaction with biological material (see Chapters 2 and 5). Therefore, Fe release was measured from DE samples over 8 days. French samples, with the highest bulk Fe content, released the most Fe. Both by mass and surface area, total Fe release for French samples was in the order unprocessed>calcined>flux-calcined. This suggests Fe is readily available in the large Fe-rich phases observed in the unprocessed samples, where 44% of bulk Fe was released, but once calcined the Fe-rich patches seen throughout calcined samples are less available (only 6% bulk Fe released). In the flux-calcined sample (DE_14), the binding of Fe in the silicate melt (see above) makes this less available and only 2% of bulk Fe was released after 8 days.

All other samples released <5 μmol/m^2 Fe by surface area and the amount of total available Fe did not correlate with bulk Fe, ranging from 4-13% of bulk Fe. By mass, DE_22 (USA-1 calcined sample) released more total Fe than the other samples (except French DE_15 and DE_16), releasing 13% of its bulk Fe, but did not have higher bulk Fe compared to other samples. The higher surface area of this sample compared to other calcined samples (Table 4.2) can explain this increase in Fe release as, by surface area dose, there was no elevation in Fe release compared to other samples (Figure 4.8b).

The importance of the state of iron in its effect on toxicity is well established; metallic iron can have an inhibitory effect of the ability of quartz to produce an inflammatory effect (Cullen et al., 1997), whereas ferric and ferrous iron has no effect on quartz cytotoxicity (Cullen et al., 1997) but Fe contamination can cause an increase in the release of hydroxyl radicals from quartz (Castranova et al., 1997). Here, the dominant state of Fe released changed over time. Initially, Fe^{3+} was the dominant Fe species released for all samples except those from Spain, which had very low total Fe release. After 8 days Fe^{2+} was the dominant species released by most samples. This suggests that Fe^{2+} was less readily available initially. As Fe^{2+} can lead to the production of free radicals, which can be involved in silica toxicity (see Chapter 2), this is a primary concern and Fe in DE has previously been hypothesised as a source of free radicals (Elias et al., 2006). Here, Fe^{2+} release was similar for all DE samples post-2 h and post-8 days, except in DE_15 and DE_16, where Fe^{2+} release was elevated. The potential effect of Fe release on free radical production and *in vitro* reactivity for DE is tested and discussed in Chapter 5.

4.4.3 Surface structure

Broad O-H banding signals were observed in the three samples analysed by IR spectroscopy (Figure 4.10). This indicates high concentrations of H-bonded and interacting silanols, as the band remains after outgassing to remove weakly adsorbed water. In DE_15, many of these sites are readily

exchanged when exposed to D_2O indicating that many of the sites reside on the surface of the particles. In DE_11 and DE_24, no isotopic exchange was observed, indicating that the O-H banding sites are intra-particle and are not readily available to react. This could have important implications in their reactivity *in vitro*, which is discussed in Chapter 5. Unfortunately, the broad band (due to the complex surfaces of these particles) and particle scattering means finer details cannot be observed in these spectra.

4.4.4 The variability of physical properties of DE

Physical properties varied substantially among the samples. Flux-calcined particles had complex morphologies, and were coarser and had lower surface area than calcined and unprocessed samples, due to sintering of particles into large agglomerates and the closure of pore spaces (Ediz et al., 2010). Due to the high porosity of these samples no correlation between surface area and particle size could be made (Figure 4.12). It is likely that in unprocessed samples, especially, a large proportion of the surface area is pore space. In calcined and flux-calcined particles, the morphologies are also complex and, therefore, the surface area is not reflected in the particle size.

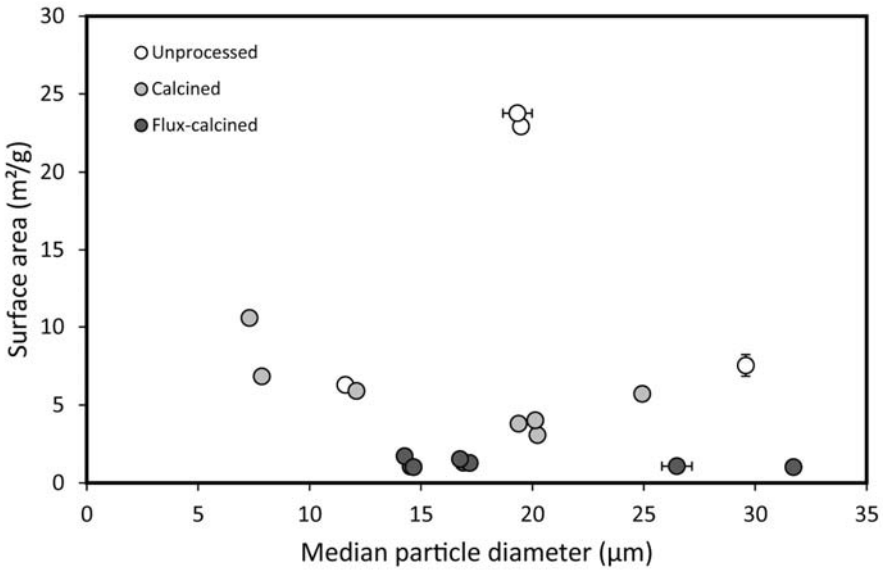

Figure 4.12: Median particle size of unprocessed, calcined and flux-calcined DE against specific surface area. Error bars represent 1 standard deviation (n=2 for particle diameter, n=3 for surface area).

The morphology of diatom frustules varied with source (Figure 4.11); however, the abundance of fragmented frustules in all samples meant diatom species, alone, could not be used as a good proxy for particle morphology. Particle morphology assessed by SEM image analysis and how this relates to the potential toxicity of DE is discussed in detail in Chapter 5.

4.5 Conclusions

Here, the variability of the properties of DE worldwide is considered, and how these properties are affected by different processing techniques. Crystalline silica is a primary health concern, as it is a known carcinogen and can cause respiratory disease, and forms in DE during processing. Crystalline silica was most abundant in flux-calcined samples, as cristobalite patches, whereas calcined DE often contained both quartz and cristobalite. The cristobalite patches contained Na, Al, Ca and Fe impurities, but these differed by source. Spanish DE contained high Ca contents in bulk, as calcite, calcium silicates and in amorphous material, and Spanish DE cristobalite was also enriched in Ca compared to other locations. French DE contained Fe-rich phases and cristobalite in these samples was enriched in Fe impurities. Mexican DE cristobalite was enriched in Al, but this could not be correlated to the bulk impurities.

Contaminant phases were detected in all samples. French DE had high bulk Fe content and high Fe release. Calcination reduced the available Fe due to the formation of Fe-rich phases throughout particles, whereas flux-calcination reduced the available Fe further, likely by binding of Fe into the silicate melt during processing. Samples from other locations had less bulk Fe and less available Fe in comparison. The dominant Fe species released differed among samples and with time and is discussed in Chapter 5 in relation to free radical production and potential toxicity. The main bulk impurity observed in samples from Chile, China, Mexico and USA-1 was Al, suggesting Al may be the

most common impurity in cristobalite in these samples. However, samples sourced from the same location had variable chemistries, sometimes greater than differences among samples from different sources.

The physical properties of DE also varied. Flux-calcination led to agglomeration of particles and a reduced surface area. Diatom morphology varied by location and fragmentation and agglomeration led to complex particle morphologies in all samples, which are discussed further in relation to the effect on potential toxicity in Chapter 5.

As the physicochemical characteristics of DE control its pathogenicity, determining the variability of these characteristics is key in understanding the variability of the DE hazard. The effect of the physicochemical variability measured here on the potential toxicity of DE is discussed in detail in Chapter 5 alongside *in vitro* toxicological and surface reactivity data.

References

BYE, E., DAVIES, R., GRIFFITHS, D. M., GYLSETH, B. & MONCRIEFF, C. B. 1984. In vitro cytotoxicity and quantitative silica analysis of diatomaceous earth products. *British Journal of Industrial Medicine,* 41**,** 228-234.

CARPENTER, M. A., SALJE, E. K. H. & GRAEME-BARBER, A. 1998. Spontaneous strain as a determinant of thermodynamic properties for phase transitions in minerals. *European Journal of Mineralogy,* 10**,** 621-691.

CASTRANOVA, V., VALLYATHAN, V., RAMSEY, D. M., MCLAURIN, J. L., PACK, D., LEONARD, S., BARGER, M. W., MA, J. Y., DALAL, N. S. & TEASS, A. 1997. Augmentation of pulmonary reactions to quartz inhalation by trace amounts of iron-containing particles. *Environmental Health Perspectives,* 105**,** 1319-1324.

CHAO, C. H. & LU, H. Y. 2000. Crystallization of Na2O-doped colloidal gel-derived silica. *Materials Science and Engineering a-Structural Materials Properties Microstructure and Processing,* 282**,** 123-130.

CHECKOWAY, H., HEYER, N. J., DEMERS, P. A. & BRESLOW, N. E. 1993. Mortality among workers in the diatomaceous earth industry. *British Journal of Industrial Medicine,* 50**,** 586-597.

CLOUTER, A., BROWN, D., HÖHR, D., BORM, P. & DONALDSON, K. 2001. Inflammatory Effects of Respirable Quartz Collected in Workplaces versus Standard DQ12 Quartz: Particle Surface Correlates. *Toxicological Sciences,* 63**,** 90-98.

CULLEN, R. T., VALLYATHAN, V., HAGEN, S. & DONALDSON, K. 1997. Protection by Iron Against the Toxic Effects of Quartz. *Annals of Occupational Hygiene,* 41**,** 420-425.

DAMBY, D. E. 2012. *From Dome to Disease: The Respiratory Toxicity of Volcanic Cristobalite.* Durham theses, Durham University.

DAMBY, D. E., LLEWELLIN, E. W., HORWELL, C. J., WILLIAMSON, B. J., NAJORKA, J., CRESSEY, G. & CARPENTER, M. 2014. The [alpha]-[beta] phase transition in volcanic cristobalite. *Journal of Applied Crystallography,* 47.

DEER, W. A., HOWIE, R. A. & ZUSSMAN, J. 2013. *An Introduction to the Rock-forming Minerals*, Mineralogical Society of Great Britain & Ireland.

DONALDSON, K. & BORM, P. J. A. 1998. The Quartz Hazard: A Variable Entity. *Annals of Occupational Hygiene,* 42**,** 287-294.

DOWNS, R. T. 2006. The RRUFF Project: an integrated study of the chemistry, crystallography, Raman and infrared spectroscopy of minerals. *Program and Abstracts of the 19th General Meeting of the International Mineralogical Association.* Kobe, Japan. O03-13 (available at: rruff.info/).

EDIZ, N., BENTLI, İ. & TATAR, İ. 2010. Improvement in filtration characteristics of diatomite by calcination. *International Journal of Mineral Processing,* 94**,** 129-134.

ELIAS, Z., POIROT, O., DANIÈRE, M. C., TERZETTI, F., MARANDE, A. M., DZWIGAJ, S., PEZERAT, H., FENOGLIO, I. & FUBINI, B. 2000. Cytotoxic and transforming effects of silica particles with different surface properties in Syrian hamster embryo (SHE) cells. *Toxicology in Vitro,* 14**,** 409-422.

ELIAS, Z., POIROT, O., FENOGLIO, I., GHIAZZA, M., DANIÈRE, M. C., TERZETTI, F., DARNE, C., COULAIS, C., MATEKOVITS, I. & FUBINI, B. 2006. Surface Reactivity, Cytotoxic, and Morphological Transforming Effects of Diatomaceous Earth Products in Syrian Hamster Embryo Cells. *Toxicological Sciences,* 91**,** 510-520.

ENGH, K. R. 2000. Diatomite. *Kirk-Othmer Encyclopedia of Chemical Technology.* John Wiley & Sons, Inc.

FLÖRKE, O. W., GRAETSCH, H. A., BRUNK, F., BENDA, L., PASCHEN, S., BERGNA, H. E., ROBERTS, W. O., WELSH, W. A., LIBANATI, C., ETTLINGER, M., KERNER, D., MAIER, M., MEON, W., SCHMOLL, R., GIES, H. & SCHIFFMANN, D. 2000. Silica. *Ullmann's Encyclopedia of Industrial Chemistry.* Wiley-VCH Verlag GmbH & Co. KGaA.

GHIAZZA, M., GAZZANO, E., BONELLI, B., FENOGLIO, I., POLIMENI, M., GHIGO, D., GARRONE, E. & FUBINI, B. 2009. Formation of a Vitreous Phase at the Surface of Some Commercial Diatomaceous Earth Prevents the Onset of Oxidative Stress Effects. *Chemical Research in Toxicology,* 22**,** 136-145.

GUNASEKARAN, S., ANBALAGAN, G. & PANDI, S. 2006. Raman and infrared spectra of carbonates of calcite structure. *Journal of Raman Spectroscopy,* 37**,** 892-899.

HART, G. A. & HESTERBERG, T. M. 1998. *In vitro toxicity of respirable-size particles of diatomaceous earth and crystalline silica compared with asbestos and titanium dioxide,* Hagerstown, MD, ETATS-UNIS, Lippincott Williams & Wilkins.

HEANEY, P. J., PREWITT, C. T. & GIBBS, G. V. 1994. *Silica: Physical Behavior, Geochemistry and Materials Applications,* Washington D.C., Mineralogical Society of America.

HORWELL, C., WILLIAMSON, B., DONALDSON, K., LE BLOND, J., DAMBY, D. & BOWEN, L. 2012. The structure of volcanic cristobalite in relation to its toxicity; relevance for the variable crystalline silica hazard. *Particle and Fibre Toxicology,* 9**,** 44.

HORWELL, C., WILLIAMSON, B., LLEWELLIN, E., DAMBY, D. & BLOND, J. 2013. The nature and formation of cristobalite at the Soufrière Hills volcano, Montserrat: implications for the petrology and stability of silicic lava domes. *Bulletin of Volcanology,* 75**,** 1-19.

IMERYS MINERALS LTD. 2012. *Diatomite Product List* [Online]. http://www.imerys-perfmins.com/diatomite/eu/diatomite-products.htm. [Accessed 11/06/2015 2015].

MORROW, B. A., AND GAY, I. D. . 2000. Infrared and NMR characterization of the silica surface. *In:* PAPIRER, E. (ed.) *Adsorption on Silica Surfaces.* New York: Marcel Dekker Inc.

MORROW, B. A. & GAY, I. D. 2000. Infrared and NMR characterization of the silica surface. *In:* PAPIRER, E. (ed.) *Adsorption on Silica Surfaces.* New York: Marcel Dekker Inc.

PARK, R., RICE, F., STAYNER, L., SMITH, R., GILBERT, S. & CHECKOWAY, H. 2002. Exposure to crystalline silica, silicosis, and lung disease other than cancer in diatomaceous earth industry

workers: a quantitative risk assessment. *Occupational and Environmental Medicine,* 59**,** 36-43.

QUALITY OF URBAN AIR REVIEW GROUP 1996. Airborne particulate matter in the United Kingdom. *In:* DEPARTMENT OF THE ENVIRONMENT (ed.). London, UK.

RICE, F. L., PARK, R., STAYNER, L., SMITH, R., GILBERT, S. & CHECKOWAY, H. 2001. Crystalline silica exposure and lung cancer mortality in diatomaceous earth industry workers: a quantitative risk assessment. *Occupational and Environmental Medicine,* 58**,** 38-45.

RODRIGUEZ-NAVARRO, C., RUIZ-AGUDO, E., LUQUE, A., RODRIGUEZ-NAVARRO, A. B. & ORTEGA-HUERTAS, M. 2009. Thermal decomposition of calcite: Mechanisms of formation and textural evolution of CaO nanocrystals. *American Mineralogist,* 94**,** 578-593.

VENEZIA, A. M., LA PAROLA, V., LONGO, A. & MARTORANA, A. 2001. Effect of Alkali Ions on the Amorphous to Crystalline Phase Transition of Silica. *Journal of Solid State Chemistry,* 161**,** 373-378.

Chapter 5

Global variability of the potential toxicity of diatomaceous earth

5.1 Introduction

Diatomaceous Earth can contain significant amounts of crystalline silica, especially once processed, as shown in Chapter 4, which is known to cause disease such as silicosis and cancer (see Chapter 2). However, the variability of the DE hazard is poorly constrained. Epidemiology studies show increased mortality (Checkoway et al., 1993, Seixas et al., 1997), pneumoconiosis (Cooper and Sargent, 1984, Dutra, 1965, Harber et al., 1998, Smart and Anderson, 1952), increased risk of lung cancer (Checkoway et al., 1993, Rice et al., 2001, Seixas et al., 1997) and other lung diseases (Park et al., 2002) in DE workers, compared to unexposed populations in California. However, the few smaller studies from elsewhere give varying results as to DE pathogenicity (see Chapter 2 for full review). Therefore, little is known about how the pathogenicity of DE varies globally.

Many of the above studies indicate crystalline silica as the cause of pathogenicity, however, Harber et al. (1998) demonstrate no link between crystalline silica exposure and the pathogenicity observed in DE workers, and Vigliani and Mottura (1948) show pathological changes in the lungs which differ from typical quartz-induced silicosis. As with epidemiological studies, there is discrepancy among the existing toxicological studies as to whether crystalline silica content is the determinant factor for disease (Chapter 2). This knowledge is essential for the effective management of occupational risk.

Previous studies have focussed on few samples and single locations and, therefore, have not been able to investigate the source-dependent compositional and morphological variability of DE and the effect of this variability on toxicity endpoints. This study overcomes this limitation by determining the *in vitro* toxicity of DE sourced from seven quarries across the world, and trying to relate this to the variable physicochemical characteristics of the material (see Chapter 4) to understand the factors that control DE toxicity. Specifically, the role of crystalline silica in controlling DE toxicity and factors that may alter its toxic potential, such as the presence of other minerals and structural substitutions (see Chapters 2 and 4), is investigated. Samples chosen cover a spectrum of deposit types, purities and processing techniques. A range of *in vitro* toxicological assays were chosen, commonly used in particle toxicology and designed to highlight any causal effects of crystalline silica. Haemolysis allows for the assessment of particle-induced membrane damage, while cytotoxicity and cytokine release from macrophages are used to assess cell viability and the potential to induce inflammation.

5.2 Methods

5.2.1 Separation of the fine fraction

As only particle <100 µm are inhalable, and only those <10 µm are thoracic (see Chapter 2), the fine fractions (close to PM10) were separated from five bulk samples for toxicological assessment alongside their bulk counterparts (Table 4.1). The five samples were chosen based on XRF and XRD data (Chapter 4) to encompass a range of crystalline silica contents, bulk impurities, and processing techniques. These samples were separated by dry-resuspension as previously described by Moreno et al. (2005) (see Chapter 3). Quantitative assessment (up to 2000 particles per sample) of particle size and the abundance of fibre-like particles (defined by an aspect ratio >3 (Ziemann et al., 2014))

(see Chapter 3), was conducted on the five fine fractions used in toxicology experiments and their corresponding bulk samples (DE_05, DE_08, DE_10, DE_20 and DE_24).

5.2.2 In vitro toxicology

The *in vitro* methodologies used here are explained in full detail in Chapter 3 but are briefly outlined here. Haemolysis is a measure of the ability of particles to rupture cell membranes, and has been shown to be a good indicator of the pro-inflammatory potential of crystalline silica (Pavan et al., 2014). Haemolysis was performed on all 19 bulk samples (see Chapter 4 for sample details) and 5 separated fine fractions by treating red blood cells with 63-1000 μg/ml DE powder for one hour.

Cytotoxicity was measured using alamarBlue® (a measure of mitochondrial enzyme activity) and lactate dehydrogenase (LDH; a measure of membrane integrity) assays after 24 h exposure of J774 macrophages to 100 μl of 8-500 μg/ml DE suspensions. These assays were performed on the five fine fractions, their corresponding bulk samples, two bulk samples chosen due to their haemolytic potential (DE_11 and DE_22), as well as a further unprocessed bulk sample (DE_15).

To determine if soluble components of DE were haemolytic, two highly haemolytic DE powders (DE_05, DE_11) were leached in saline for one hour at the top treatment concentration (1000 μg/ml) by shaking gently, the suspension was then centrifuged at 5000 rcf for 15 minutes and filtered through a 0.2 μm Nalgene syringe filter, and the collected leachates were used in the haemolysis assay. All samples used in the cytotoxicity assays were also leached in complete medium for 24 hours at 63 μg/ml (in the absence of cells), centrifuged at 5000 rcf for 10 minutes and the collected leachate used to treat the cells, and their toxicity assessed using the alamarBlue® assay.

Cytokine production was measured as a marker of inflammation using BD™ Cytometric Bead Array cytokine flex sets. Keratinocyte chemoattractant (KC), interleukin 1β (IL-1β), tumour necrosis factor alpha (TNF-α) and interleukin 10 (IL-10) were measured for cells treated with 125 µg/ml or lower of the fine fractions of DE only. For samples demonstrating cytotoxicity, the LC20 concentration, two times the LC20 and half the LC20 would generally be assessed to investigate cytokine production. However, in low toxicity samples, where an LC20 was not reached, only a concentration of 125 µg/ml was chosen to evaluate the inflammatory response.

Cells treated with the five fine fractions were imaged by light microscopy to qualitatively assess particle uptake. J774 cells (2.5×10^5) were treated with 600 µl of 63 µg/ml DE in a 24 well plate. Cells were scraped from the plate and 50 µl of the cell suspension diluted in 300 µl saline and centrifuged onto a microscope slide at 1160 rcf for 5 minutes. The treated cells were dried and stained with Diff-Quik (Fisher Scientific). Briefly, slides were dipped in methanol, then Eosin G in phosphate buffer and Thiazine dye in phosphate buffer, rinsed with H_2O and air dried.

In all assays Triton-X was used as a positive control and untreated cells as a negative control. DQ12 was used as a positive crystalline silica standard and TiO_2 as a negative particle standard. A calcite standard was also used in the alamarBlue® and haemolysis assays, due to a high calcite content in some samples. Results are presented as the relative percentages of the positive and negative controls.

5.2.3 Free radical release

The production of hydroxyl free radicals ($HO^{\bullet}$) by DE was assessed using EPR with spin trap. First, 250 µl phosphate buffer solution, 125 µl DMPO and 250 µl H_2O_2 were added to 37.5 mg of sample. The suspension was continually stirred in the dark (using a plastic-coated magnet and stirring plate)

and aliquots taken at 10, 30 and 60 minutes, filtered through 0.25 µm filter and analysed using a Miniscope MS100 (Università degli Studi di Torino).

5.2.4 Statistical analysis

Student's t-test and ANOVA general linear model with a Tukey's post-hoc test were performed to determine the significance of differences among samples in the *in vitro* assays (Minitab 15). Pearson's correlation test was used to determine significant correlations amongst different physicochemical characteristics and toxicological results (* $p < 0.05$, ** $p < 0.01$, *** $p < 0.001$).

5.3 Results

Full physicochemical characterisation of all samples is presented in Chapter 4 (see Table 4.2 which also states sample information). Here, SEM image analysis was used to determine if separation of the fine fraction was successful and to determine the aspect ratio of particles and if this differed among samples. The maximum particle diameter observed in the separated fine fractions was 51 µm, reduced from 73 µm in the bulk fractions (Table 5.1). Additionally, 83-99% of particles, by number, in the fine fractions were <10 µm in diameter, compared to 73-96% in the bulk samples (Table 5.1). The separated fraction of flux-calcined samples was coarser (median diameter 1.5-2.6 µm) than the fine fractions of calcined and unprocessed samples (median diameters 0.8 µm; Table 5.1). These data are not comparable to laser diffraction data (Chapter 4), which present equivalent spherical diameter in volume % so are heavily mass-biased.

Table 5.1: Particle size measured by SEM image analysis. Includes maximum particle diameter, median particle diameter, the number % of particles <10 µm, and the number % of fibre-like particles in five bulk samples and their corresponding fine fractions.

Sample	Maximum particle diameter (µm)		Median particle diameter (µm)		Particles <10 µm diameter (number %)		Fibre-like particles (%)	
	Bulk	Fine fraction	Bulk	Fine fraction	Bulk	Fine fraction	Bulk	Fine fraction
DE_05	26.9	18.5	1.7	0.8	96.6	99.2	17.9	15.4
DE_20	52.0	31.5	1.9	0.8	94.1	96.5	21.2	18.8
DE_24	47.0	17.3	1.8	0.8	96.5	99.0	17.8	16.4
DE_08	73.0	43.7	5.0	1.5	73.2	82.7	3.3	5.7
DE_10	46.2	51.3	4.1	2.6	77.9	83.0	4.9	9.8

In the five bulk samples and equivalent fine fractions, between 3 and 21% of particles, by number, were classified as fibre-like (Table 5.1). The total number of fibre-like particles was 2 to 6 times lower in flux-calcined samples than in unprocessed or calcined samples, for both bulk samples and fine fractions (Table 5.1).

5.3.1 Haemolysis

Haemolysis results are shown in Figure 5.1 for bulk samples. Haemolysis caused by the fine fractions did not differ significantly from their corresponding bulk samples (data given in Appendix 1). Unprocessed samples from Spain (DE_05 and DE_11) were two of the most haemolytic samples,

with DE_11 as haemolytic as DQ12. The most haemolytic calcined sample, DE_22 (USA-1), was one third as haemolytic as DQ12 at the highest concentration. All other samples were not significantly haemolytic at any concentration tested, including the calcite standard (Figure 5.1).

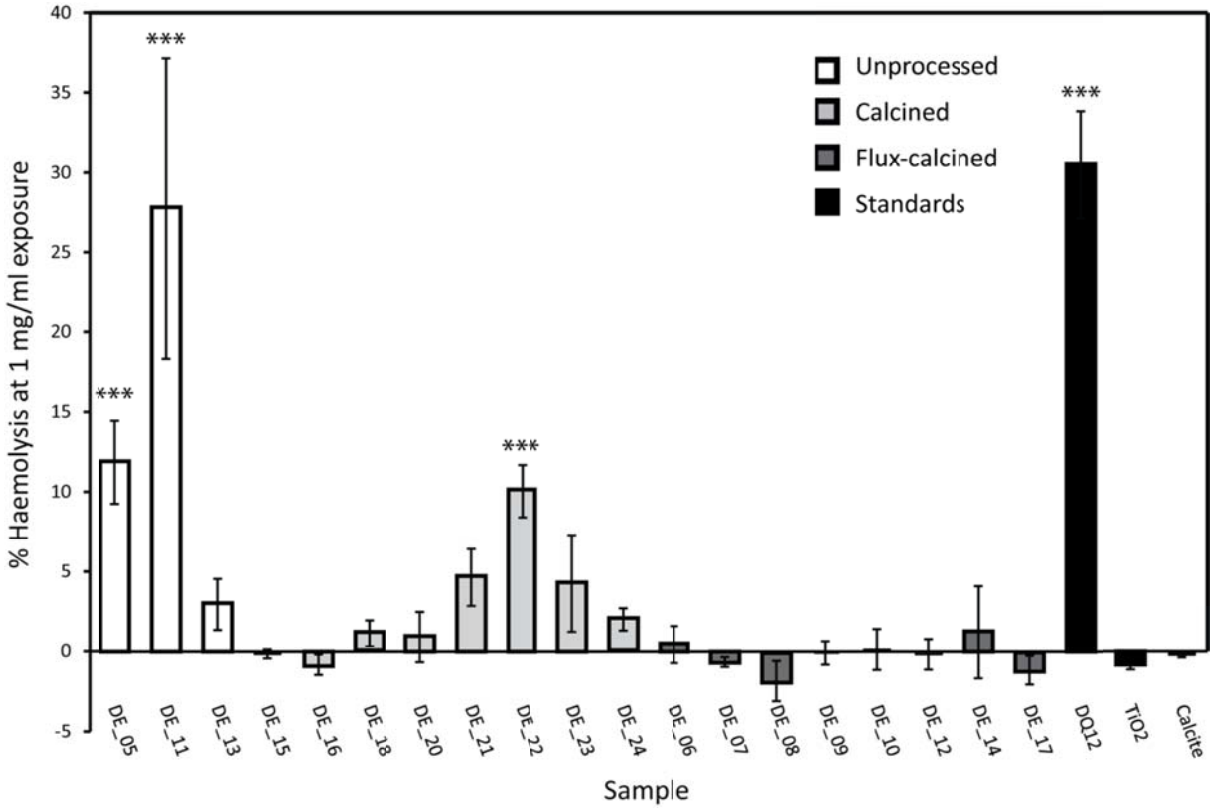

Figure 5.1: Haemolytic potential of DE samples. Per cent haemolysis relative to an untreated control, of sheep red blood cells post-exposure to 1 mg/ml of unprocessed (white), calcined (light grey) and flux-calcined (dark grey) DE and positive (DQ12) and negative (TiO_2) standards (black). Error bars represent standard error (n=3), *** p = <0.001 difference from untreated control.

The leachates of DE_05 and DE_11 (both Spain, unprocessed) were not haemolytic (Appendix 1). Therefore, soluble components of the DE were not the cause of the observed haemolytic response of these samples.

5.3.2 Cytotoxicity

In the alamarBlue® assay (Figure 5.2), there was no statistically significant difference in cytotoxicity of bulk DE samples and their separated fine fractions. Bulk flux-calcined samples, and DE_20 (Mexico, calcined) and DE_15 (France, unprocessed), TiO_2 and calcite did not differ from the untreated control. All other samples exhibited a cytotoxic response, and DE_24 (bulk and fine, Mexico, calcined), DE_22 (USA-1, calcined), DE_11 (Spain, unprocessed) and the fine fraction of DE_05 (Spain, unprocessed) did not differ significantly from DQ12 ($p>0.2$). LDH release data were in broad agreement with cell viability measurements via the alamarBlue® assay, in that flux-calcined samples were less cytotoxic than unprocessed and calcined samples (Figure 5.3).

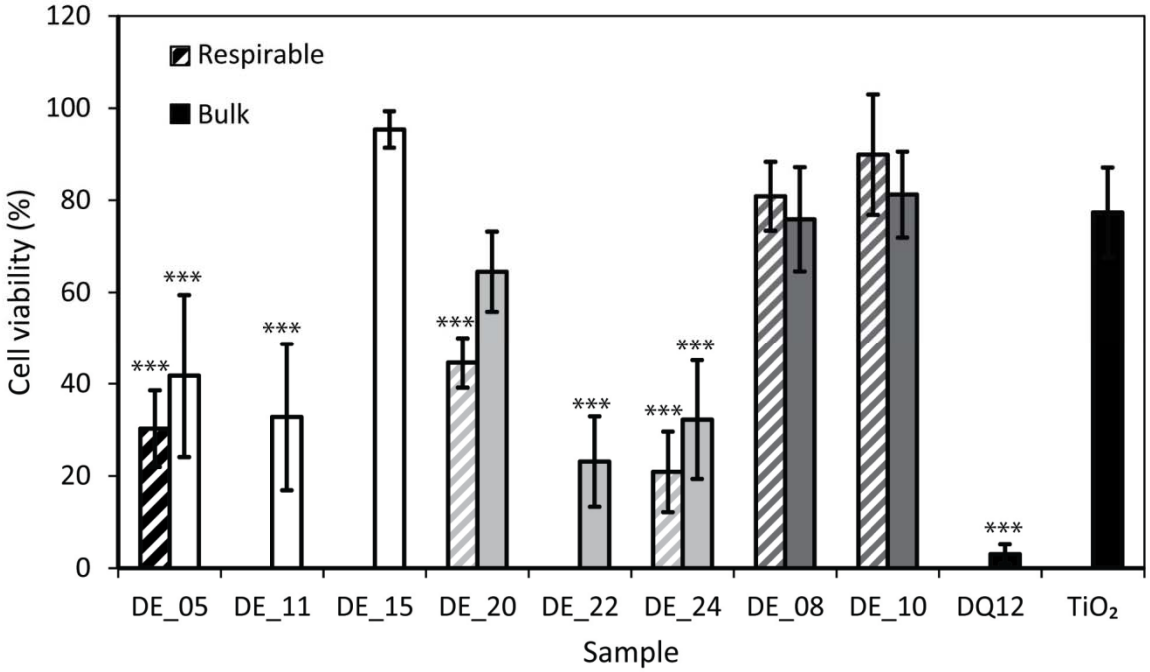

Figure 5.2: Cell viability of J774 macrophages exposed to DE. Cell viability relative to an untreated control (% of untreated control – positive control), measured by the alamarBlue® assay, of J774 macrophages exposed to 500 µg/ml of bulk (solid) or the fine fraction (hashed) of unprocessed (white), calcined (light grey) and flux-calcined (dark grey) DE, and positive (DQ12) and negative (TiO_2) standards (black) for 24 hours. Fine fractions of DE_11, DE_15 and DE_22 not separated so there are no data. Error bars represent standard error (n=4), *** p = <0.001 difference from untreated control.

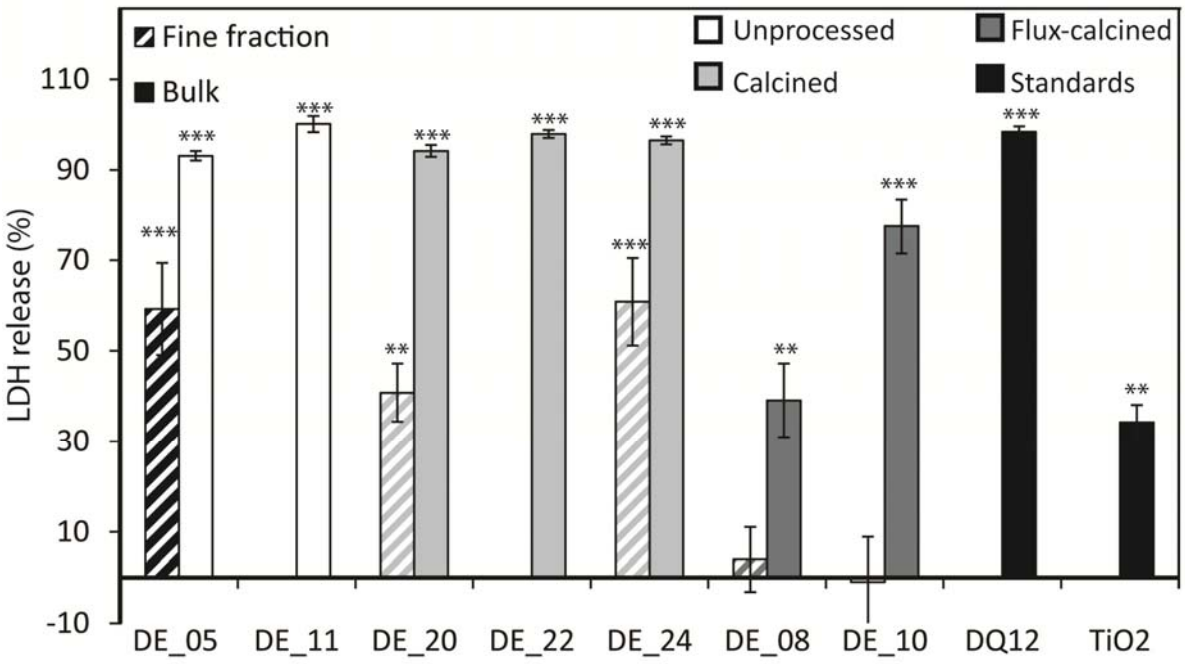

Figure 5.3: Lactate dehydrogenase release from J774 macrophages treated with 500 µg/ml of the fine fraction (hashed) and bulk (solid) samples of unprocessed (white), calcined (light grey), and flux-calcined (dark grey) DE for 24 h (n=4). Fine fractions were not separated for DE_11 or DE_22 so there are no data. Error bars represent standard error (n=4), *** p = <0.001 difference from untreated control.

The leachates were non-cytotoxic in the alamarBlue® assay (Appendix 1) and, therefore, soluble components of the DE were not the cause of the observed cytotoxic responses, which must be particle dependent.

5.3.3 Cytokine release

Only TNF-α was produced by macrophages in concentrations greater than untreated cells following exposure to the fine-fraction samples (Figure 5.4, data for other cytokines given in Table 5.2). DE_05 (Spain, unprocessed), DE_20 and DE_24 (both Mexico, calcined) all increased TNF-α production, with DE_05 inducing the greatest TNF-α production at 125 µg/ml, which was 2.7 times greater than that

released following treatment with DQ12. For the calcined samples (DE_20, DE_24 (Mexico)), the induction of TNF-α production by treated cells was comparable to that induced by DQ12. In contrast, DE_10 (Mexico, flux-calcined) and DE_08 (USA-2, flux-calcined) did not enhance TNF-α production.

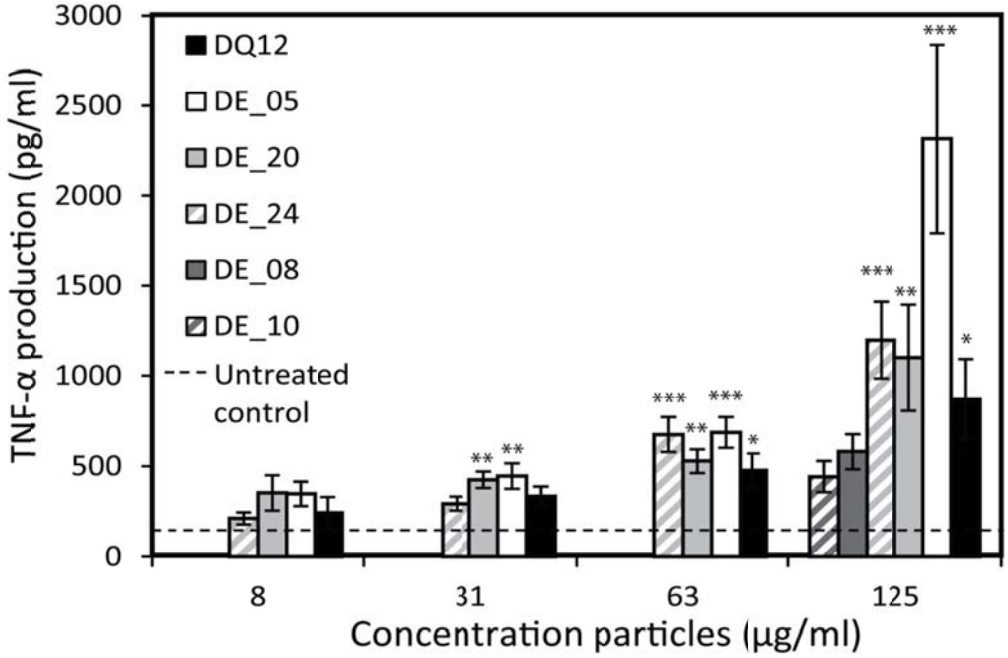

Figure 5.4: TNF-α production by macrophages exposed to the fine fractions of DE. Exposure to unprocessed (white), calcined (light grey) and flux-calcined (dark grey) DE and a positive standard (DQ12) for 24 hours. Error bars represent standard error (n=8). * p = <0.05, ** p = <0.01, *** p = <0.001 compared to untreated control.

Table 5.2: Cytokine release from J774 macrophages exposed to the separated fine fractions of DE for 24h. KC, IL-1 and IL-10 were not produced in concentrations significantly different to the negative control.

Sample *Concentration*	Cytokine release (pg/ml) KC	IL-1β	IL_10	TNF-α
DE_05				
125	0.28	1.33	0.41	2213.44
63	0.22	2.69	0.00	686.29
31	0.21	0.20	0.00	445.73
8	0.40	0.18	0.04	347.68
DE_20				
125	0.88	0.47	0.00	1100.59
63	0.22	7.54	0.64	527.63
31	0.21	9.55	0.00	424.62
8	1.08	7.82	3.79	352.96
DE_24				
125	0.26	4.96	0.21	1197.32
63	0.22	20.17	0.00	674.44
31	0.25	40.87	0.00	363.80
8	0.42	25.30	0.00	259.97
DE_08				
125	0.42	2.58	0.00	579.55
63				
31				
8				
DE_10				
125	0.75	16.56	1.90	442.05
63				
31				
8				
DQ12				
125	0.32	2.97	0.00	869.63
63	0.50	13.68	0.00	475.91
31	0.43	1.49	0.00	333.53
8				
Untreated control				
	0.27	13.65	0.07	217.03

5.3.4 Cell imaging

Imaged cells treated with the fine fractions of DE and an untreated control are shown in Figure 5.5. In the treated cells, there was some degree of frustrated phagocytosis, with instances of numerous cells attempting to phagocytise the same particle and particles not fully engulfed (Figure 5.5b-d). Qualitatively, evidence of frustrated phagocytosis was more abundant in cells treated with calcined or unprocessed samples, compared to flux-calcined samples, but were observed in all cases.

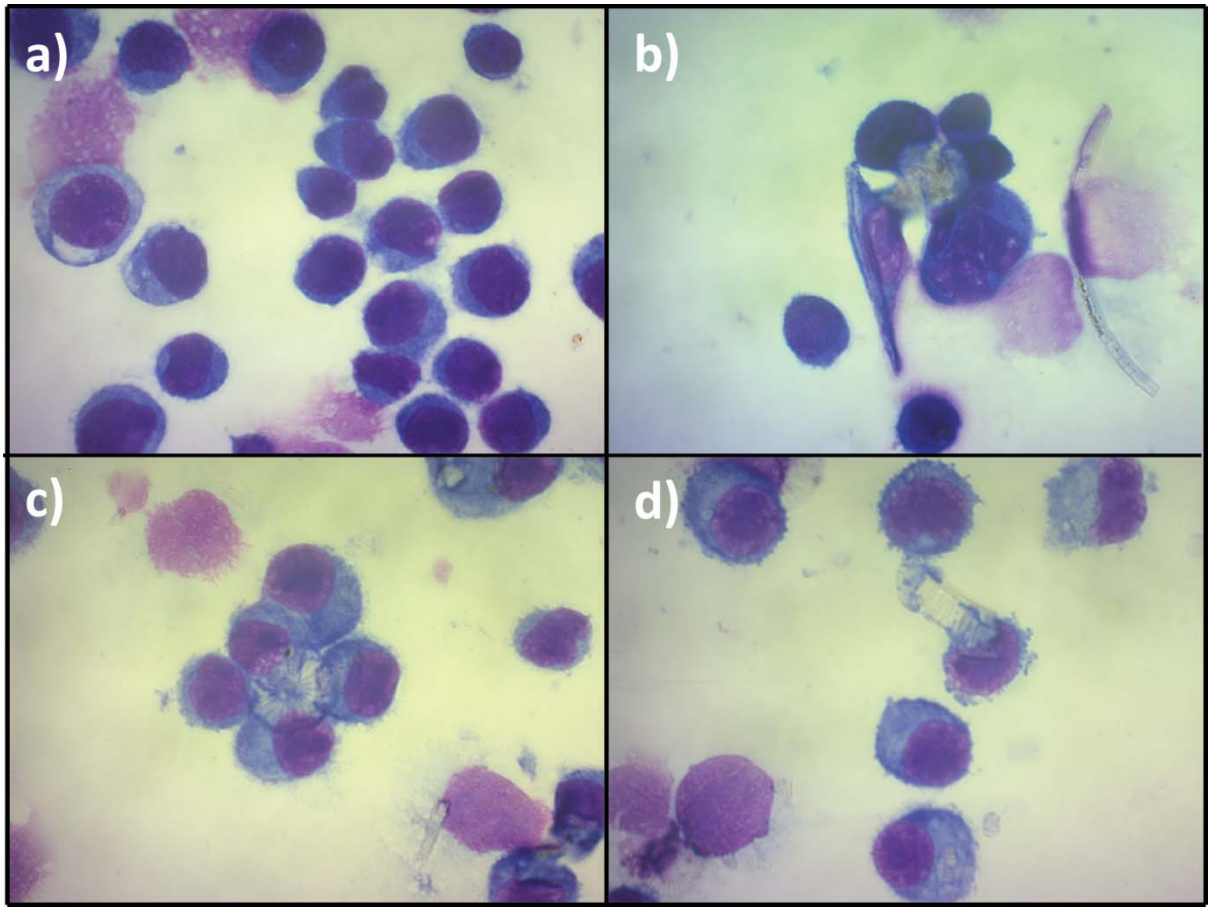

Figure 5.5: Frustrated phagocytosis in macrophages treated with DE. Light microscopy image of **a)** untreated macrophages, and **b-d)** macrophages treated with DE showing indicators of frustrated phagocytosis where a number of cells tried to phagocytise the same particle **(c-d)**, or particles were not fully engulfed **(b)**. Image **b)** is of DE_20-treated cells, and images **c-d)** are of DE_24-treated cells, as the best examples of frustrated phagocytosis. However, frustrated phagocytosis, as well as fully engulfed particles were seen in all samples (see Appendix 2 for catalogue of images).

5.3.5 Free radical release

$HO^{\bullet}$ radicals were produced by all samples tested but varied in amount, as determined by the intensity of the signal (Figures 5.6-5.8). In both unprocessed and flux-calcined Spanish DE (DE_11 and DE_12), $HO^{\bullet}$ production was low but increased slightly overtime from 10 to 60 minutes (Figure 5.6). In the French samples, $HO^{\bullet}$ release decreased with time in all three samples (Figure 5.7). In the unprocessed sample (DE_15), $HO^{\bullet}$ production was barely measureable at 10 minutes and was not detected at 60 minutes (Figure 5.7a). Calcined (DE_16) and flux-calcined (DE_14) French samples produced much larger amounts (Figure 5.7b-c). Calcined samples from USA-1 (DE_22) and Mexico (DE_24) produced slightly less $HO^{\bullet}$ than the French calcined sample (DE_16) at 10 minutes, but $HO^{\bullet}$ levels were maintained over the 60 minutes (Figure 5.8a-b). DE_10, a flux-calcined, Mexican sample caused the highest production of $HO^{\bullet}$ of all the samples, which decreased over time (Figure 5.8c).

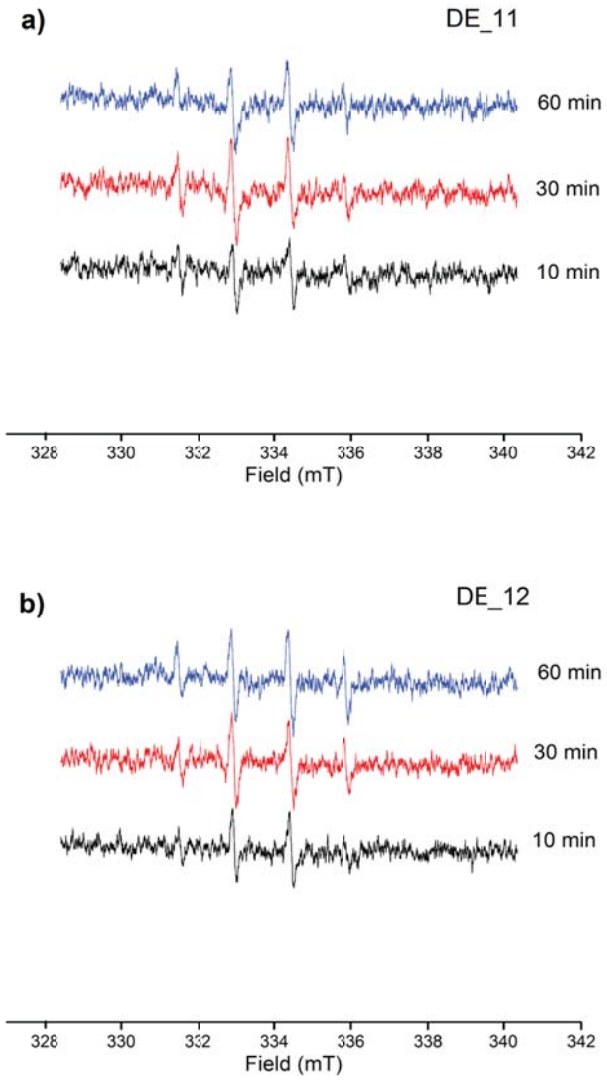

Figure 5.6: $HO^{\bullet}$ release after 10, 30 and 60 minutes exposure to H_2O_2 from **a)** unprocessed (DE_11) and **b)** flux-calcined (DE_12) Spanish DE.

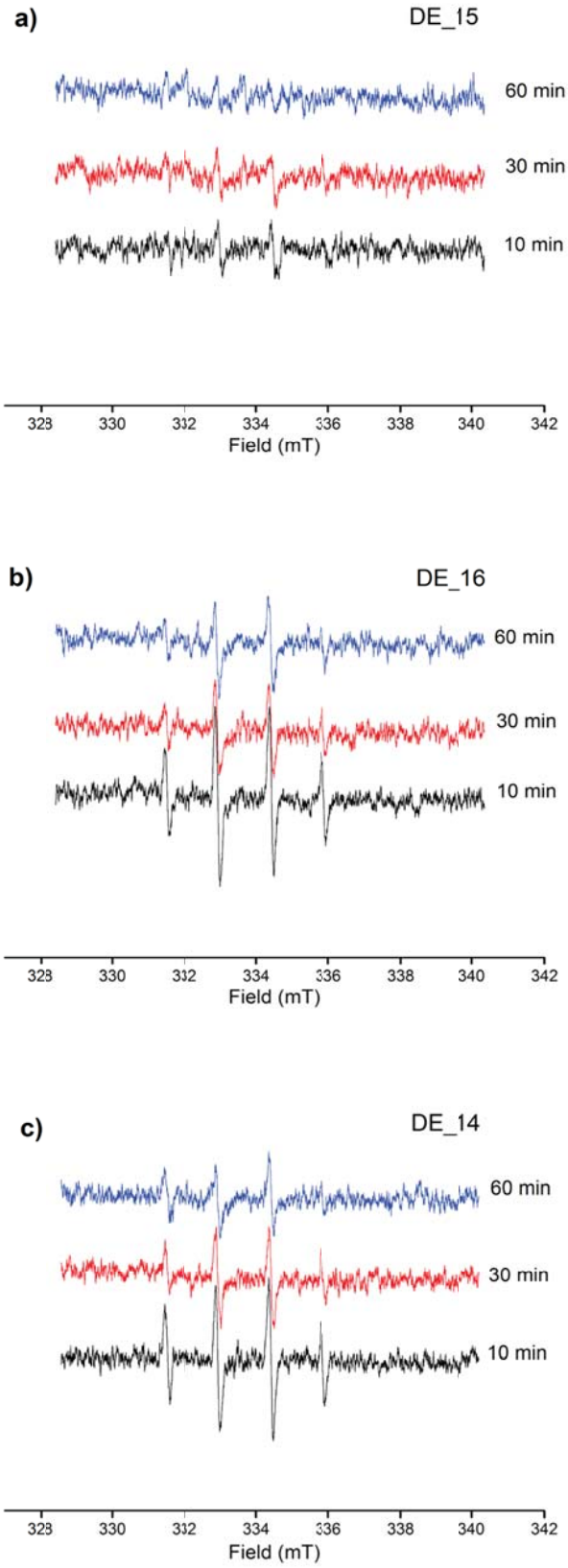

Figure 5.7: $HO^{\bullet}$ release after 10, 30 and 60 minutes exposure to H_2O_2 from **a)** unprocessed (DE_15), **b)** calcined (DE_16) and **c)** flux-calcined (DE_14) French DE.

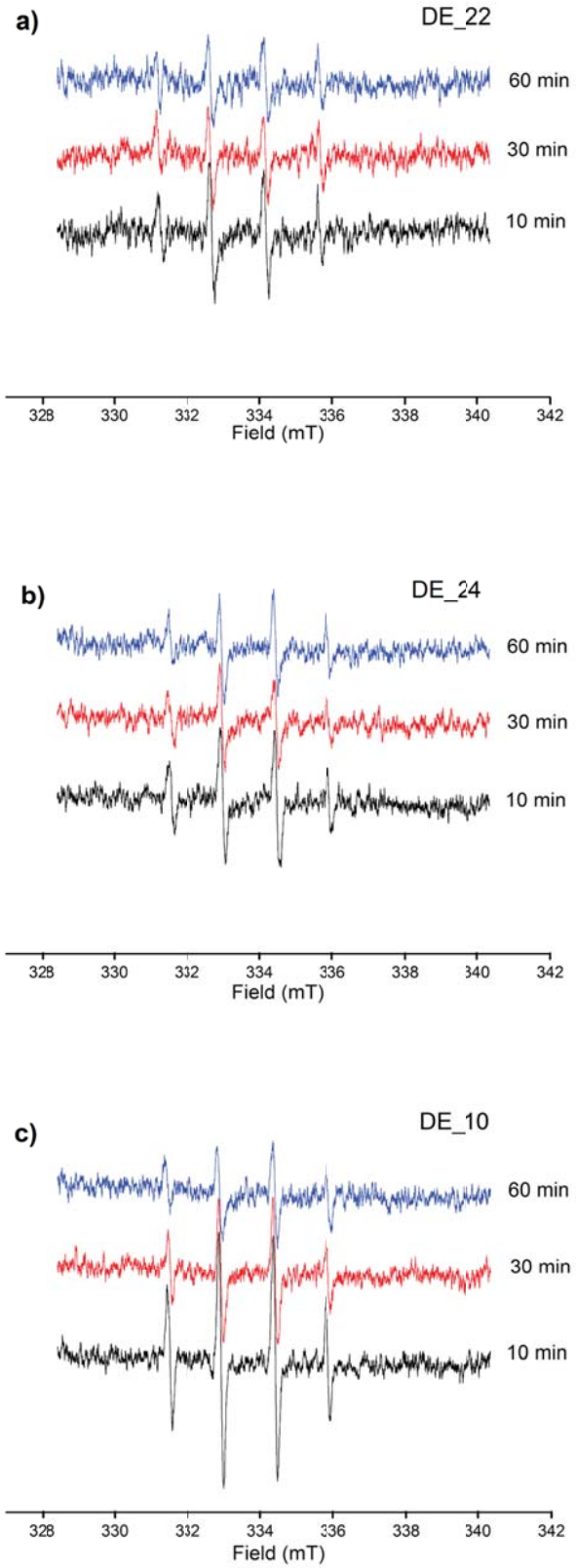

Figure 5.8: $HO^{\bullet}$ release after 10, 30 and 60 minutes exposure to H_2O_2 from **a)** calcined DE from USA-1 (DE_22), **b)** calcined DE from Mexico (DE_24), and **c)** flux-calcined DE from Mexico (DE_10).

5.4 Discussion

5.4.1 The variability of diatomaceous earth toxicity

Previous studies of DE toxicity insufficiently constrain the respiratory hazard posed by exposure to DE deposits worldwide: epidemiology studies have mainly focussed on DE workers in a single location (California) (e.g. Checkoway et al., 1993, Harber et al., 1998, Hughes et al., 1998, Park et al., 2002, Rice et al., 2001, Seixas et al., 1997), and are unable to distinguish between exposure to unprocessed or processed DE, while toxicology studies rarely state the sample source and investigate few samples. Therefore, variability among deposits and processing techniques has not been fully considered. Here, we show that DE is not a single entity, with a toxic potential that ranges from unreactive to as haemolytic or cytotoxic as the positive standard α-quartz (DQ12).

Unprocessed samples from Spain (DE_05 and DE_11) were haemolytic and induced significant cytotoxicity to macrophages. Furthermore, DE_05 induced a large increase in TNF-α release from treated macrophages relative to processed samples, indicating the potential for unprocessed DE to incite inflammation if inhaled. However, unprocessed samples from France did not induce any measurable haemolysis or cytotoxicity, suggesting that the potential toxicity of DE can vary substantially by deposit source.

Flux-calcined samples all displayed low haemolytic potential, cytotoxicity and cytokine release from treated cells. This suggests that short-term exposure to flux-calcined samples may not result in toxicity or an inflammatory response. There was no variation in the reactivity of flux-calcined samples from different locations, suggesting that flux-calcination is key to dampening the adverse effects attributed to DE. This is likely due to alteration of the physicochemical properties of DE during flux-calcination and is discussed in detail below.

DE_22 from USA-1 was the only calcined sample that elicited a haemolytic response and was also one of the most cytotoxic samples analysed. This introduces the possibility that data in epidemiological studies from this location may not be representative of likely disease outcomes worldwide. However, other calcined samples from USA-1 were non-haemolytic, emphasising the variable reactivity that exists amongst samples from a single deposit source. Calcined samples from Mexico were cytotoxic but not haemolytic. The haemolysis and cytotoxicity assays assess different mechanisms of toxicity. Therefore, that some samples are highly active in both assays yet others are cytotoxic but not haemolytic, suggests samples from different locations may cause toxicity by different mechanistic pathways.

5.4.2 Factors affecting the potential toxicity of DE

As DE is a natural, heterogeneous dust there are a number of factors which may influence its toxicity including chemistry, mineralogy, surface reactivity, surface area and particle size and shape. All of these variables were shown to differ substantially among the samples in Chapter 4 (and Table 5.1). As the potential toxicity of DE has also been shown to differ among different samples, any causal relationships between these characteristics and DE reactivity *in vitro* are assessed here. These variables and, in particular, the presence of impurities, may also alter the toxicity of crystalline silica (see Chapter 2), therefore, their effect on the reactivity of the cristobalite in these samples (Chapter 4) is also considered.

5.4.2.1 Presence of crystalline silica

Until now, the cause of pathogenicity related to DE exposure was assumed to be crystalline silica (e.g. Checkoway et al., 1993, Harber et al., 1998) despite existing *in vitro* toxicology studies not supporting that concept (Bye et al., 1984, Elias et al., 2006, Ghiazza et al., 2009, Hart and Hesterberg, 1998). In this study, we have shown that total crystalline silica (quartz plus cristobalite) content alone does not control the potential toxicity of DE. Figure 5.9 shows that crystalline silica content does not influence haemolysis (if anything, low crystalline silica content correlates with haemolytic activity) and cell viability is greatest at highest crystalline silica contents.

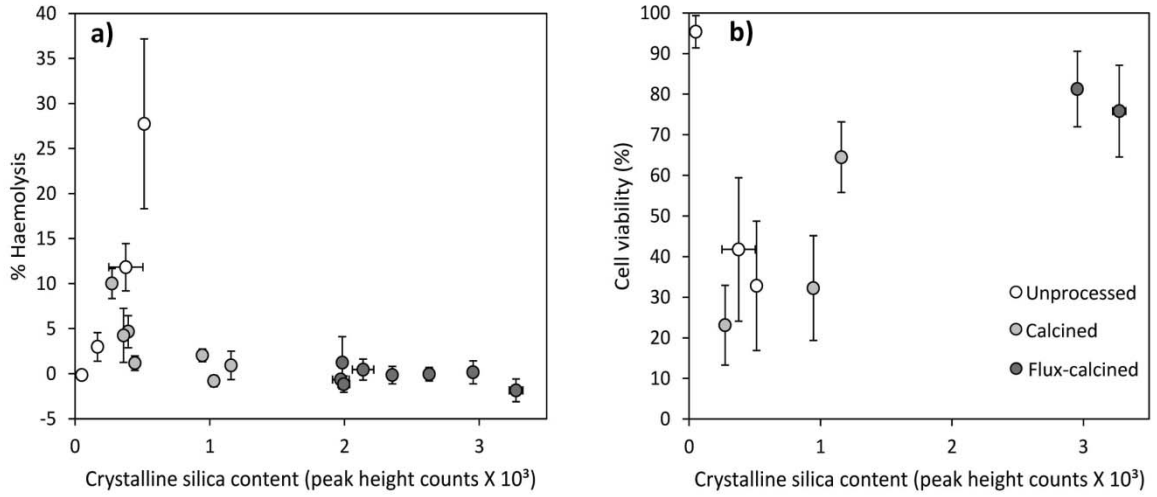

Figure 5.9: Relationship between crystalline silica content and reactivity *in vitro.* Correlation of crystalline silica content of DE (measured by the addition of cristobalite and quartz peak heights, accounting for different diffraction power using standards) with **a)** haemolysis post-exposure to 1 mg/ml bulk DE, and **b)** cell viability post-exposure to 500 µg/ml bulk DE.

The low haemolytic and cytotoxic potency of all flux-calcined samples, despite high crystalline-silica content, agrees with previous reports on discrete samples (Bye et al., 1984, Ghiazza et al., 2009, Hart and Hesterberg, 1998, Wagner et al., 1968). The lack of toxicity may be due to inherent characteristics of the crystalline silica, such as low surface area of the particles, or structural impurities, or external factors, especially the presence of other minerals, altering the crystalline silica toxicity (Chapter 2). The factors potentially affecting the crystalline silica reactivity are discussed

here. Below (in Section 5.4.2.2), the potential of some of these factors to cause toxicity in their own right is considered.

Ghiazza et al. (2009) suggested that the low toxicity of crystalline silica-rich flux-calcined DE was due to the formation of a vitreous rim during flux-calcination, which obscured cell exposure to cristobalite in these samples. No vitreous rim, per se, was observed in this study but the cristobalite is partly occluded, occurring in patches within the otherwise amorphous particles, resulting in a variable percentage of cristobalite at the particle surface (Chapter 4). The low surface areas of cristobalite-rich, flux-calcined samples (Table 4.2, Chapter 4) means even if cristobalite accounted for a large per cent of the surface of the particles, overall exposure of cells to crystalline silica may be reduced compared to calcined samples with larger surface areas. This may account for the lack of correlation between crystalline silica content and toxicity. The hosting of crystalline silica within heterogeneous particles has previously been suggested to explain variations in the toxic potential of quartz-rich coal dusts (Donaldson and Borm, 1998, Tourmann and Kaufmann, 1994), and to mask the toxicity of cristobalite in volcanic ash (Horwell et al., 2012). Here, exposure times for the cytotoxicity assays were short (24 hours), and the amorphous matrix may have low bio-durability, thereby exposing more cristobalite at the surface of the particle over time. Therefore, future, longer exposures and *in vivo* experiments may be necessary.

Coating of the crystalline silica by other crystalline minerals was not commonly observed by SEM and it is not likely these phases physically mask crystalline silica toxicity. However, as some of these minerals (clays and calcite especially) were broken down during calcination, reaction of ion impurities with the silica surface could act to dampen its toxicity. Impurity content directly on the surface of the crystalline silica particles could not be measured but cation substitutions were seen in the cristobalite structure (Chapter 4). As structural impurities have been hypothesised to decrease the toxic potential of cristobalite in volcanic ash (Horwell et al., 2012) it is possible these structural

impurities dampen the toxicity of the cristobalite in DE. The total quantity of Na+Al+Ca+Fe impurities ranged from 0 to 13 oxide wt.% in cristobalite in DE (mainly flux-calcined samples analysed due to high cristobalite contents (Chapter 4)) but did not differ by the location (Spain, France, Mexico, USA-2). However, the amount of individual elements did (see Chapter 4): in flux-calcined DE, cristobalite was enriched in Al in Mexican samples, whereas cristobalite in French DE was enriched in Fe and Spanish DE cristobalite was enriched in Ca.

As the flux-calcined samples from different locations were all non-reactive in the haemolysis and cytotoxicity assays, it is possible that all structural impurities (Al, Na, Fe and Ca) have the potential to dampen crystalline silica toxicity, and there is potential evidence of this in the literature. The effect of Al treatment on quartz toxicity is well established: treating quartz with aluminium salts or clay extracts has been shown to reduce its toxicity and haemolytic potential (Cullen et al., 1997, Duffin et al., 2001, Nolan et al., 1981, Stone et al., 2004), and quartz in coal with clay mineral impurities had lower toxicity than pure, coal-sourced quartz (Tourmann and Kaufmann, 1994) (see Chapter 2). The effect of Fe on crystalline silica toxicity is still poorly constrained: treating quartz with ferric or ferrous iron does not change its toxic potency *in vivo* (Cullen et al., 1997) and can decrease its haemolytic potential (Nolan et al., 1981). However, Fubini et al. (1995) showed iron can increase silica toxicity via production of free radicals. Therefore, the role of iron in determining DE crystalline silica toxicity remains unclear but the role of Fe and available Fe in DE toxicity overall is discussed in detail below. Ca can dampen coalmine dust toxicity, possibly by reaction with crystalline silica in the coal dust (Aladdin et al., 2013), however, studies addressing the effect of Ca on crystalline silica are limited. The effect of these impurities when they are incorporated as structural impurities is not constrained. The ability of structural impurities (alone) to alter cristobalite toxicity is addressed in Chapter 7, although only Al and Na impurities are considered and further work would be required to consider the effect of Fe or Ca substitutions.

It is possible that structural impurities play a role in dampening crystalline silica toxicity, however, given that some calcined samples elicited cytotoxicity (DE_22, DE_24, DE_20) and haemolysis (DE_22) and also contained structural impurities in the cristobalite (although only based on 18 particles), it is clear that the presence of structural impurities are not the only controlling factor on DE toxicity.

5.4.2.2 Reactivity of contaminant phases

Some samples with little to no crystalline silica were highly reactive, indicating that some other factor is, at least in part, controlling the *in vitro* response. Contaminant phases, such as clays and calcite, are therefore considered here.

The presence of calcite could explain the high reactivity of Spanish unprocessed samples; Aladdin et al. (2013) have shown exposure to calcite alone caused inflammation in mice, indicated by an increase in Il-1α and Il-1β gene expression, and Diler and Ergene (2010) showed that micronuclei and nuclei abnormalities were more common in calcite factory workers than control groups. That Il-1β production was not elevated in cells treated with DE_05 (a high calcite sample), suggests the same mechanisms of toxicity are not occurring here, suggesting other components are causing the observed toxicity. However, the use of *in vitro* rather than animal studies means these studies are not directly comparable. The calcite standard was non-reactive in both the haemolysis and alamarBlue® assays, supporting the hypothesis that calcite content alone is not responsible for the different reactivity of Spanish unprocessed and flux-calcined DE. However, the toxicity of calcite is poorly defined and it is not known if the calcite present in the DE could differ in reactivity to the calcite standard or react with other components of the DE mixed dust. Aladdin et al. (2013) showed that, although calcite alone could cause inflammation, treatment of coal dust with calcite decreased its inflammatory potential by neutralising acidity and decreasing bioavailable Fe.

The presence of clays may also have an effect, as some clays have been shown to be more haemolytic than crystalline silica (Oscarson et al., 1986, Vallyathan et al., 1988). However, the lack of clay in processed DE samples and the low reactivity of French, unprocessed samples, suggests that clay minerals are not the cause of DE induced toxicity. The effect of Al-rich phases (predominantly clay minerals) on toxicity is considered by a correlation of bulk Al_2O_3 content and DE haemolytic potential and cell viability (Figure 5.10). No relationship was observed between bulk Al content and reactivity *in vitro*.

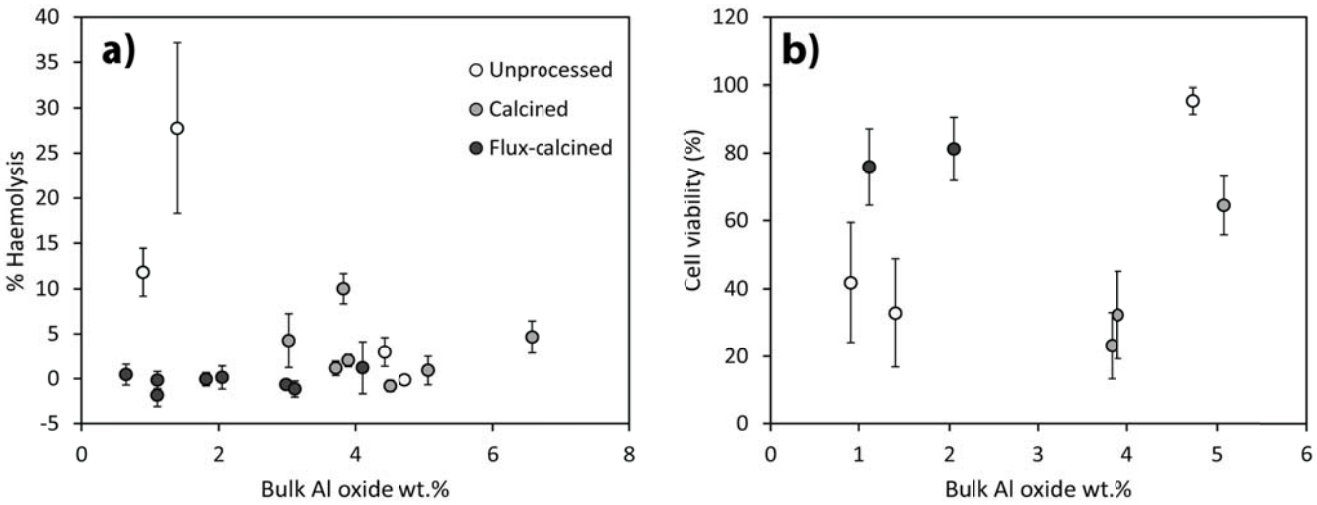

Figure 5.10: Correlation between bulk Al oxide content and **a)** haemolysis post-exposure to 1 mg/ml bulk DE, and **b)** cell viability post-exposure to 500 µg/ml bulk DE.

Iron has been hypothesised as a source for free radical generation in DE (Elias et al., 2006), and was measured in quantities of up to 4 oxide wt.% here in the bulk DE, and therefore could be contributing to the toxicity. However, bulk iron content, total Fe release and Fe^{2+} release did not correlate with either haemolysis (Figure 5.11a and c), cytotoxicity (Figure 5.11b and d) or $HO^{\bullet}$ release. DE_15 (French, unprocessed) had the highest total Fe and Fe^{2+} release but was non-haemolytic, non-cytotoxic and $HO^{\bullet}$ generation was barely detectible. Calcined samples all contained

iron-rich phases (Chapter 4) but had variable toxicity, suggesting Fe does not control the reactivity of these samples. Also, previous studies have shown ferric and ferrous oxides to have low cytotoxicity (Karlsson et al., 2009), although exposure to ultrafine iron oxide particles has been shown to lead to oxidative stress and a pro-inflammatory response in rats (Zhou et al., 2003, Zhu et al., 2008). Soluble iron oxide has also been shown to be cytotoxic to human mesothelioma MSTO-211H cells (Brunner et al., 2006). However, as soluble components of the DE were non-cytotoxic, this is unlikely to be the case here. Fe^{2+} can produce $HO^{\bullet}$ via Fenton chemistry (see Chapter 2 (Castranova et al., 1997)) and the removal of Fe by acid treatment has been shown to decrease the production of $HO^{\bullet}$ by silica (Daniel et al., 1995). However, Fe^{2+} or total Fe release did not correlate with $HO^{\bullet}$ production here. Fe^{3+} can be reduced to Fe^{2+} in the presence of H_2O_2, and only trace quantities of Fe^{2+} are needed for Fenton chemistry, as this reaction is catalytic. Therefore, it is not surprising that the quantity of available Fe^{2+} or total Fe is not directly correlated with $HO^{\bullet}$ production.

Amorphous silica is generally perceived as less toxic than crystalline silica (Donaldson and Borm, 1998) but can be reactive *in vitro* (Costantini et al., 2011, Pavan et al., 2013). The ability of amorphous, unprocessed DE to elicit a haemolytic or cytotoxic response, or induce abnormal nuclei growth *in vitro* (Adamis et al., 2000, Bye et al., 1984, Hart and Hesterberg, 1998), and cause fibrosis *in vivo* (Pratt, 1983), has also previously been demonstrated. Unprocessed samples from Spain, the most haemolytic of all samples, were predominantly amorphous. The cytotoxic (DE_20, DE_22 and DE_24) and haemolytic (DE_22) calcined samples also contained a substantial amount of amorphous material. It is possible that the amorphous phases of these samples are linked to their toxicity, as certain vitreous silicas have been shown to be more haemolytic than quartz (Pavan et al., 2013). However, the lack of haemolysis caused by French, unprocessed samples, which were also predominantly amorphous, means that amorphous material is unlikely the predominant control on the observed toxicity. The high levels of impurities in processed amorphous material in DE particles

(Chapter 4) may also play a role in their biological reactivity, but further work is needed to determine this.

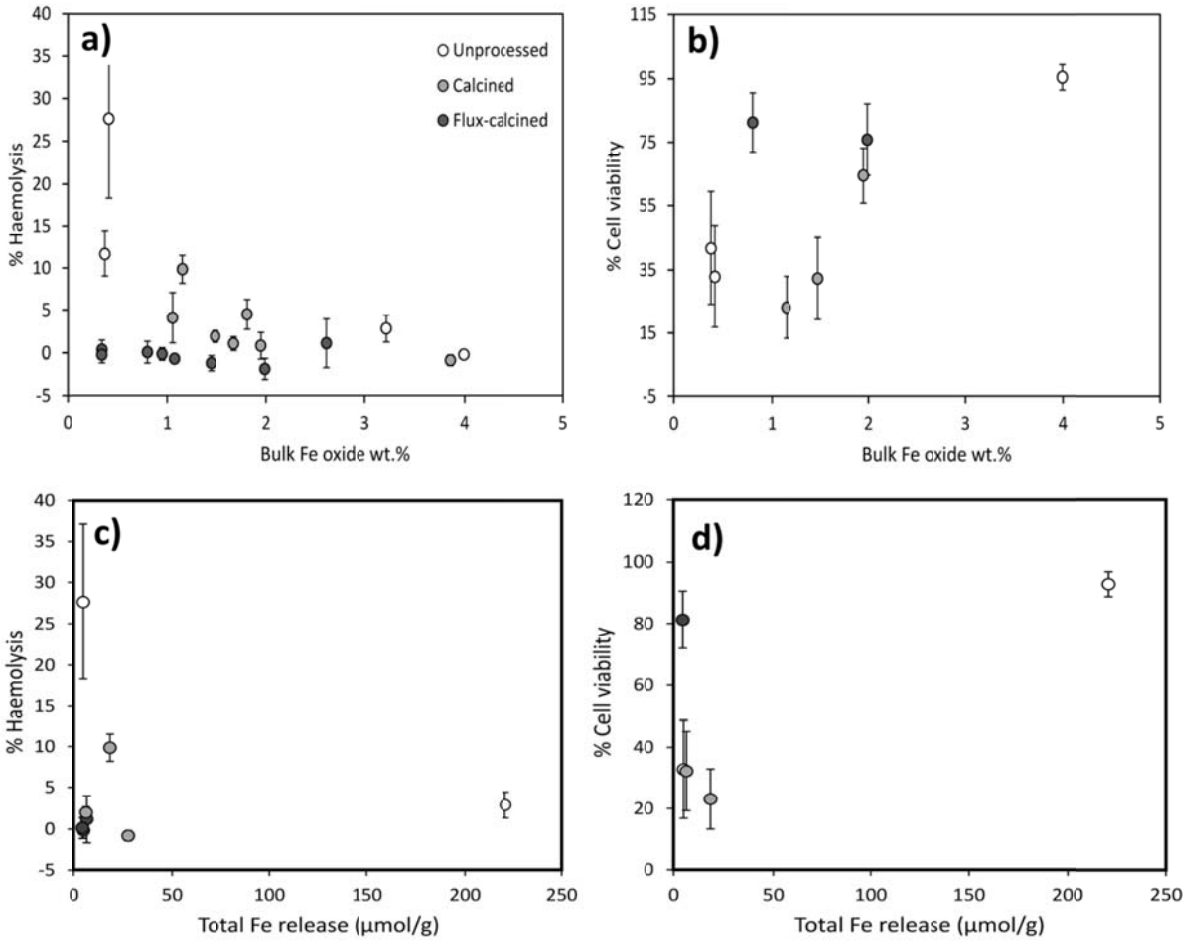

Figure 5.11: Relationships between bulk and available Fe and *in vitro* reactivity of DE. Correlation between bulk iron oxide content and **a)** haemolysis post-exposure to 1 mg/ml bulk DE, and **b)** cell viability post-exposure to 500 µg/ml bulk DE; and correlations between total Fe release from the particle surface and **c)** haemolysis post-exposure to 1 mg/ml bulk DE, and **d)** cell viability post-exposure to 500 µg/ml bulk DE.

5.4.2.3 Surface reactivity

The importance of silanol populations in determining silica toxicity is well known (see Chapter 2). Silanol groups are involved in the haemolytic potency of crystalline silica (Hemenway et al., 1993,

Pandurangi et al., 1990, Pavan et al., 2013), and conversion of silanols to siloxanes upon heating, causing an increasingly hydrophobic surface (Fubini et al., 1995), has been shown to decrease the cytotoxicity of cristobalite (Fubini et al., 1999). Although surface features were difficult to identify by IR, the ability of H-bonded or interacting silanols to exchange with D_2O indicated that DE_11 (Spanish, unprocessed DE) and DE_24 (Mexican, calcined DE) had unreactive surfaces, whereas DE_15 (French, unprocessed DE) had exchangeable sites on its surface, indicative of surface silanols free to react with cell membranes or other molecules (Chapter 4). This, however, is in disagreement with haemolysis, cytotoxicity and $HO^{\bullet}$ generation data: DE_15 was unreactive in all aspects and DE_11 was the most haemolytic and cytotoxic sample. It has recently been shown that the distribution of associated and dissociated silanols on the silica surface is important in determining haemolyis and not only the quantity of silanols (Pavan et al., 2013). However, the lack of exchangeable OH sites in the most reactive samples meant IR characterisation could not be used to assess the potential reactivity of the DE surface in a biological environment.

The ability of $HO^{\bullet}$ to be produced by the DE surface was not related to the haemolytic potential nor cytotoxicity of the samples. DE_10, a flux-calcined Mexican sample, caused the greatest $HO^{\bullet}$ generation of samples tested, but was non-haemolytic and non-cytotoxic. Other flux-calcined samples (DE_12, DE_14), which were non-reactive *in vitro*, also generated $HO^{\bullet}$. This lack of correlation between $HO^{\bullet}$ production and cytotoxicity has been seen previously for DE, and it is suggested that Fe impurities at the surface may cause $HO^{\bullet}$ production, whereas silanol distribution is important for cytotoxicity (Elias et al., 2006).

Elias et al. (2006) have shown the ability of unprocessed DE to produce $HO^{\bullet}$. $HO^{\bullet}$ generation increases dramatically upon heating of the sample to 900 or 1200 °C. This suggests a transformation of surface sites on the amorphous DE to active sites upon crystallisation, increasing the ability to generate $HO^{\bullet}$ radicals. This is in agreement with the French samples here, where calcination and

flux-calcination caused a dramatic increase in $HO^{\bullet}$ production (Figure 5.7). However, flux-calcination did not increase $HO^{\bullet}$ production from Spanish samples (Figure 5.6). A correlation between $HO^{\bullet}$ production and the morphological transforming potency (a possible indicator of tumorigenicity) of silica dusts (including one DE sample) has been reported (Elias et al., 2006, Fubini et al., 2001). However, the ability of DE to induce transformation in cells and its genotoxic potency should be extended to cover a wider range of samples from different locations and processes, as both unprocessed and flux-calcined DE have been shown to cause abnormal nucleic growth, which is not correlated to, and therefore cannot be induced from, their cytotoxic potential (Hart and Hesterberg, 1998).

5.4.2.4 Physical properties

Particle surface area has been related to pro-inflammatory responses *in vitro* (Duffin et al., 2002, Duffin et al., 2007), and the surface area of processed DE may be a key factor controlling toxicity. A positive correlation between bulk surface area of processed samples (calcined and flux-calcined) and haemolysis was observed (Figure 5.12a) and a corresponding negative correlation with cell viability (Figure 5.12b), indicative that surface area could play a role in particle reactivity/toxicity. The correlation between surface area and haemolysis could not be extended to unprocessed samples and appears not to correlate for cell viability either (3 data points). This suggests that other parameters are at least partly responsible for their observed toxicity.

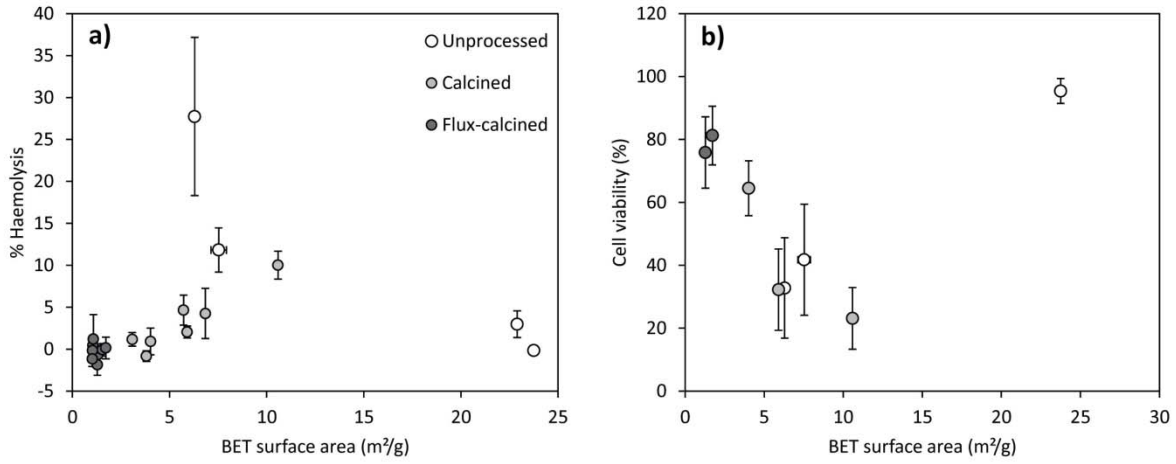

Figure 5.12: Relationship between BET surface area and DE reactivity *in vitro.* Correlation between surface area and **a)** haemolysis post-exposure to 1 mg/ml bulk DE, and **b)** cell viability post-exposure to 500 µg/ml bulk DE.

In flux-calcined samples, up to 27% of particles were >10 µm by number % (Table 5.1), which may account for their low surface area (Table 4.1) and, accordingly, their low reactivity. The variable particle size distributions of unprocessed and calcined DE could not be correlated to their haemolytic potential (Figure 5.13a). A possible negative correlation was observed between cell viability and cumulative vol.% of particles <10 µm and < 4 µm (Figure 5.13b and d), indicating that increased fine material can cause increased cytotoxicity, as expected (Chapter 2). This, however, is in disagreement with Hart and Hesterberg (1998), who suggest particles >7.5 µm determine DE toxicity.

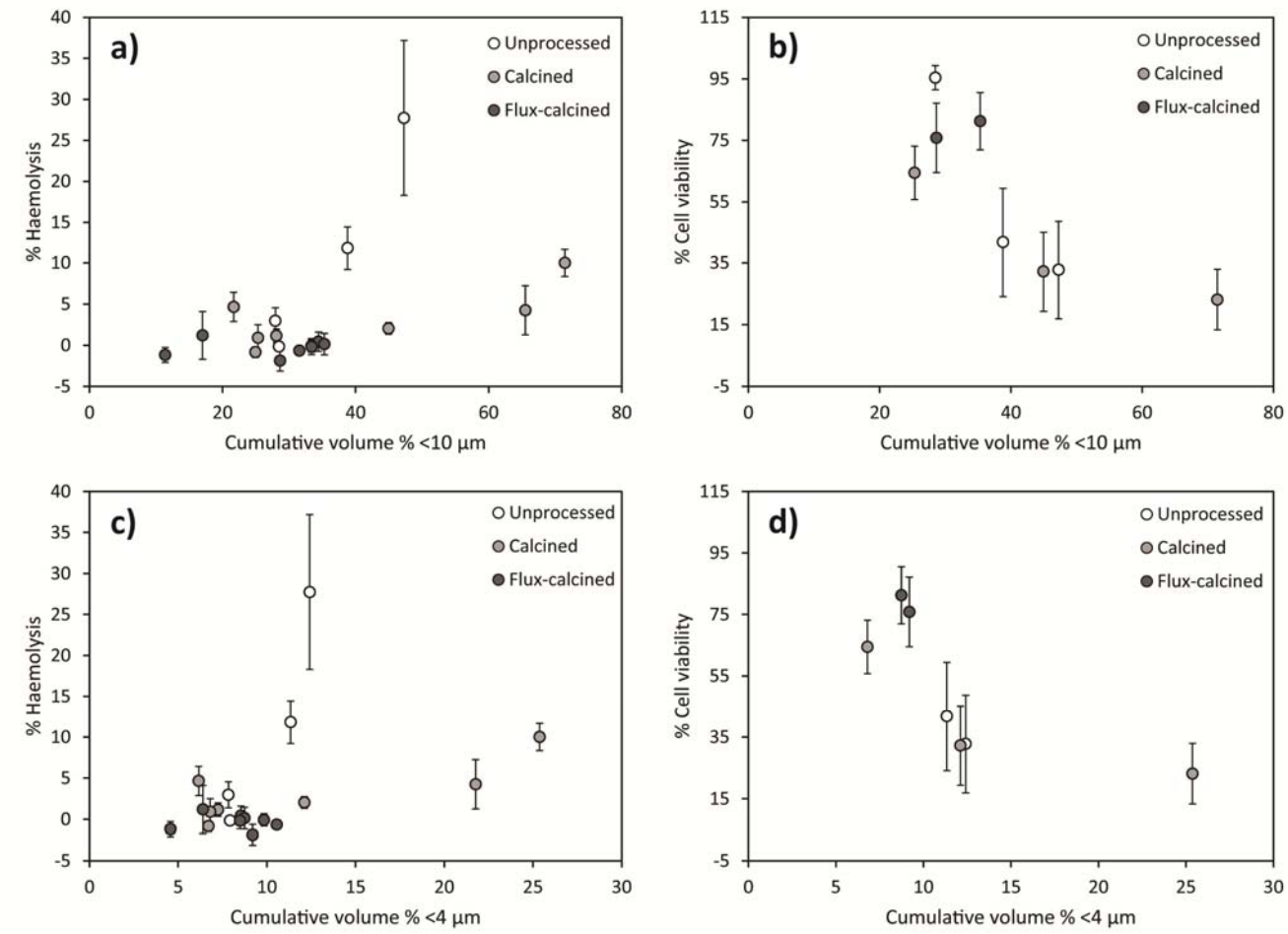

Figure 5.13: Relationship between particle size and DE reactivity *in vitro.* Correlation between cumulative volume % particle size <10 µm and **a)** haemolysis post-exposure to 1 mg/ml bulk DE, and **b)** cell viability post-exposure to 500 µg/ml bulk DE, and between cumulative volume % <4 µm **c)** haemolysis, and **b)** cell viability.

Fibres can cause frustrated phagocytosis, where macrophages struggle to fully engulf particles (Schinwald and Donaldson, 2012). Fibre-like particles, up to 21%, in calcined and unprocessed samples (Table 5.1), were mainly in the form of diatom 'rinds' or small fragments of diatoms (Chapter 4). The lower abundance in flux-calcined samples is likely due to sintering of fragments into large agglomerates and may explain their low cytotoxicity compared to the calcined and unprocessed samples. Previously, DE containing fibre-like particles (aspect ratio >3) was shown to be more potent *in vitro* than 'non-fibrous' DE (Chamberlain et al., 1982), suggesting that particle

morphology could play a role in the observed cytotoxicity, although this paper did not express what percentage of the DE was fibre-like. Particle morphology is important in phagocytosis (Champion and Mitragotri, 2006) and, here, frustrated phagocytosis was observed and some fibre-like particles were not phagocytosed. This was most evident for calcined and unprocessed samples, where TNF-α production and LDH release, potential indicators of frustrated phagocytosis (Ye et al., 1999), were also elevated above flux-calcined samples. Frustrated phagocytosis was also observed as a number of cells attempted to engulf larger, disc-shaped diatoms. This was observed after treatment of cells with all of the fine fraction samples, suggesting that large disc-shaped particles may play a role in DE toxicity, as platelets have been recently identified as a novel respiratory hazard (Schinwald et al., 2012), and DE particles with at least one diameter >7.5 μm have previously been suggested to determine DE toxicity (Hart and Hesterberg, 1998). The number of fibres was less able to explain differences in particle toxicity, therefore, it is possible that the parameter of particle diameter >7.5 μm accounts for both fibres and large disc-shaped diatoms that can increase DE toxicity. However, this was not discussed (Hart and Hesterberg, 1998).

5.5 Conclusions

This study, the first to systematically characterise the physicochemical properties and potential toxicity of a range of globally sourced DE samples, shows that the toxic potential of DE varies by processing technique and source. Flux-calcined samples were non haemolytic and non-cytotoxic, whereas unprocessed and calcined DE had variable reactivity in these assays. However, all samples had the ability to produce $HO^{\bullet}$, where flux-calcined samples were highly reactive. As $HO^{\bullet}$ generation has previously been shown to correlate with genotoxicity for DE treated cells (Elias et al., 2006), further investigation into sublethal, genotoxic effects of these samples should be performed.

No correlation was observed between crystalline silica content and DE's potential toxicity, despite previously being implicated in epidemiological studies of DE exposure. The dearth of crystalline silica at the particle surface, due to its crystallisation within an amorphous matrix, its presence in a heterogeneous dust, and impurities within the crystalline silica, likely reduce the potential reactivity of these crystalline silica-bearing particles. The ability of structural and external impurities to alter cristobalite toxicity is assessed in Chapter 7.

It is likely that a number of physicochemical properties play a role in DE toxicity. Calcium-rich phases may be important in the toxicity of some unprocessed samples, and amorphous phases may be involved in calcined DE toxicity. Surface area, especially, was positively correlated to calcined and flux-calcined DE reactivity here, and the importance of surface reactivity and the unique particle morphologies of DE merits further investigation.

Although no single physicochemical property of DE considered here could be linked to its potential toxicity, a clear outcome of this study is that the crystalline silica content, alone, should not be used to determine the DE hazard, nor should it be assumed that it is the cause of disease observed in epidemiological or clinical studies without further investigation.

References

ADAMIS, Z., TÁTRAI, E., HONMA, K., SIX, É. & UNGVÁRY, G. 2000. In Vitro and in Vivo Tests for Determination of the Pathogenicity of Quartz, Diatomaceous Earth, Mordenite and Clinoptilolite. *Annals of Occupational Hygiene,* 44**,** 67-74.

ALADDIN, M., JIAN, J., YANG, Q., CHEN, L.-C., FINKELMAN, R. B. & HUANG, X. 2013. Laboratory studies of the impact of calcite on in vitro and in vivo effects of coal dust: A potential preventive agent for coal workers' pneumoconiosis? *American Journal of Industrial Medicine,* 56**,** 292-299.

BRUNNER, T. J., WICK, P., MANSER, P., SPOHN, P., GRASS, R. N., LIMBACH, L. K., BRUININK, A. & STARK, W. J. 2006. In Vitro Cytotoxicity of Oxide Nanoparticles: Comparison to Asbestos, Silica, and the Effect of Particle Solubility†. *Environmental Science & Technology,* 40**,** 4374-4381.

BYE, E., DAVIES, R., GRIFFITHS, D. M., GYLSETH, B. & MONCRIEFF, C. B. 1984. In vitro cytotoxicity and quantitative silica analysis of diatomaceous earth products. *British Journal of Industrial Medicine,* 41**,** 228-234.

CASTRANOVA, V., VALLYATHAN, V., RAMSEY, D. M., MCLAURIN, J. L., PACK, D., LEONARD, S., BARGER, M. W., MA, J. Y., DALAL, N. S. & TEASS, A. 1997. Augmentation of pulmonary reactions to quartz inhalation by trace amounts of iron-containing particles. *Environmental Health Perspectives,* 105**,** 1319-1324.

CHAMBERLAIN, M., DAVIES, R., BROWN, R. C. & GRIFFITHS, D. M. 1982. In Vitro Tests For The Pathogenicity of Mineral Dusts. *Annals of Occupational Hygiene,* 26**,** 583-592.

CHAMPION, J. A. & MITRAGOTRI, S. 2006. Role of target geometry in phagocytosis. *Proceedings of the National Academy of Sciences of the United States of America,* 103**,** 4930-4934.

CHECKOWAY, H., HEYER, N. J., DEMERS, P. A. & BRESLOW, N. E. 1993. Mortality among workers in the diatomaceous earth industry. *British Journal of Industrial Medicine,* 50**,** 586-597.

COOPER, W. C. & SARGENT, E. N. 1984. A 26-Year Radiographic Follow-Up of Workers in a Diatomite Mine and Mill. *Journal of Occupational and Environmental Medicine,* 26**,** 456-460.

COSTANTINI, L. M., GILBERTI, R. M. & KNECHT, D. A. 2011. The phagocytosis and toxicity of amorphous silica. *PLoS One,* 6**,** e14647.

CULLEN, R. T., VALLYATHAN, V., HAGEN, S. & DONALDSON, K. 1997. Protection by Iron Against the Toxic Effects of Quartz. *Annals of Occupational Hygiene,* 41**,** 420-425.

DANIEL, L. N., MAO, Y., WANG, T. C. L., MARKEY, C. J., MARKEY, S. P., SHI, X. L. & SAFFIOTTI, U. 1995. DNA Strand Breakage, Thymine Glycol Production, and Hydroxyl Radical Generation Induced by Different Samples of Crystalline Silica in Vitro. *Environmental Research,* 71**,** 60-73.

DILER, S. B. & ERGENE, S. 2010. Nuclear anomalies in the buccal cells of calcite factory workers. *Genet Mol Biol,* 33**,** 374-8.

DONALDSON, K. & BORM, P. J. A. 1998. The Quartz Hazard: A Variable Entity. *Annals of Occupational Hygiene,* 42**,** 287-294.

DUFFIN, R., GILMOUR, P. S., SCHINS, R. P. F., CLOUTER, A., GUY, K., BROWN, D. M., MACNEE, W., BORM, P. J., DONALDSON, K. & STONE, V. 2001. Aluminium Lactate Treatment of DQ12 Quartz Inhibits Its Ability to Cause Inflammation, Chemokine Expression, and Nuclear Factor-κB Activation. *Toxicology and Applied Pharmacology,* 176**,** 10-17.

DUFFIN, R., TRAN, C. L., CLOUTER, A., BROWN, D. M., MACNEE, W., STONE, V. & DONALDSON, K. 2002. The Importance of Surface Area and Specific Reactivity in the Acute Pulmonary Inflammatory Response to Particles. *Annals of Occupational Hygiene,* 46**,** 242-245.

DUFFIN, R., TRAN, L., BROWN, D., STONE, V. & DONALDSON, K. 2007. Proinflammogenic effects of low-toxicity and metal nanoparticles in vivo and in vitro: highlighting the role of particle surface area and surface reactivity. *Inhal Toxicol,* 19**,** 849-56.

DUTRA, F. R. 1965. Diatomaceous earth pneumoconiosis. *Archives of environmental health,* 11**,** 613-619.

ELIAS, Z., POIROT, O., FENOGLIO, I., GHIAZZA, M., DANIÈRE, M. C., TERZETTI, F., DARNE, C., COULAIS, C., MATEKOVITS, I. & FUBINI, B. 2006. Surface Reactivity, Cytotoxic, and Morphological Transforming Effects of Diatomaceous Earth Products in Syrian Hamster Embryo Cells. *Toxicological Sciences,* 91**,** 510-520.

FUBINI, B., BOLIS, V., CAVENAGO, A. & VOLANTE, M. 1995. Physicochemical properties of crystalline silica dusts and their possible implication in various biological responses. *Scandinavian Journal of Work, Environment and Health,* 21 suppl 2**,** 9-14.

FUBINI, B., FENOGLIO, I., ELIAS, Z. & POIROT, O. 2001. Variability of biological responses to silicas: effect of origin, crystallinity, and state of surface on generation of reactive oxygen species and morphological transformation of mammalian cells. *J Environ Pathol Toxicol Oncol,* 20 Suppl 1**,** 95-108.

FUBINI, B., ZANETTI, G., ALTILIA, S., TIOZZO, R., LISON, D. & SAFFIOTTI, U. 1999. Relationship between Surface Properties and Cellular Responses to Crystalline Silica: Studies with Heat-Treated Cristobalite. *Chemical Research in Toxicology,* 12**,** 737-745.

GHIAZZA, M., GAZZANO, E., BONELLI, B., FENOGLIO, I., POLIMENI, M., GHIGO, D., GARRONE, E. & FUBINI, B. 2009. Formation of a Vitreous Phase at the Surface of Some Commercial Diatomaceous Earth Prevents the Onset of Oxidative Stress Effects. *Chemical Research in Toxicology,* 22**,** 136-145.

HARBER, P., DAHLGREN, J., BUNN, W., LOCKEY, J. & CHASE, G. 1998. Radiographic and Spirometric Findings in Diatomaceous Earth Workers. *Journal of Occupational and Environmental Medicine,* 40**,** 22-28.

HART, G. A. & HESTERBERG, T. M. 1998. *In vitro toxicity of respirable-size particles of diatomaceous earth and crystalline silica compared with asbestos and titanium dioxide,* Hagerstown, MD, ETATS-UNIS, Lippincott Williams & Wilkins.

HEMENWAY, D. R., ABSHER, M. P., FUBINI, B. & BOLIS, V. 1993. What is the relationship between hemolytic potential and fibrogenicity of mineral dusts? *Arch Environ Health,* 48**,** 343-7.

HORWELL, C., WILLIAMSON, B., DONALDSON, K., LE BLOND, J., DAMBY, D. & BOWEN, L. 2012. The structure of volcanic cristobalite in relation to its toxicity; relevance for the variable crystalline silica hazard. *Particle and Fibre Toxicology,* 9**,** 44.

HUGHES, J., WEILL, H., CHECKOWAY, H., JONES, R., HENRY, M., HEYER, N., SEIXAS, N. & DEMERS, P. 1998. Radiographic Evidence of Silicosis Risk in the Diatomaceous Earth Industry. *American Journal of Respiratory and Critical Care Medicine,* 158**,** 807-814.

KARLSSON, H. L., GUSTAFSSON, J., CRONHOLM, P. & MOLLER, L. 2009. Size-dependent toxicity of metal oxide particles--a comparison between nano- and micrometer size. *Toxicol Lett,* 188**,** 112-8.

MORENO, T., HIGUERAS, P., JONES, T., MCDONALD, I. & GIBBONS, W. 2005. Size fractionation in mercury-bearing airborne particles (HgPM10) at Almadén Spain: Implications for inhalation hazards around old mines. . *Atmospheric Environment,* 39**,** 6409–6419.

NOLAN, R. P., LANGER, A. M., HARINGTON, J. S., OSTER, G. & SELIKOFF, I. J. 1981. Quartz hemolysis as related to its surface functionalities. *Environmental Research,* 26**,** 503-520.

OSCARSON, D. W., VAN SCOYOC, G. E. & AHLRICHS, J. L. 1986. Lysis of erythrocytes by silicate minerals. *Clays and Clay Minerals,* 34**,** 74-80.

PANDURANGI, R. S., SEEHRA, M. S., RAZZABONI, B. L. & BOLSAITIS, P. 1990. Surface and bulk infrared modes of crystalline and amorphous silica particles: a study of the relation of surface structure to cytotoxicity of respirable silica. *Environmental Health Perspectives,* 86**,** 327-336.

PARK, R., RICE, F., STAYNER, L., SMITH, R., GILBERT, S. & CHECKOWAY, H. 2002. Exposure to crystalline silica, silicosis, and lung disease other than cancer in diatomaceous earth

industry workers: a quantitative risk assessment. *Occupational and Environmental Medicine,* 59**,** 36-43.

PAVAN, C., RABOLLI, V., TOMATIS, M., FUBINI, B. & LISON, D. 2014. Why does the hemolytic activity of silica predict its pro-inflammatory activity? *Particle and Fibre Toxicology,* 11**,** 76.

PAVAN, C., TOMATIS, M., GHIAZZA, M., RABOLLI, V., BOLIS, V., LISON, D. & FUBINI, B. 2013. In Search of the Chemical Basis of the Hemolytic Potential of Silicas. *Chemical Research in Toxicology,* 26**,** 1188-1198.

PRATT, P. C. 1983. Lung dust content and response in guinea pigs inhaling three forms of silica. *Archives of Environmental Health,* 38**,** 197-204.

RICE, F. L., PARK, R., STAYNER, L., SMITH, R., GILBERT, S. & CHECKOWAY, H. 2001. Crystalline silica exposure and lung cancer mortality in diatomaceous earth industry workers: a quantitative risk assessment. *Occupational and Environmental Medicine,* 58**,** 38-45.

SCHINWALD, A. & DONALDSON, K. 2012. Use of back-scatter electron signals to visualise cell/nanowires interactions in vitro and in vivo; frustrated phagocytosis of long fibres in macrophages and compartmentalisation in mesothelial cells in vivo. *Particle and Fibre Toxicology,* 9**,** 34.

SCHINWALD, A., MURPHY, F. A., JONES, A., MACNEE, W. & DONALDSON, K. 2012. Graphene-based nanoplatelets: a new risk to the respiratory system as a consequence of their unusual aerodynamic properties. *ACS Nano,* 6**,** 736-46.

SEIXAS, N. S., HEYER, N. J., WELP, E. A. E. & CHECKOWAY, H. 1997. Quantification of Historical Dust Exposures in the Diatomaceous Earth Industry. *Annals of Occupational Hygiene,* 41**,** 591-604.

SMART, R. H. & ANDERSON, W. M. 1952. Pneumoconiosis due to diatomaceous earth; clinical and x-ray aspects. *Industrial medicine & surgery,* 21**,** 509-518.

STONE, V., JONES, R., ROLLO, K., DUFFIN, R., DONALDSON, K. & BROWN, D. M. 2004. Effect of coal mine dust and clay extracts on the biological activity of the quartz surface. *Toxicology Letters,* 149**,** 255-259.

TOURMANN, J. L. & KAUFMANN, R. 1994. Biopersistence of the mineral matter of coal mine dusts in silicotic human lungs: is there a preferential release of iron? *Environ Health Perspect,* 102 Suppl 5**,** 265-8.

VALLYATHAN, V., SCHWEGLER, D., REASOR, M., STETTLER, L., CLERE, J. & GREEN, F. H. Y. 1988. Comparative In Vitro Cytotoxicity and Relative Pathogenicity of Mineral Dusts. *Annals of Occupational Hygiene,* 32**,** 279-289.

VIGLIANI, E. C. & MOTTURA, G. 1948. Diatomaceous Earth Silicosis. *British Journal of Industrial Medicine,* 5**,** 148-160.

WAGNER, W. D., FRASER, D. A., WRIGHT, P. G., DOBROGORSKI, O. J. & STOKINGER, H. E. 1968. Experimental Evaluation of the Threshold Limit of Cristobalite—Calcined Diatomaceous Earth. *American Industrial Hygiene Association Journal,* 29**,** 211-221.

YE, J., SHI, X., JONES, W., ROJANASAKUL, Y., CHENG, N., SCHWEGLER-BERRY, D., BARON, P., DEYE, G. J., LI, C. & CASTRANOVA, V. 1999. *Critical role of glass fiber length in TNF-α production and transcription factor activation in macrophages*.

ZHOU, Y. M., ZHONG, C. Y., KENNEDY, I. M. & PINKERTON, K. E. 2003. Pulmonary responses of acute exposure to ultrafine iron particles in healthy adult rats. *Environ Toxicol,* 18**,** 227-35.

ZHU, M. T., FENG, W. Y., WANG, B., WANG, T. C., GU, Y. Q., WANG, M., WANG, Y., OUYANG, H., ZHAO, Y. L. & CHAI, Z. F. 2008. Comparative study of pulmonary responses to nano- and submicron-sized ferric oxide in rats. *Toxicology,* 247**,** 102-11.

ZIEMANN, C., HARRISON, P. T., BELLMANN, B., BROWN, R. C., ZOITOS, B. K. & CLASS, P. 2014. Lack of marked cyto- and genotoxicity of cristobalite in devitrified (heated) alkaline earth silicate wools in short-term assays with cultured primary rat alveolar macrophages. *Inhal Toxicol,* 26**,** 113-27.

Chapter 6

The effect of Al and Na doping on crystalline silica structure and chemistry

6.1 Introduction

Although silica's chemical composition is SiO_2, Al or Fe ions can substitute into the silica tetrahedra with interstitial cations to balance the charge (e.g. Na, Li, Ca) (see Chapter 2, (Deer et al., 2013)). These substitutions are more common in cristobalite and tridymite than quartz, as their structure allows more ready substitution of impurities than denser quartz (Shackelford and Doremus, 2008). Structural substitutions in cristobalite have been hypothesised to decrease the toxic potential of diatomaceous earth and volcanic ash (Chapters 4 and 5, Damby, 2012, Horwell et al., 2012, Nattrass et al., 2015). However, confounding factors, such as the presence of other minerals in these heterogeneous dusts, means the role of structural substitutions in cristobalite toxicity remains unknown.

Here, the aim was to produce a suite of crystalline silica samples, systematically produced to have incremental amounts of impurities within the structure, with a focus on cristobalite generation, thereby eliminating the confounding factors found in natural dusts. These samples are to be used in *in vitro* toxicology studies to understand the role that impurities play in crystalline silica toxicity (Chapter 7). To further our understanding of how impurities affect crystalline silica reactivity, the effect of doping (i.e. the addition of impurities) on crystal structure and chemistry was assessed. A method was employed where Al and Na dopants were added to a silica sol/gel, as these are common

impurities observed in natural or occupationally formed crystalline silica (see Chapters 2 and 4) and Al and Na have previously been shown to be some of the most readily substituted and interstitial cations in synthetic cristobalite, respectively (Saltzberg et al., 1992).

A number of studies have doped silica with Al and Na impurities pre-crystallisation, and assessed the effect on crystalline silica structure (Chapter 2). The displacive transition between the low temperature (α) and high temperature (β) forms of cristobalite can occur between 170-270 °C (Frondel, 1962), and the transition temperature can be altered by structural imperfections, including the presence of impurities (Chao and Lu, 2002a, Stevens et al., 1997). At high levels of dopants, e.g., >16 wt.% Al_2O_3 + Na_2O, the β to α cristobalite transition is supressed upon cooling and β-cristobalite is stabilised at room temperature (named chemically stabilised cristobalite (CSC)) (Chao and Lu, 2002b, Perrotta et al., 1989, Saltzberg et al., 1992). At lower dopant levels of Al and Na (e.g., <15 wt.% Al_2O_3 + Na_2O), the co-existence of α- and β-cristobalite can occur, although α-cristobalite is the dominant phase (Chao and Lu, 2002b, Perrotta et al., 1989). β-cristobalite can also be converted to α-cristobalite during grinding due to stress-induced transformation (Chao and Lu, 2002b). Dopant concentrations <8 wt.% (Chao and Lu, 2002b) or <12wt.% (Perrotta et al., 1989, Saltzberg et al., 1992) led to the formation of α-cristobalite only, and β-cristobalite was not stabilised. Where α-cristobalite formed, a shift in the (101) α-cristobalite XRD peak was observed, indicating a proportional increase in d-spacing (i.e. increased dimensions of the crystal lattice) with increased concentrations of dopants (Chao and Lu, 2002b). By IR spectroscopy, discrimination between β-cristobalite-only samples and those containing α-cristobalite could be determined by the presence of a band at 618 cm^{-1}, which is only found in α-cristobalite (Saltzberg et al., 1992).

These dopant studies aim to stabilise β-cristobalite or CSC at ambient conditions, as they have preferential properties for the ceramics industry (Şan and Özgür, 2009). Therefore, although these studies examine the structural effect of adding dopants, dopant concentrations are usually higher

(always >5 oxide wt.% Al+Na) than those observed in volcanic cristobalite (up to 4 oxide wt.% Al+Na (Horwell et al., 2012)), although up to 13 oxide wt.% Al+Na was observed in DE cristobalite (semi-quantitative data; Chapter 4). Here, lower concentrations were used, to span the concentrations found in volcanic cristobalite, and the aim was to produce α-cristobalite, as this is the form found in most natural samples (Damby et al., 2014).

Although the key aim of this study was to produce and fully characterise samples for toxicological assays (Chapter 7), testing of the silica sol/gel-dopant method at different temperature and durations also allowed insight into the effect of impurities on cristobalite formation and is also discussed in this Chapter.

6.2 Methods

6.2.1 Crystalline silica synthesis

Crystalline silica was produced using a silica sol/gel method adapted from Chao and Lu (2002b) and is shown in Figure 6.1. Colloidal silica sol (Ludox TM-40, Sigma Aldrich) was dried at 120 °C for at least 12 h, in its pure form or with dopants added. Samples were doped with aluminium and sodium nitrates in equivalent concentrations of 1, 2 and 3 wt.% Al_2O_3 in a 1:1 molar ratio of Al to Na, while accounting for the Al and Na already in the silica sol, as measured by X-ray fluorescence (XRF; Table 6.1; method in Chapter 3). One Al-only doped sample was also produced to constrain the role of Na, where only 3 wt.% Al_2O_3 (and no additional Na) was added to the starting material. The dried cake was gently ground by hand and 5 g pressed into 32 mm diameter pellets at a pressure of 120 MPa, using a uniaxial press. Pellets were then heated at 800, 900, 1000 or 1100 °C in a Carbolite horizontal tube furnace (Durham University), and pure samples were also heated at 1500 °C and 1600 °C.

Samples were placed on a 'sacrificial pellet' (of the same composition as the sample pellet) in an aluminium crucible inside the furnace, to avoid contamination from the crucible itself. Samples were heated at 4.4 °C/min and held at the target temperature for 4, 12, 24 or 48 h, before being cooled at the rate of the furnace. Table 6.2 lists the samples produced and which samples were used for each analysis.

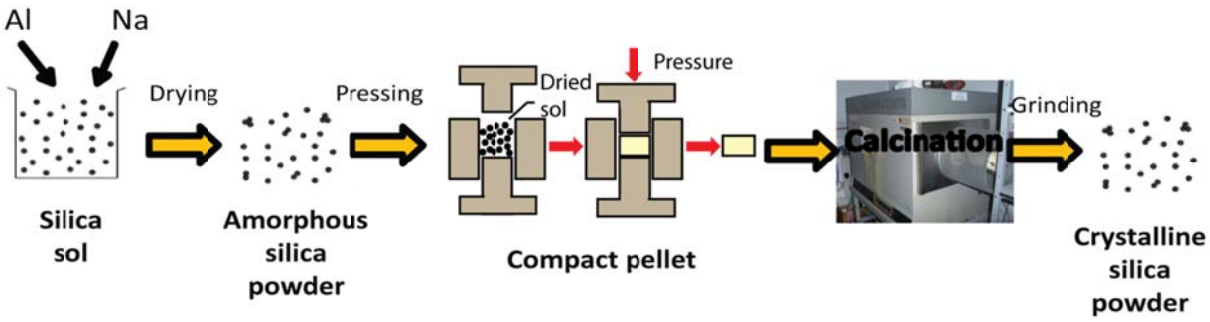

Figure 6.1: Schematic of the crystalline silica synthesis method

Table 6.1: Chemical composition of dried silica sol as determined by XRF given in wt.%.

	Chemical composition (wt.%)										
Sample	**SiO_2**	**TiO_2**	**Al_2O_3**	**Fe_2O_3**	**MnO**	**MgO**	**CaO**	**Na_2O**	**K_2O**	**P_2O_5**	**SO_3**
Silica sol	99.58	0.02	0.06	0.03	0.00	-0.01	-0.01	0.89	0.00	0.01	0.14

A slice of each pellet was taken and a thin section made in resin for scanning electron microscopy (SEM), electron microprobe (EMPA), and Raman spectroscopy analyses. The rest of the pellet was crushed by agate pestle and mortar and then ground in a cryogenic mill in air at 12 cycles per second for 30 minutes, to produce a powder for toxicology studies (Chapter 7), particle size distribution, XRD, IR spectroscopy, and surface analyses (Chapter 7).

Table 6.2: A list of samples produced including treatment temperature, time, dopant concentrations, and analyses performed. XRD GM = fixed parallel beam (using Goebel mirror) XRD, XRD HR = high resolution scanning XRD, IR = infrared spectroscopy, Raman = Raman spectroscopy, CL = cathodoluminescence, EBSD = electron backscatter diffraction, EMPA = electron microprobe analysis, EDS maps = mapping using SEM-EDS.

Sample ID	Treatment conditions				Analytical techniques							
	Dopants added (wt.%)				Crystal structure						Chemistry	
	Al_2O_3	Na_2O	Temp. (°C)	Time (h)	XRD GM	XRD HR	IR	Raman	CL	EBSD	EMPA	EDS maps
800_12	0.0	0.0	800	12	X							
900_12	0.0	0.0	900	12	X							
1000_12	0.0	0.0	1000	12	X							
1100_12	0.0	0.0	1100	12	X							
1500_12	0.0	0.0	1500	12	X							
1600_12	0.0	0.0	1600	12	X	X		X	X	X	X	X
1600_8	0.0	0.0	1600	8	X							
1600_4	0.0	0.0	1600	4	X	X	X				X	
2Al+Na_800_12	1.0	0.6	800	12	X							
2Al+Na_900_12	1.0	0.6	900	12	X							
2Al+Na_1000_12	1.0	0.6	1000	12	X							
2Al+Na_1100_12	1.0	0.6	1100	12	X						X	
3Al+Na_800_12	2.0	1.2	800	12	X							
3Al+Na_900_12	2.0	1.2	900	12	X							
3Al+Na_1000_12	2.0	1.2	1000	12	X							
3Al+Na_1100_12	2.0	1.2	1100	12	X						X	
5Al+Na_800_12	3.0	1.8	800	12	X							
5Al+Na_900_12	3.0	1.8	900	12	X							
5Al+Na_1000_12	3.0	1.8	1000	12	X							
5Al+Na_1100_12	3.0	1.8	1100	12	X						X	
1100_24	0.0	0.0	1100	24	X	X	X	X			X	
2Al+Na_1100_24	1.0	0.6	1100	24	X	X		X	X		X	X
3Al+Na_1100_24	2.0	1.2	1100	24	X	X		X	X		X	X
5Al+Na_1100_24	3.0	1.8	1100	24	X	X	X	X	X		X	X
3Al_1100_24	3.0	0.0	1100	24	X	X	X					
1100_48	0.0	0.0	1100	48	X							
2Al+Na_1100_48	1.0	0.6	1100	48	X							
3Al+Na_1100_48	2.0	1.2	1100	48	X							
5Al+Na_1100_48	3.0	1.8	1100	48	X							

6.2.2 Crystal phases and crystal structure

Mineralogy and crystal structure, and how these changed with the addition of dopants, were assessed using a number of techniques. Bulk mineralogy was assessed by XRD using a Bruker AXS D8 ADVANCE with DAVINCI design at Durham University. Initially, identification of phases was performed using a locked-coupled scan from 2-90° 2θ (see Chapter 3) and, on select samples (those used for toxicology, see Chapter 7), an 8 h long scan time was used to increase the resolution and to highlight trace phases. A scan using a fixed parallel beam, using a Goebel mirror, and moving detector was also performed from 18-35° 2θ and the peak area and full width half maximum (FWHM) of the primary cristobalite peak at ~21.8° 2θ was used to assess crystal abundance and level of crystallinity, respectively, in cristobalite-only samples. Peak position, measured at half the FWHM, and intensity were also measured.

Further analysis of the bulk crystal structure was performed by IR spectroscopy (Università degli Studi di Torino). Samples were mixed with KBr and pressed into pellets. IR adsorption was measured from 400-1600 cm^{-1} on a Bruker IFS88 instrument with DTGS detector. Raman spectroscopy was used to assess the crystal structure of 10 individual sites in each sample using a confocal micro-Raman spectrometer (HORIBA XploRA Raman Microscope; Mineralogical State Collection, Munich) with an excitation wavelength of 532 nm. Cathodoluminescence (CL) was also used to assess the crystallinity of selected areas of each sample (Durham University). A voltage of 8 kV was applied to cause sample luminescence. Panchromatic scans, and those with a red, green or blue filter, were applied to determine the wavelength of sample luminescence. Electron backscattered diffraction (EBSD) was performed using an Oxford Nordlys HKL detector on a focussed ion beam (FIB) SEM (FEI Helios Nanolab 600, Durham University) to determine the crystal abundance of sample 1600_12.

6.2.3 Elemental composition

Elemental composition of cristobalite was determined by EMPA using a Cameca SX100 (Ludwig Maximilian University of Munich). A voltage of 15 keV and current of 4 nA was applied to measure Na, Al and Si concentrations, and 15 keV and 40 nA was used for analysis of Mg, S, K and Fe (data in Appendix 2). A single elemental map was produced using EMPA using 15 keV and 40 nA, and analysing for Si, Al, Na, S (present in section resin), Fe. Elemental maps were also produced using SEM-EDS to show the distribution of the dopants throughout the samples semi-quantitatively (Hitachi SU-70 FEG-SEM, Durham University). A voltage of 12 kV was applied and a dwell time of 300 s to produce elemental maps. From these raw elemental maps, phase identification was performed using Aztec (Oxford Instruments), to identify grains with high Al and Na concentrations. All analytical methods are described in full detail in Chapter 3.

6.3 Results

6.3.1 Cristobalite formation and abundance

XRD patterns for identification of the mineral phases in samples treated for 12 h at 800-1100 °C are shown in Figure 6.2. Data for all samples are given in Table 6.3. At 800 °C, only non-doped samples began to crystallise and a small, broad cristobalite peak was observed (Figure 6.2a, Table 6.3). Doped samples remained amorphous at the 800 °C treatment. As the treatment temperature was increased, non-doped samples crystallised to a mixture of cristobalite and tridymite, preferentially crystallising tridymite (Figure 6.2b-d). Tridymite was observed in non-doped samples at temperatures as high as 1500 °C, and only treatment at 1600 °C (at 4, 8 or 12 h duration) led to the formation of cristobalite only (Figure 6.3). Samples doped with 2, 3 and 5 oxide wt.% Al+Na began to

crystallise in substantial quantities after 12 h at 900, 1000 and 1100 °C, respectively. Cristobalite was the only crystalline silica polymorph detected in these samples. Peak area and intensity decreased with increased doping at each temperature (Table 6.3).

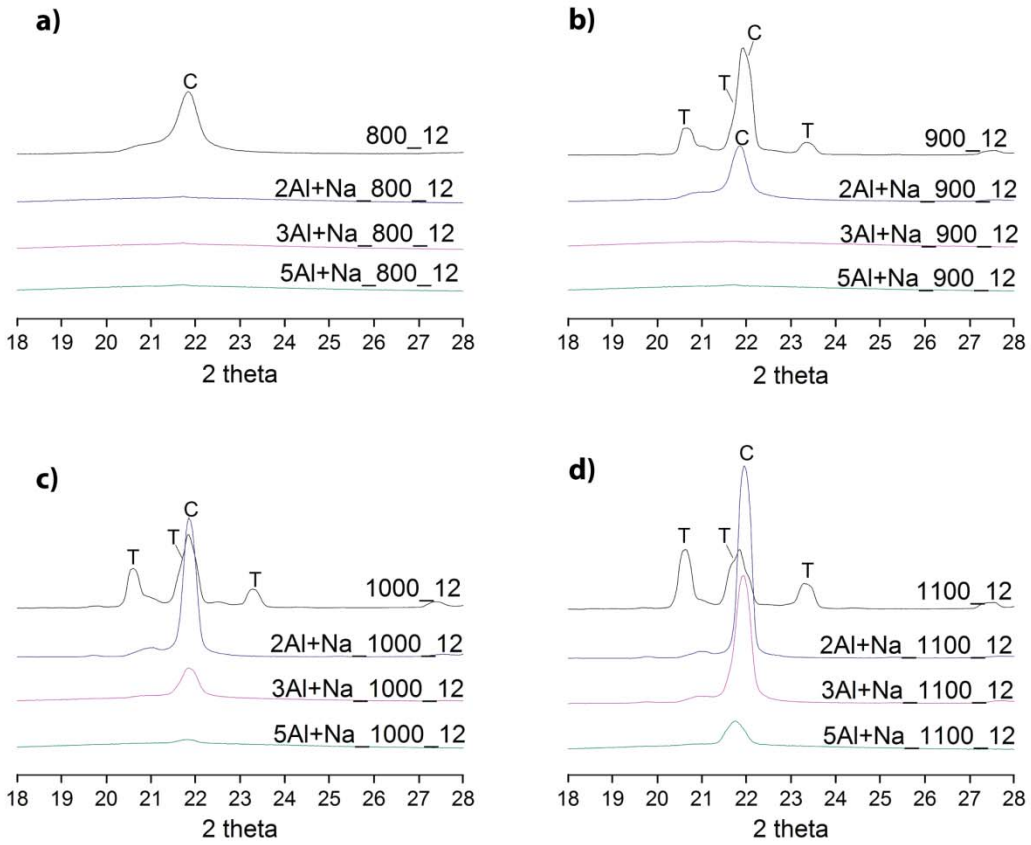

Figure 6.2: XRD patterns for synthetic samples heated for 12 h at **a)** 800, **b)** 900, **c)** 1000 and **d)** 1100 °C. C = cristobalite, T = tridymite (only primary peaks are labelled for clarity).

Table 6.3: FWHM (indicator of degree of crystallinity), peak area and intensity (indicators of crystal abundance) and peak position (indicator of crystal structure) measurements of the primary cristobalite peak in XRD patterns of samples.

Sample	N	FWHM (%)	Peak area (%)	Peak position (° 2θ)	Peak intensity (%)
1600_4	5	0.67 ± 0.04	0.87 ± 0.08	21.96 ± 0.04	0.84 ± 0.10
1600_8	2	0.67 ± 0.03	0.95 ± 0.06	22.00 ± 0.01	0.90 ± 0.14
1600_12	2	0.68 ± 0.02	0.92 ± 0.04	21.95 ± 0.02	0.85 ± 0.06
800_12	2	0.93 ± 0.06	0.39 ± 0.02	21.81 ± 0.02	0.29 ± 0.00
2Al+Na_800_12	1	- -	0.00 -	- -	0.00 -
3Al+Na_800_12	1	- -	0.00 -	- -	0.00 -
5Al+Na_800_12	1	- -	0.00 -	- -	0.00 -
2Al+Na_900_12	2	0.82 ± 0.02	0.31 ± 0.04	21.86 ± 0.02	0.27 ± 0.01
3Al+Na_900_12	1	0.58 -	0.01 -	21.70 -	0.05 -
5Al+Na_900_12	2	0.68 ± 0.13	0.01 ± 0.00	21.69 ± 0.00	0.04 ± 0.01
2Al+Na_1000_12	2	0.71 ± 0.05	0.71 ± 0.07	21.90 ± 0.06	0.64 ± 0.02
3Al+Na_1000_12	2	0.86 ± 0.06	0.17 ± 0.04	21.87 ± 0.02	0.15 ± 0.02
5Al+Na_1000_12	2	0.91 ± 0.05	0.02 ± 0.01	21.78 ± 0.03	0.05 ± 0.01
2Al+Na_1100_12	2	0.66 ± 0.05	0.86 ± 0.13	21.92 ± 0.05	0.82 ± 0.06
3Al+Na_1100_12	2	0.85 ± 0.07	0.50 ± 0.36	21.90 ± 0.03	0.39 ± 0.27
5Al+Na_1100_12	2	0.99 ± 0.02	0.20 ± 0.05	21.80 ± 0.09	0.16 ± 0.03
2Al+Na_1100_24	5	0.67 ± 0.04	0.88 ± 0.09	21.94 ± 0.03	0.81 ± 0.07
3Al+Na_1100_24	2	0.82 ± 0.05	0.64 ± 0.09	21.89 ± 0.04	0.48 ± 0.10
5Al+Na_1100_24	2	0.87 ± 0.11	0.63 ± 0.19	21.79 ± 0.03	0.47 ± 0.17
3Al_1100_24	2	0.70 ± 0.05	0.59 ± 0.03	21.87 ± 0.05	0.52 ± 0.01
2Al+Na_1100_48	2	0.63 ± 0.02	0.76 ± 0.01	21.97 ± 0.05	0.76 ± 0.04
3Al+Na_1100_48	2	0.73 ± 0.00	0.65 ± 0.02	21.86 ± 0.02	0.56 ± 0.01
5Al+Na_1100_48	2	0.77 ± 0.00	0.69 ± 0.04	21.80 ± 0.01	0.57 ± 0.02

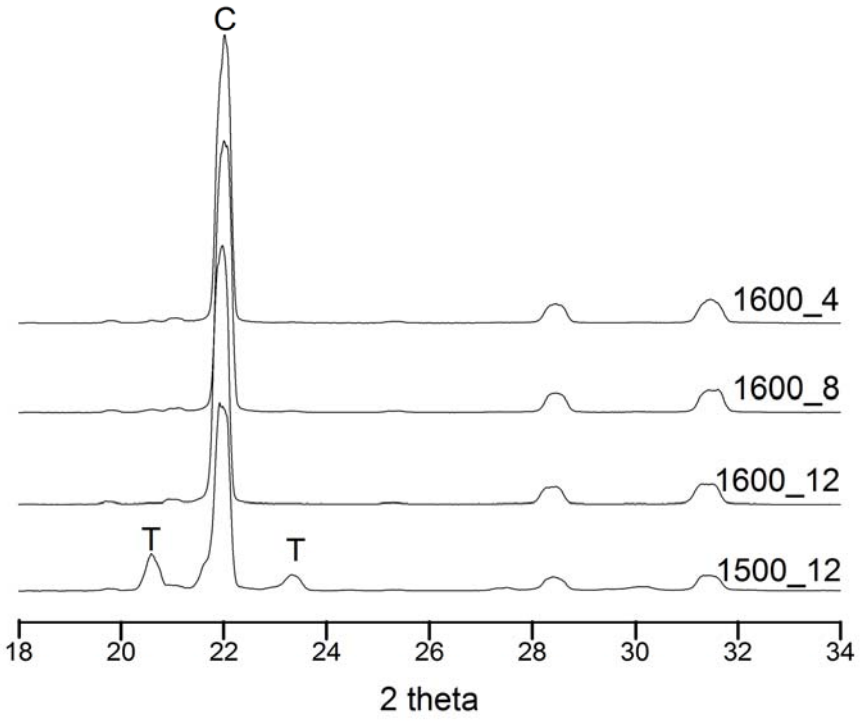

Figure 6.3: XRD pattern of non-doped samples treated at 1500 °C for 12 h or at 1600 °C for 4, 8, or 12 h. C = cristobalite, T = tridymite (only primary peaks are labelled for clarity).

The peak area of the cristobalite (101) peak increased and FWHM decreased when samples were heated at 1100 °C for 24 h compared to those heated for 12 h (Figure 6.4). Heating for 48 h did not substantially increase peak area (indicative of crystal abundance) compared to 24 h (Table 6.3) and, therefore, samples heated at 1100 °C for 24 h were chosen for further analysis (below) and toxicological experiments (Chapter 7). Increasing the heating duration from 12 to 24 to 48 h at 1100 °C did not alter the crystal polymorphs formed; non-doped samples produced predominantly tridymite and doped samples formed cristobalite.

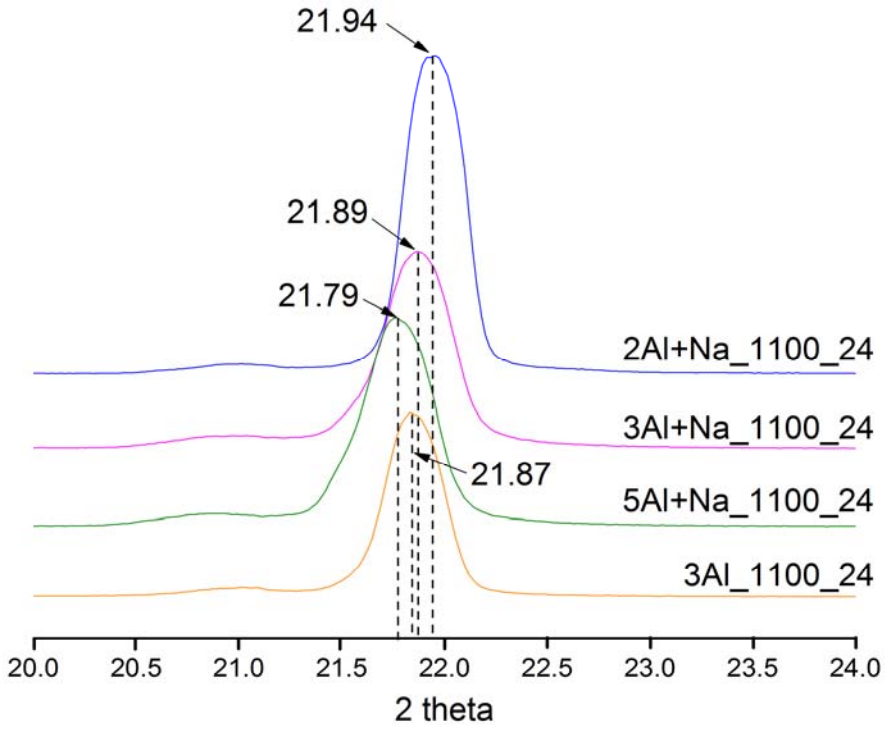

Figure 6.4: XRD patterns of doped cristobalite samples treated at 1100 °C for 24 h, showing the primary cristobalite peak shift from 21.94° 2θ at low dopant concentrations (2Al+Na) to 21.79° 2θ at the highest dopant concentrations (5Al+Na).

Comparison of the IR spectra of doped samples (Figure 6.5) to previous studies (Table 6.4) and of the Raman spectra to a cristobalite standard (Figure 6.6) and previous studies (Table 6.5) shows good agreement with the peak positions for cristobalite. Tridymite in the non-doped sample (1100_24) was distinguished from cristobalite by small peaks between 621 and 792 cm^{-1} and the peak at 567 cm^{-1} in the IR spectrum (Figure 6.5) (Hofmeister et al., 1992). Raman spectroscopy also confirmed that the non-doped sample treated at 1100 °C for 24 h produced tridymite, although cristobalite may also be present in this sample (Figure 6.7).

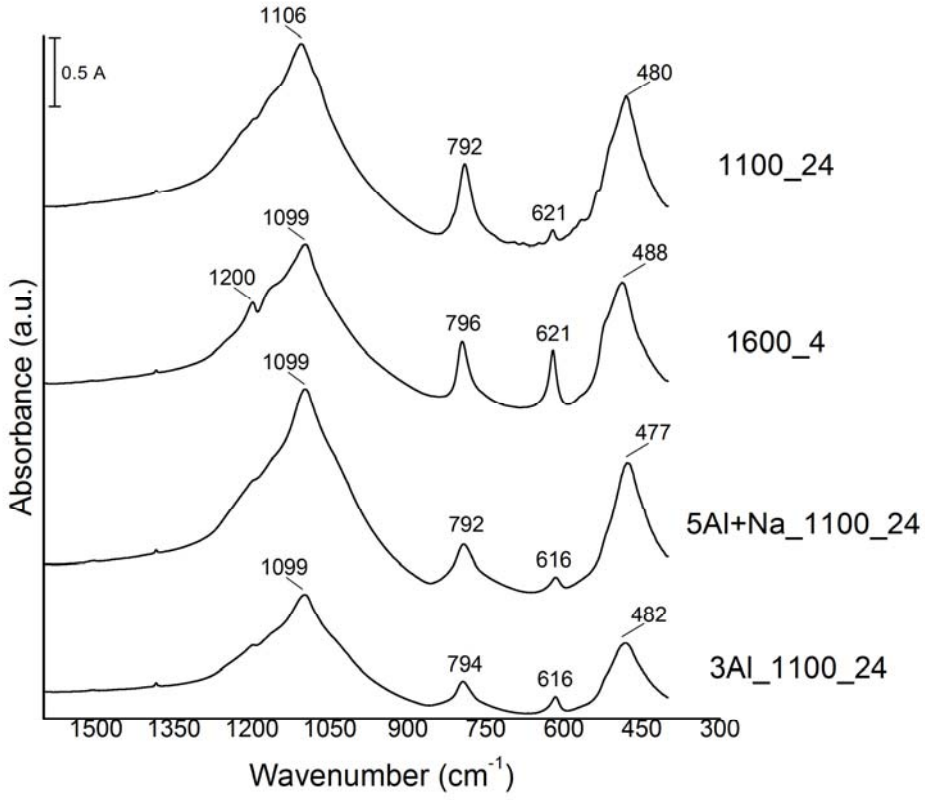

Figure 6.5: IR spectra from 400-1600 cm^{-1} of non-doped tridymite (1100_24), non-doped cristobalite (1600_4), Al+Na doped cristobalite (5Al+Na_1100_24), and Al-only doped cristobalite (3Al_1100_24).

Table 6.4: Comparison of experimental and calculated IR frequencies for cristobalite from previous studies (Bates, 1972, Cherukuri et al., 1985, Etchepare et al., 1978, Finnie et al., 1994, Lippincott et al., 1958, Sanders et al., 1984, Swainson et al., 2003) and the current study. Values in cm^{-1}. Shading = frequency range covered in this study.

	Previous studies							Current study		
	Bates	Cherukuri	Etchepare	Finnie	Lippincott	Sanders	Swainson	1600_4	5Al+Na	3Al
Anti-symmetric Si-O-Si stretching	1204 1160 1120 1100	1195 1107 1040	1160 1120 1100	1198 1110 1074	1204 1160 1104	1121 1077 944 927 925 924	1196 1144 1100	1200 1099	1099	1099
Symmetric Si-O-Si stretching	790 620	791 618	790 620	798 621	798 620	822 821 815 811 622	797 625	796 621	792 616	794 616
Lattice and O-Si-O bending modes	495 480 380 295 285	495 480 387 300 276	495 480 380 295 285	498	515 485	534 441 411 384 365 364 340 285 271 255	495 480 380 300 276	488	477	482

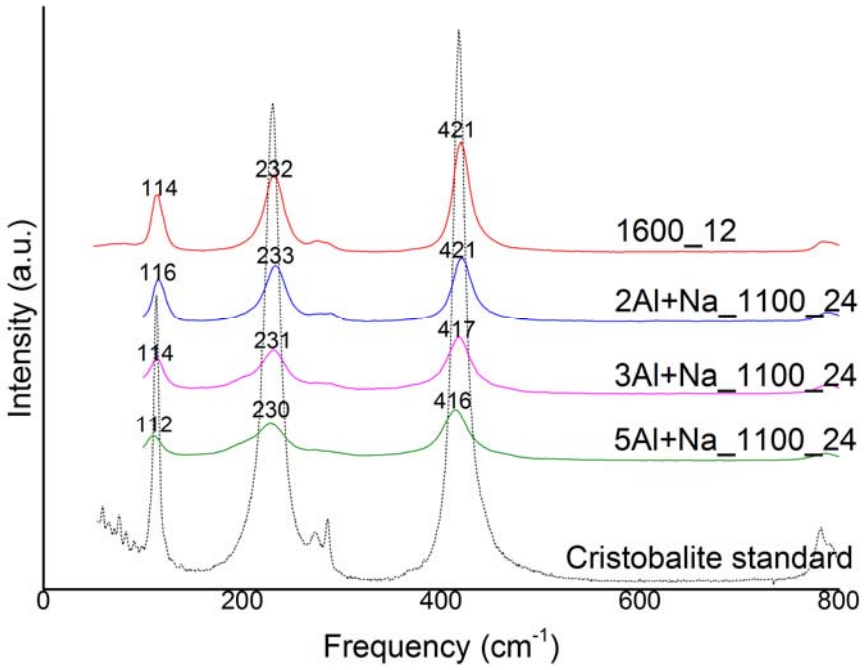

Figure 6.6: Raman spectra for non-doped (1600_12) and doped cristobalite. Cristobalite standard relates to data taken from Kingma and Hemley (1994).

Table 6.5: Comparison of Raman spectroscopy signal frequencies of cristobalite from previous studies (Bates, 1972, Cherukuri et al., 1985, Etchepare et al., 1978, Kingma and Hemley, 1994, Richet and Mysen, 1999, Swainson et al., 2003) and the current study. Values in cm^{-1}. Shading = frequency range covered in this study.

	Previous studies						Current study			
	Bates	Cherukuri	Etchepare	Kingma	Richet	Swainson	1600_12	2Al+Na	3Al+Na	5Al+Na
Anti-symmetric Si-O-Si stretching	1195	1193	1195		1200	1193	1193	1197	1197	1196
					1113	1188	1117			
	1089		1089		1083	1086				
	1079	1077	1079	1075	1054	1076	1080	1082	1082	1080
					995			998		
					923					
					904		832			
Symmetric Si-O-Si stretching	795	794	795	792	798	796				
	785		785	780	786	785	788	789	789	787
							642		643	
Lattice and O-Si-O bending modes		447	485		442	485				
	416	421	416	419	421	426	421	421	417	416
			380			380				
		374	368			368				
	287	288	287	286	294	286	286	288	288	285
	275	277	275	274	281	275	275	276	275	273
	230	233	230	230	237	233	232	233	231	230
	110		110	114			114	116	114	112

The abundance of cristobalite across a section of sample 1600_12 was assessed by EBSD and showed cristobalite to be the only phase present in this sample (Figure 6.8). CL was used, in conjunction with elemental mapping by EDS, to identify the distribution of cristobalite. CL of the 1600_12 showed a uniform emission of blue light across the areas analysed, indicative of cristobalite (Figure 6.9f), and both EBSD and CL highlighted grain boundaries not observed by SE or BSE imaging (Figures 6.8 and 6.9). CL and EDS showed the abundance of cristobalite decreased with increased dopant concentrations.

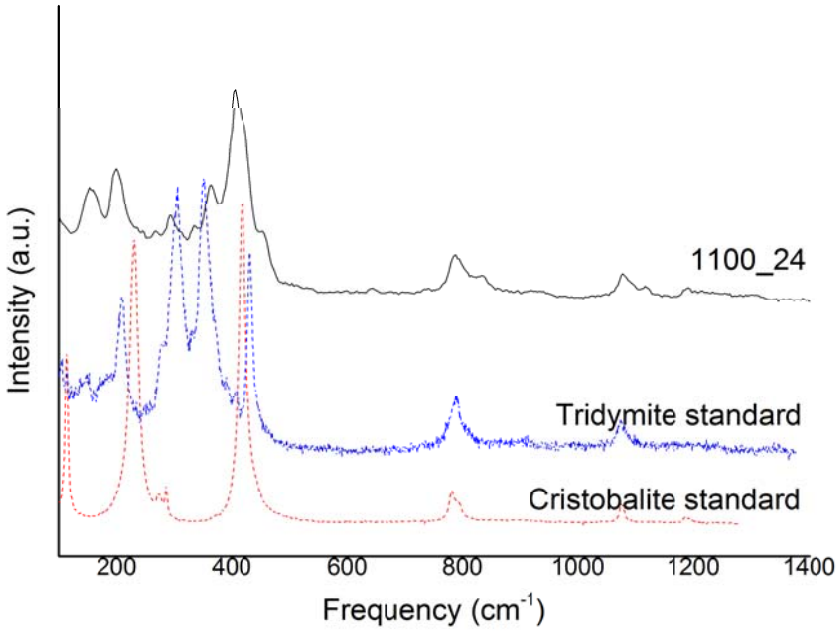

Figure 6.7: Raman spectra for non-doped 1100_24, showing predominantly tridymite**,** but some cristobalite structures. Tridymite standard is data taken from Kingma and Hemley (1994). Peak at ~405 cm^{-1} can be accounted for by tridymite as a peak forms at this wavelength (Kingma and Hemley, 1994). It is possible the intensity of this peak differs from the tridymite standard presented due to different crystal orientation.

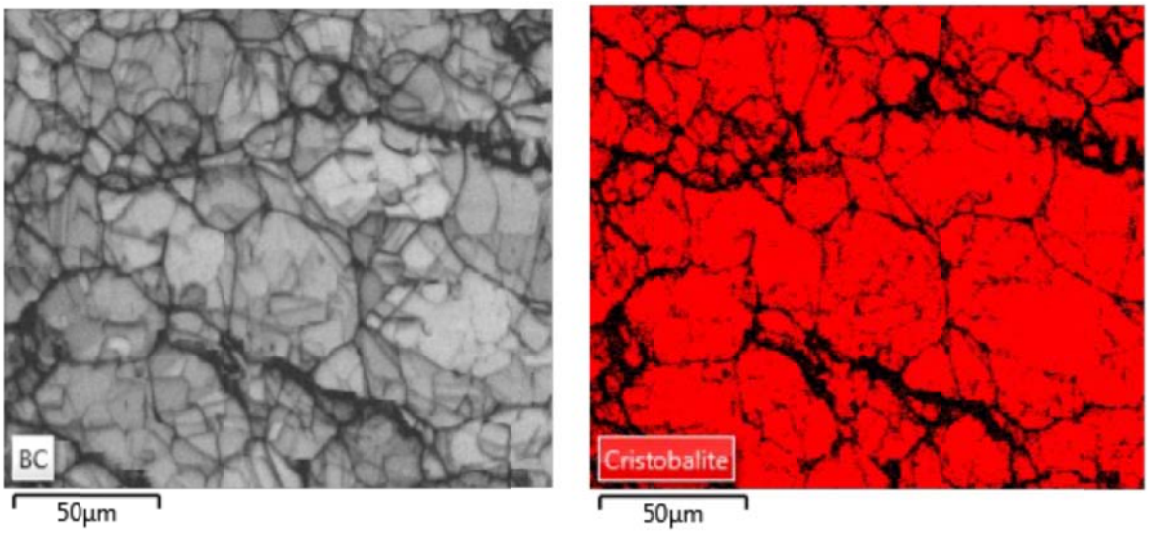

Figure 6.8: Band contrast image showing grain boundaries and phase map showing only cristobalite is present from EBSD analyses of 1600_12.

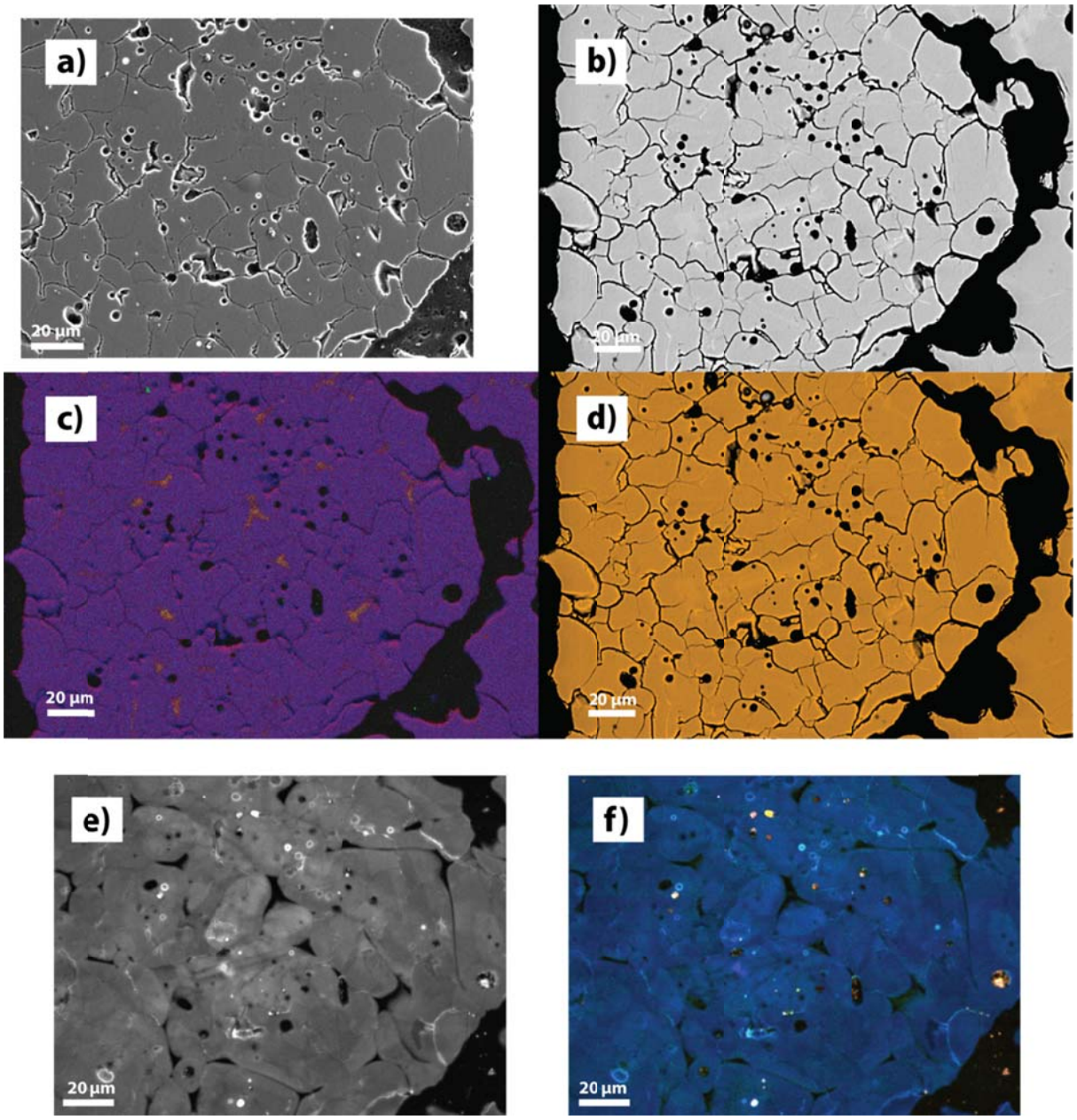

Figure 6.9: Section images, elemental maps and CL images of 1600_12. **a)** Secondary electron image, **b)** backscatter image, **c)** elemental composition map (blue = Si, red = O, yellow = Na), **d)** phase map (orange = average SiO_2 content of 99.7 wt.% by EDS), **e)** panchromatic CL image, and **f)** red, green and blue true colour composite CL image of **1600_12** (non-doped cristobalite).

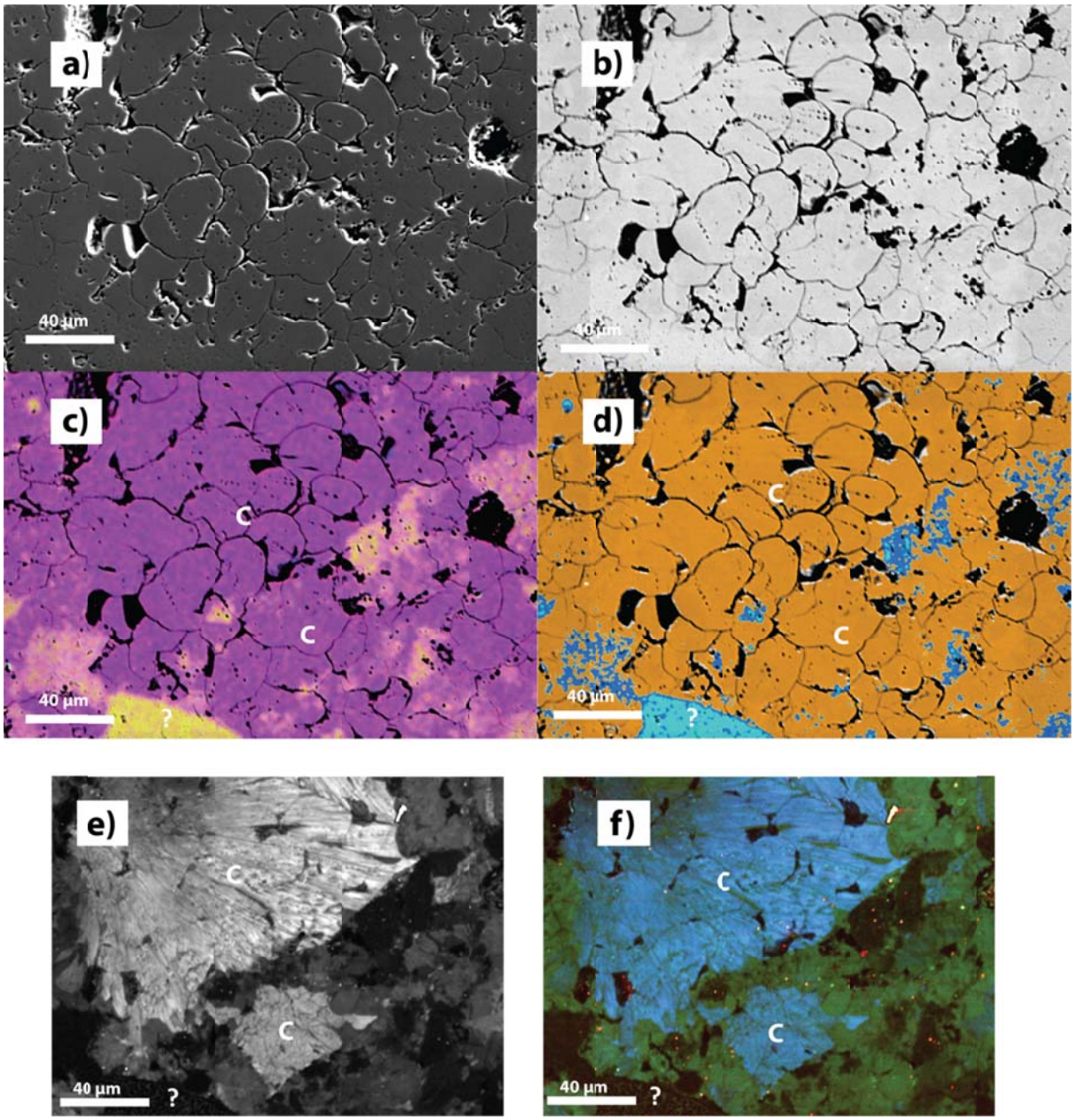

Figure 6.10: Section images, elemental maps and CL images of 2Al+Na_1100_24. **a)** Secondary electron image, **b)** backscatter image, **c)** elemental composition map (blue = Si, red = O, yellow = Na, green = Al), **d)** phase map (average SiO_2 content of: orange = 98 wt.%; dark blue = 92 wt.%; light blue = 88 wt.% by EDS), **e)** panchromatic CL image, and **f)** red, green and blue true colour composite CL image of **2Al+Na_1100_24**. C = cristobalite, ? = unknown phase.

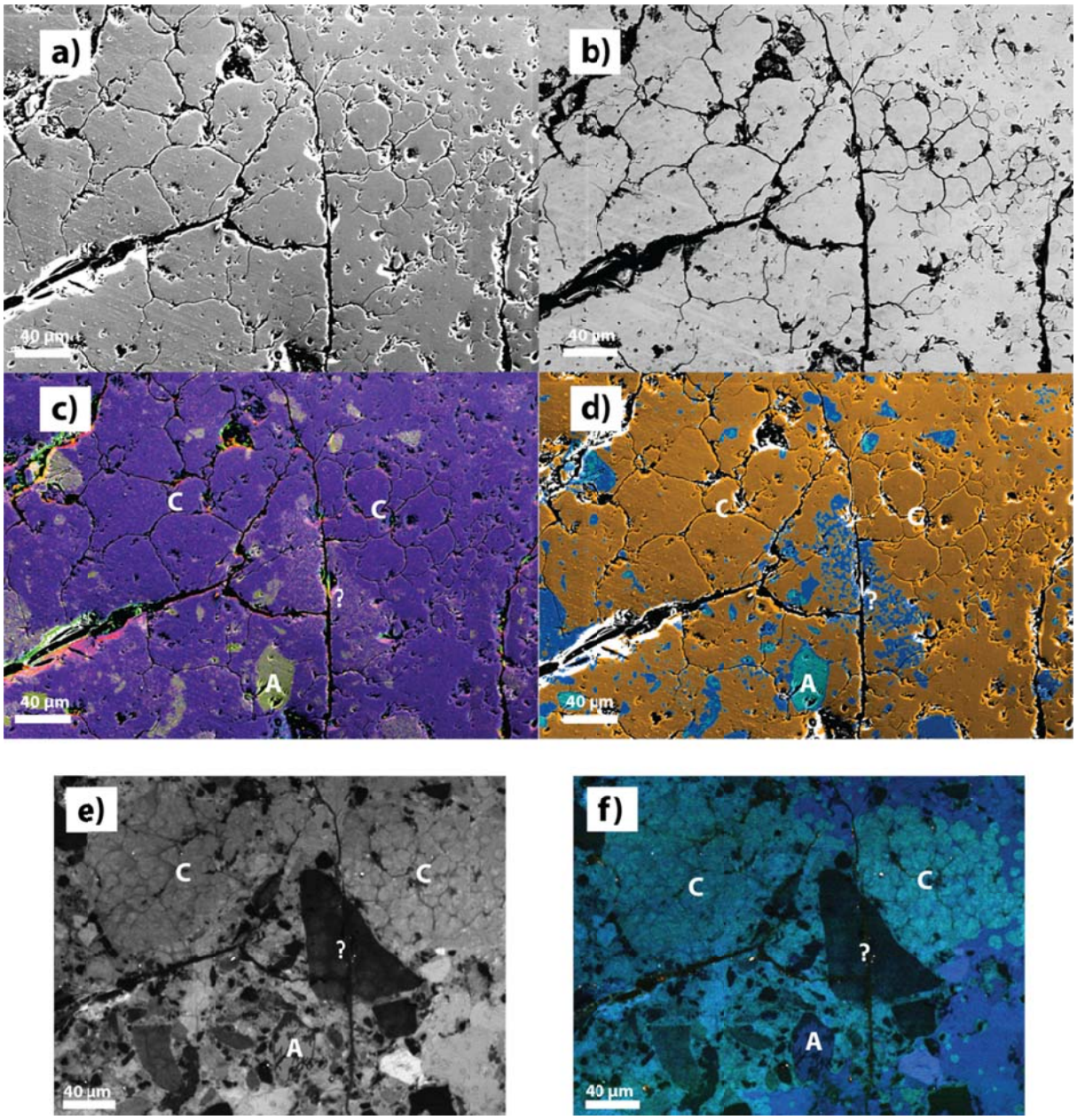

Figure 6.11: Section images, elemental maps and CL images of 3Al+Na_1100_24. **a)** Secondary electron image, **b)** backscatter image, **c)** elemental composition map (blue = Si, red = O, yellow = Na, green = Al), **d)** phase map (average SiO_2 content of: orange = 98 wt.%; dark blue = 91 wt.%; light blue = 85 wt.% by EDS), **e)** panchromatic CL image, and **f)** red, green and blue true colour composite CL image of **3Al+Na_1100_24**. C = cristobalite, A = albite, ? = unknown phase.

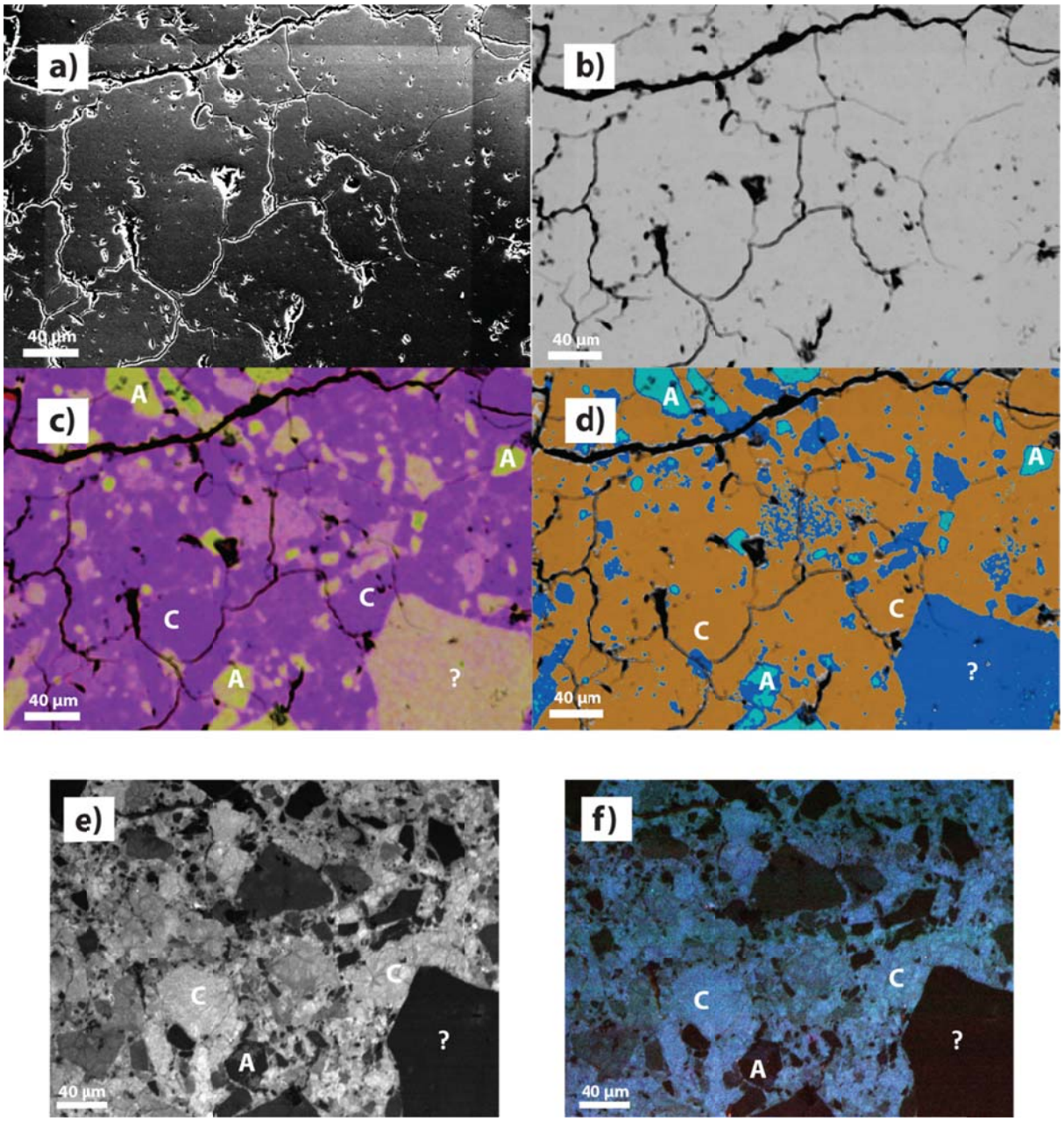

Figure 6.12: Section images, elemental maps and CL images of 5Al+Na_1100_24. **a)** Secondary electron image, **b)** backscatter image, **c)** elemental composition map (blue = Si, red = O, yellow = Na, green = Al), **d)** phase map (average SiO_2 content of: orange = 97 wt.%; dark blue = 92 wt.%; light blue = 86 wt.%, turquoise = 78 wt.% by EDS), **e)** panchromatic CL image, and **f)** red, green and blue true colour composite CL image of **5Al+Na_1100_24**. C = cristobalite, A = albite, ? = unknown phase.

6.3.2 Cristobalite chemistry and structure

Elemental analysis by electron microprobe on selected cristobalite areas showed that Al and Na increased in cristobalite as the amount of dopant was increased (Table 6.6). There was no difference in Al and Na concentrations in the cristobalite between 12 h or 24 h treatment duration.

Table 6.6: Elemental composition of cristobalite in non-doped and doped samples. Average Na, Al and Si oxide wt.% values from EMPA are given. n = number of spot analyses, s.d. = one standard deviation.

Sample	N	Na_2O	s.d.	Al_2O_3	s.d.	SiO_2	s.d.
1600_4	27	0.08	0.07	0.04	0.03	99.58	0.42
1600_12	39	0.05	0.06	0.03	0.02	99.94	0.41
1100_24	22	0.18	0.19	0.06	0.03	99.32	0.32
2Al+Na_1100_24	32	0.51	0.23	0.68	0.30	98.40	0.66
3Al+Na_1100_24	71	0.79	0.39	1.36	0.74	97.63	1.13
5Al+Na_1100_24	31	1.39	0.58	2.52	1.22	95.87	1.95
2Al+Na_1100_12	31	0.31	0.32	0.06	0.03	99.25	0.59
3Al+Na_1100_12	32	0.80	0.63	1.27	1.09	97.49	1.76
5Al+Na_1100_12	45	1.24	0.73	2.12	1.33	96.29	2.09

At 1100 °C (12, 24 or 48 h duration), the primary cristobalite peak shifted to lower 2θ values in the XRD pattern and peak intensity decreased from samples doped with 2 oxide wt.% Al+Na to samples doped with >3 oxide wt.% Al+Na (Figure 6.2d; Figure 6.4; Table 6.3). Treatment of samples doped with 3 oxide wt.% Al-only, at 1100 °C for 24 h (3Al_1100_24), also showed a shift in the primary cristobalite peak to lower 2θ values compared to samples doped with 2 oxide wt.% Al+Na or non-doped samples treated at 1600 °C (Table 6.3).

The mid-IR spectra (Figure 6.5) show the bulk crystal structure of tridymite (1100_24) and non-doped (1600_4) and doped cristobalite (5Al+Na_1100_24 and 3Al_1100_24). Doping with Al-only,

and with Al+Na, caused a slight shift in the IR peak between 400-550 cm^{-1} and caused a shift in the peak at 621 cm^{-1} to 616 cm^{-1} and a decrease in the intensity of this band. Doping also caused a slight shift and broadening of the peak at ~796 cm^{-1}. Doping with 5Al+Na caused an increase shift in peak positions (peaks at ~796 and ~480 cm^{-1}) and a greater decrease in peak intensity than doping with Al-only, when compared to non-doped 1600_4.

Figure 6.6 and Table 6.5 show the peak positions of non-doped (1600_12) and Al+Na doped cristobalite in Raman spectra. As dopants were increased from 0 to 5 oxide wt.% Al+Na, the band at ~420 cm^{-1} decreased in frequency from 421 to 416 cm^{-1}. Low levels of doping caused an increase in frequency of the ~114 and ~230 cm^{-1} bands compared to non-doped samples, however, as doping was increased, the frequency of the peaks decreased.

By CL areas of cristobalite, identified by the cracking textures, emitted blue light. However, this was brighter than the non-doped cristobalite (Figures 6.10-6.12f).

6.3.3 Formation of other phases

To determine if any other minor phases were present in the samples treated at 1100 °C for 24 h (those selected for toxicological assays), long scan times were used to produce high resolution XRD patterns (Figure 6.13). Albite was observed in 3Al+Na_1100_24, 5Al+Na_1100_24, and in trace quantities in 2Al+Na_1100_24 and 3Al_1100_24 by comparison with library standards (ICDD, 2015). Albite was not detected in non-doped samples.

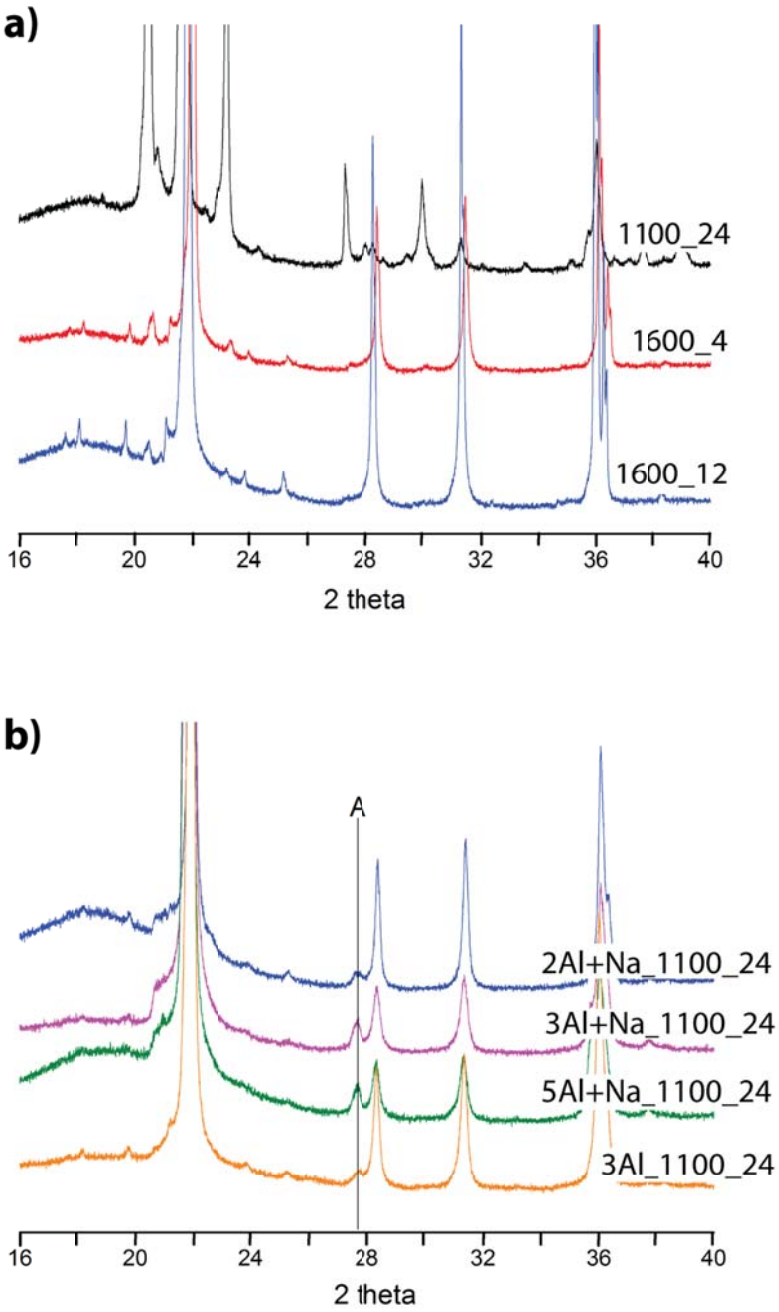

Figure 6.13: Long scan time XRD patterns of **a)** non-doped samples, and **b)** doped samples, showing albite (A) present in 3Al+Na_1100_24 and 5Al+Na_1100_24, and in trace quantities in 2Al+Na_1100_24 and 3Al_1100_24, but not in non-doped samples.

Elemental mapping by EMPA (Figure 6.14) and by EDS (Figures 6.9-6.12) showed grains of different composition (containing up to 15 wt.% Al_2O_3 by EMPA), which were not observable by BSE (Figures

6.9-6.12). A comparison of the EDS maps and CL scans indicates that areas of blue and red luminescence were those grains with the highest concentrations of Al and Na and have similar chemistries to albite (Figures 6.9-6.12). CL imaging of doped samples also highlighted grains of non-luminescent crystals (almost black in Figures 6.10-6.12), which contained 8-9 oxide wt.% Al+Na by EDS. These phases could not be identified. EDS maps showed that the abundance of discrete Al and Na-rich phases increased with increased dopant concentrations (Figures 6.9-6.12d). The composition of these phases also became more Al- and Na-rich with increased dopants. The most doped sample (5Al+Na_1100_24) contained phases with up to 22 oxide wt.% Al+Na by EDS, whereas, in the least doped sample (2A+Na_1100_24), only phases with up to 12 oxide wt.% Al+Na were observed.

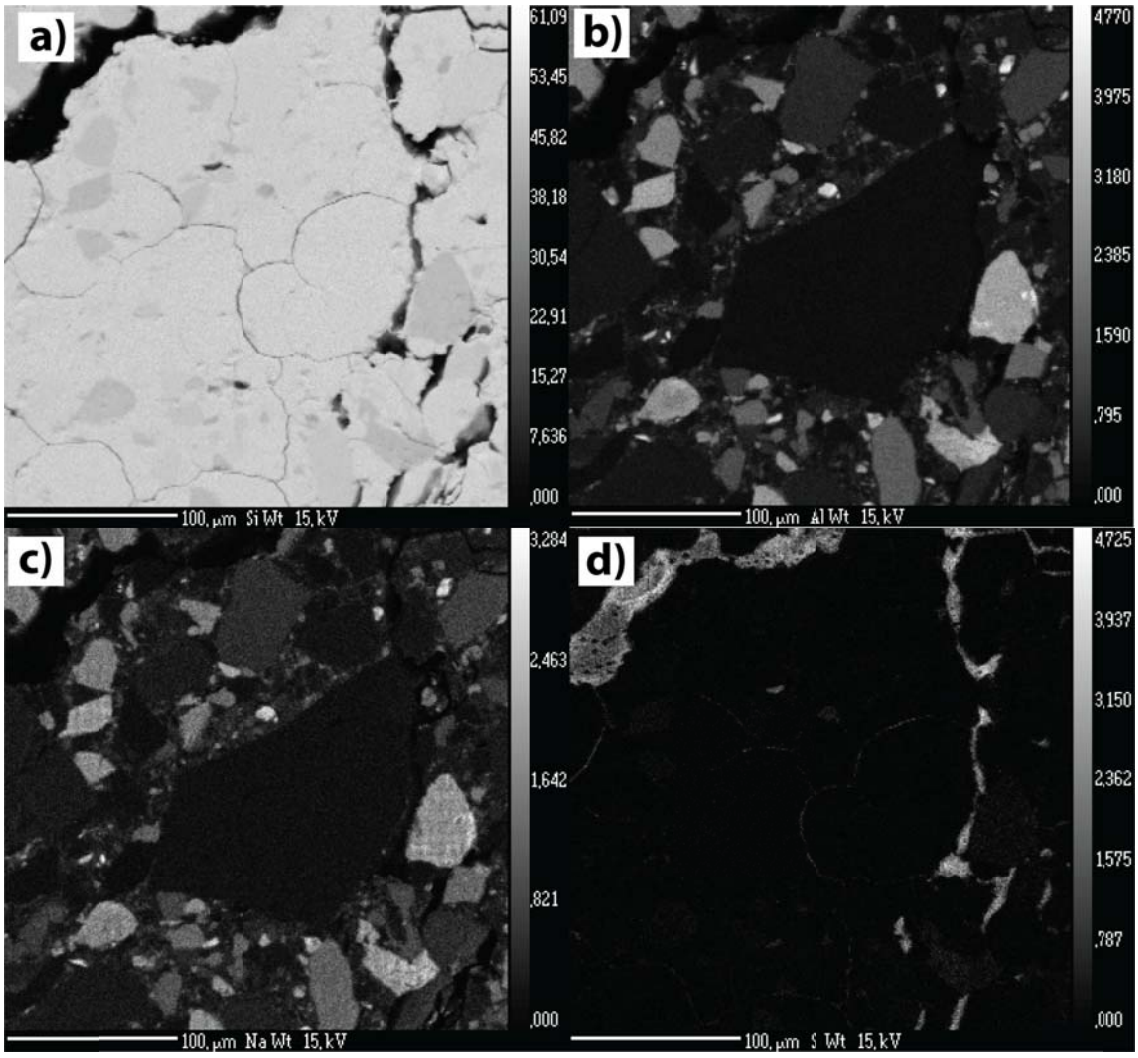

Figure 6.14: Electron microprobe maps for **a)** Si, **b)** Al, **c)** Na and **d)** S (wt.%) for 5Al+Na_1100_24. Scale bars are in wt.%.

Higher resolution scans of the primary cristobalite peak of the doped samples show that, in samples doped with 5Al+Na, the peak is split (Figure 6.15). The primary peak resides at 21.89° 2θ, so is still shifted to lower values than less doped samples (21.94° 2θ for 2Al+Na_1100_24), however, a second peak is also observed at 21.68° 2θ (Figure 6.15). A shoulder at the same 2θ value was also observed in the sample doped with 3Al+Na, but not in samples doped with only 2Al+Na, only Al, or non-doped cristobalite samples.

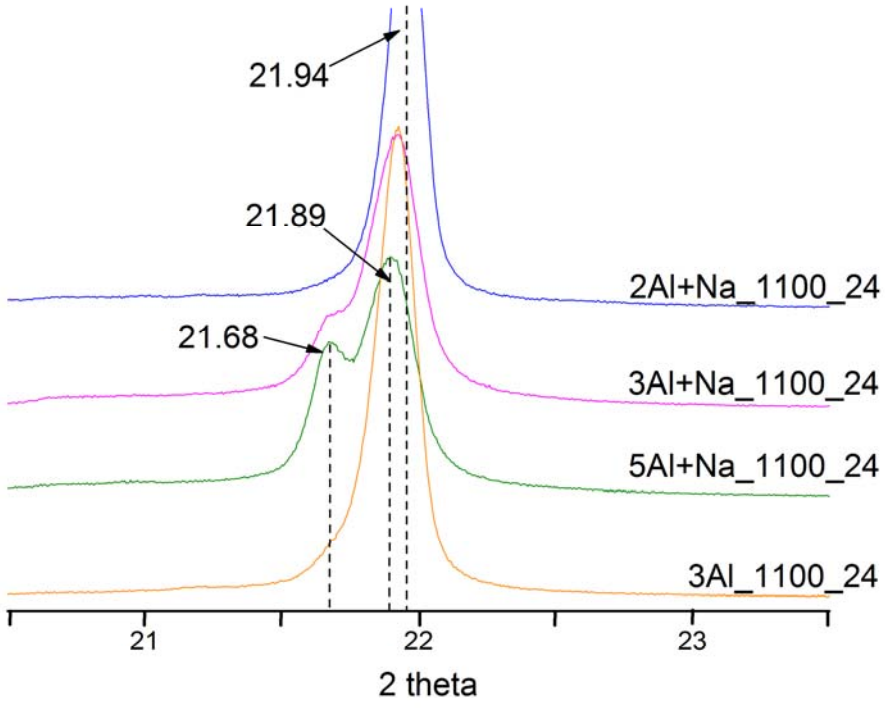

Figure 6.15: Long scan time XRD patterns from 18-26° 2θ for doped samples treated at 1100 °C for 24 h showing primary peak shift from 21.94° 2θ for low dopant concentrations (2Al+Na) to 21.89° 2θ for high dopant concentrations (5Al+Na), and peak splitting of the primary cristobalite peak in 5Al+Na_1100_24.

6.4 Discussion

Here, co-doping silica sol with Al+Na or doping with Al-only before crystallisation was used to produce chemically modified crystalline silica. Characterisation of the samples showed that impurities were successfully incorporated into the crystalline structure (see Section 6.4.2.2), although some Al and Na rich phases, including albite (a Na-rich feldspar), were also produced as a result of high doping (Section 6.4.3). Non-doped cristobalite was also produced by treatment at 800 or 1600 °C for cristobalite with a low or high degree of crystallinity, respectively, for comparison. Treatment of crystalline silica with Al can alter its toxicity (see Chapter 2, Duffin et al., 2001, Stone et al., 2004). The presence of Al and Na impurities in volcanic and diatomaceous earth cristobalite and the presence of other minerals has been hypothesised to alter its toxic potential (Chapter 5, Damby, 2012, Horwell et al., 2012, Nattrass et al., 2015). Therefore, it is important to fully characterise the samples produced, to determine the effect of dopants on the crystal structure, crystal chemistry, and presence of other phases. This allows factors that may affect surface properties of the particles produced and, therefore, contribute to changes in sample toxicity, to be determined (Chapter 7).

6.4.1 Production of non-doped α-cristobalite

Non-doped cristobalite formed at 800 or 1600 °C. Treatment at all other temperatures produced a mix of cristobalite and tridymite and this is discussed in section 6.4.4. Treatment at 800 °C produced cristobalite in low abundances and with a low level of crystallinity (determined by XRD peak area and FWHM respectively), whereas treatment at 1600 °C produced cristobalite in high abundance and with high degree of crystallinity. The high temperature treatment falls within the cristobalite stability field and, therefore, a well-ordered structure is expected, and heating silica glass or silicic acid to >1450 °C has been used previously to produce highly ordered cristobalite (Shinohara, 1990, Swainson and Dove, 1995). At 800 °C, cristobalite has formed metastably in the β-quartz stability

field (the mechanisms by which are explained below), and the lower 2θ values and larger FWHM of the XRD cristobalite peak suggest the crystal lattice is expanded.

6.4.2 Production of impure α-cristobalite

Production of impure cristobalite was achieved by adapting the method of Chao and Lu (2002a). In their study, silica sol was doped with >5 oxide wt.% Al+Na with an aim to stabilise β-cristobalite. Here, dopant concentrations of 0, 2, 3 and 5 oxide wt.% Al+Na were considered, as these cover the range of impurities found in volcanic cristobalite, and, as α-cristobalite is the usual form of cristobalite in natural samples (Damby et al., 2014), it was not the aim to stabilise β-cristobalite. Al-only doping was also considered, to constrain the role of Na in incorporation of impurities into the crystal structure.

6.4.2.1 Crystalline silica phases and crystal abundance

Increasing the treatment temperature increased the crystal abundance and crystallinity of cristobalite produced, indicated by an increase in peak area and a decrease in FWHM respectively (Figure 6.2, Table 6.3). Therefore, samples produced at 1100 °C (the highest temperature used for doped samples) were used for further analysis. The effect of temperature and dopants on cristobalite formation is discussed in detail in Section 6.4.4 below.

Samples were treated for 12, 24 or 48 h at 1100 °C. At all treatment times, cristobalite was the crystalline silica polymorph formed in doped samples, whereas tridymite was the dominant phase in non-doped samples. Altering the duration of heating from 12 to 48 h did not alter the crystalline polymorphs produced. However, increasing the treatment time from 12 to 24 h led to a substantial

increase in crystal abundance and crystallinity in doped samples. Heating for 48 h did not substantially increase crystal abundance compared to 24 h. Therefore, samples become fully crystallised after ~24 h at 1100 °C. Slight decreases in FWHM from 24 to 48 h indicated that the crystal structure was more ordered at longer heating times, as has been seen previously (Chao and Lu, 2002a).

The sample doped with Al-only (3Al_1100_24) and treated at 1100 °C for 24 h produced cristobalite as the only crystalline phase visible in XRD patterns. This sample had similar crystal abundance and degree of cristobalite crystallinity to samples co-doped with 3 or 5 oxide wt.% Al+Na (Table 6.3), indicating similar mechanisms of crystallisation.

6.4.2.2 Incorporation of impurities into α-cristobalite and the effect on crystal structure

EMPA of cristobalite showed an increase in impurities with increased dopant concentrations for samples treated at 1100 °C for 12 or 24 h. Averages of 2.5 and 1.4 wt.% Al_2O_3 and Na_2O, respectively, were observed in cristobalite in the most doped sample heated for 24 h (5Al+Na_1100_24; Table 6.6). As, cristobalite has an open structure allowing easy addition of these dopants into the structure, the concentrations seen here are not surprising. This observation is supported by XRD, where a shift in the primary cristobalite peak to lower 2θ values as dopant concentrations were increased was observed (Figures 6.2d and 6.4; Table 6.3). This has been shown previously in doped cristobalite and is indicative of larger d-spacing in the crystal lattice caused by Al substitution of Si and interstitial Na (Chao and Lu, 2002b), indicating successful uptake of Al and Na into the cristobalite structure here.

Peak position was not shifted to lower 2θ values (an indicator of impurity substitutions) with increased treatment duration (from 12 to 48 h) for any level of dopant at 1100 °C. Therefore, it is

possible that no additional Al was substituted into the crystal structure after 12 h. This is supported by EMPA, where there was no significant difference between the Al+Na measured in the cristobalite between samples heated for 12 or 24 h. This suggests that by 12 h, Al and Na in the sample have been incorporated into relatively stable forms, either within cristobalite, or other phases formed in the sample (see below).

As samples treated at 1100 °C for 24 h produced cristobalite with high crystal abundance and impurities incorporated into the crystal structure, these were chosen for further analysis. IR and Raman spectroscopy of these samples also showed a change in crystal structure with doping, indicating Al and Na incorporation into the crystal structure. The bands at ~620 cm^{-1} and ~796 cm^{-1} in the IR spectra represent E symmetry and symmetric T-O-T stretching (where T = tetrahedrally coordinated Si or Al, (Swainson et al., 2003); Table 6.4). The intensity of these bands decreased and FWHM was increased with doping (Figure 6.5), as seen previously in doped cristobalite (Saltzberg et al., 1992). This is similar to changes in these bands when α-cristobalite is heated near the transition temperature (Swainson et al., 2003), indicating lattice expansion caused by the incorporation of Al and Na into the structure, and is in agreement with the increased d-spacing observed by XRD.

Raman data of individual crystals also indicates a shift toward a β-cristobalite-like structure, indicative of lattice expansion and O-T-O bending (Swainson et al., 2003, McMillan et al., 1994); as α-cristobalite is heated towards the transition temperature, bands at 114, 231 and 418 cm^{-1} decrease in frequency and FWHM increases (Bates, 1972, Richet and Mysen, 1999), which is observed here as the amount of dopant is increased. Above the transition temperature, in the β-cristobalite structure, these bands are converted to Raman inactive modes (are not produced in the Raman spectra) (Bates, 1972). Therefore, the Raman spectra of doped samples here show that α-cristobalite is present, however, its structure is similar to the cristobalite structure near the transition temperature. Alternatively, the similarities of the IR and Raman spectra to that of α-cristobalite

heated near the transition temperature may indicate the co-existence of both α- and β-cristobalite (discussed below).

CL data of samples heated for 24 h may also indicate impurities in the cristobalite structure in doped samples, as areas of α-cristobalite (showing the characteristic cracking) showed intense blue luminescence in doped samples (bright blue in Figures 6.10-6.12f) compared to non-doped cristobalite (Figure 6.9f). The blue luminescence of cristobalite has been related to the presence of $[AlO_4/M^+]^0$ defects in its structure, where M is an interstitial cation such as Na^+, which can easily diffuse through the sample upon exposure to the electron beam (Kayama et al., 2009). Therefore, the initial intensity of the blue emissions would increase with increased Al content, a correlation which has previously been shown in quartz (Perny et al., 1992).

In Al-only doped samples, a shift in the primary cristobalite peak to lower 2θ values also indicates that Al was incorporated into the structure in this sample. The peak position was similar to sample doped with 3 oxide wt.% Al+Na, suggesting a similar level of substitution (average of 2 wt.% Al+Na; Table 6.6). Decreases in peak intensity, increased FWHM and shifted positions of IR bands were observed in Al-only doped sample compared to non-doped cristobalite (1600_4). These deviances from the non-doped cristobalite structure are similar but less pronounced than those observed for samples doped with 5 oxide wt.% Al+Na, again suggesting uptake of Al into the structure. As Al ions cannot substitute for Si ions without a charge balancing cation, it is likely that the Na present in the starting material (Table 6.1) allows incorporation of Al into the structure in the Al-only doped sample. However, in this Al-only doped sample, Na content may be a limiting factor for Al substitution, as when additional Na is provided with the same concentration of Al doping (5Al+Na_1100_24), Al content in the crystalline silica structure is greater than in the Al-only doped sample (3Al_1100_24).

6.4.3 Crystallisation of other phases

Above, it is shown that α-cristobalite has been produced with impurities incorporated into its structure causing expansion of the crystal lattice. However, on average, the concentration of Al and Na impurities in cristobalite were less than the concentrations of dopant added. This is due to the incorporation of Al and Na into other phases produced, detected by XRD, elemental mapping and CL scans.

6.4.3.1 Al- and Na-rich phases

Elemental mapping showed that, in doped samples, Al- and Na-rich phases were present, and their abundance increased with increased dopant concentrations. High resolution XRD identified some of these phases as albite, most abundant in 5Al+Na_1100_24. This was supported by CL analysis, which showed grains with the highest concentrations of Al and Na (measured by EDS) emitted both blue and red light, which has previously been shown in albite (Dalby et al., 2010, Kayama et al., 2011, Richter et al., 2002). The phase diagram of cristobalite to nepheline is shown in Figure 6.16. Nepheline is a stuffed derivative of silica, where half of the Si atoms are replaced with Al (Heaney et al., 1994). Here, the starting composition was heavily silica saturated and, therefore, nepheline was not formed (Hefferan and O'Brien, 2010). However, albite, with a ratio of ~1:3 Al:Si was formed in small quantities. Other non-luminescent phases with concentrations of up to 10 oxide wt.% Al+Na, were also present but could not be identified. As the grains were not visible by BSE they could not be selected for Raman spectroscopy analysis to determine their crystal structure. However, it is likely these Al- and Na-rich phases are formed by the over saturation of silica in the system, where the excess Si prevents albite formation in large quantities (Hefferan and O'Brien, 2010).

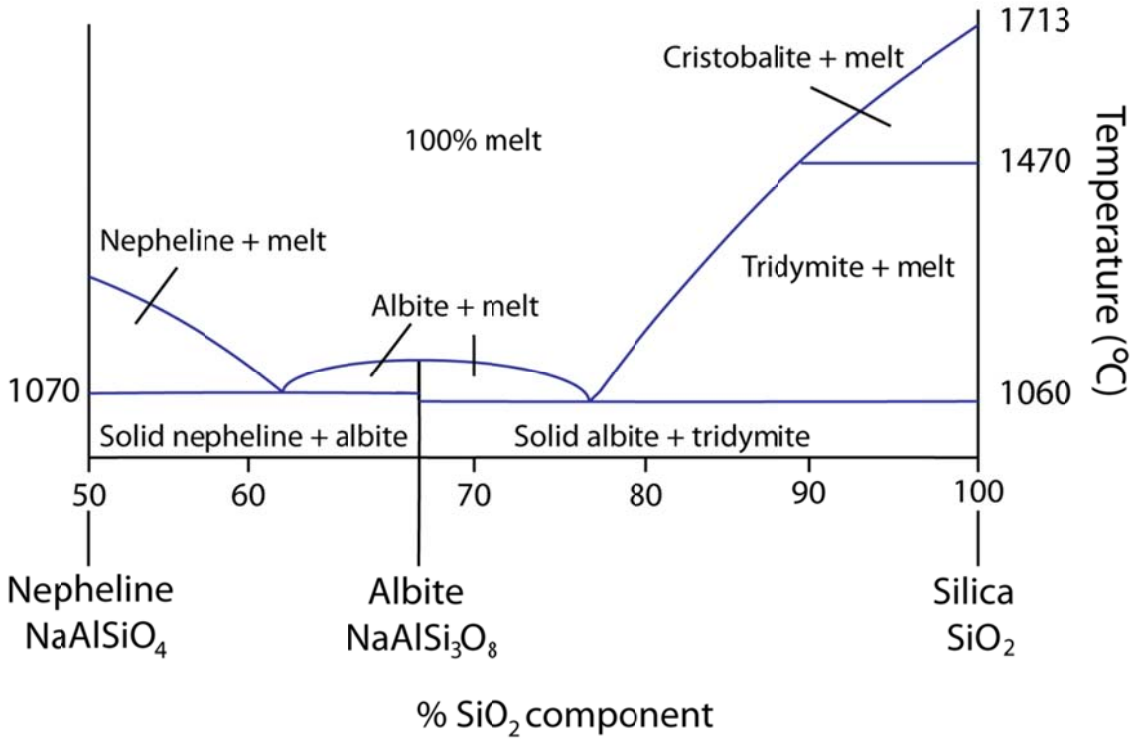

Figure 6.16: The cristobalite to nepheline phase diagram, showing the conditions at which albite forms. Adapted from Hefferan and O'Brien (2010).

6.4.3.2 Potential production of β-cristobalite or β-like cristobalite

In the most doped sample (5Al+Na_1100_24) a distinct peak was observed in the high resolution XRD pattern at 21.68° 2θ, separate from the primary cristobalite peak at 21.89° 2θ. A shoulder in the XRD pattern of 3Al+Na_1100_24 at the same 2θ was also observed. It is possible this peak represents β-cristobalite, where peaks fall between 21.5–21.7 °2θ (ICDD, 2015). Alternatively, this peak may represent a secondary population of α-cristobalite with a β-cristobalite-like structure. Evidence for and against each hypothesis is presented here, however, thermal analyses are required to confirm if any β-cristobalite has been stabilised and will be the focus of future work.

Retention of β-cristobalite in doped samples at room temperature has been observed previously (Chao and Lu, 2002a, Chao and Lu, 2002b, Perrotta et al., 1989, Saltzberg et al., 1992), however,

dopant concentrations >10 oxide wt.% were needed to produce a mixture of α- and β-cristobalite. It is possible that localised high concentrations of Al and Na allowed the stabilisation of β-cristobalite in some areas here. A maximum of 9 oxide wt.% Al+Na was observed in cristobalite in the most doped sample (5Al+Na_1100_24), by EMPA. However, areas for analysis were chosen based on the cracking associated with the β to α transition (as this is a clear visual indication of the presence of cristobalite) and, therefore, it is likely no β-cristobalite was analysed. EDS maps show much higher Al and Na concentrations in some areas, and it is possible some of these areas are chemically stabilised β-cristobalite. The reduction in peak intensities and peak broadening in both the IR and Raman spectra for doped samples compared to non-doped cristobalite (1600_4 or 1600_12) could indicate a change in the α-cristobalite structure (as discussed above), or could indicate the co-existence of α- and β-cristobalite; a steady change in intensities, frequencies and FWHM of IR and Raman peaks is observed in cristobalite heated towards the transition temperature, and has been attributed to the co-existence of α- and β-cristobalite within individual grains (Swainson et al., 2003). In Al-only doped samples, no peak was observed at 21.68° 2θ in the XRD pattern. Al-only doping does not lead to the stabilisation of β-cristobalite (Chao and Lu, 2002a). Therefore, the presence of this peak in Al and Na co-doped samples but not Al-only doped samples may support the stabilisation of β-cristobalite.

It is also possible that this peak represents a secondary population of impure α-cristobalite, as identification of β-cristobalite has not been confirmed by high-temperature XRD here and impure α-cristobalite can be mistaken for β-cristobalite based purely on peak position (Damby et al., 2014). Also, the low dopant concentrations compared to other studies make it unlikely that β-cristobalite has been stabilised here even though there may be localised high concentrations of impurities suggested above; previous studies using the dopant-sol/gel method are in good agreement that initial dopant concentrations >10 oxide wt.% Al+Na are needed to stabilise β-cristobalite. Another argument that β-cristobalite has not been stabilised in these samples is the alteration of bands in the IR and Raman spectra that differ from β-cristobalite, suggesting an impurity-specific alteration of the

α-cristobalite structure, rather than the retention of β-cristobalite alone. The lack of shoulder on the band at ~480 cm^{-1} in doped compared to non-doped cristobalite is similar to the transition to β-cristobalite, as two bands at 480 and 495 cm^{-1}, representing E and A_2 modes respectively, convert to only one IR-active band at 500 cm^{-1} in the β-cristobalite structure (Swainson et al., 2003). However, here, these bands, which represent O-T-O bending, shift to lower frequencies indicating they are also affected by the presence of Al and Na in a way dissimilar to just the β-cristobalite-like structure.

6.4.4 Crystal polymorph, abundance and crystallisation kinetics

During the production of the impure cristobalite and tridymite samples explained above and used for toxicological study (Chapter 7), different treatment temperatures were used allowing the effect of temperature and dopants on crystal polymorph and crystal abundance to be assessed. This provided insight to the crystallisation kinetics of cristobalite with and without dopants.

6.4.4.1 Effect of temperature on crystal polymorph

From XRD, it can be observed that, in non-doped samples, temperature determines the crystalline silica polymorph formed at a 12 h treatment time. At 900-1100 °C, tridymite and cristobalite were formed, where tridymite became more prominent at higher temperatures. It might be expected that tridymite would form at these temperatures, as they fall within the tridymite stability field (867-1470 °C (Heaney et al., 1994)) and may not have been able to undergo the reconstructive transition to quartz upon cooling, as the conversion rate is slow at these temperatures (Roy and Roy, 1964). The formation of cristobalite at 1600 °C can be explained in the same way, as the cristobalite stability field is 1470-1727 °C (Heaney et al., 1994). However, the formation of cristobalite at low temperatures (800 °C) cannot be explained this way.

It is known that cristobalite can form at metastable temperatures from volcanic samples and diatomaceous earth, where cristobalite forms at temperatures within the β-quartz and tridymite stability fields (see Chapter 4, Damby, 2012). In synthetic samples, cristobalite begins to crystallise from a silica sol at 800 °C with Na doping (Chao and Lu, 2000, Venezia et al., 2001). Here, cristobalite formation is seen in non-doped samples at 800 °C (Figure 6.2); its presence may be explained by the existence of small amounts of Na in the original silica sol up to 0.9 oxide wt.%, which may have acted to promote cristobalite stabilisation (Table 6.1). Concentrations as low as 1.3 or 1.5 oxide wt.% Na were shown to promote crystallisation in studies of Chao and Lu (2000) and Venezia et al. (2001) respectively. Crystallisation of cristobalite has also been shown to begin at 1100 °C from silicic acid, below its stability field, without impurities (Shinohara, 1990). The formation of cristobalite below its stability field here may also be explained by this system adhering to Ostwald's rule of stages, where the least stable polymorph is crystallised first and, subsequently, there is insufficient energy for the reconstructive transformation to the stable polymorph, as has previously been suggested for the formation of metastable cristobalite in volcanic domes (Horwell et al., 2013).

6.4.4.2 Effect of temperature on crystal abundance and crystallinity

Increasing the temperature increased the crystal abundance and degree of crystallinity of cristobalite (estimated by peak area and FWHM respectively), as shown by comparing non-doped cristobalite formed at 800 °C and 1600 °C for 12 h (Table 6.3). An increase in crystal abundance is seen in doped samples as the temperature increased, with maximum crystal abundance reached at 1100 °C, the highest temperature used (Table 6.3). As industrial and natural cristobalite is formed at metastable temperatures in the DE industry and in volcanic domes, the cristobalite formed in these environments is likely to be less well ordered than synthetic samples produced in the cristobalite stability field. Indeed, metastably formed cristobalite in natural samples is shown to have broad XRD

peaks indicating lower order of the cristobalite at lower formation temperatures (Damby et al., 2014).

6.4.4.3 Effect of doping on crystal phase and crystallisation kinetics

The crystallisation temperature of cristobalite varied depending on the amount of dopant added. As the amount of dopants increased, the crystallisation-onset temperature also increased (measureable quantities of cristobalite were produced at 900, 1000 and 1100 °C for samples doped with 2, 3, and 5 oxide wt.% Al+Na respectively (Figure 6.2)). It has been hypothesised that the presence of structural substitutions facilitates the metastable formation of cristobalite in natural samples of volcanic dome lava (Damby et al., 2014), and the addition of a Na-based flux during DE calcination, promotes the formation of cristobalite at ~1000 °C (Chapters 2 and 4). Other authors have also shown that doping synthetic samples allows cristobalite formation as low as 800 °C (Chao and Lu, 2000, Venezia et al., 2001). However, the results here suggest that increasing Al and Na impurities can actually prevent the formation of cristobalite at low temperatures. In Chao and Lu (2000), although the initial onset of cristobalite crystallisation occurred at progressively lower temperatures as the concentration of Na dopants was increased, the abundance of cristobalite plateaued at slightly lower concentrations in the more heavily doped samples than the less doped samples. Doping with Al-only has also previously been shown to decrease crystal abundance (Chao and Lu, 2002a). However, co-doping with Al and Na did not lead to a decrease in crystal abundance at higher dopant concentrations and no explanation is given as to why Al- or Na-only doping decreased crystal abundance (Chao and Lu, 2002a). A comparison of the synthetic sample doped with Al-only (3Al_1100_24) and Al+Na (5Al+Na_1100_24) treated under the same conditions, showed no increase in cristobalite abundance when Na was added (Table 6.3). Therefore, it is unknown why increased Al+Na doping would decrease crystal abundance here, and the apparent role of Na in promoting cristobalite formation in DE was not mirrored by these synthetic samples.

Cristobalite still formed at metastable conditions (<1100 °C), and is formed preferentially over tridymite throughout the tridymite stability field, when samples were doped. It is possible that tetrahedral Al and interstitial Na prevent the tridymite structure forming. Addition of $NaAlSiO_4$ to tridymite or cristobalite produced cristobalite at temperatures of 1320 °C, indicating impurities can decrease the cristobalite-tridymite transition temperature by at least 150 °C (no lower temperatures were assessed in this study) (Roy and Roy, 1964). Therefore, the addition of dopants here may have supressed the cristobalite-tridymite transition temperature so that cristobalite remains stable at room temperature. However, substitutions of impurities into the tridymite structure are also common (Heaney et al., 1994) and it has been argued that impurities are required for tridymite stabilisation (Deer et al., 2013). Therefore, it is it is not known why impurities cause the preferential crystallisation of cristobalite over tridymite. However, the preferential crystallisation of cristobalite over tridymite in the presence of impurities may explain why cristobalite is formed at temperatures <1000 °C in the DE industry or volcanic domes, as cristobalite is formed in the presence of impurities in these settings (Damby, 2012, Horwell et al., 2012, Nattrass et al., 2015).

6.5 Conclusions

The addition of Al and Na dopants to silica sol resulted in the formation of cristobalite with different amounts of structural substitutions; their inclusion dramatically altered the crystal structure and chemistry. Substitutions of Al and Na (up to 9 oxide wt.% Al+Na) into the α-cristobalite structure caused crystal lattice expansion. The α-cristobalite structure was also expanded by doping with Al-only, indicating Al substitution into the lattice, possibly facilitated by Na in the original material. Doping with Al-only produced samples of impure α-cristobalite only, whereas co-doping with Al and Na allowed the formation of albite in small quantities and other Al+Na-rich phases. It is also possible that β-cristobalite was stabilised in the Al and Na co-doped samples, however this could also be a

second population of impure α-cristobalite, and thermal treatments are needed to clarify what these phases are. This means that the samples produced for Chapter 7 were not pure cristobalite as was hoped, with the exception of 3Al_1100_24 and non-doped cristobalite samples treated at 1600 °C.

The polymorphs formed and crystallisation kinetics of cristobalite were also altered with changing temperature and addition of dopants. Only cristobalite formed at low (800 °C) and high (1600 °C) temperatures in non-doped samples, whereas tridymite was formed in its stability field (samples treated at 900-1100 °C). Doping increased the temperature needed to crystallise cristobalite but led to the preferential crystallisation of cristobalite over tridymite. As impurities are abundant in volcanic settings and DE deposits, this may explain why cristobalite is formed in these environments below its stability field.

The effect of dopants on the crystal structure, chemistry and the production of other mineral phases could all have implications for their surface reactivity and reactivity *in vitro*. Substitutions of Al and Na have been hypothesised to dampen cristobalite toxicity in DE and volcanic ash (Horwell et al., 2012, Nattrass et al., 2015), and the effect of the substitutional impurities on surface properties, surface reactivity and toxicity will be discussed in detail in Chapter 7.

References

BATES, J. B. 1972. Raman Spectra of α and β Cristobalite. *The Journal of Chemical Physics,* 57**,** 4042-4047.

CHAO, C. H. & LU, H. Y. 2000. Crystallization of Na2O-doped colloidal gel-derived silica. *Materials Science and Engineering a-Structural Materials Properties Microstructure and Processing,* 282**,** 123-130.

CHAO, C. H. & LU, H. Y. 2002a. beta-cristobalite stabilization in (Na2O+Al2O3)-added silica. *Metallurgical and Materials Transactions a-Physical Metallurgy and Materials Science,* 33**,** 2703-2711.

CHAO, C. H. & LU, H. Y. 2002b. Stress-induced beta ->alpha-cristobalite phase transformation in (Na2O+Al2O3)-codoped silica. *Materials Science and Engineering a-Structural Materials Properties Microstructure and Processing,* 328**,** 267-276.

CHERUKURI, S. C., PYE, L. D., CHAKRABORTY, I. N., CONDRATE, R. A., FERRARO, J. R., CORNILSEN, B. C. & MARTIN, K. 1985. The Vibrational Spectra and Normal Coordinate Analysis of 28Si- and 29Si-Substituted α-Cristobalite. *Spectroscopy Letters,* 18**,** 123-137.

DALBY, K. N., ANDERSON, A. J., MARIANO, A. N., GORDON, R. A., MAYANOVIC, R. A. & WIRTH, R. 2010. An investigation of cathodoluminescence in albite from the A-type Georgeville granite, Nova Scotia. *Lithos,* 114**,** 86-94.

DAMBY, D. E. 2012. *From Dome to Disease: The Respiratory Toxicity of Volcanic Cristobalite.* Durham theses, Durham University.

DAMBY, D. E., LLEWELLIN, E. W., HORWELL, C. J., WILLIAMSON, B. J., NAJORKA, J., CRESSEY, G. & CARPENTER, M. 2014. The [alpha]-[beta] phase transition in volcanic cristobalite. *Journal of Applied Crystallography,* 47.

DEER, W. A., HOWIE, R. A. & ZUSSMAN, J. 2013. *An Introduction to the Rock-forming Minerals*, Mineralogical Society of Great Britain & Ireland.

DUFFIN, R., GILMOUR, P. S., SCHINS, R. P. F., CLOUTER, A., GUY, K., BROWN, D. M., MACNEE, W., BORM, P. J., DONALDSON, K. & STONE, V. 2001. Aluminium Lactate Treatment of DQ12 Quartz Inhibits Its Ability to Cause Inflammation, Chemokine Expression, and Nuclear Factor-κB Activation. *Toxicology and Applied Pharmacology,* 176**,** 10-17.

ETCHEPARE, J., MERIAN, M. & KAPLAN, P. 1978. Vibrational normal modes of SiO2. II. Cristobalite and tridymite. *The Journal of Chemical Physics,* 68**,** 1531-1537.

FINNIE, K. S., THOMPSON, J. G. & WITHERS, R. L. 1994. Phase transitions in cristobalite and related structures studied by variable temperature infra-red emission spectroscopy. *Journal of Physics and Chemistry of Solids,* 55**,** 23-29.

FRONDEL, C. 1962. *The system of mineralogy, Vol. III The silica minerals,* New York, J. Wiley and Sons.

HEANEY, P. J., PREWITT, C. T. & GIBBS, G. V. 1994. *Silica: Physical Behavior, Geochemistry and Materials Applications,* Washington D.C., Mineralogical Society of America.

HEFFERAN, K. & O'BRIEN, J. 2010. *Earth Materials*, Wiley.

HOFMEISTER, A. M., ROSE, T. P., HOERING, T. C. & KUSHIRO, I. 1992. Infrared spectroscopy of natural, synthetic, and oxygen-18-substituted .alpha.-tridymite: structural implications. *The Journal of Physical Chemistry,* 96**,** 10213-10218.

HORWELL, C., WILLIAMSON, B., DONALDSON, K., LE BLOND, J., DAMBY, D. & BOWEN, L. 2012. The structure of volcanic cristobalite in relation to its toxicity; relevance for the variable crystalline silica hazard. *Particle and Fibre Toxicology,* 9**,** 44.

HORWELL, C., WILLIAMSON, B., LLEWELLIN, E., DAMBY, D. & BLOND, J. 2013. The nature and formation of cristobalite at the Soufrière Hills volcano, Montserrat: implications for the petrology and stability of silicic lava domes. *Bulletin of Volcanology,* 75**,** 1-19.

ICDD. 2015. *The International Centre for Diffraction Data* [Online]. http://www.icdd.com/: The International Centre for Diffraction Data. [Accessed 20/06/2015 2015].

KAYAMA, M., NISHIDO, H. & NINAGAWA, K. 2009. Effect of impurities on cathodoluminescence of tridymite and cristobalite. *Mineralogical Journal,* 104**,** 401-406.

KAYAMA, M., NISHIDO, H., TOYODA, S., KOMURO, K. & NINAGAWA, K. 2011. Radiation effects on cathodoluminescence of albite. *American Mineralogist,* 96**,** 1238-1247.

KINGMA, K. J. & HEMLEY, R. J. 1994. Raman spectroscopic study of microcrystalline silica. *American Mineralogist,* 79**,** 269-273.

LIPPINCOTT, E. R., VAN VALKENBURG, A., WEIR, C. E. & BUNTING, E. N. 1958. Infrared Studies on Polymorphs of Silicon Dioxide and Germanium Dioxide. *Journal of Research of the National Bureau of Standards,* 61**,** 61-70.

MCMILLAN, P. F., POE, B. T., GILLET, P. H. & REYNARD, B. 1994. A study of SiO2 glass and supercooled liquid to 1950 K via high-temperature Raman spectroscopy. *Geochimica et Cosmochimica Acta,* 58**,** 3653-3664.

NATTRASS, C., HORWELL, C. J. H., DAMBY, D. E. D., KERMANIZADEH, A., BROWN, D. M. & STONE, V. 2015. The global variability of diatomaceous earth toxicity: a physicochemical and in vitro investigation. *Journal of Occupational Medicine and Toxicology,* 10**,** 23.

PERNY, B., EBERHARDT, P., RAMSEYER, K., MULLIS, J. & PANKRATH, R. 1992. Microdistribution of Al, Li, and Na in alpha quartz; possible causes and correlation with short-lived cathodoluminescence. *American Mineralogist,* 77**,** 534-544.

PERROTTA, A. J., GRUBBS, D. K., MARTIN, E. S., DANDO, N. R., MCKINSTRY, H. A. & HUARG, C.-Y. 1989. Chemical Stabilization of β-Cristobalite. *Journal of the American Ceramic Society,* 72**,** 441-447.

RICHET, P. & MYSEN, B. O. 1999. High-temperature dynamics in cristobalite (SiO2) and Carnegieite (NaAlSiO4): A Raman Spectroscopy Study. *Geophysical Research Letters,* 26**,** 2283-2286.

RICHTER, D. K., GÖTTE, T. & HABERMANN, D. 2002. Cathodoluminescence of authigenic albite. *Sedimentary Geology,* 150**,** 367-374.

ROY, D. M. & ROY, R. 1964. Tridymite-Cristobalite Relations and Stable Solid Solutions. *The American Mineralogist,* 49**,** 952-962.

SALTZBERG, M. A., BORS, S. L., BERGNA, H. & WINCHESTER, S. C. 1992. Synthesis of Chemically Stabilized Cristobalite. *Journal of the American Ceramic Society,* 75**,** 89-95.

ŞAN, O. & ÖZGÜR, C. 2009. Investigation of a high stable β-cristobalite ceramic powder from CaO–Al2O3–SiO2 system. *Journal of the European Ceramic Society,* 29**,** 2945-2949.

SANDERS, M. J., LESLIE, M. & CATLOW, C. R. A. 1984. Interatomic potentials for SiO2. *Journal of the Chemical Society, Chemical Communications***,** 1271-1273.

SHACKELFORD, J. F. & DOREMUS, R. I. 2008. *Ceramic and Glass Materials: Structure, Properties and Processing,* New York, Springer Science+Business Media.

SHINOHARA, Y. 1990. Synthesis of well crystallized cristobalite as a reference mineral. *Industrial Health,* 28**,** 139-143.

STEVENS, S. J., HAND, R. J. & SHARP, J. H. 1997. Temperature dependence of the cristobalite α-β inversion. *Journal of thermal analysis,* 49**,** 1409-1415.

STONE, V., JONES, R., ROLLO, K., DUFFIN, R., DONALDSON, K. & BROWN, D. M. 2004. Effect of coal mine dust and clay extracts on the biological activity of the quartz surface. *Toxicology Letters,* 149**,** 255-259.

SWAINSON, I. P. & DOVE, M. T. 1995. On the Thermal Expansion of beta-Cristobalite. *Phys Chem Minerals,* 22**,** 61-65.

SWAINSON, I. P., DOVE, M. T. & PALMER, D. C. 2003. Infrared and Raman spectroscopy studies of the α–β phase transition in cristobalite. *Physics and Chemistry of Minerals,* 30**,** 353-365.

VENEZIA, A. M., LA PAROLA, V., LONGO, A. & MARTORANA, A. 2001. Effect of Alkali Ions on the Amorphous to Crystalline Phase Transition of Silica. *Journal of Solid State Chemistry,* 161**,** 373-378.

Chapter 7

The effect of impurities on the potential toxicity of crystalline silica

7.1 Introduction

The hazard posed by the inhalation of crystalline silica is well known and cristobalite and quartz are both carcinogenic (IARC, 1997). Numerous epidemiology studies highlight the potential for exposure to quartz-rich dusts to cause disease such as silicosis, or lung cancer in a number of industries, such as granite or coal mining (Donaldson and Borm, 1998). Cristobalite is less well studied, however, epidemiology studies of workers in the diatomaceous earth industry have shown the potential for these cristobalite-rich dusts to cause respiratory disease, lung and other cancers (see Chapter 2; Checkoway et al., 1993, Park et al., 2002, Rice et al., 2001). *In vitro* studies of cristobalite have also shown an increase in gene expression and cytokine release in macrophage and lung epithelium models (Perkins et al., 2012, Barrett et al., 1999), as well as inflammasome activation (Peeters et al., 2014). However, the mechanisms by which crystalline silica causes disease are complex, and are still not fully understood (see Chapter 2).

Despite crystalline silica clearly having the capability to cause lung disease, it has been described as 'a variable entity' (Donaldson and Borm, 1998, Chapter 2), with reviews of quartz toxicity highlighting the variability of its fibrogenic, mutagenic and carcinogenic potency (Donaldson and Borm, 1998, Meldrum and Howden, 2002, Mossman and Glenn, 2013). Fewer studies have been performed on cristobalite or tridymite. However, the toxicity of cristobalite has been shown to vary in the diatomaceous earth industry (Chapter 5, Nattrass et al., 2015), and exposure to cristobalite in

pottery workers did not cause any adverse effects (Cherry et al., 1998). Cristobalite-rich volcanic ash has also been shown to have low toxicity *in vitro* (Damby, 2012). The cause of this variability has been attributed to a number of factors, both inherent characteristics of the silica particles and external factors which can alter their surface reactivity (IARC, 1997). The crystalline silica polymorph may be important (King et al., 1953), however, studies suggest surface characteristics are more important in determining differences in crystalline silica toxicity (Mossman and Glenn, 2013, Elias et al., 2000).

Surface silanols and surface radicals have been linked with silica reactivity (Fubini, 1998, Fubini et al., 1995, Pavan et al., 2013). It is known that the age of the crystal surface can alter its reactivity, and that a freshly fractured surface can produce more free radicals than an aged surface (Vallyathan et al., 1988) (Chapter 2). Surface modifications have also been shown to alter the reactivity of the silica surface. Treatment of a quartz surface with Al lactate or PVNO has been shown to dampen its cytotoxicity, haemolytic potential or ability to damage DNA (Duffin et al., 2001, Knaapen et al., 2002, Stone et al., 2004, Nolan et al., 1981). Treatment with Fe has led to inconclusive results, in some cases causing an increase in reactivity, in others no change and in some cases a reduction in toxicity (Cullen et al., 1997, Fubini et al., 1995). In mixed dusts containing crystalline silica, the presence of other mineral and amorphous phases are thought to occlude the surface (Donaldson and Borm, 1998, Ghiazza et al., 2009, Horwell et al., 2012, Tourmann and Kaufmann, 1994), and may also interact with the silica surface, as clay extracts have been shown to dampen quartz toxicity (Stone et al., 2004).

In volcanic and diatomaceous earth samples, Al, Na, Fe and Ca impurities have been shown to reside in the crystal structure of cristobalite (Chapter 4, Horwell et al., 2012, Damby et al., 2014, Nattrass et al., 2015). It is hypothesised that these impurities can decrease the toxicity of the cristobalite in these samples in a similar way to treating the crystalline silica surface with Al. Due to confounding

factors, such as the presence of other minerals and differences in particle size and shape, the role of these structural impurities in controlling the toxicity of these dusts has not yet been determined. The aim of this study, therefore, is to address this important question through testing of the *in vitro* reactivity of synthetic cristobalite, with structural impurities introduced by systematic doping with incremental amounts of either Al and Na, or Al-only impurities (samples developed in Chapter 6). This enables the role of structural impurities in silica toxicity to be examined, and surface characterisation of these particles allows an insight into how impurities may alter crystalline silica toxicity. The aim of this chapter is to consider the effect of structural impurities on cristobalite toxicity, however, the fact that some of the samples produced also contained other minerals (e.g., albite; see Chapter 6), means that the presence of these minerals must be considered when interpreting the toxicological findings here.

7.2 Materials and methods

The method used to produce the crystalline silica samples for this study is described in Chapter 6 and all methods employed in this chapter are described in detail in Chapter 3. Here, a brief description of these methods and the samples chosen for analysis is given.

7.2.1 Samples

Twelve samples were chosen for the investigation of their *in vitro* toxicity (Table 7.1). Five non-doped samples were chosen: one tridymite-containing sample (1100_24; treated at 1100 °C for 24 h), three cristobalite samples produced at high temperature (1600_4, 1600_8, 1600_12; treated at 1600 °C for 4, 8 and 12 h), and one cristobalite sample produced at low temperature (800_12; treated at 800 °C for 12 h). These samples were selected to allow comparisons between cristobalite

with a high or low degree of crystallinity, and to compare to doped cristobalite. Cristobalite samples co-doped with the equivalent of 1, 2 and 3 wt.% Al_2O_3 plus Na_2O in a 1:1 molar ratio were chosen, heated at 1100 °C for a duration of 12 h (2Al+Na_1100_12, 3Al+Na_1100_12 and 5Al+Na_1100_12) or 24 h (2Al+Na_1100_24, 3Al+Na_1100_24 and 5Al+Na_1100_24), and a sample doped with only 3 wt.% Al_2O_3 (3Al_1100_24). Doped samples were chosen to assess the effect of structural impurities on crystalline silica reactivity. The starting materials (Ludox TM-40 colloidal silica, with and without impurities before heat treatment) were included as controls and are denoted as SS and 5Al+Na_SS.

Table 7.1: List of samples used for each analysis method. PSD = particle size distribution by laser diffraction, BET = surface area, Zeta pot. = zeta potential measured in water (W) or cell medium (M), SEM = particle images by scanning electron microscopy, EPR = electron paramagnetic resonance of the solid, Haem = haemolysis, Cytotox = cytotoxicity assays (alamarBlue®, LDH or WST-1).

Sample	Particle Characterisation					Toxicology					
	PSD	BET	Zeta pot.	SEM	EPR	Haem	Cytotox.	TNF-α	NF-κB	Cell imaging	Radical release
1600_4	X	X	M, W	X	X	X	X			X	X
1600_8	X	X				X					
1600_12	X	X	M	X		X	X	X	X	X	X
800_12	X	X				X					
1100_24	X	X	M, W	X		X	X	X	X	X	X
2Al+Na_1100_12	X	X				X					
3Al+Na_1100_12	X	X				X					
5Al+Na_1100_12	X	X				X					
2Al+Na_1100_24	X	X	M	X		X	X	X		X	
3Al+Na_1100_24	X	X	M	X		X	X			X	
5Al+Na_1100_24	X	X	M, W	X	X	X	X	X	X	X	X
3Al_1100_24	X	X	M, W	X		X	X	X	X	X	X
SS		X	M			X	X				
5Al+Na_SS		X	M			X	X				
DQ12		X	M			X	X	X	X	X	
Cristobalite standard		X				X					
TiO_2			M			X	X	X			

7.2.2 Particle characterisation

The crystalline silica samples chosen were ground from a pellet into a fine powder using cryogenic grinding (see Chapter 3). Particle size distributions were analysed by laser diffraction using a Coulter LS analyser (Durham University), with polarization intensity differentiation scattering (PIDS). Data were analysed by Fraunhofer theory and are presented as cumulative volume %. Particle size was also qualitatively assessed by SEM imaging. Surface area was measured by the BET method of nitrogen adsorption and was used to calculate the surface area dose for *in vitro* studies. Zeta potential measurements were made to assess the effect of dopants on surface charge on a Malvern Nanosizer instrument from pH 0.5 to 8.5. Two non-doped samples (1600_4 and 1100_24) and two doped (5Al+Na_1100_24 and 3Al_1100_24) samples suspended in water at 0.6 mg/ml were analysed. The pH of the samples in suspension in water was also recorded before the pH was altered. Zeta-potential measurements in water under these conditions allow differences in the surface structure between doped and non-doped samples to be assessed. Zeta potential measurements complete medium were performed to determine how surface charge may affect the cytotoxicity of the particles in the assays used (below). Samples were analysed after 20 minutes of sonication at concentrations of 62 µg/ml, the conditions used in the cytotoxicity assays.

EPR of the solid in vacuum at 77 K using a Bruker EMX spectrometer (Università degli Studi di Torino) was used to measure silica surface radicals of a non-doped sample (1600_4) and a doped sample (5Al+Na_1100_24) to see the effect of dopants on surface radicals. To determine paramagnetic centres, a large scan range was used (6000 G), to observe Fe and Al based centres and $Si^{\bullet}$. A higher resolution scan was also performed over 200 G focussing on Si- and O-based radicals. At this resolution, the microwave power was progressively decreased (from 20 to 0.001 mV) to increase the visibility of saturated signals.

7.2.3 Free radical generation

The ability of samples to generate free radicals was assessed using EPR spin trapping. For analysis of $HO^{\bullet}$ generation, 250 µl phosphate buffer solution, 125 µl DMPO and 250 µl H_2O_2 were added to 37.5 mg of sample. For $COO^{\bullet}$ generation, 125 µl of DMPO and 125 µl of 1.36 g sodium formate in 10 ml 0.5 M phosphate buffer solution were added to 37.5 mg of sample. Negative controls were produced in the same way but without particles. The suspension was continually stirred in the dark and aliquots taken at 10, 30 and 60 minutes for analysis using a Miniscope MS100.

7.2.4 In vitro toxicology

Haemolysis was performed for all samples by treating sheep red blood cells with 150 µl of 63-1000 µg/ml powder for 30 minutes. A cristobalite standard was also employed in this assay, produced from heating sandstone quartz and fully characterised by Michnowicz (2014), to compare to the cristobalite samples. Results are presented based on both mass and surface area dose. Cytotoxicity was measured using alamarBlue®, WST-1 (measures of mitochondrial enzyme activity; only one repeat for WST-1 assay) and lactate dehydrogenase (LDH; a measure of membrane integrity) assays (Heriot Watt University) by treatment of J774 macrophages with seven selected samples for 24 h. In the alamarBlue® assay, an exposure time of 48 h was also tested to assess if impurities are removed from the surface over this period. Leachate solutions were also assessed by the alamarBlue® assay, to constrain the contribution of soluble components to observed reactivity. Particle suspensions at 500 µg/ml (the top concentration tested) in complete medium were incubated for 24 h and centrifuged at 10000 rpm for 10 minutes to remove particles. The leachate was then used in the alamarBlue® assay at 24 h exposure. Imaging of untreated and particle-treated cells post-24 h exposure was performed using light microscopy. The samples selected for cytotoxicity assays were two high temperature non-doped cristobalite samples (1600_4, 1600_12), non-doped tridymite

(1100_24), and three cristobalite samples doped with incremental amounts of Al and Na (2Al+Na_1100_24, 3Al+Na_1100_24 and 5Al+Na_1100_24), and cristobalite doped with Al only (3Al_1100_24).

Tumour necrosis factor alpha (TNF-α) was measured as a marker of inflammation as TNF-α is a pro-inflammatory cytokine associated with silica induced toxicity (Mossman and Glenn, 2013, Piguet et al., 1990). TNF-α was measured in the supernatant of cell cultures treated with 125 µg/ml or lower of the samples for 4 and 24 h using BD™ Cytometric Bead Array cytokine flex sets according to the manufacturer's instructions (BD Biosciences, Heriot Watt University).

NF-κB activation was measured in treated J774 macrophages post-exposure to treatment with 250 µl particle suspensions (125 µg/ml) for 4 h, using a staining method and fluorescence microscopy (Zeiss Axioscope) to determine if NF-κB had translocated into the nuclei (activated). Images were analysed using the method employed by Noursadeghi et al. (2008) using ImageJ image analysis software.

7.2.5 Statistical analyses

Student's t-test and ANOVA general linear model with a Tukey's post-hoc test were performed to determine the significance of differences among samples in the *in vitro* assays (Minitab 15). Significance levels were set at * $p = <0.05$, ** $p = <0.01$, *** $p = <0.001$.

7.3 Results

7.3.1 Particle characterisation

Median particle diameter was between 5 and 7 μm for doped samples and 1600_4 (Table 7.2). The other non-doped samples were slightly coarser, on average, with median diameters between 9-13 μm. Most samples were 100% <30 μm and all were 100% <70 μm (Figure 7.1a), had between 45 and 72 cumulative vol. % particles <10 μm (the thoracic fraction) and 18-44 cumulative vol. % < 4 μm (respirable fraction) (Table 7.2). However, by SEM imaging, very few particles were observed that were >5 μm (Figure 7.2); as laser diffraction data are presented as cumulative volume %, this is heavily mass biased and so cannot be compared directly to number % values produced by SEM image analysis. These results suggest that representative inhalable powders have been successfully produced for experimental use. The particle size distributions were bimodal for most samples (Figure 7.1b).

Table 7.2: Particle size (laser diffraction), surface area (BET) and surface charge in complete medium (RPMI + 10 % foetal bovine serum + antibiotics; zeta potential) for non-doped and doped samples, starting material and standards. * Data taken from Michnowicz (2014).

Sample	Particle size distribution			Surface area		Surface charge (medium)	
	Median particle diameter (µm)	Cumulative vol. % <4 µm	<10 µm	(m^2/g)	s.d.	(mV)	s.d.
1600_4	7.3	36.6	62.6	4.0	0.1	-11.4	0.8
1600_8	9.3	27.8	56.5	1.0	0.1		
1600_12	10.9	22.6	50.3	0.9	0.1	-9.8	1.1
800_12	13.1	18.1	44.6	8.1	1.2		
1100_24	8.9	31.3	55.9	4.0	0.5	-11.1	0.6
2Al+Na_1100_12	7.4	30.3	56.2	3.0	0.1		
3Al+Na_1100_12	5.9	41.5	70.5	5.0	0.1		
5Al+Na_1100_12	5.4	43.6	71.9	4.2	0.5		
2Al+Na_1100_24	7.4	36.5	61.4	2.1	0.2	-9.8	0.8
3Al+Na_1100_24	6.4	37.0	60.4	4.7	0.0	-10.7	1.1
5Al+Na_1100_24	6.6	35.9	62.1	2.7	0.1	-10.0	0.8
3Al_1100_24	6.0	42.0	68.9	4.9	0.2	-10.7	1.2
SS				94.6	2.8	-9.5	0.8
5Al+Na_SS				87.0	0.8	-9.7	1.0
DQ12				9.2	0.2	-10.5	0.8
Cristobalite standard		8.4*	18.0*	2.3			
TiO_2						-9.8	1.4

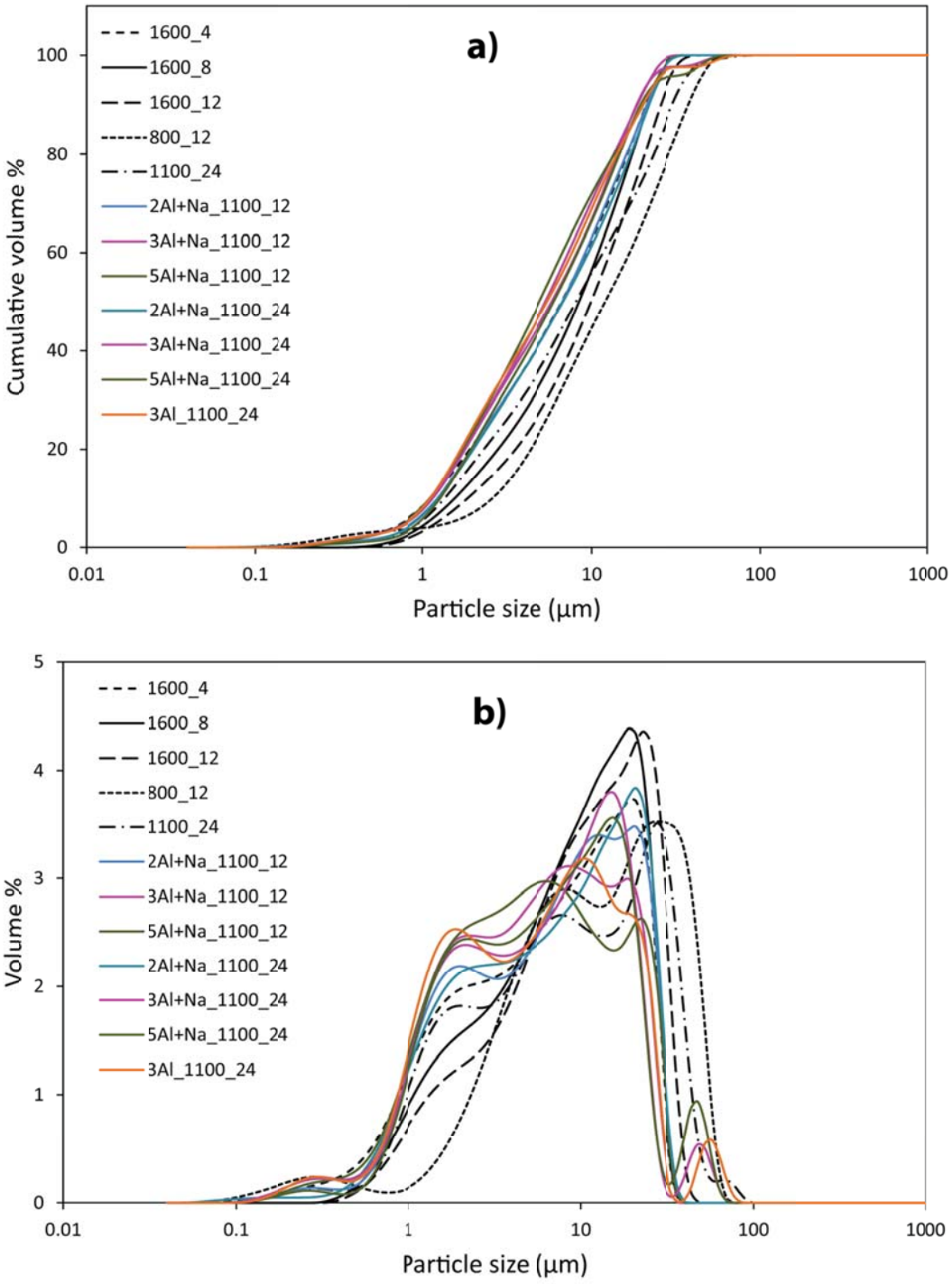

Figure 7.1: Particle size distribution of non-doped and doped crystalline silica ground cryogenically presented as **a)** cumulative volume % and **b)** volume %.

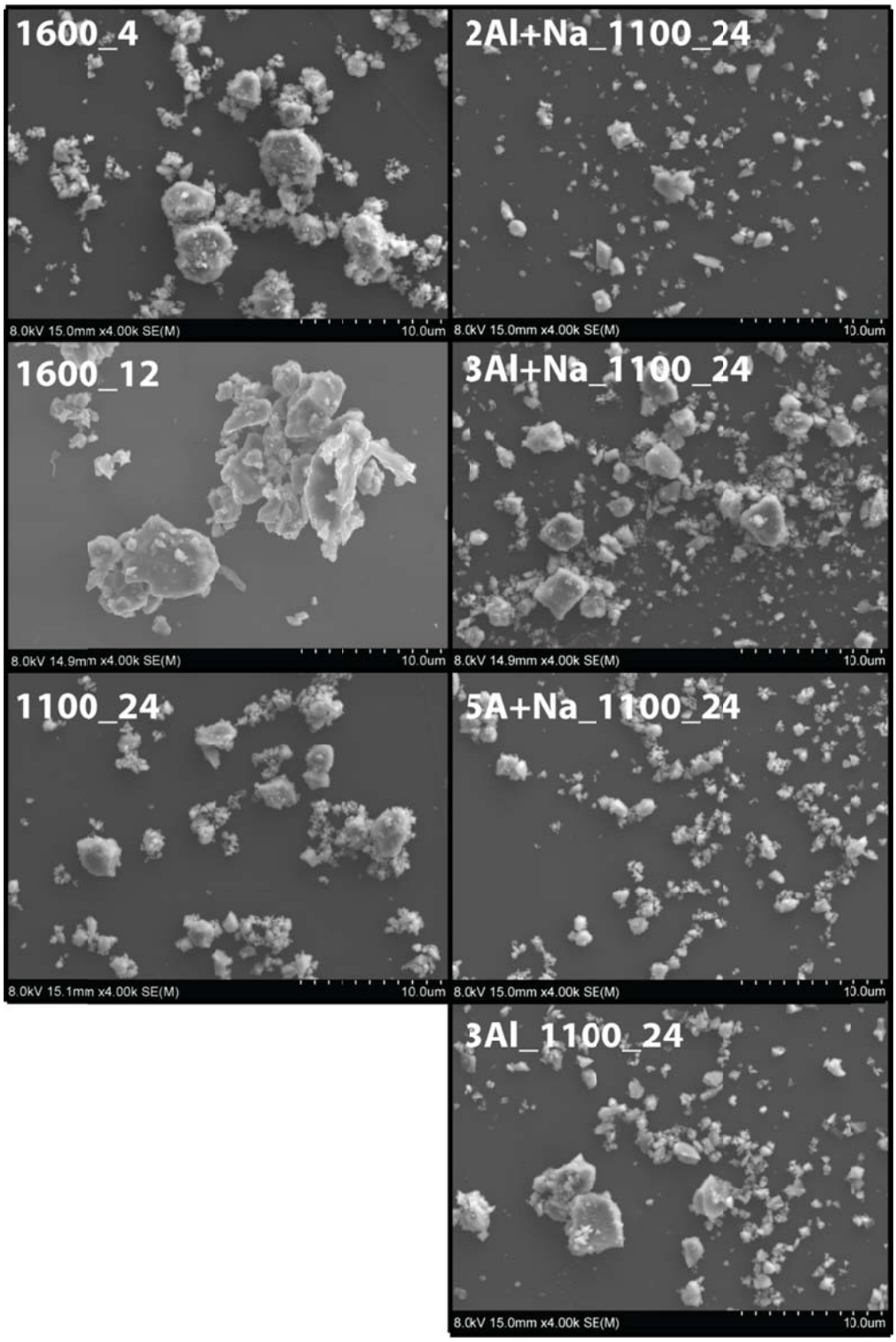

Figure 7.2: Representative scanning electron microscopy images of particles used in cytotoxicity assays.

Surface area varied substantially amongst the synthesised samples, ranging from 1 to 8 m^2/g, but was at least 10 times higher in the starting materials (Table 7.2). Surface charge for selected samples measured in water, from 0.5-8.5 pH, is shown in Figure 7.3. All samples had negative zeta-potential at all pH values. The two non-doped samples had a zeta-potential of >-3.8 at pH ~0.5, whereas doped samples were <-7.1 mV. The most prominent difference between non-doped and doped samples is the plateau in the zeta potential observed between pH ~2 and 3.5 for doped samples, but not in non-doped samples (1600_4, 1100_24). The two non-doped samples had a starting pH of 7, whereas both doped samples had a pH of 6.

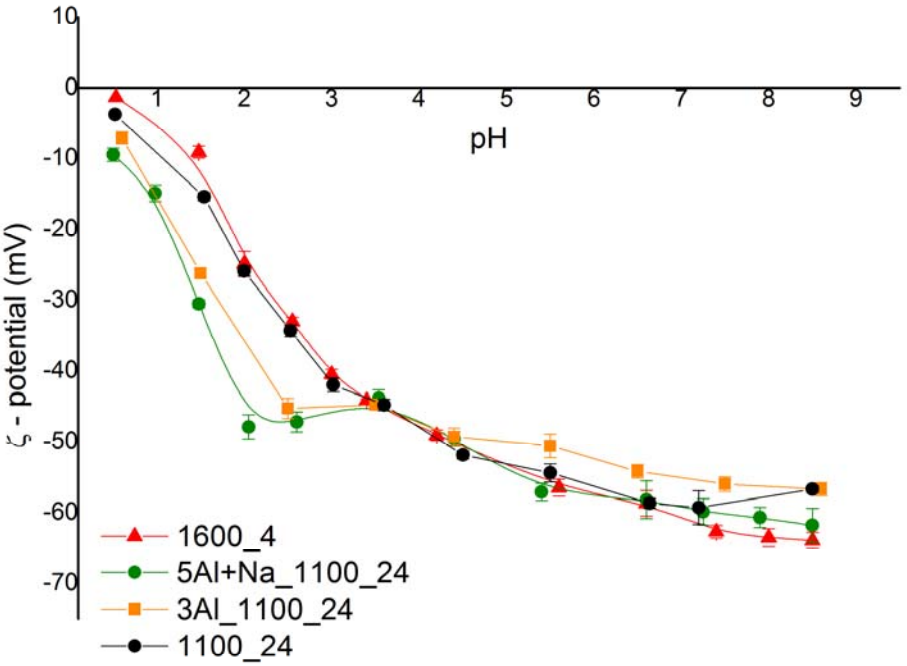

Figure 7.3: Zeta potential measurements for non-doped tridymite (1100_24), non-doped cristobalite (1600_4) and doped cristobalite (5Al+Na_1100_24 and 3Al_1100_24) over pH range of 0.5-8.5 in water.

Surface charge, as determined by zeta potential measurements in complete medium at ~pH 7, fell between -9.5 and -11.4 mV for all samples and standards (Table 7.2). These are not comparable to the zeta potential measurements of particles in solution in Figure 7.3, as different dispersants can

alter the surface charge and different masses of material were used in each instance. In medium, a concentration of 62 μg/ml was used as a mid-range dose used in toxicology experiments, whereas, in water, 0.6 mg/ml was used to achieve the best concentration for accurate characterisation.

7.3.1.1 Surface radicals

EPR was used to detect paramagnetic centres in a non-doped cristobalite (1600_4) and a cristobalite doped with Al+Na (5Al+Na_1100_24). Paramagnetic centres detected over 6000 G at 77 K and 10 mW are shown in the EPR spectra in Figure 7.4.

The spectra of both non-doped and doped cristobalite are characterized by two distinct features, which occur at effective *g* values (see Chapter 3) of around 2.0 and $3.0 < g < 4.5$ (Figure 7.4). The first spectral feature at $g \approx 2$ can be assigned to silicon- and oxygen-based radicals produced by the cleavage of Si–O–Si bonds during grinding, and subsequent reaction with atmospheric components, while the second, at $3.0 < g < 4.5$, is associated with paramagnetic metal impurities. Non-doped and doped cristobalite exhibited similar spectral patterns but there was a remarkable reduction of the intensity and a very slight broadening of the signals in the doped sample compared to those of the non-doped cristobalite.

The signal at $g = 4.3$ is indicative of iron-based paramagnetic centres, in particular, of isolated tetrahedral or octahedral Fe^{3+} under rhombic distortion (Bordiga et al., 1996, Decyk et al., 2003, Parmaliana et al., 2002), as Fe is present in the starting material (Table 6.1, Chapter 6). These centres have been altered by doping with Al+Na, whereby the peak at $g = 4.3$ has broadened and reduced in intensity.

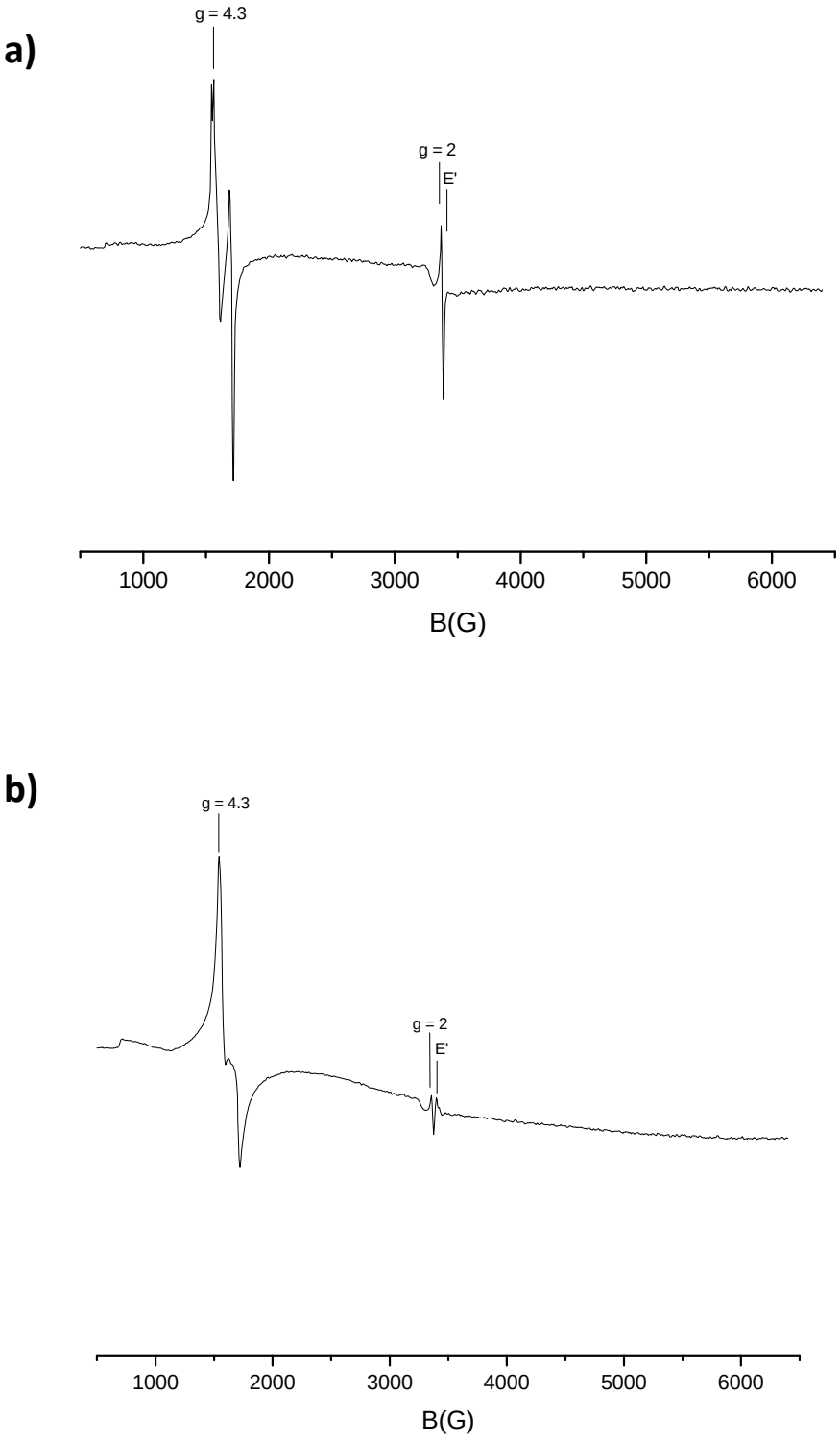

Figure 7.4: EPR spectra of **a)** non-doped cristobalite (1600_4) and **b)** Al+Na doped cristobalite (5Al+Na_1100_24) at 10 mW and 77 K over 6000 G.

At *g*≈ 2 the signal for silicon and oxygen based surface radicals is observed in both spectra. This is shown at higher resolution in Figure 7.5, where spectra are normalized by intensity and converted to g-factor. At high microwave power (>1 mW) complex signals are shown around *g*≈ 2 associated to the superimposition of Si and O based radicals (Costa et al., 1991, Fubini et al., 1989). By reducing the microwave power the complex signals begin to deconvolve. At microwave power >1 mW, a shoulder at g=2.007 and a signal at g=1.987 were observed in doped but not non-doped samples. As the microwave power is decreased, saturated signals, such as $SiO^{\bullet}$, $SiO_2^{\bullet}$, $SiO_3^{\bullet}$ and $O_2^{\bullet\,-}$, are decreased in intensity, leaving the $Si^{\bullet}$ (E') centre signal which falls at 2.000 and 2.0017 (Fubini et al., 1987) and making this more visible. The E' centre is clearly visible in both the doped and non-doped samples below 0.01 mW.

7.3.2 Free radical release

The EPR spin trapping technique showed that all samples analysed produced $HO^{\bullet}$ in low quantities by 60 minutes exposure to H_2O_2 (Figure 7.6). The 1600_12 sample produced slightly more $HO^{\bullet}$ than other samples, as determined by peak intensity, however, the quantities were still low overall. There was no detectable $COO^{\bullet}$ release from all samples except 5Al+Na_1100_25, where a slight signal was detected (Figure 7.7).

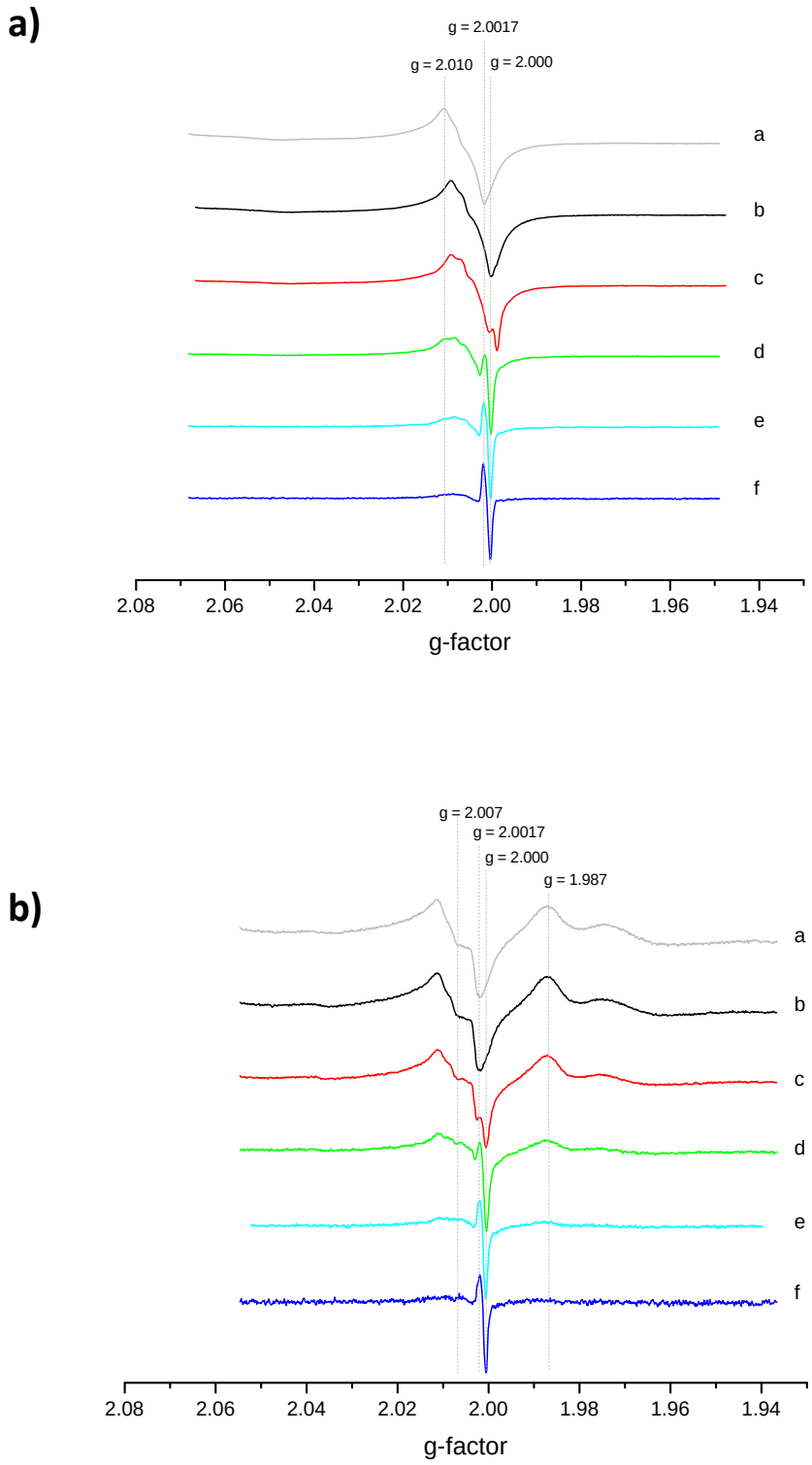

Figure 7.5: EPR spectra of **a)** non-doped cristobalite (1600_4) and **b)** Al+Na doped cristobalite (5Al+Na_1100_24) at 77 K over 200 G at microwave powers of 20 (a), 10 (b), 1 (c), 0.1 (d), 0.01 (e) and 0.001 (f) mW.

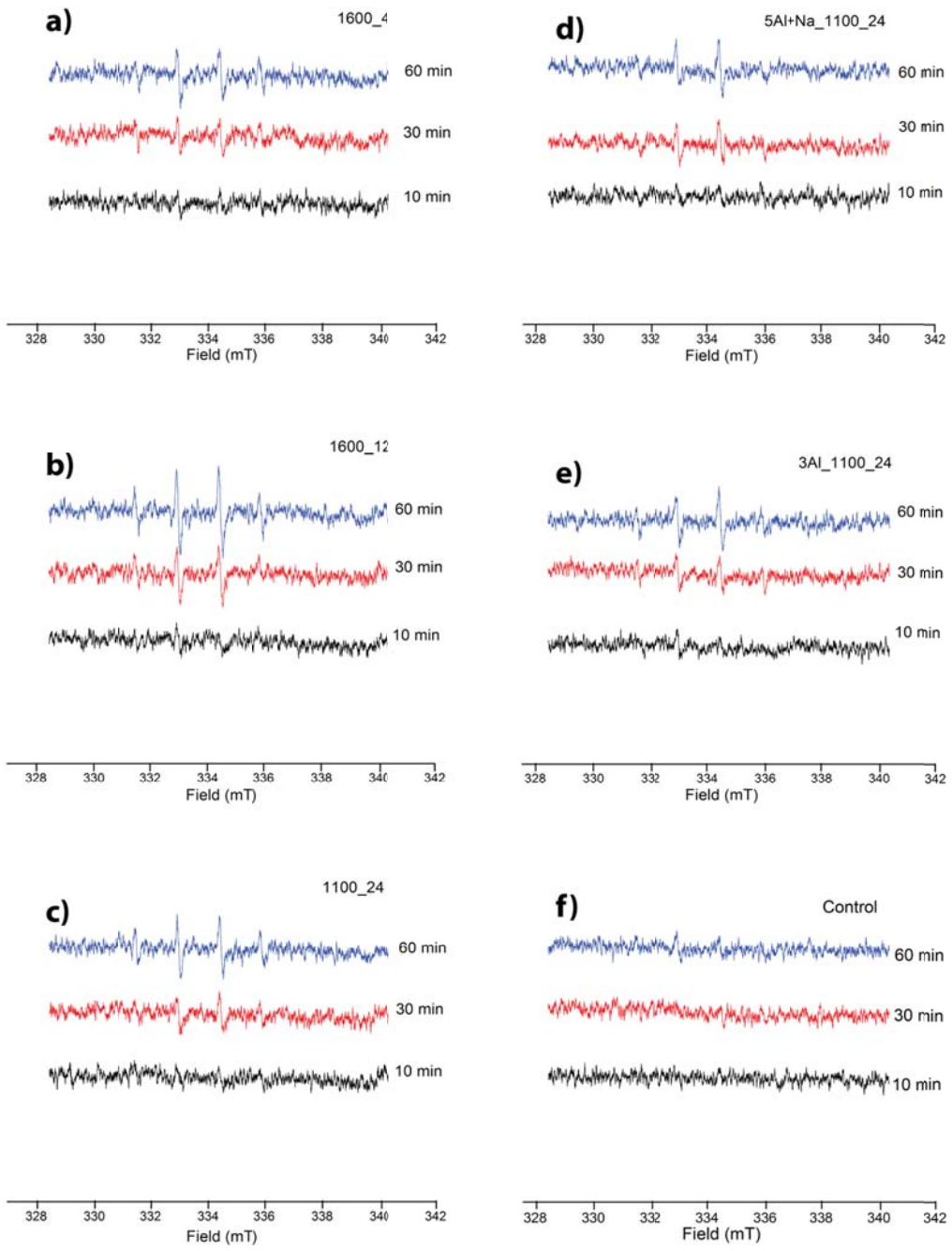

Figure 7.6: Release of hydroxyl radicals (EPR) from the surface of synthetic crystalline silica samples. **a)**-**b)** non-doped cristobalite, **c)** non-doped tridymite, **d)** A**l** and Na doped cristobalite, **e)** Al doped cristobalite, and **f)** the negative control (particle-free suspension) at 10, 30 and 60 minutes exposure to H_2O_2.

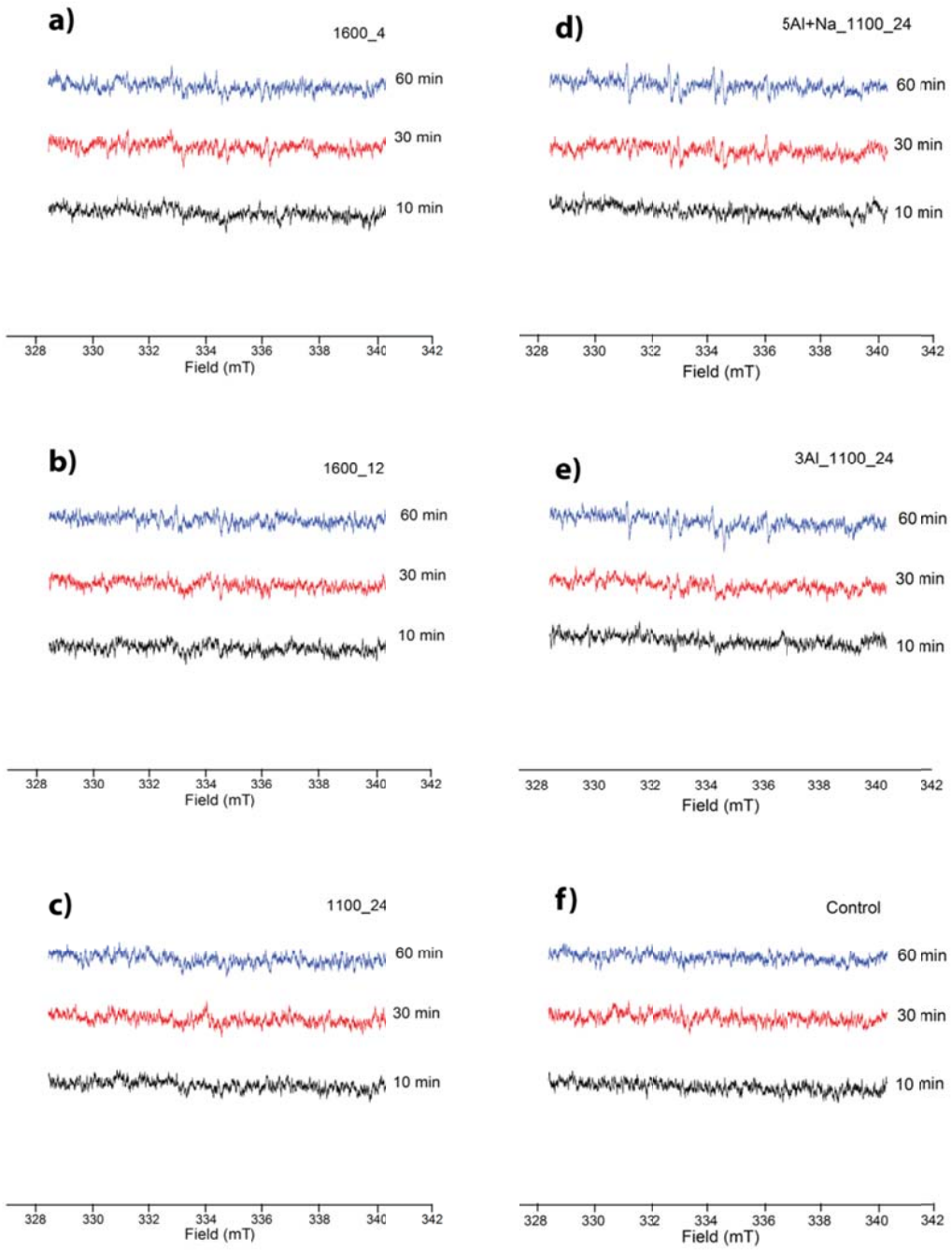

Figure 7.7: Release of carboxyl radicals (EPR) from the surface of synthetic crystalline silica samples. **a)**-**b)** non-doped cristobalite, **c)** non-doped tridymite, **d)** A**l** and Na doped cristobalite, **e)** Al doped cristobalite, and **f)** the negative control (particle-free suspension) at 10, 30 and 60 minutes exposure to sodium formate.

7.3.3 Haemolysis

Most samples showed a dose-dependent increase in haemolysis, with the exception of the Al-only doped sample (3Al_1100_24), which did not elicit any haemolytic response at the doses tested (Figure 7.8). Sample 1100_24 was the most haemolytic sample and was equally as haemolytic as DQ12 by mass dose (Figure 7.8a). Haemolytic potential varied by mass and surface area dose (Figure 7.8), due to large differences in the surface area between samples (Table 7.2).

7.3.3.1 Effect of temperature

In Figure 7.8a-b, the effect of formation temperature of non-doped cristobalite on haemolytic potency can be observed. Samples heated at lower temperatures (800 and 1100 °C; 800_12 and 1100_24) were more haemolytic than those heated at 1600 °C (1600_4, 1600_8, 1600_12) on a mass dose basis (Figure 7.8a). At the highest concentration, 1100_24 was 4-5 times more haemolytic than samples heated at 1600 °C and 800_12 was 3 times as haemolytic as 1600_12.

The trends observed by mass dose were not observed when surface area dose was considered (Figure 7.8b). Non-doped samples heated at 1600 °C for >8 h and 1100_24 were more haemolytic than those heated at 800 °C for 12 h and at 1600 °C for 4 h.

7.3.3.2 Effect of time

For non-doped samples heated at 1600 °C there was no difference in haemolytic potential between samples treated for 4, 8 or 12 h by mass dose (Figure 7.8a). However, when surface area dose was

considered, samples heated for >8 h were more haemolytic than the sample heated for only 4 h (Figure 7.8b).

For doped samples, there was no significant difference between the haemolytic potential of samples treated for 12 or 24 h at 1100 °C on a mass dose basis (Figure 7.8c). By surface area dose, 3Al+Na_1100_24 was less haemolytic than 3Al+Na_1100_12; however, this trend could not be extended to the samples treated with 2Al+Na and 5Al+Na (Figure 7.8d).

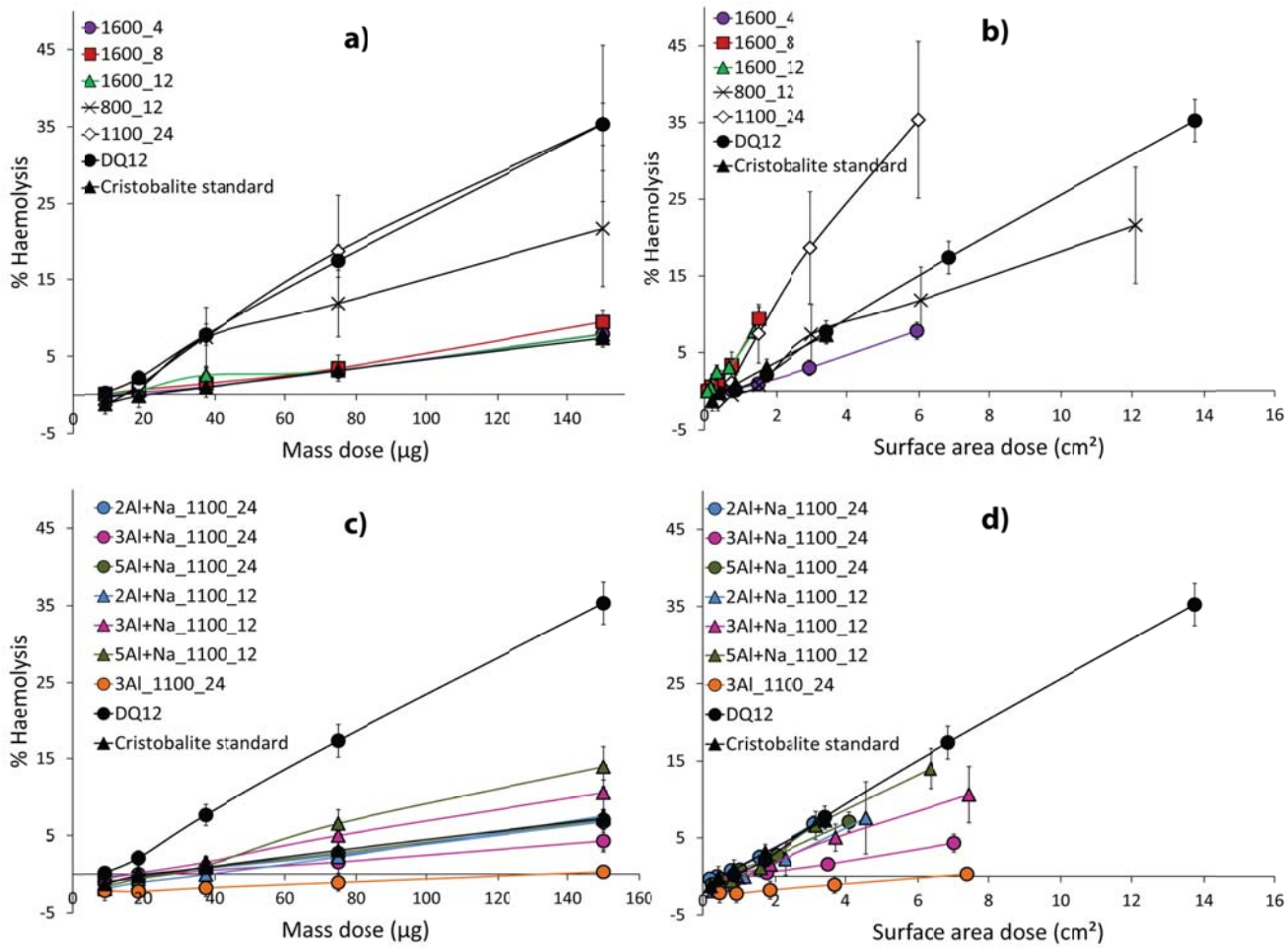

Figure 7.8: Haemolytic potential of crystalline silica samples. Per cent haemolysis relative to an untreated control, of sheep red blood cells post-exposure to **a-b)** non-doped, and **c-d)** doped samples by mass dose (left) and surface area dose (right). DQ12 and cristobalite standards included for comparisons. Error bars represent standard error (n=4).

7.3.3.3 Effect of dopants

Doping with Al and Na decreased the haemolytic potential of the synthetic samples. A comparison of the 1100 °C samples (Figure 7.8) shows a decrease of >28 % haemolysis, at the top dose, with doping (2Al+Na_1100_24, 3Al+Na_1100_24, 5Al+Na_1100_24; Figure 7.8c) compared to the non-doped sample (1100_24; Figure 7.8a); however, there is no difference between doping at 2, 3 or 5 oxide wt. % Al+Na. Doping with Al-only (3Al_1100_24) eliminated the haemolytic potential altogether. This trend was observed for both mass and surface area doses (Figure 7.8).

On a surface area dose basis, non-doped cristobalite, heated at 1600 °C for 8 and 12 h (1600_8, 1600_12), was as haemolytic as the non-doped tridymite (1100_24) (Figure 7.8b), whereas doped samples heated for 12 or 24 h at 1100 °C were less haemolytic (Figures 7.8d). However, non-doped cristobalite heated at 800 °C (800_12) or for only 4 h (1600_4) were not different in haemolytic potential to doped samples (Figure 7.8b and d).

The starting materials, non-doped dried silica sol (SS) and doped dried silica sol (5Al+Na_SS), were as haemolytic as the cristobalite standard by mass dose, however, due to their large surface area (Table 7.2), had very low reactivity by surface area dose (Figure 7.9).

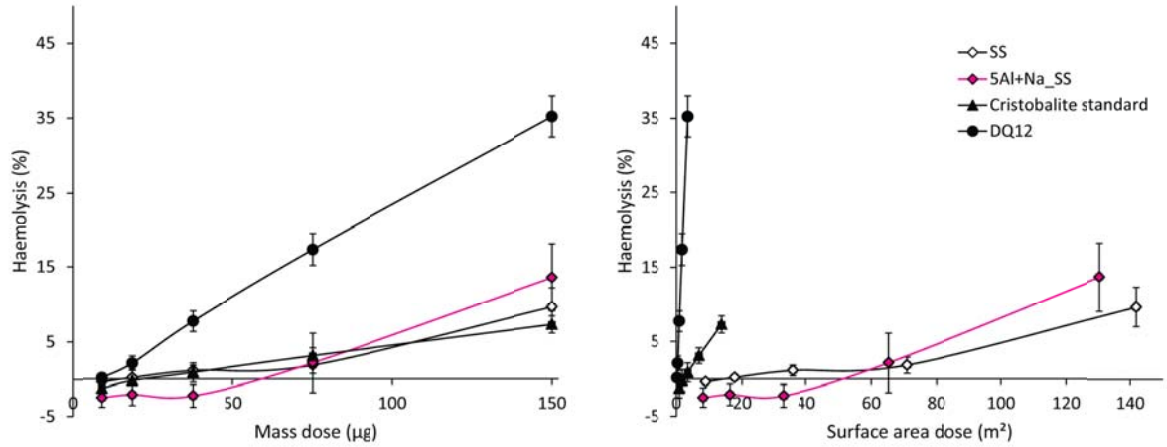

Figure 7.9: Haemolytic potential of starting materials. Per cent haemolysis relative to an untreated control, of sheep red blood cells post-exposure to non-doped (SS) and doped (5Al+Na_SS) starting materials by mass dose and surface area dose, compared to DQ12 and the cristobalite standard. Error bars represent standard error (n=4).

7.3.4 Cytotoxicity

7.3.4.1 AlamarBlue® assay

As cell viability of J774 macrophages only differed from the untreated control post-exposure to the top dose of sample particles, this is the only dose presented (Figure 7.10; other data available in Appendix 2). Only non-doped samples (1100_24 and 1600_12) showed a significant decrease in cell viability measured by the alamarBlue® assay at 24 hour exposure. All other samples did not differ from the untreated control. Only 1600_4, 1100_24, 3Al_1100_24 and DQ12 showed a decrease in cell viability at 48 h compared to 24 h exposure. However, 1600_4 and 3Al_1100_24 still did not differ from the negative control. Leachates and the starting materials (SS and 5Al+Na_SS) were non-reactive in the alamarBlue® assay (data in Appendix 2).

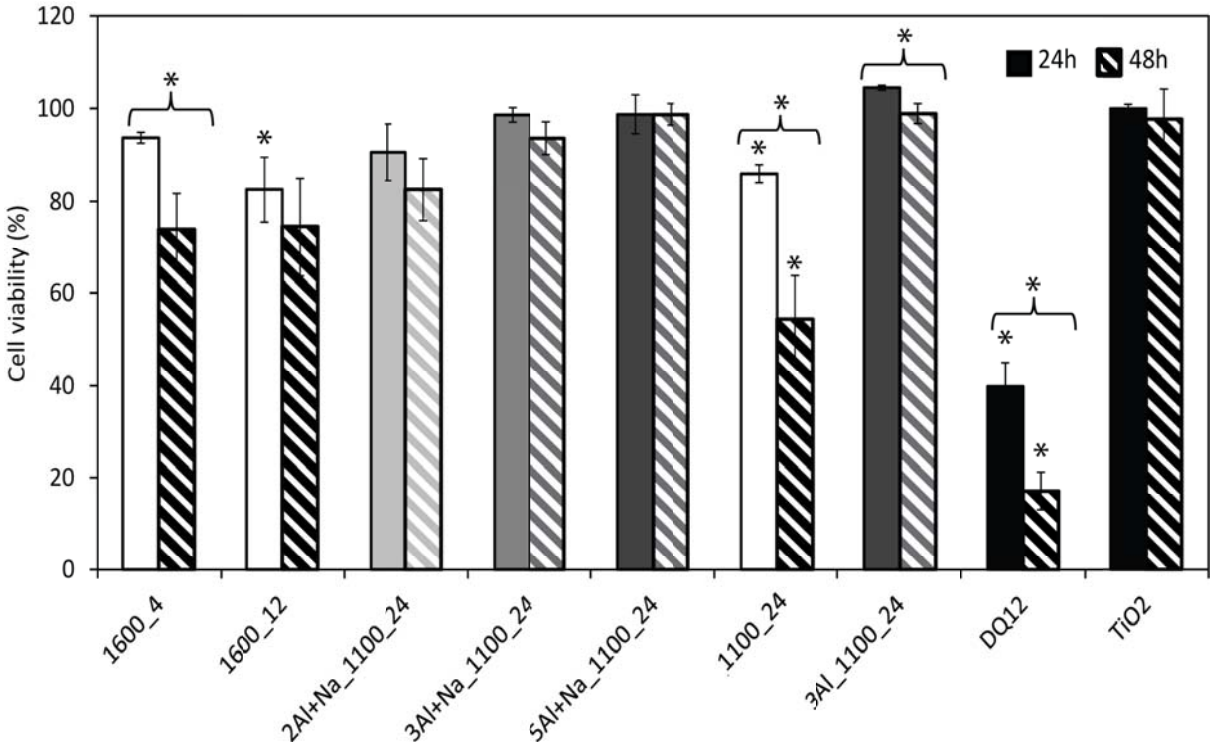

Figure 7.10: Cell viability of J774 macrophages treated with crystalline silica samples measured by the alamarBlue® assay. Cell viability compared to an untreated control of J774 macrophages treated with 500 µg/ml non-doped samples (white), doped samples (grey), and standards (black) for 24 h (solid) or 48 h (striped). Error bars represent standard error (n=4). * p = <0.05 difference from untreated control, brackets indicate significant differences between exposure for 24 or 48 h.

7.3.4.2 Lactate dehydrogenase assay

The LDH assay was only performed for a 24 h exposure. Sample-induced cytotoxicity was not significantly different from the untreated control at concentrations 125 µg/ml and below, so these are not shown (Figure 7.11; other data in Appendix 2). At 250 µg/ml there was significant cytotoxicity caused by exposure to all non-doped samples and 2Al+Na_1100_24 only, whereas samples treated with >3 oxide wt.% Al or Al+Na were non-cytotoxic. On treatment with 500 µg/ml, all samples were as cytotoxic as the positive control except 3Al_1100_24.

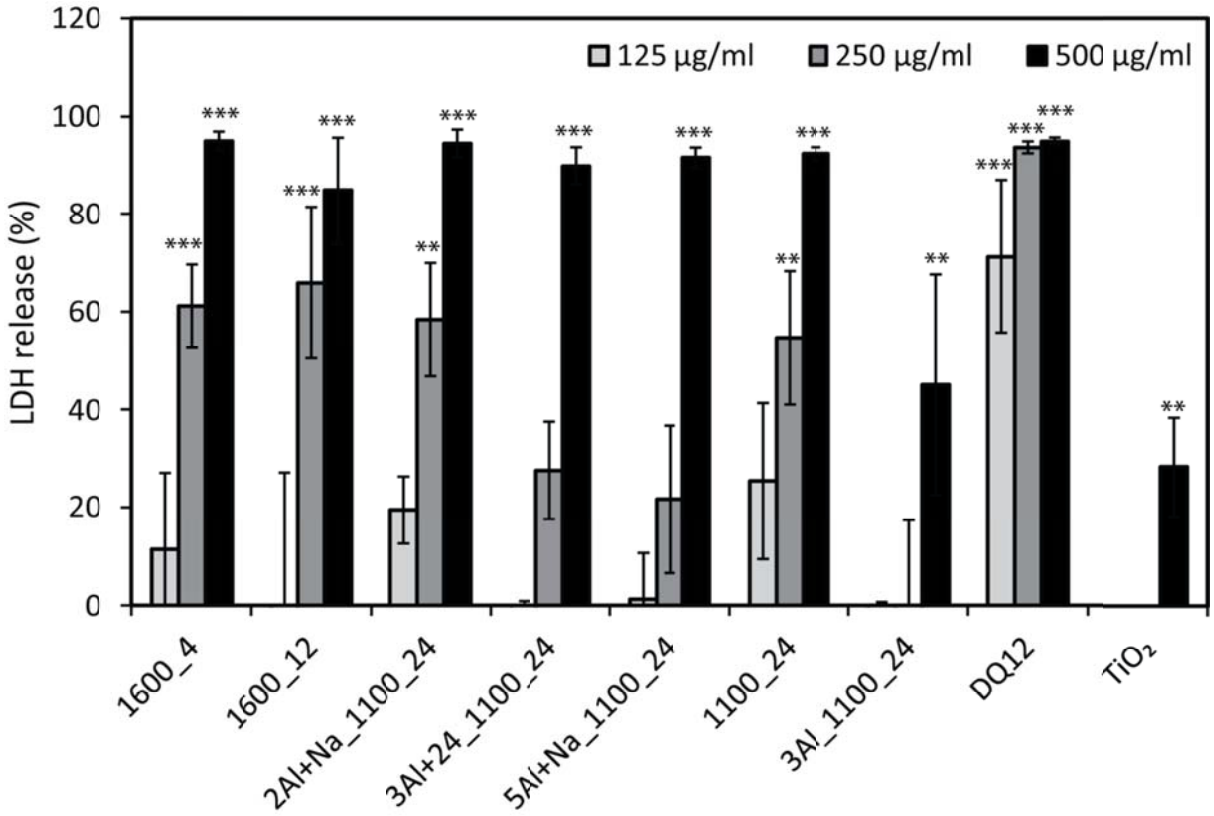

Figure 7.11: Cytotoxicity of crystalline silica samples to J774 macrophages measured by the LDH assay. LDH release as a percentage of a positive and untreated control for J774 macrophages treated with 125-500 µg/ml sample concentrations for 24 h. Error bars represent standard error (n=4). * p = <0.05, ** p = <0.01, *** p = <0.001 difference from untreated control.

7.3.4.3 WST-1 assay

The WST-1 assay was performed for an exposure of 24 h only. A decrease in cell viability was only seen at the top concentration tested so only this concentration is shown (Figure 7.12; other data in Appendix 2). All samples, with the exception of 3Al_1100_24, showed a significant decrease in cell viability compared to the untreated control. Samples 3Al_1100_24 and 5Al+Na_1100_24 were the least cytotoxic and cell viability remained >91%. 1100_24 was the most cytotoxic sample with cell viability reduced to 28%.

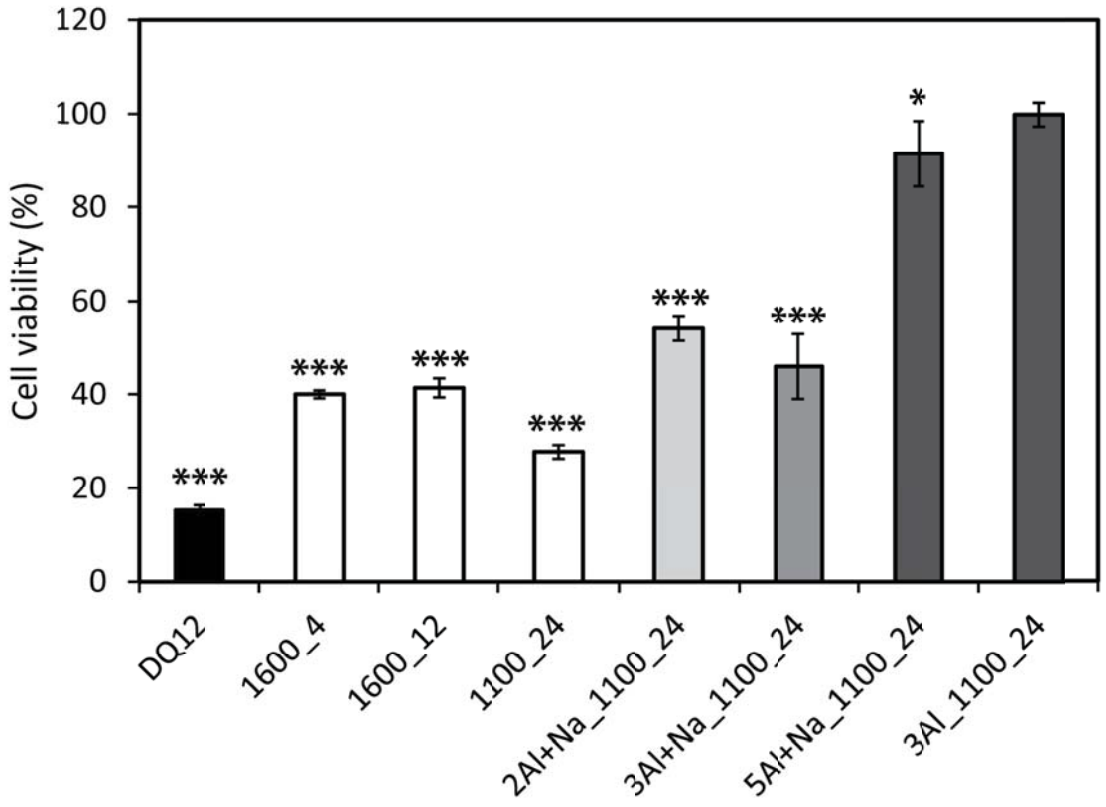

Figure 7.12: Cell viability of J774 macrophages treated with crystalline silica samples measured by the WST-1 assay. Cell viability at 500 µg/ml as a percentage of a positive and untreated control for J774 macrophages treated with non-doped (white) and doped (grey) samples for 24 h (n=1). Error bars represent standard error calculated from three separate wells of one experiment. * p = <0.05, *** p = <0.001 difference from untreated control.

7.3.5 TNF-α release and NF-κB activation

The production of TNF-α by macrophages was measured after exposure for 4 and 24 h. There was no significant difference between TNF-α production by treated cells and the untreated control at either exposure time (Figure 7.13), whereas DQ12 showed a strong dose-response relationship at 24 h (Figure 7.13b).

NF-κB activation did not differ from the untreated controls for any sample treatment, or the UFCB positive control for this method (Figure 7.14). Errors were exceptionally large (Figure 7.14) and no clear trend could be observed from the images. It is likely that the fluorescent markers did not bind properly, or that concentrations of the dye were too low. The fluorescence also faded quickly under the microscope and may contribute to the large errors observed.

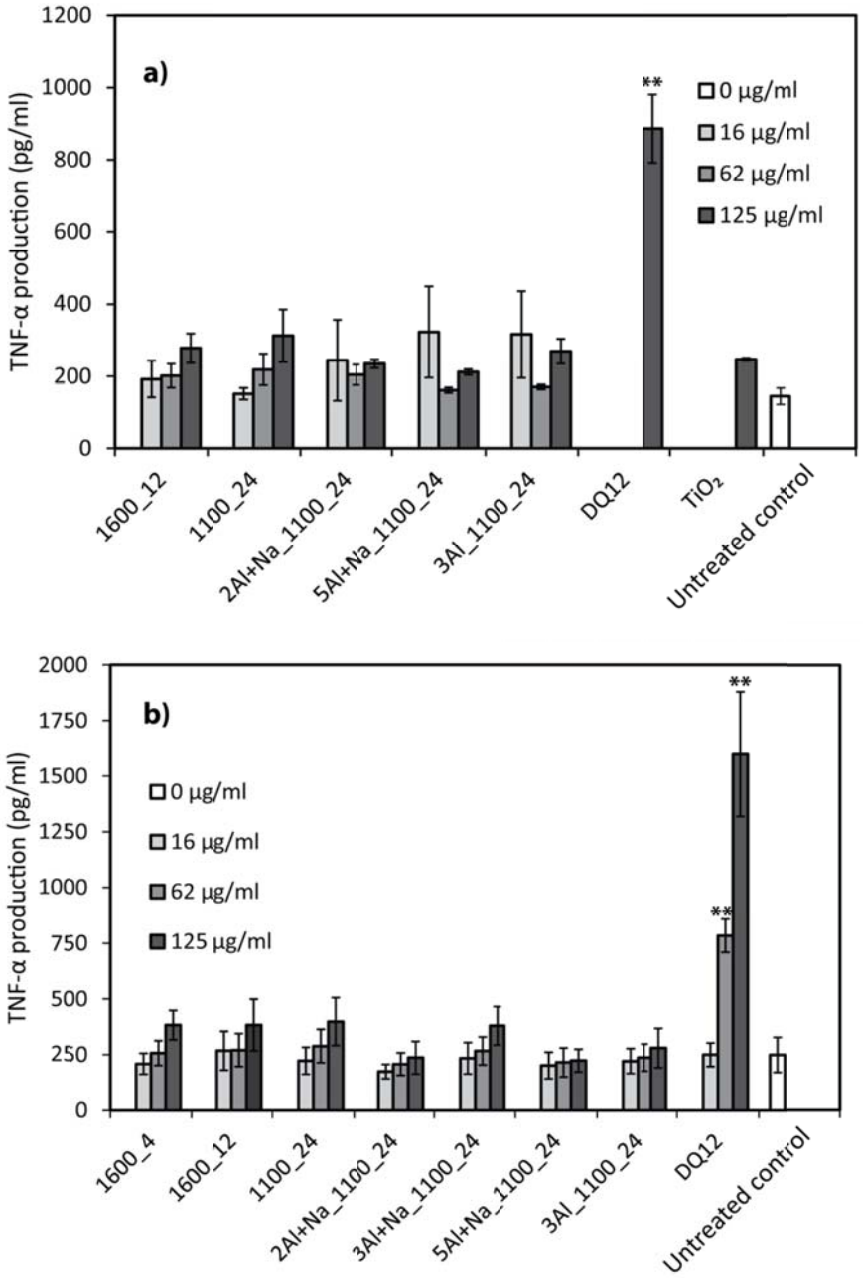

Figure 7.13: TNF-α production by J774 macrophages exposed to concentrations of 16-125 µg/ml sample suspensions for **a)** 4, and **b)** 24 h. Error bars represent standard error (n=3). ** p = <0.01 difference from untreated control.

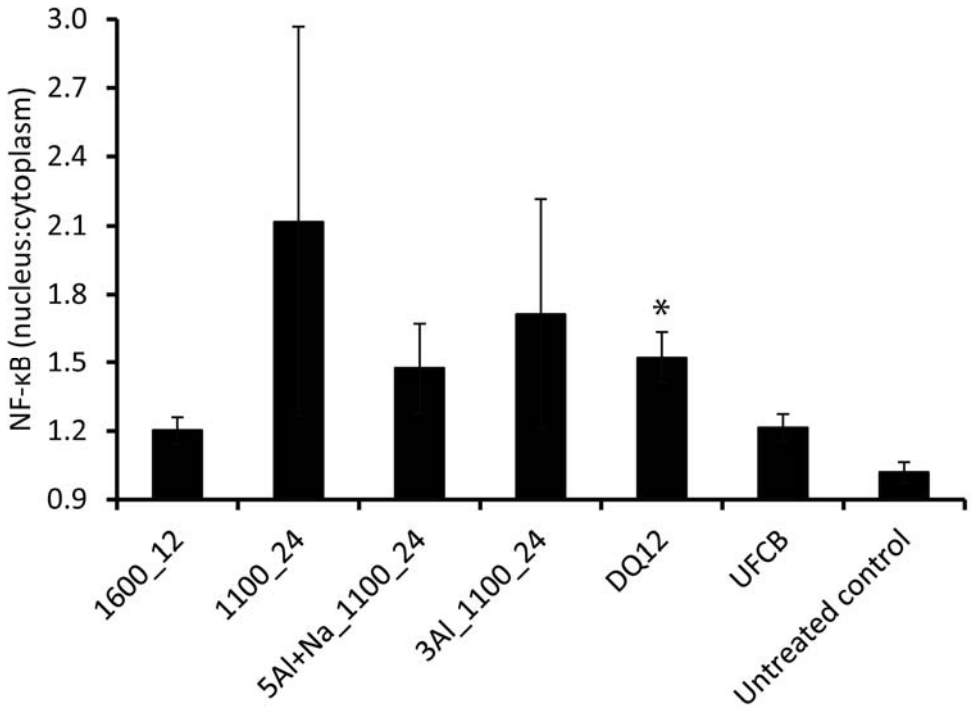

Figure 7.14: Ratio of NF-κB measured in the nucleus and the cytoplasm of J774 macrophages treated with crystalline silica for 4 h. DQ12 used as a positive crystalline silica control and ultra-fine carbon black (UFCB) as a positive control for the method. * $p < 0.05$ difference from untreated control. UFCB and samples did not differ from untreated control.

7.3.6 Particle uptake

Light microscopy imaging of treated cells showed clear cellular uptake of particles from all samples (Figure 7.15). However, some particles were not engulfed, especially in non-doped 1600_12 and 1100_24.

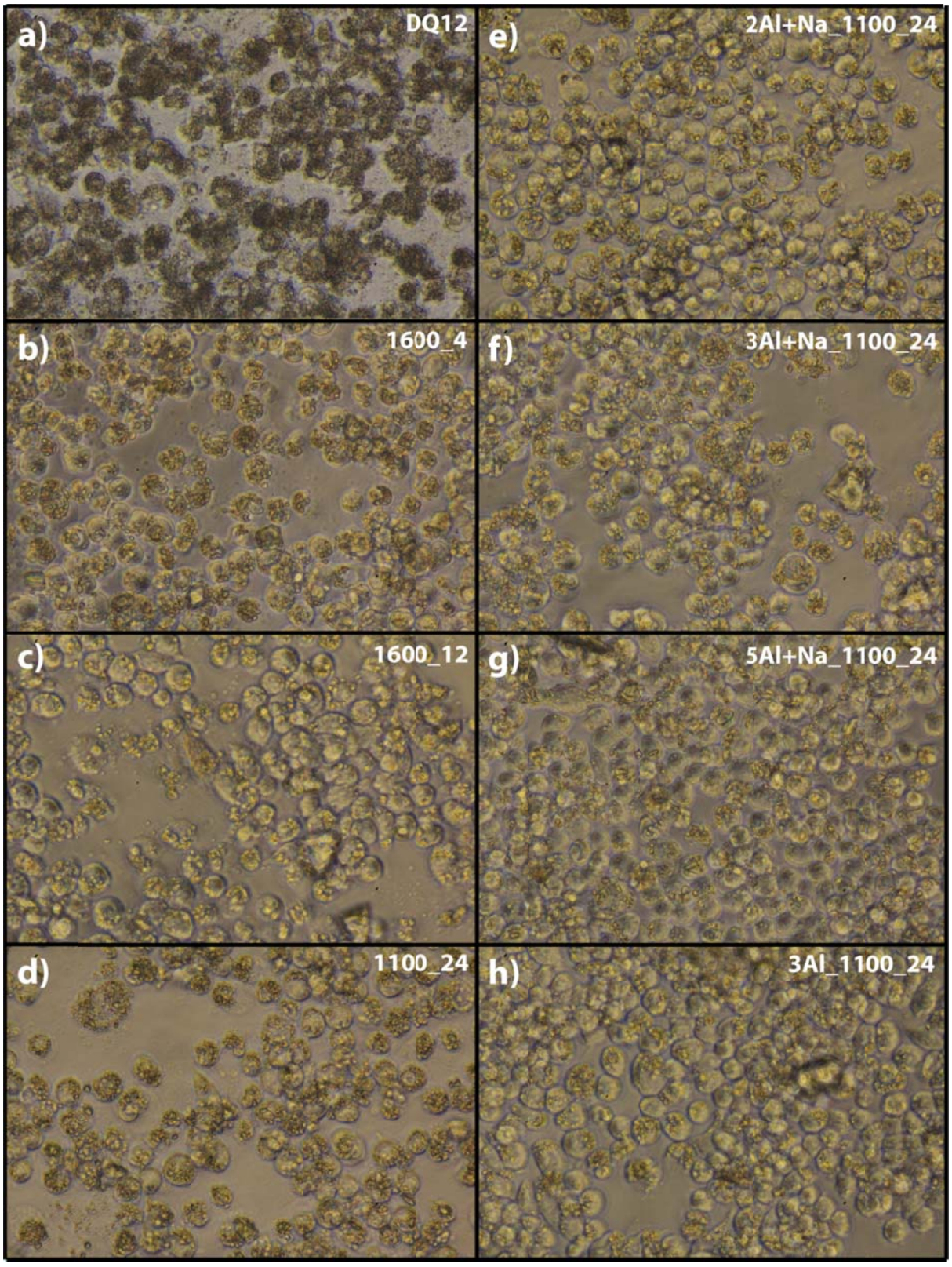

Figure 7.15: Light microscopy images of J774 macrophages post-24 h treatment with 500 µg/ml **a)** DQ12, **b-c)** non-doped cristobalite, **d)** non-doped tridymite, and **e-h)** doped cristobalite (x32 magnification). All images show particle uptake into the cells. In **a, c and d,** particles that have not been engulfed are present.

7.4 Discussion

Crystalline silica toxicity is a variable entity (Chapter 2) and Al treatment can significantly dampen crystalline silica reactivity (Duffin et al., 2001, Knaapen et al., 2002, Stone et al., 2004). Therefore, it has been hypothesised that structural Al impurities may play a similar role in dampening the toxicity of volcanic and diatomaceous earth cristobalite-rich powders (Chapter 5, Damby, 2012, Horwell et al., 2012, Nattrass et al., 2015). However, the effect of structural impurities on crystalline silica toxicity has not been defined. Here, the potential toxicity of synthetic cristobalite, doped with different concentrations of Al and Na or Al-only (see Chapter 6), was analysed to determine whether structural impurities and the presence of Al-and Na-rich phases can alter the reactivity of these powders *in vitro*.

7.4.1 Particle characterisation

In order to determine potential toxicity, the synthetic sample pellets were ground and the particles characterised to provide an insight to the properties which may influence their reactivity in the *in vitro* assays employed.

Median particle size did not vary much amongst the samples and particle distributions were similar for most samples although non-doped samples were slightly coarser, whereas surface area varied substantially ranging from 1-8 m^2/g in the crystallised samples. No correlation between surface area and particle size was observed, possibly due to the presence of pore spaces as, when a sol is heated and crystallised, water and N_2 are removed, potentially leaving pores. Alternatively, as particle size is measured in solution, it is possible that there was preferential aggregation of some samples compared to others. Samples showed bimodal particle size distributions to varying degrees (Figure 7.1b), which may indicate particle aggregation.

Surface charge has been shown to be important in the lung inflammatory process in rats treated with surface modified polystyrene nanoparticles (Kim et al., in press) and in the cytotoxicity of silica nanoparticles to keratinocytes (Park et al., 2013). All samples analysed exhibited a negative surface charge across the full pH range in water. At pH <3.5, the zeta potential of doped samples deviated away from non-doped samples and remained more negative than non-doped samples. It is likely this is caused by the presence of Al at the surface causing an increase in the acidity of the surface silanols. Framework Al has been shown to decrease the pH at which a zeta-potential of zero (iso-electric point) is reached in zeolites, which is attributed to higher acidic strength of Al atoms, thereby requiring higher proton concentrations (lower pH) to protonate the surface (Kuzniatsova et al., 2007, Mäurer et al., 2001, Nikolakis, 2005). Bridging hydroxide groups with Al (Si-OH-Al) have also been suggested to cause a more negatively charged surface, as this is easily de-protonated to negative $Si\text{-}O^-$ (Kuzniatsova et al., 2007), and may explain the more negative charge of doped samples than non-doped samples at lower pH. As the same effect is seen for samples doped with Al+Na, or Al only, it is clear that the effect is predominantly caused by Al. Therefore, it is likely that Al is present at the surface of the doped samples and that some of this Al is tetrahedrally coordinated (as substitution into the crystal framework was observed where Al ions replace Si ions in tetrahedra, Chapter 6).

However, surface charge of the synthetic samples suspended in complete medium at ~pH 7 (the conditions used for cell treatment) did not differ amongst samples or from DQ12, TiO_2 and starting materials. This is likely due to proteins coating the particles, as foetal bovine serum is included in complete medium (see Chapter 3). Therefore, surface charge is unlikely to control cytotoxicity directly. However, if there is tetrahedrally coordinated Al at the surface, it may alter the toxic potency of the surface of these particles (discussed in Section 7.4.2.4 below).

Doping dramatically reduced the amount of surface radicals present. Si and O based radicals are produced by cleavage of the silica surface during grinding (Fubini et al., 1987), and the present results showed a different surface reconstruction after the crystal fracture (Figures 7.4 and 7.5) between non-doped and doped cristobalite, which is possibly due to the presence of Al and Na impurities. Although no clear signal relating to $[AlO_4]^0$ centres was seen (usually a multiline signal across the Si and O based radical region (Goetze and Ploetze, 1997)), the shoulder at g=2.007 and the additional signal at g=1.987 not seen in non-doped samples (Figure 7.5) show dopants have some effect on the nature of the surface radicals. As the samples were tested months post-grinding, the radicals shown here are stable and are likely to reside on the surface of the particles for a long time. The observed reduction in surface radicals in doped cristobalite samples indicates a potential mechanism by which toxicity may be reduced and is discussed further in Section 7.4.4.

Doping also caused alterations of the band at g≈4.3, which represents paramagnetic metallic centres and usually Fe-based centres, as small amounts of Fe were present in the starting material (Table 6.1, Chapter 6). This is possibly due to the presence of Al^{3+}, which reduces the sites available for Fe^{3+} substitutions in the tetrahedral structure. Alternatively, Al^{3+} and Na^{+} in adjacent tetrahedral or interstitial sites could alter the paramagnetic signal of the iron contaminant.

7.4.2 Effect of dopants on the potential toxicity of crystalline silica

In general, doped samples were less reactive than non-doped cristobalite in the conducted assays. Doping with Al-only led to the most significant reduction in haemolytic potency and cytotoxicity (in all three assays conducted) compared with non-doped cristobalite. Doping with >3 oxide wt.% Al+Na also decreased cytotoxicity compared to non-doped samples by alamarBlue® and LDH release assays, although the magnitude of cytotoxicity varied by assay. Some particles were not engulfed by cells and this was most commonly observed in cells treated with non-doped samples (1600_12 and

1100_24), possibly due to cell apoptosis. Doping with Al+Na decreased the haemolytic potential compared to the non-doped tridymite-containing sample produced under the same temperature/time conditions and, by surface area dose, non-doped cristobalite heated at 1600 °C for >8h, although the amount of dopant did not appear to influence the extent of haemolysis. However, there was no difference in haemolytic potential between Al+Na doped samples and non-doped samples heated at low temperature (800_12) or at high temperature for 4 h (1600_4).

From these results it is clear that doping has altered the potential toxicity of the crystalline silica. Below, the properties of crystalline silica that are altered by doping are discussed in relation to these differences in toxicity.

7.4.2.1 Crystal polymorph and abundance

As shown in Chapter 6, doping led to a temperature-dependent change in the crystalline silica polymorph produced: the non-doped sample crystallised predominantly tridymite and the doped samples crystallised cristobalite. Studies of tridymite toxicity are limited, but its toxic potential is thought to be similar to cristobalite (Smith, 1998). Here, we see no categorical differences in toxicity between tridymite and cristobalite samples. For example, 1600_12 (cristobalite) and 1100_24 (mainly tridymite) had similar haemolytic potentials by surface area dose and were cytotoxic in all assays. Also, there is a large variability in the reactivity of different cristobalite samples. This finding is in agreement with previous studies that indicate that the crystalline silica polymorph does not control toxicity and that surface properties are more important (Elias et al., 2000, Mossman and Glenn, 2013).

Doped samples of cristobalite produced at 1100 °C had lower crystal abundance than the non-doped cristobalite produced at 1600 °C (Chapter 6). As the non-doped sample at 1100 °C produced

predominantly tridymite, crystal abundance could not be estimated, therefore, it is unknown if the reduction in crystal abundance is due to the lower treatment temperature or due to the dopants themselves. Regardless, it is possible that lower crystal abundance in the doped cristobalite samples may account for their lowered reactivity compared to non-doped cristobalite. However, the complete elimination of cytotoxicity and haemolysis in the Al-only doped sample, and the decrease in haemolysis and cytotoxicity in >3 oxide wt.% Al+Na doped samples, which all contained ~60% crystal abundance, suggests other alterations of the particles due to doping must be controlling its toxic potential (discussed below).

7.4.2.2 Cristobalite structure and purity

Doping with Al+Na or Al-only produced α-cristobalite with substitutions in its structure, which altered the crystal lattice parameters compared to non-doped samples (Chapter 6). Such structural Al impurities in diatomaceous earth cristobalite and volcanic cristobalite have previously been hypothesised to dampen their toxicity (Chapter 5, Horwell et al., 2012, Nattrass et al., 2015); the findings here further suggest that the alteration of the crystal structure could result in dampened haemolytic and cytotoxic potential. In the case of doping with Al-only, it is possible that these structural impurities can actually eliminate the cytotoxicity and haemolytic potential of α-cristobalite. Although not statistically different from samples doped with >3 oxide wt.% Al+Na, this sample (3Al_1100_24) was consistently the least reactive in the haemolysis and cytotoxicity assays.

Samples co-doped with Al+Na also had reduced haemolytic potential and cytotoxicity compared to non-doped samples, although the effect was less pronounced than doping with Al-only. Crystallisation of impure cristobalite seems the likely cause of the decreased reactivity compared to non-doped samples, as suggested for Al-only samples. A significant reduction in cytotoxicity was not seen for samples doped with 2 oxide wt.% Al+Na, which corresponds with <1 oxide wt.% Al in its

structure (Chapter 6), compared to non-doped samples. However, samples doped with >3 oxide wt.% Al+Na (>1.4 oxide wt.% Al in their structure (Chapter 6)) had diminished cytotoxicity. Therefore, we see an empirical threshold of >1 oxide wt.% Al required to alter crystalline silica reactivity in this model. These substitutions can alter the surface of the particles and the effect of these surface alterations on toxicity are discussed in Section 7.4.2.4.

The addition of a Na dopant has reduced the ability of Al to decrease the reactivity of crystalline silica *in vitro* here. The 5Al+Na_1100_24 sample had a greater crystal lattice dimensions than the 3Al_1100_24 sample (both doped with 3 oxide wt.% Al), indicative that additional Na has allowed greater uptake of impurities into the crystal (Chapter 6). As discussed above, structural substitutions of Al decrease reactivity, shown conclusively by the Al-only doped sample, but Na in the structure may somehow hinder the ability of Al to decrease reactivity. It is unknown how this would occur, therefore, the role of Na in determining toxicity remains unclear and is the focus of future work. Additional Na led to the stabilisation of other phases and their possible role in determining sample toxicity is discussed below. The presence of Al and Na dopants are more representative of natural or occupational cristobalite, which is unlikely to be formed with exposure to Al impurities only. Therefore, although structural impurities may dampen the potential toxicity of cristobalite, the role of interstitial Na, and the role of Na promoting the formation of other phases should be explored further.

7.4.2.3 Presence of other phases

The presence of other mineral phases has been considered to have an effect on crystalline silica toxicity in mixed dusts, such as diatomaceous earth, volcanic ash and coalmine dust, by altering or masking the surface of the crystalline silica or interacting with the silica particle once inhaled (Chapter 5, Donaldson and Borm, 1998, Ghiazza et al., 2009, Horwell et al., 2012, Nattrass et al.,

2015). Therefore, the presence of Al and Na-rich phases (albite and unidentified Al- and Na-rich crystals as indicated by XRD and EDS; Chapter 6) may also alter the toxicity of cristobalite here. Feldspars are generally considered to have low toxicity (e.g. Housley et al., 2002, personal communication D. Damby) so it is unlikely that albite would contribute to the toxicity of these samples, and toxicity decreased as the concentration of dopant, and hence the amount of albite, increased. It is possible, however, that albite can mask the surface of the crystalline silica, thereby reducing its toxic potency. However, as albite was observed in Al+Na doped samples but was barely detected in Al-only doped samples (Chapter 6), and Al-only doped samples were always less reactive, it is not fully responsible for the decreased reactivity of doped samples.

Co-doping also led to the possible chemical stabilisation of a small proportion of β-cristobalite (Chapter 6). As β-cristobalite has a different crystal structure compared to α-cristobalite (cubic rather than tetragonal) it is possible that they have different toxicities. However, the toxicity of β-cristobalite is completely unconstrained. β-cristobalite is rarely found in nature but may exist in volcanic ash (Reich et al., 2009). However, impure α-cristobalite is often misidentified as β-cristobalite from the XRD peak position (Damby et al., 2014). Here, any β-cristobalite would be chemically stabilised, containing more Al and Na impurities than the α-cristobalite areas analysed (Chapter 6). Therefore, it is likely Al and Na in these particles would reduce their toxicity similar to the effect in α-cristobalite.

7.4.2.4 Surface properties

In both Al-only and Al+Na doped samples there was an alteration of surface groups when compared to non-doped samples, as indicated by zeta potential changes at low pH (Figure 7.3). The alteration of surface silanols by Al treatment has previously been suggested to decrease the toxic potency of silica (Fubini et al., 1995). An alteration of surface silanol populations may explain the decrease in

haemolysis, as the distribution of silanols has been shown to be vital in determining the haemolytic potential of quartz (Pavan et al., 2013). An alteration in surface silanols could also affect particle interaction with macrophages by preventing adsorption of the cell membrane to the silica surface (Fubini, 1998), although, here, no qualitative effect on particle uptake by macrophages was observed by light microscopy. The reduction in cytotoxicity caused by doping with Al or co-doping with Al and Na, has been seen in Al-treated quartz (Duffin et al., 2001, Knaapen et al., 2002). Treatment of quartz in these studies only affects the surface of the particles, therefore, it is likely that, here, these surface modifications are the main contributors to inhibiting silica reactivity. An expansion of the crystal structure with doping (Chapter 6) and the presence of Al at the surface of the particles may alter the silanol distributions, known to be important in the haemolytic potency of crystalline silica (Pavan et al., 2013). However, unfortunately, IR spectroscopy could not be performed on these samples (as it was impossible to prepare the samples into a pellet for analyses), so it cannot be confirmed how Al or Al+Na dopants alter the surface silanol populations.

Surface radicals were only measured for 1600_4 (non-doped cristobalite) and 5Al+Na_1100_24 (Al and Na doped cristobalite) samples. Therefore, the effect of Al-only doping on surface radicals cannot be assessed. However, the dramatic decrease in siloxyl radicals by doping with Al+Na could contribute to the reduced toxic potential of this sample compared to non-doped samples. The mechanism by which a reduction in surface radicals may decrease the potential toxicity of crystalline silica is discussed in Section 7.4.4.

The effect of Al impurities at the surface in reducing cytotoxicity is not dampened with time over 48 h (Figure 7.10). This suggests that impurities are not released from the surface over this period. Therefore, the reduced toxic potential due to structural Al impurities is likely to be permanent. However, acid treatment experiments of the surface, and longer term *in vitro* and *in vivo* studies would be needed to confirm this.

7.4.3 Effect of crystallinity on the haemolytic potential of non-doped crystalline silica

The non-doped cristobalite samples had variable reactivities; therefore, it is not only the presence of impurities that can alter silica toxicity. Heating can anneal the surface silanols, converting them to less reactive siloxane bridges and decrease surface radicals (Fubini, 1998, Fubini et al., 1989). However, as samples were crystallised first and then ground into a powder (Chapter 6) variations in heating time should not have an effect on surface properties. In the haemolysis assay, by surface area dose, low temperature and short crystallisation times (800_12 and 1600_4) were less haemolytic than cristobalite crystallised at high temperature for a long duration (1600 °C for >8h). At low crystallisation temperatures, poorly-ordered cristobalite is produced (see Chapter 6), which may decrease the haemolytic potential compared to higher ordered samples. However, 1600_4 had the same degree of crystallinity as 1600_12 (Figure 6.3, Chapter 6), so a difference in structure does not account for their different reactivity. There was also no significant difference between the cytotoxicity of non-doped 1600_4 and 1600_12 samples in any cytotoxicity assay. In both the low temperature and short duration samples, there was a greater amount of residual amorphous starting material, which had very low haemolytic potential by surface area (Figure 7.9) and could also account for the decreased haemolysis from these samples relative to the high temperature long crystallisation period sample.

7.4.4 Mechanism of toxicity

Through the *in vitro* experiments, a specific mechanism of toxicity could not be determined as TNF-α production was not elevated above control levels and NF-κB activation measurements were unclear. TNF-α and NF- κB have previously been shown to be involved in the pathway of silica pathogenicity

(Piguet et al., 1990, Rojanasakul et al., 1999). They are intrinsically linked, as the inhibition of NF-κB activity has been shown to inhibit TNF-α release from RAW 264.7 macrophages (Gozal et al., 2002, Rojanasakul et al., 1999). Therefore, although NF-κB activation results could not be used, the low TNF-α release indicates that NF-κB activation is also likely to be low in sample-treated cells. The lack of TNF-α production here, in cells treated at sublethal concentrations, suggests that either another pathway leading to cytotoxicity is occurring, or that no adverse effects occur to the cells until treatment concentrations are high enough to also cause cell death. The different cell type, compared to previous studies, may be a factor as Gozal et al. (2002) showed NF-κB activation and TNF-α release differs for different types of macrophages exposed to silica. They also showed silica can induce apoptosis in cells with no increase in TNF-α protein production or NF-κB activation. Al treatment of quartz has been shown to decrease its ability to induce cytokine release and NF-κB activation (Duffin et al., 2001) but is not linked to the differences in cytotoxicity here, as there was no increase in TNF-α production compared to untreated controls.

Al lactate treatment was shown to decrease particle uptake by epithelial cells (Schins et al., 2002); however, doping with Al or Al+Na did not have any observable effect on particle uptake by light microscopy (Figure 7.15). This is likely due to coating of the particles with serum. However, once engulfed, this protein-coating may be removed and the effect of different functional groups at the surface of doped and non-doped samples, as indicated by zeta potential measurements in water, and a reduction in surface radicals with doping, may have an effect on the particle reactivity in the cell.

Freshly fractured crystalline silica surfaces produce free radicals (Vallyathan et al., 1988). Silanol populations have been indicated in radical production (Fubini et al., 1995) and the presence of surface silica radicals can promote $HO^{\bullet}$ and $COO^{\bullet}$ production (Fubini et al., 1990, Giamello et al., 1990). Free radicals can cause DNA damage that can be inhibited by the treatment of quartz with Al

(Knaapen et al., 2002), decreasing radical release (Schins et al., 2002). A comparison of surface siloxyl radicals in 1600_4 and 5Al+Na_1100_24, showed a dramatic decrease in these radicals with doping (Figure 7.4), but the inferred difference in silanol populations between non-doped and doped samples here, did not cause any difference in free radical production. Here, $HO^{\bullet}$ radicals were produced in small quantities by all samples, the 1600_12 (a highly crystallised non-doped cristobalite) sample producing slightly more than other samples. No samples produced substantial amounts of $COO^{\bullet}$ radicals. Therefore, a mechanism by which a decrease in surface radicals decreases toxicity via radical production could not be discerned.

The low levels of particle-derived free radicals may account for low TNF-α and NF-κB activation in treated cells, as free radicals have previously been implied in the silica toxicity pathway involving TNF-α production and activation of NF-κB (Barrett et al., 1999, Castranova, 2004, Chen et al., 1995, Rojanasakul et al., 1999). Regardless, as particle-derived free radical release, TNF-α production and NF-κB activation were all low, the mechanism by which the samples in this study may be toxic is unknown and, therefore, the mechanism by which Al+Na or Al-only dopants deceased reactivity also remains unknown. However, it is clear that Al and Na substitutions in the structure of crystalline silica can play a role in its cytotoxic and haemolytic potential, likely due to the presence of Al at the surface altering surface silanol populations.

7.6 Conclusions

Doping silica with Al or co-doping with Al and Na pre-crystallisation led to a decrease in haemolytic potential and cytotoxicity compared to non-doped samples. The inhibition of cristobalite-induced haemolysis and cytotoxicity by Al-only doping was attributed to structural Al present at the surface of the sample, causing a similar effect to treatment of the crystalline silica surface with Al salts (e.g.

Duffin et al., 2001). The decrease in haemolysis and cytotoxicity of co-doped samples compared to non-doped samples was also attributed to structural Al at the surface. However, the additional Na and the presence of albite in these samples may moderate this effect, although their individual roles could not be deciphered.

In agreement with previous studies, the crystalline silica polymorph was shown not to influence toxicity, whereas surface properties, such as a decrease in siloxyl radicals and an increased acidity of surface silanols, likely related to the presence of impurities, are potentially important in determining the toxic potential of crystalline silica. The lack of TNF-α production, NF-κB activation and $HO^{\bullet}$ or $COO^{\bullet}$ release means that a mechanism of toxicity could not be determined and, therefore, it is not known how impurities dampened the toxic potential here.

It has previously been hypothesised that Al and Na substitutions in volcanic and diatomaceous earth cristobalite may dampen their toxicity (Chapter 5, Damby, 2012, Horwell et al., 2012, Nattrass et al., 2015) but assessment has been hindered by the presence of other phases in these mixed dusts. Here, by Al-only doping it has been shown that structural Al impurities can indeed eliminate the potential toxicity of cristobalite by altering surface groups on the silica particles and may, therefore, explain the low reactivity of cristobalite-rich volcanic ash and diatomaceous earth *in vitro* (Chapter 5, Damby, 2012, Nattrass et al., 2015), although the presence of Na in natural samples likely makes the effect less profound than would be seen with solely Al. As Al and Na impurities were shown throughout the synthetic cristobalite structure (Chapter 6), it is assumed that the ameliorating effect on toxic potential will be long term. However, *in vivo* models and longer exposure times are needed to confirm this. Chapter 8 discusses the implications of these findings in the context of the natural samples analysed in this thesis and in the literature.

References

BARRETT, E. G., JOHNSTON, C., OBERDÖRSTER, G. & FINKELSTEIN, J. N. 1999. Antioxidant Treatment Attenuates Cytokine and Chemokine Levels in Murine Macrophages Following Silica Exposure. *Toxicology and Applied Pharmacology,* 158**,** 211-220.

BORDIGA, S., BUZZONI, R., GEOBALDO, F., LAMBERTI, C., GIAMELLO, E., ZECCHINA, A., LEOFANTI, G., PETRINI, G., TOZZOLA, G. & VLAIC, G. 1996. Structure and Reactivity of Framework and Extraframework Iron in Fe-Silicalite as Investigated by Spectroscopic and Physicochemical Methods. *Journal of Catalysis,* 158**,** 486-501.

CASTRANOVA, V. 2004. Signaling Pathways Controlling The Production Of Inflammatory Mediators in Response To Crystalline Silica Exposure: Role Of Reactive Oxygen/Nitrogen Species. *Free Radical Biology and Medicine,* 37**,** 916-925.

CHECKOWAY, H., HEYER, N. J., DEMERS, P. A. & BRESLOW, N. E. 1993. Mortality among workers in the diatomaceous earth industry. *British Journal of Industrial Medicine,* 50**,** 586-597.

CHEN, F., SUN, S. C., KUH, D. C., GAYDOS, L. J. & DEMERS, L. M. 1995. Essential Role of NF-κB Activation in Silica-Induced Inflammatory Mediator Production in Macrophages. *Biochemical and Biophysical Research Communications,* 214**,** 985-992.

CHERRY, N. M., BURGESS, G. L., TURNER, S. & MCDONALD, J. C. 1998. Crystalline silica and risk of lung cancer in the potteries. *Occupational and Environmental Medicine,* 55**,** 779-785.

COSTA, D., FUBINI, B., GIAMELLO, E. & VOLANTE, M. 1991. A novel type of active site at the surface of crystalline SiO2 (a-quartz) and its possible impact on pathogenicity. *Canadian Journal of Chemistry,* 69**,** 1427-1434.

CULLEN, R. T., VALLYATHAN, V., HAGEN, S. & DONALDSON, K. 1997. Protection by Iron Against the Toxic Effects of Quartz. *Annals of Occupational Hygiene,* 41**,** 420-425.

DAMBY, D. E. 2012. *From Dome to Disease: The Respiratory Toxicity of Volcanic Cristobalite.* Durham theses, Durham University.

DAMBY, D. E., LLEWELLIN, E. W., HORWELL, C. J., WILLIAMSON, B. J., NAJORKA, J., CRESSEY, G. & CARPENTER, M. 2014. The [alpha]-[beta] phase transition in volcanic cristobalite. *Journal of Applied Crystallography,* 47.

DECYK, P., TREJDA, M., ZIOLEK, M., KUJAWA, J., GŁASZCZKA, K., BETTAHAR, M., MONTEVERDI, S. & MERCY, M. 2003. Physicochemical and catalytic properties of iron-doped silica—the effect of preparation and pretreatment methods. *Journal of Catalysis,* 219**,** 146-155.

DONALDSON, K. & BORM, P. J. A. 1998. The Quartz Hazard: A Variable Entity. *Annals of Occupational Hygiene,* 42**,** 287-294.

DUFFIN, R., GILMOUR, P. S., SCHINS, R. P. F., CLOUTER, A., GUY, K., BROWN, D. M., MACNEE, W., BORM, P. J., DONALDSON, K. & STONE, V. 2001. Aluminium Lactate Treatment of DQ12 Quartz Inhibits Its Ability to Cause Inflammation, Chemokine Expression, and Nuclear Factor-κB Activation. *Toxicology and Applied Pharmacology,* 176**,** 10-17.

ELIAS, Z., POIROT, O., DANIÈRE, M. C., TERZETTI, F., MARANDE, A. M., DZWIGAJ, S., PEZERAT, H., FENOGLIO, I. & FUBINI, B. 2000. Cytotoxic and transforming effects of silica particles with different surface properties in Syrian hamster embryo (SHE) cells. *Toxicology in Vitro,* 14**,** 409-422.

FUBINI, B. 1998. Surface Chemistery and Quartz Hazard. *Annals of Occupational Hygiene,* 42**,** 521-530.

FUBINI, B., BOLIS, V., CAVENAGO, A. & VOLANTE, M. 1995. Physicochemical properties of crystalline silica dusts and their possible implication in various biological responses. *Scandinavian Journal of Work, Environment and Health,* 21 suppl 2**,** 9-14.

FUBINI, B., BOLIS, V. & GIAMELLO, E. 1987. The surface chemistry of crushed quartz dust in relation to its pathogenicity. *Inorganica Chimica Acta,* 138**,** 193-197.

FUBINI, B., GIAMELLO, E., PUGLIESE, L. & VOLANTE, M. 1989. Mechanically induced defects in quartz and their impact on pathogenicity. *Solid State Ionics,* 32–33, Part 1**,** 334-343.

FUBINI, B., GIAMELLO, E., VOLANTE, M. & BOLIS, V. 1990. Chemical functionalities at the silica surface determining its reactivity when inhaled. Formation and reactivity of surface radicals. *Toxicol Ind Health,* 6**,** 571-98.

GHIAZZA, M., GAZZANO, E., BONELLI, B., FENOGLIO, I., POLIMENI, M., GHIGO, D., GARRONE, E. & FUBINI, B. 2009. Formation of a Vitreous Phase at the Surface of Some Commercial Diatomaceous Earth Prevents the Onset of Oxidative Stress Effects. *Chemical Research in Toxicology,* 22**,** 136-145.

GIAMELLO, E., FUBINI, B., VOLANTE, M. & COSTA, D. 1990. Surface oxygen radicals originating via redox reactions during the mechanical activation of crystalline SiO2 in hydrogen peroxide. *Colloids and Surfaces,* 45**,** 155-165.

GOETZE, J. & PLOETZE, M. 1997. Investigation of trace-element distribution in detrital quartz by Electron Paramagnetic Resonance (EPR). *European Journal of Mineralogy,* 9**,** 529-537.

GOZAL, E., ORTIZ, L. A., ZOU, X., BUROW, M. E., LASKY, J. A. & FRIEDMAN, M. 2002. Silica-induced apoptosis in murine macrophage: involvement of tumor necrosis factor-alpha and nuclear factor-kappaB activation. *Am J Respir Cell Mol Biol,* 27**,** 91-8.

HORWELL, C., WILLIAMSON, B., DONALDSON, K., LE BLOND, J., DAMBY, D. & BOWEN, L. 2012. The structure of volcanic cristobalite in relation to its toxicity; relevance for the variable crystalline silica hazard. *Particle and Fibre Toxicology,* 9**,** 44.

HOUSLEY, D. G., BERUBE, K. A., JONES, T. P., ANDERSON, S., POOLEY, F. D. & RICHARDS, R. J. 2002. Pulmonary epithelial response in the rat lung to instilled Montserrat respirable dusts and their major mineral components. *Occup Environ Med,* 59**,** 466-72.

IARC 1997. Silica, some silicates, coal dust and para-aramid fibrils. . Lyon: International Agency for Research on Cancer.

KIM, J., CHANKESHWARA, S. V., THIELBEER, F., JEONG, J., DONALDSON, K., BRADLEY, M. & CHO, W.-S. in press. Surface charge determines the lung inflammogenicity: A study with polystyrene nanoparticles. *Nanotoxicology,* 0**,** 1-8.

KING, E. J., MOHANTY, G. P., HARRISON, C. V. & NAGELSCHMIDT, G. 1953. The Action of Different Forms of Pure Silica on the Lungs of Rats. *British Journal of Industrial Medicine,* 10**,** 9-17.

KNAAPEN, A. M., ALBRECHT, C., BECKER, A., HÖHR, D., WINZER, A., HAENEN, G. R., BORM, P. J. A. & SCHINS, R. P. F. 2002. DNA damage in lung epithelial cells isolated from rats exposed to quartz: role of surface reactivity and neutrophilic inflammation. *Carcinogenesis,* 23**,** 1111-1120.

KUZNIATSOVA, T., KIM, Y., SHQAU, K., DUTTA, P. K. & VERWEIJ, H. 2007. Zeta potential measurements of zeolite Y: Application in homogeneous deposition of particle coatings. *Microporous and Mesoporous Materials,* 103**,** 102-107.

MÄURER, T., MÜLLER, S. P. & KRAUSHAAR-CZARNETZKI, B. 2001. Aggregation and Peptization Behavior of Zeolite Crystals in Sols and Suspensions. *Industrial & Engineering Chemistry Research,* 40**,** 2573-2579.

MELDRUM, M. & HOWDEN, P. 2002. Crystalline Silica: Variability in Fibrogenic Potency. *Annals of Occupational Hygiene,* 46**,** 27-30.

MICHNOWICZ, S. A. K. 2014. *Exploratory Study of the Potential Airborne Health Hazard of Dusts Generated by Quarrying Volcanic Deposits.* Durham University.

MOSSMAN, B. T. & GLENN, R. E. 2013. Bioreactivity of the crystalline silica polymorphs, quartz and cristobalite, and implications for occupational exposure limits (OELs). *Critical Reviews in Toxicology,* 43**,** 632-660.

NATTRASS, C., HORWELL, C. J. H., DAMBY, D. E. D., KERMANIZADEH, A., BROWN, D. M. & STONE, V. 2015. The global variability of diatomaceous earth toxicity: a physicochemical and in vitro investigation. *Journal of Occupational Medicine and Toxicology,* 10**,** 23.

NIKOLAKIS, V. 2005. Understanding interactions in zeolite colloidal suspensions: A review. *Current Opinion in Colloid & Interface Science,* 10**,** 203-210.

NOLAN, R. P., LANGER, A. M., HARINGTON, J. S., OSTER, G. & SELIKOFF, I. J. 1981. Quartz hemolysis as related to its surface functionalities. *Environmental Research,* 26**,** 503-520.

NOURSADEGHI, M., TSANG, J., HAUSTEIN, T., MILLER, R. F., CHAIN, B. M. & KATZ, D. R. 2008. Quantitative imaging assay for NF-κB nuclear translocation in primary human macrophages. *Journal of Immunological Methods,* 329**,** 194-200.

PARK, R., RICE, F., STAYNER, L., SMITH, R., GILBERT, S. & CHECKOWAY, H. 2002. Exposure to crystalline silica, silicosis, and lung disease other than cancer in diatomaceous earth industry workers: a quantitative risk assessment. *Occupational and Environmental Medicine,* 59**,** 36-43.

PARK, Y.-H., BAE, H., JANG, Y., JEONG, S., LEE, H., RYU, W.-I., YOO, M., KIM, Y.-R., KIM, M.-K., LEE, J., JEONG, J. & SON, S. 2013. Effect of the size and surface charge of silica nanoparticles on cutaneous toxicity. *Molecular & Cellular Toxicology,* 9**,** 67-74.

PARMALIANA, A., ARENA, F., FRUSTERI, F., MARTíNEZ-ARIAS, A., LÓPEZ GRANADOS, M. & FIERRO, J. L. G. 2002. Effect of Fe-addition on the catalytic activity of silicas in the partial oxidation of methane to formaldehyde. *Applied Catalysis A: General,* 226**,** 163-174.

PAVAN, C., TOMATIS, M., GHIAZZA, M., RABOLLI, V., BOLIS, V., LISON, D. & FUBINI, B. 2013. In Search of the Chemical Basis of the Hemolytic Potential of Silicas. *Chemical Research in Toxicology,* 26**,** 1188-1198.

PEETERS, P. M., EURLINGS, I. M., PERKINS, T. N., WOUTERS, E. F., SCHINS, R. P., BORM, P. J., DROMMER, W., REYNAERT, N. L. & ALBRECHT, C. 2014. Silica-induced NLRP3 inflammasome activation in vitro and in rat lungs. *Part Fibre Toxicol,* 11**,** 58.

PERKINS, T. N., SHUKLA, A., PEETERS, P. M., STEINBACHER, J. L., LANDRY, C. C., LATHROP, S. A., STEELE, C., REYNAERT, N. L., WOUTERS, E. F. & MOSSMAN, B. T. 2012. Differences in gene expression and cytokine production by crystalline vs. amorphous silica in human lung epithelial cells. *Part Fibre Toxicol,* 9**,** 6.

PIGUET, P. F., COLLART, M. A., GRAU, G. E., SAPPINO, A.-P. & VASSALLI, P. 1990. Requirement of Tumour Necrosis Factor for Development of Silica-Induced Pulmonary Fibrosis. *Nature,* 344**,** 245.

REICH, M., ZÚÑIGA, A., AMIGO, Á., VARGAS, G., MORATA, D., PALACIOS, C., PARADA, M. Á. & GARREAUD, R. D. 2009. Formation of cristobalite nanofibers during explosive volcanic eruptions. *Geology,* 37**,** 435-438.

RICE, F. L., PARK, R., STAYNER, L., SMITH, R., GILBERT, S. & CHECKOWAY, H. 2001. Crystalline silica exposure and lung cancer mortality in diatomaceous earth industry workers: a quantitative risk assessment. *Occupational and Environmental Medicine,* 58**,** 38-45.

ROJANASAKUL, Y., YE, J., CHEN, F., WANG, L., CHENG, N., CASTRANOVA, V., VALLYATHAN, V. & SHI, X. 1999. Dependence of NF-kappaB activation and free radical generation on silica-induced TNF-alpha production in macrophages. *Mol Cell Biochem,* 200**,** 119-25.

SCHINS, R. P. F., DUFFIN, R., HÖHR, D., KNAAPEN, A. M., SHI, T., WEISHAUPT, C., STONE, V., DONALDSON, K. & BORM, P. J. A. 2002. Surface Modification of Quartz Inhibits Toxicity, Particle Uptake, and Oxidative DNA Damage in Human Lung Epithelial Cells. *Chemical Research in Toxicology,* 15**,** 1166-1173.

SMITH, D. K. 1998. Opal, cristobalite, and tridymite: Noncrystallinity versus crystallinity, nomenclature of the silica minerals and bibliography. *Powder Diffraction,* 13**,** 2-19.

STONE, V., JONES, R., ROLLO, K., DUFFIN, R., DONALDSON, K. & BROWN, D. M. 2004. Effect of coal mine dust and clay extracts on the biological activity of the quartz surface. *Toxicology Letters,* 149**,** 255-259.

TOURMANN, J. L. & KAUFMANN, R. 1994. Biopersistence of the mineral matter of coal mine dusts in silicotic human lungs: is there a preferential release of iron? *Environ Health Perspect,* 102 Suppl 5**,** 265-8.

VALLYATHAN, V., SCHWEGLER, D., REASOR, M., STETTLER, L., CLERE, J. & GREEN, F. H. Y. 1988. Comparative In Vitro Cytotoxicity and Relative Pathogenicity of Mineral Dusts. *Annals of Occupational Hygiene,* 32**,** 279-289.

Chapter 8

Implications and Conclusions

8.1 Introduction

As discussed throughout this thesis, crystalline silica toxicity is a variable entity (Donaldson and Borm, 1998), and when quartz and cristobalite were classified as carcinogenic to humans, it was noted that crystalline silica does not exhibit carcinogenicity to humans in all industrial circumstances (IARC, 1997, IARC, 2012). This variability is attributed to differences in the inherent characteristics of the silica particle, such as the crystalline polymorph, age of the surface, or impurities (e.g. Fubini et al., 1995, Meldrum and Howden, 2002). External factors can also alter crystalline silica toxicity, such as the presence of other minerals or amorphous material and both inherent impurities and external minerals have been hypothesised to decrease the toxic potency of volcanic cristobalite (Horwell et al., 2012). In this thesis, the same hypothesis was applied to diatomaceous earth (DE) and has been tested through the production and toxicological analysis of synthetic crystalline silica.

The production of synthetic crystalline silica, with and without impurities in its structure (Chapter 6), and the assessment of their biological reactivity *in vitro* (Chapter 7) showed that Al substitutions into the crystal structure can eliminate the potential toxicity of cristobalite. This is likely due to changes in crystal structure and Al present at the surface of the particles. Incorporation of Al and Na into the crystal structure and the presence of other Al- and Na-rich minerals, such as albite, also reduced cristobalite toxicity compared to non-doped, cristobalite-only samples. These central findings have

important implications for the potential toxicity of natural cristobalite which, as this thesis has confirmed, usually contains impurities in its crystal structure.

8.2 Implications for the biological reactivity of volcanic and DE cristobalite

Volcanic ash has been shown to be less toxic than expected (Damby, 2012), in samples which contain substantial quantities of cristobalite (up to ~30 wt.% (Horwell et al., 2014, Jones and BéruBé, 2011)). The cristobalite in volcanic material has been shown to be impure and contains up to 4 oxide wt.% Al+Na (Horwell et al., 2012). Here, it is shown that structural impurities are not limited to volcanic cristobalite but are also observed in cristobalite formed during the processing of DE (Chapter 4). As with volcanic ash, the most cristobalite-rich DE was found to be much less toxic than expected, giving further weight to the hypothesis that impurities within the cristobalite structure may act to dampen cristobalite toxicity (Chapter 5). This hypothesis, tested on synthetic impure and pure cristobalite (containing between 0 and 4 oxide wt.% Al+Na, spanning the range seen in volcanic cristobalite) in Chapter 7, appears to hold true, providing strong evidence for at least one mechanism that may be acting to reduce the toxicity of cristobalite in natural samples.

Volcanic cristobalite primarily contains Al and Na impurities in its structure (Damby, 2012, Horwell et al., 2012). Here, it was shown that DE cristobalite can contain a range of impurities (Al, Na, Ca, Fe) that vary with location (Chapter 4). It is possible that the element type is not important, but that the presence of any impurity in the cristobalite structure dampens its toxic potential. Chapter 7 indicated that Al, alone, would have the greatest effect in reducing the potential toxicity of cristobalite, with additional Na impurities lessening that effect. However, further work is needed to determine if the type of impurity is important or whether any elemental substitution would decrease crystalline silica reactivity (see Section 8.5).

That both DE and volcanic cristobalite forms in the presence of other minerals, including feldspars, clays and carbonates, means that these external minerals may also act to dampen the potential toxicity of cristobalite in natural or occupational exposures. Synthetic, impure cristobalite, formed in conjunction with albite and other Al- and Na-rich phases, had a reduced toxic potential compared to non-doped cristobalite samples where no other mineral phases were present. The reduction of cristobalite reactivity was less than for cristobalite with structural impurities alone. However, the samples containing both impure cristobalite and other mineral impurities are more representative of natural samples, and prove that cristobalite in the presence of other minerals and containing structural impurities has a reduced reactivity to pure cristobalite-only samples. To conclude, the findings of this thesis strongly support the hypothesis that the low reactivity of DE and volcanic cristobalite *in vitro* is controlled by the presence of internal and external impurities.

8.3 Implications for crystalline silica regulation and hazard management

The 'crystalline silica conundrum', that crystalline silica is not equally toxic in all instances, is well established. However, regulations, including occupational exposure limits (OELs) or permissible exposure limits (PELs) do not take into account this variability. Mostly, a single OEL value is used for quartz and cristobalite in all industries, although, sometimes, cristobalite is given a lower OEL than quartz (Table 8.1). Recently, a review was conducted to provide information on whether the different crystalline silica polymorphs warrant different OELs, concluding that, overall, there is no difference in the toxic potency of quartz and cristobalite (Mossman and Glenn, 2013). In 2013, the Occupational Safety and Health Administration (OSHA) also proposed to make the PEL of quartz and cristobalite the same (both at 50 $\mu g/m^3$ time weighted average (TWA)) whereas, previously, the quartz PEL was double that of cristobalite. Exposure to tridymite is rare, however, it is often given the same PEL as quartz and cristobalite (Table 8.1).

Table 8.1: OELs for respirable inert dust, quartz, cristobalite, tridymite, DE and amorphous silica in European countries and the USA. (IMA-Europe, 2014, NIOSH, 2002). * based on inhalable fraction; ** Germany does not enforce OELs but employers are obliged to decrease exposure as much as possible; *** Occupational Safety and Health Administration (OSHA) base PELs on the % quartz in the sample (if quartz is 100 % the PEL is 0.1 mg/m^3); **** National Institute for Occupational Safety and Health (NIOSH) provide recommended exposure limits (RELs) based on 10 h exposure 40 h per week; $ for unprocessed DE.

Country	Occupational exposure limits (OEL) in mg/m^3 8 hours time weighted average (TWA) respirable dust					
	Inert dust	Quartz	Cristobalite	Tridymite	DE	Amorphous silica
Austria	5	0.15	0.15	0.15		
Belgium	3	0.05	0.05	0.05	3	2
Bulgaria	4	0.07	0.07	0.07	*1	
Czech Republic		0.1	0.1	0.1		
Denmark	5	0.1	0.05	0.05	1.5	
Estonia		0.1	0.05	0.05		2
Finland		0.05	0.05	0.05	5	
France	5	0.05	0.05	0.05		
Germany**	0.5					
Greece	5	0.1	0.05	0.05		
Hungary		0.15	0.15	0.15		
Ireland	4	0.1	0.1	0.1		2.4
Italy	3	0.05	0.05	0.05		
Lithuania	10	0.1	0.05	0.05		
Luxembourg	6	0.15	0.15	0.15		
Netherlands	5	0.075	0.075	0.075		
Norway	5	0.1	0.05	0.05	1.5	1.5
Poland	0.3	0.3	0.3	0.3	2	2
Portugal	5	0.025	0.025	0.025		
Romania	10	0.1	0.05	0.05		
Slovakia		0.1	0.1	0.1		2
Slovenia		0.15	0.15	0.15		
Spain	3	0.1	0.05			
Sweden	5	0.1	0.05	0.05		
Switzerland	6	0.15	0.15	0.15		0.3
UK	4	0.1	0.1	0.1	1.2	2.4
USA (OSHA)***	5	10 / %SiO_2 +2	Quartz PEL/2	Quartz PEL/2	80 / %$SiO_2$$^{\$}$	80 / %SiO_2
USA (NIOSH)******		0.05	0.05	0.05		

As shown throughout this thesis, and by others (Elias et al., 2002, Mossman and Glenn, 2013), the crystal polymorph is less important than the surface characteristics of the particle and the crystal purity. The presence of external minerals can also affect crystalline silica toxicity. Therefore, it may be more appropriate to set OELs based on the purity of the crystalline silica deposit being utilised, rather than the crystal polymorph. However, it is important to note that the long term effects of these impurities in dampening crystalline silica toxicity have not been examined here. Epidemiology studies of coalminers indicated that impurities can inhibit the development of disease in quartz exposure workers (Donaldson and Borm, 1998), but further work, investigating the long term effects of both internal and external impurities and consideration of other structural impurities (including Fe and Ca seen in DE cristobalite), is needed before any advice can be provided.

As well as implications for setting crystalline silica regulations and occupational exposures, the response to cristobalite exposure post-volcanic eruption may also be impacted by this and future research. Previous research has focussed on crystalline silica content in respirable volcanic ash, to determine the respiratory health hazard to the exposed population. Substantial quantities of cristobalite were found in volcanic ash from the 1980 Mount St Helens eruption (Dollberg et al., 1986), and the sustained eruptions, spanning decades, of Soufriere Hills Volcano (SHV), Montserrat, produced volcanic ash containing up to 30 wt.% cristobalite (Horwell et al., 2014, Jones and BéruBé, 2011). Long-term exposure to ashfall and resuspended ash during clean-up operations led to concern over the potential for development of silicosis and, to a lesser extent, lung cancer in exposed populations (Baxter et al., 2014, Hincks et al., 2006). This led to costly clean-up operations, and temporary and permanent relocation of populations (Baxter et al., 2014). However, analysis of SHV cristobalite shows it to contain up to 4 oxide wt.% Al+Na, and other phases, such as glass or feldspars, occluded the crystalline silica surface (Horwell et al., 2012). Subsequently, the ash from SHV was shown to have lower bioreactivity *in vitro* (Damby, 2012, Jones and BéruBé, 2011) and *in vivo* than expected (Cullen et al., 2002, Housley et al., 2002). Currently, the protocol used for rapid

analysis to assess the potential health hazard of volcanic ash (also used on past eruption) focusses on its particle size distribution (to determine if it is respirable) and measures crystalline silica content (e.g. Damby et al., 2013, Horwell et al., 2010a, Horwell et al., 2013, Horwell et al., 2010b, Hillman et al., 2012, Le Blond et al., 2010). If further work, including well-controlled epidemiology and *in vivo* studies (see Section 8.5), proves that impurities can reduce crystalline silica pathogenicity in the long-term, addition of SEM-EDS analyses of the cristobalite (to determine its purity) to the protocol could provide information on its likely ability to induce silicosis. With further work, analysis of crystalline silica purity could impact policy and hazard management both in industry and post-volcanic eruptions.

8.4 Implications for the DE hazard and regulations

Although the potential toxicity of DE could not be related to its crystalline silica content, it was shown to be highly variable among the samples used in this study. Biological reactivity varied both by processing technique and by deposit source (Chapter 5). Flux-calcined DE, those heated at ~1000 °C with the addition of a flux, were unreactive in the assays employed (Chapter 5), despite the fact they had the highest cristobalite content. As discussed above, this may be partly due to impurities in the crystal structure and the presence of other phases. The reduction in surface area due to fusion of particles during flux-calcination may also account for their low reactivity. Some of the most reactive DE samples were unprocessed, containing only trace quantities of crystalline silica. Currently, regulations for DE are primarily based on crystalline silica content and so focus on processed DE, although some countries have separate DE OELs (Table 8.1). However, little attention is given to unprocessed DE, where most of the material comprises amorphous silica, which is often given a lower OEL (similar to that of DE OELs) than inert dust, but much higher than crystalline silica (Table 8.1). Amorphous silica is generally less of a health concern than crystalline silica due, in part, to its easier removal from the lung. The assays employed here cannot assess particle removal and,

therefore, *in vivo* studies are needed to determine if these unprocessed samples are of concern in the long term. That the reactivity of unprocessed and calcined DE differed by location also warrants further investigation, to determine whether a single OEL value can be applied to all DE, or if DE regulation should/could be based on processing technique with an inbuilt factor for cristobalite purity (as described above) and presence of certain external impurities that would need to be defined. Although this may be possible in DE mines and processing plants, this would be difficult to implement for DE products, due to the exportation and importation of DE globally. Ideally, protection methods should be employed in all workplaces utilising DE to reduce personal exposure at all stages of mining and processing to prevent inhalation of both unprocessed and processed DE.

8.5 Future work

This study, the first to address the effect of chemical substitutions in the crystalline silica structure on its potential toxicity, using specifically produced synthetic samples, has strongly indicated that structural substitutions and external phases can decrease the toxic potency of cristobalite. However, to determine the impact of these impurities in occupational and environmental exposures to cristobalite requires further work. Here, J774 murine macrophages were used in all cytotoxicity cell studies, as macrophages are actively involved in defence and particle clearance from the lung, and are important in silica-induced toxicity. However, the effect of non-doped and doped crystalline silica samples on different cell types should also be addressed. Different types of macrophages can respond in different ways, for example, TNF-α production and NF-κB activation can be elevated in RAW 264.7 macrophages under conditions where no response is recorded in IC-21 macrophages (both derived from mice) (Gozal et al., 2002). Lung epithelial cells should also be considered as, although these are not actively involved in particle clearance, they can interact with particles and other cells, inducing cell-signalling pathways important in development of silicosis or cancers.

Further endpoints should also be considered; here, cytotoxicity, TNF-α generation and NF-κB activation were the main endpoints studied, as these have been shown to be important in silica-induced disease (Chen et al., 1995, Gozal et al., 2002, Hamilton et al., 2008, Rojanasakul et al., 1999). However, other pro-inflammatory cytokines should also be assessed. Recently, the importance of Il-1β in silica-induced toxicity has become apparent and is linked to the inflammasome activation pathway of silica induced disease (Cassel et al., 2008, Peeters et al., 2014). No Il-1β was released from DE-treated cells (Chapter 5), however, Il-1β was not analysed for cells treated with synthetic crystalline silica samples. Other pathways, such as activator protein activation, and oxidative stress could also be analysed, to determine the mechanisms causing silica-induced toxicity and how this varies between non-doped and doped crystalline silica.

Here, particle-derived free radicals were measured, however, no assessment of cell-derived free radicals was made. This could be indicated by assessing oxidative stress in treated cells. Genotoxicity should also be considered, specifically, as an endpoint for cells exposed to DE as, previously, it has been shown that, although some DE is non-cytotoxic, it has a high transforming potency (Elias et al., 2006). Flux-calcined DE, in particular, should be considered as, although this was unreactive in the assays employed here (Chapter 5), flux-calcined samples induced substantial particle derived hydroxyl radical ($OH^{\bullet}$) generation, which has been shown to correlate with particle transforming potency indicative of genotoxicity (Elias et al., 2006). However, a previous study showed no link between $OH^{\bullet}$ generation or oxygen consumption and direct DNA damage (Daniel et al., 1995).

Although further information may be gathered from more *in vitro* studies of both synthetic silica and DE as to the mechanisms of toxicity and potential to cause damage, a major limitation of this project is the lack of long term exposure times to assess if both inherent and external impurities in crystalline silica dusts have the ability to reduce the effect of crystalline silica toxicity over a long period. *In vivo* studies could go some way to answer this question. The use of synthetic silica with

and without impurities in an animal model would allow determination of whether doped and non-doped cristobalite induce disease to different extents as well as assessment of whether there is preferential dissolution of other phases that mask the crystalline silica surface and, therefore, if disease may develop over time. *In vivo* studies would also allow the assessment of removal or retention of particles in the lung and reactions of particle in lung lining fluids, which is difficult to measure *in vitro*. This may be particularly important for DE, where unprocessed samples consisting mainly of amorphous silica, some of which were highly reactive *in vitro* (Chapter 5), may not cause adverse effects in the long term if particles are easily cleared.

To date, only volcanic and DE cristobalite have been assessed for their purity. Although, DE is the main source of occupational exposure to cristobalite, other industries should also be considered. Cristobalite forms during calcining in the ceramics industry and can form from the heating of quartz in refractory brick works. In both volcanic settings and the DE industry, cristobalite is crystallised from an amorphous source of silica. Crystallisation from quartz may affect uptake of impurities into the cristobalite structure and this should be assessed to determine if impurities are found in cristobalite in all occupational settings.

Improvements and advancements to the method of crystalline silica synthesis employed here could also be made. In samples co-doped with Al and Na, phases other than cristobalite were formed (Chapter 6), some of which could not be identified. It is possible there was localised formation of these phases due to poor mixing of the silica sol and impurities. Saltzberg et al. (1992), used a spray dry technique in order to adequately mix the sol and impurities and this could be employed in the future. Here, samples were crystallised in pellet-form, some removed for sectioning (Chapter 6), and the rest cryogenically ground for particle characterisation and toxicological assays (Chapter 7). This process creates a fractured surface as would be experienced in occupational or natural crystalline silica dusts. However, imperfections at the surface due to grinding cannot be controlled, beyond

ensuring grinding settings are kept the same. Therefore, further work may look at the reactivity of these crystallised samples pre- and post-annealing at 800 °C, to remove surface defects introduced through grinding. Acid treatment, with HF, may also remove the surface layer of the particles, as well as amorphous material, leaving a cleaner crystalline silica surface, although this is likely to preferentially remove impurities from the surface. These techniques were not employed here, as a sample analogous to cristobalite formed in volcanic or occupational settings was required. However, these treatments may provide further information as to how impurities alter the crystalline silica toxicity.

Surface characterisation of the particles using X-ray photoelectron spectroscopy to analyse surface chemistry, infrared spectroscopy to analyse the effect of doping on surface silanols, and nuclear magnetic resonance spectroscopy to determine the coordinative state of Al would provide additional information to help determine the mechanisms by which Al and Na doping can decrease crystalline silica reactivity. Treatment of a non-doped cristobalite (e.g. 1600_12, Chapter 6) with Al and/or Na post-crystallisation, to determine if reactions of these elements with the cristobalite surface decreases its toxic potency, as seen for quartz (see Chapter 2, Table 2.1 for references), to the same extent as treatment before crystallisation, would also be informative. Again, this was not employed here, as it is not representative of cristobalite formation in nature, however, this could be utilised to determine if coating with impurities or incorporation of impurities into the crystal structure have similar of different effects on crystalline silica toxicity.

Further work should also consider other impurities. Saltzberg et al. (1992) showed that Al and Na or Ca were the most readily incorporated elements into the crystalline silica structure, and Al and Na are the impurities most commonly seen in volcanic cristobalite (Damby, 2012, Horwell et al., 2012) and, therefore, Al and Na were chosen here as dopants. However, in DE cristobalite, Fe and Ca were also observed in substantial quantities (Chapter 4). The effect of Fe on silica toxicity is not well

established (Chapter 2) and is dependent on the redox and coordinative state of Fe (Fubini et al., 2001). Therefore, synthetic samples with incremental Fe could be produced to analyse the ease of Fe incorporation into the crystal structure, the form this takes (likely Fe^{3+} substituting for Si^{4+} in the silica tetrahedra), and its effect on crystalline silica toxicity. The effect of Ca on crystalline silica toxicity is also unconstrained and should be the consideration of future work.

Co-doping with Al+Na did not reduce the toxic potential of cristobalite as much as the Al-only doped sample, when compared to non-doped cristobalite (Chapter 7). This difference could potentially be attributed to the presence of other phases in the co-doped sample but the finding was based on only one Al-only doped sample. Further work, with the production of a range of Al-only doped samples, alongside Al+Na doped samples, could provide information as to the role that Na plays and why there is a difference in toxicity. Further characterisation of the current particles, discussed above, may also help to elucidate the role that Na plays in Al uptake into the crystal structure or at the crystal surface and how this alters toxicity.

Although not a key aim of the present study, further understanding the source and uptake of impurities into the crystalline silica structure should be considered. Unfortunately, unprocessed DE samples were not available from all locations to determine the differences in the types of impurities among DE deposits from different locations. Unprocessed French and Spanish samples were enriched in clays and calcite respectively (Chapter 4), and had contrasting reactivity *in vitro* (Chapter 5). Therefore, an understanding of variability of impurities in unprocessed samples globally is important in understanding DE toxicity. Here, we showed that clays and carbonates were broken down during calcination, however, the change in the form of impurities during processing should be examined further, and how impurities are taken into the cristobalite structure should be investigated using diffusion profiles away from the cristobalite patches observed within the amorphous groundmass of the processed DE particles (Chapter 4).

8.6 Concluding remarks

This thesis has shown that cristobalite in processed DE is structurally impure, regardless of the location of the deposit, as has previously been observed for volcanic cristobalite. It is likely that most cristobalite, regardless of source, contains these impurities. The research here showed that these impurities in the crystalline silica structure, and at its surface, can reduce and even eliminate the *in vitro* reactivity of cristobalite as was hypothesised for DE and, previously, for volcanic cristobalite.

Other factors also controlled the potential toxicity of DE. The low surface area, and cristobalite formation within an amorphous matrix, in flux-calcined DE, means exposure of cristobalite at the surface of the particles is limited and may also explain their low reactivity *in vitro*. Other contaminant phases may contribute to DE toxicity and the different particle morphologies in DE may present a unique respiratory hazard. Therefore, using crystalline silica content alone in regulation and exposure assessments of DE may not be sufficient in determining the respiratory hazard.

Although further work is needed to substantiate the findings here and provide information on long term impacts of impurities on crystalline silica toxicity, these initial findings have potentially large implications for crystalline silica regulation, health hazard assessment in different crystalline silica-dust industries, and when considering exposure to natural cristobalite in volcanic ash.

References

BAXTER, P. J., SEARL, A. S., COWIE, H. A., JARVIS, D. & HORWELL, C. J. 2014. Chapter 22 Evaluating the respiratory health risks of volcanic ash at the eruption of the Soufrière Hills Volcano, Montserrat, 1995 to 2010. *Geological Society, London, Memoirs,* 39**,** 407-425.

CASSEL, S. L., EISENBARTH, S. C., IYER, S. S., SADLER, J. J., COLEGIO, O. R., TEPHLY, L. A., CARTER, A. B., ROTHMAN, P. B., FLAVELL, R. A. & SUTTERWALA, F. S. 2008. The Nalp3 inflammasome is essential for the development of silicosis. *Proceedings of the National Academy of Sciences of the United States of America,* 105**,** 9035-9040.

CHEN, F., SUN, S. C., KUH, D. C., GAYDOS, L. J. & DEMERS, L. M. 1995. Essential Role of NF-κB Activation in Silica-Induced Inflammatory Mediator Production in Macrophages. *Biochemical and Biophysical Research Communications,* 214**,** 985-992.

CULLEN, R. T., JONES, A. D., MILLER, B. G., TRAN, C. L., DAVIS, J. M. G., DONALDSON, K., WILSON, M., STONE, V. & MRGAN, A. 2002. Toxicity of volcanic ash from Montserrat. Edinburgh: Institute of Occupational Medicine. IOM TM/02/01

DAMBY, D., HORWELL, C., BAXTER, P., DELMELLE, P., DONALDSON, K., DUNSTER, C., FUBINI, B., MURPHY, F., NATTRASS, C. & SWEENEY, S. 2013. The respiratory health hazard of tephra from the 2010 Centennial eruption of Merapi with implications for occupational mining of deposits. *Journal of Volcanology and Geothermal Research,* 261**,** 376-387.

DAMBY, D. E. 2012. *From Dome to Disease: The Respiratory Toxicity of Volcanic Cristobalite.* Durham theses, Durham University.

DANIEL, L. N., MAO, Y., WANG, T. C. L., MARKEY, C. J., MARKEY, S. P., SHI, X. L. & SAFFIOTTI, U. 1995. DNA Strand Breakage, Thymine Glycol Production, and Hydroxyl Radical Generation Induced by Different Samples of Crystalline Silica in Vitro. *Environmental Research,* 71**,** 60-73.

DOLLBERG, D. D., BOLYARD, M. L. & SMITH, D. L. 1986. Chapter 6: Evaluation of Physical Health Effects Due to Volcanic Hazards: Crystalline Silica in Mount St. Helens Volcanic Ash. *American Journal of Public Health,* 76**,** 53-58.

DONALDSON, K. & BORM, P. J. A. 1998. The Quartz Hazard: A Variable Entity. *Annals of Occupational Hygiene,* 42**,** 287-294.

ELIAS, Z., POIROT, O., DANIÈRE, M. C., TERZETTI, F., BÉNA, F., FENOGLIO, I. & FUBINI, B. 2002. Role of Iron and Surface Free Radical Activity of Silica in the Induction of Morphological Transformation of Syrian Hamster Embryo Cells. *Annals of Occupational Hygiene,* 46**,** 53-57.

ELIAS, Z., POIROT, O., FENOGLIO, I., GHIAZZA, M., DANIÈRE, M. C., TERZETTI, F., DARNE, C., COULAIS, C., MATEKOVITS, I. & FUBINI, B. 2006. Surface Reactivity, Cytotoxic, and Morphological Transforming Effects of Diatomaceous Earth Products in Syrian Hamster Embryo Cells. *Toxicological Sciences,* 91**,** 510-520.

FUBINI, B., BOLIS, V., CAVENAGO, A. & VOLANTE, M. 1995. Physicochemical properties of crystalline silica dusts and their possible implication in various biological responses. *Scandinavian Journal of Work, Environment and Health,* 21 suppl 2**,** 9-14.

FUBINI, B., FENOGLIO, I., ELIAS, Z. & POIROT, O. 2001. Variability of biological responses to silicas: effect of origin, crystallinity, and state of surface on generation of reactive oxygen species and morphological transformation of mammalian cells. *J Environ Pathol Toxicol Oncol,* 20 Suppl 1**,** 95-108.

GOZAL, E., ORTIZ, L. A., ZOU, X., BUROW, M. E., LASKY, J. A. & FRIEDMAN, M. 2002. Silica-induced apoptosis in murine macrophage: involvement of tumor necrosis factor-alpha and nuclear factor-kappaB activation. *Am J Respir Cell Mol Biol,* 27**,** 91-8.

HAMILTON, J., RAYMOND F., THAKUR, S. A. & HOLIAN, A. 2008. Silica binding and toxicity in alveolar macrophages. *Free Radical Biology and Medicine,* 44**,** 1246-1258.

HILLMAN, S., HORWELL, C., DENSMORE, A., DAMBY, D., FUBINI, B., ISHIMINE, Y. & TOMATIS, M. 2012. Sakurajima volcano: a physico-chemical study of the health consequences of long-term exposure to volcanic ash. *Bulletin of Volcanology,* 74**,** 913-930.

HINCKS, T. K., ASPINALL, W. P., BAXTER, P. J., SEARL, A., SPARKS, R. S. J. & WOO, G. 2006. Long term exposure to respirable volcanic ash on Montserrat: a time series simulation. *Bulletin of Volcanology,* 68**,** 266-284.

HORWELL, C., LE BLOND, J., MICHNOWICZ, S. & CRESSEY, G. 2010a. Cristobalite in a rhyolitic lava dome: evolution of ash hazard. *Bulletin of Volcanology,* 72**,** 249-253.

HORWELL, C., WILLIAMSON, B., DONALDSON, K., LE BLOND, J., DAMBY, D. & BOWEN, L. 2012. The structure of volcanic cristobalite in relation to its toxicity; relevance for the variable crystalline silica hazard. *Particle and Fibre Toxicology,* 9**,** 44.

HORWELL, C. J., BAXTER, P. J., HILLMAN, S. E., CALKINS, J. A., DAMBY, D. E., DELMELLE, P., DONALDSON, K., DUNSTER, C., FUBINI, B., KELLY, F. J., LE BLOND, J. S., LIVI, K. J. T., MURPHY, F., NATTRASS, C., SWEENEY, S., TETLEY, T. D., THORDARSON, T. & TOMATIS, M. 2013. Physicochemical and toxicological profiling of ash from the 2010 and 2011 eruptions of Eyjafjallajökull and Grímsvötn volcanoes, Iceland using a rapid respiratory hazard assessment protocol. *Environmental Research,* 127**,** 63-73.

HORWELL, C. J., HILLMAN, S. E., COLE, P. D., LOUGHLIN, S. C., LLEWELLIN, E. W., DAMBY, D. E. & CHRISTOPHER, T. E. 2014. Chapter 21 Controls on variations in cristobalite abundance in ash generated by the Soufrière Hills Volcano, Montserrat in the period 1997 to 2010. *Geological Society, London, Memoirs,* 39**,** 399-406.

HORWELL, C. J., STANNETT, G. W., ANDRONICO, D., BERTAGNINI, A., FENOGLIO, I., FUBINI, B., LE BLOND, J. S. & WILLIAMSON, B. J. 2010b. A physico-chemical assessment of the health hazard of Mt. Vesuvius volcanic ash. *Journal of Volcanology and Geothermal Research,* 191**,** 222-232.

HOUSLEY, D. G., BERUBE, K. A., JONES, T. P., ANDERSON, S., POOLEY, F. D. & RICHARDS, R. J. 2002. Pulmonary epithelial response in the rat lung to instilled Montserrat respirable dusts and their major mineral components. *Occup Environ Med,* 59**,** 466-72.

IARC 1997. Silica, some silicates, coal dust and para-aramid fibrils. . Lyon: International Agency for Research on Cancer.

IARC 2012. Arsenic, Metals, Fibres, and Dusts. International Agency for Research on Cancer.

IMA-EUROPE. 2014. *Occupational Exposure Limits in mg/m^3 8 hours TWA – Respirable dust – in EU 27 + Norway & Switzerland* [Online]. http://www.crystallinesilica.eu/content/rcs-workplace-exposure-prevention: IMA-Europe. [Accessed 07/07/2015 2015].

JONES, T. & BÉRUBÉ, K. 2011. The bioreactivity of the sub-10µm component of volcanic ash: Soufrière Hills volcano, Montserrat. *Journal of Hazardous Materials,* 194**,** 128-134.

LE BLOND, J., HORWELL, C., BAXTER, P., MICHNOWICZ, S., TOMATIS, M., FUBINI, B., DELMELLE, P., DUNSTER, C. & PATIA, H. 2010. Mineralogical analyses and in vitro screening tests for the rapid evaluation of the health hazard of volcanic ash at Rabaul volcano, Papua New Guinea. *Bulletin of Volcanology,* 72**,** 1077-1092.

MELDRUM, M. & HOWDEN, P. 2002. Crystalline Silica: Variability in Fibrogenic Potency. *Annals of Occupational Hygiene,* 46**,** 27-30.

MOSSMAN, B. T. & GLENN, R. E. 2013. Bioreactivity of the crystalline silica polymorphs, quartz and cristobalite, and implications for occupational exposure limits (OELs). *Critical Reviews in Toxicology,* 43**,** 632-660.

NIOSH 2002. Health Effects of Occupational Exposure to Respirable Crystalline Silica. *In:* SERVICES, D. O. H. A. H. (ed.).

PEETERS, P. M., EURLINGS, I. M., PERKINS, T. N., WOUTERS, E. F., SCHINS, R. P., BORM, P. J., DROMMER, W., REYNAERT, N. L. & ALBRECHT, C. 2014. Silica-induced NLRP3 inflammasome activation in vitro and in rat lungs. *Part Fibre Toxicol,* 11**,** 58.

ROJANASAKUL, Y., YE, J., CHEN, F., WANG, L., CHENG, N., CASTRANOVA, V., VALLYATHAN, V. & SHI, X. 1999. Dependence of NF-kappaB activation and free radical generation on silica-induced TNF-alpha production in macrophages. *Mol Cell Biochem,* 200**,** 119-25.

SALTZBERG, M. A., BORS, S. L., BERGNA, H. & WINCHESTER, S. C. 1992. Synthesis of Chemically Stabilized Cristobalite. *Journal of the American Ceramic Society,* 75**,** 89-95.

Appendix 1

Referenced studies and data

Chapter 2 – Table of crystalline silica synthesis studies with dopants

Table A1: Summary of crystalline silica synthesis studies and the phases formed at different treatment temperatures, durations and dopant concentrations added. I = interstitial ions, T = tetrahedrally coordinated ions, *values expressed as oxide %. $ crist = cristobalite, trid = tridymite, ? = unknown phase

Study	Starting material	Method	Temp. (°C)	Time (h)	Doping ions	Molar ratio (I:T:Si)	Weight % (I:T:Si)*	Phase(s) formed$
Alcalá et al. (1996)	Silica	incipient wetness	1000	32	-			amorphous, α-crist
			1050	24	-			amorphous, α-crist
			1100	3	-			a crist
			1150	1	-			α-crist
			1400	1	-			α-crist
			1000	32	Ca, Al	1:2:38	2:8:90	α-crist, amorphous
			1050	24	Ca, Al	1:2:38	2:8:90	α-crist, quartz
			1150	3	Ca, Al	1:2:38	2:8:90	α-crist, quartz
			1000	32	Ca, Al	1:2:27	3:11:86	β-crist
Chao and Lu (2000)	colloidal silica sol (Ludox HS-30)	sol/gel	800	9	Na	1:0:76	1:0:99	α-crist
			825	8	Na	1:0:76	1:0:99	α-crist
			850	2.5	Na	1:0:76	1:0:99	α-crist
			750	9	Na	1:0:50	2:0:98	α-crist
			775	8	Na	1:0:50	2:0:98	α-crist
			800	2.5	Na	1:0:50	2:0:98	α-crist
			800	?	Na	1:0:38	3:0:97	α-crist
Chao and Lu (2002b)	colloidal silica sol (Ludox HS-30)	sol/gel	1100	24	Na, Al	1:1:32	3:5:92	α-crist
			1100	24	Na, Al	1:1:25	4:6:90	α- and β-crist
			1100	48	Na, Al	1:1:20	5:8:87	α-crist (β-crist?)
			1100	48	Na, Al	1:1:14	6:10:84	β-crist

			1100	48	Na, Al	1:1:32	3:5:92	α- and β-crist
			1100	48	Na, Al	1:1:25	4:6:90	α- and β-crist
			1100	48	Na, Al	1:1:20	5:8:87	α- and β-crist
Chao and Lu (2002a)	colloidal silica sol (Ludox HS-30)	sol/gel	1100	48	Al	0:1:32	0:5:95	α-crist
			1100	48	Al	0:1:25	0:6:94	α-crist
			1100	48	Al	0:1:20	0:8:92	α-crist
			1100	48	Al	0:1:14	0:11:89	amorphous (α-crist)
			1100	1	Na	1:0:50	2:0:98	α-trid, α-crist
Perrotta et al. (1989)	colloidal silica sol (Ludox AS)	sol/gel	1200	12	Na, Al	1:1:50	2:3:95	α-crist
			1200	12	Na, Al	1:1:33	3:5:92	α-crist
			1200	24	Na, Al	1:1:22	4:7:89	α-crist (amorphous)
			1200	24	Na, Al	1:1:17	5:8:86	α-crist, amorphous (β-crist)
			1200	24	Na, Al	1:1:16	5:9:86	α-crist, amorphous β-crist
			1200	24	Na, Al	1:1:15	6:9:85	β-crist, amorphous (α-crist)
			850-1200	24	Na, Al	1:1:14	6:10:84	β-crist, amorphous
			1250	24	Na, Al	1:1:14	6:10:84	amorphous, β-crist
			1300	24	Na, Al	1:1:14	6:10:84	amorphous (β-crist)
			1200	24	Na, Al	1:1:13	7:11:83	amorphous, β-crist
			1200	24	Na, Al	1:1:12	7:11:82	amorphous, β-crist
			800	24	Na, Al	1:1.8:17	5:15:80	Amorphous
			900-1000	24	Na, Al	1:1.8:17	5:15:80	amorphous (β-crist)
			1200	24	Na, Al	1:1.8:17	5:15:80	β-crist, amorphous
			1250-1300	24	Na, Al	1:1.8:17	5:15:80	β-crist, amorphous, mullite
			1000-1200	24	Ca, Al	1:1:10	7:13:79	β-crist, anorthite
			1000-1200	24	Ca, Al	1:1:15	5:10:85	β-crist, anorthite
			1000-1200	24	Ca, Al	1:1:20	4:7:88	β-crist (anorthite)
			1000-1200	24	Ca, Al	1:1:25	3:6:90	β-crist (anorthite)
			1000	24	Ca, Al	1:1:30	3:5:92	β-crist (anorthite)
			1000	24	Ca, Al	1:1:35	2:5:93	β-crist (anorthite)
			1000	24	Ca, Al	1:1:40	2:4:94	β-crist (anorthite)
			1200	24	Ca, Al	1:1:30	3:5:92	β-crist (anorthite, α-crist)
			1200	24	Ca, Al	1:1:35	2:5:93	β-crist (anorthite, α-crist)
			1200	24	Ca, Al	1:1:40	2:4:94	β-crist (anorthite, α-crist)
			1400	24	Ca, Al	1:1:10	7:13:79	β-crist (amorphous)
			1400	24	Ca, Al	1:1:15	5:10:85	β-crist (α-crist)
			1400	24	Ca, Al	1:1:20	4:7:88	β-crist (α-crist)

			1400	24	Ca, Al	1:1:25	3:6:90	β-crist (α-crist)
			1400	24	Ca, Al	1:1:30	3:5:92	β-crist (α-crist)
			1400	24	Ca, Al	1:1:35	2:5:93	β-crist, α-crist
			1400	24	Ca, Al	1:1:40	2:4:94	β-crist, α-crist
			1000	24	Ca, Na, Al	0.25:0.75:1:14	1:5:10:84	β-crist, amorphous, anorthite (?)
			1000	24	Ca, Na, Al	0.5:0.5:1:14	3:3:10:84	β-crist, anorthite (amorphous, ?)
			1000	24	Ca, Na, Al	0.75:0.25:1:14	4:2:10:84	β-crist, anorthite (?)
Saltzberg et al. (1992)	silica sol	sol/gel	1100	24	Ca, Al	1:2:165	1:2:97	quartz, α-crist
			1100	24	Ca, Al	1:2:82	1:4:95	α-crist, CSC, quartz
			1100	24	Ca, Al	1:2:38	2:8:90	CSC
			1100	24	Ca, Al	1:2:20	4:14:82	CSC, anorthite
			1100	24	Ca, Al	1:4:38	2:15:83	CSC
			1100	24	-			α-crist (quartz)
			1100	24	Ca, Al	1:2:38	-	CSC
			1100	24	Ca, B	1:2:38	-	α-crist, quartz
			1100	24	Ca, La	1:2:38	-	α-crist, $Ca_3La_6Si_6O_{24}$
			1100	24	Ca, Y	1:2:38	-	α-crist, quartz, $Ca_4Y_6Si_6O_{25}$
			1100	24	Ca, Ga	1:2:38	-	α-crist, quartz
			1100	24	K, Al	1:1:19	-	α-crist, amorphous
			1100	24	Na, Al	1:1:19	-	CSC, α-crist, amorphous (quartz)
			1100	24	Li, Al	1:1:19	-	α-crist, ? , amorphous
			1100	24	Mg, Al	1:2:38	-	amorphous, α-crist
			1100	24	Sr, Al	1:2:38	-	CSC (α-crist)
			1100	24	Ba, Al	1:2:38	-	α-crist, $BaAl_2Si_2O_8$
			1100	24	Zn, Al	1:2:38	-	amorphous, ?
			1100	24	La, Al	1:3:57	-	α-crist (quartz)
			1000	24	Ca, Al	1:2:38	-	CSC (amorphous)
			1000	24	Ca, B	1:2:38	-	α-crist, quartz
			1000	24	Ca, La	1:2:38	-	α-crist, $Ca_3La_6Si_6O_{24}$, amorphous
			1000	24	Ca, Y	1:2:38	-	α-crist, amorphous (quartz)
			1000	24	Ca, Ga	1:2:38	-	α-crist, quartz
			1000	24	K, Al	1:1:19	-	Amorphous
			1000	24	Na, Al	1:1:19	-	CSC, α-crist, amorphous (quartz)
			1000	24	Li, Al	1:1:19	-	α-crist, ? , amorphous
			1000	24	Mg, Al	1:2:38	-	amorphous (α-crist)

			1000	24	Sr, Al	1:2:38	-	CSC (α-crist)
			1000	24	Ba, Al	1:2:38	-	amorphous (α-crist)
			1000	24	Zn, Al	1:2:38	-	amorphous (?)
			1000	24	La, Al	1:3:57	-	amorphous (α-crist)
Gai-Boyes et al. (1993)	Aerosol	-	1400	24	-			α-crist
	colloidal silica sol (Ludox_AS40)	sol/gel	1100	24	Ca, Al	1:2:40	2:8:90	CSC
Şan and Özgür (2009)	colloidal silica	sol/gel	1100	24	Ca, Al	1:2:98	1:3:96	quartz, α-crist, β-crist
			1100	24	Ca, Al	1:2:48	2:6:92	quartz, α-crist, β-crist
			1100	24	Ca, Al	1:2:38	2:8:90	β-crist
			1100	24	Ca, Al	1:2:31	3:10:88	β-crist, anorthite
			1100	24	Ca, Al	1:2:27	3:11:86	β-crist, anorthite
			1100	24	Ca, Al	1:2:23	3:12:84	β-crist, anorthite
			1100	24	Ca, Al	1:2:18	4:15:81	β-crist, anorthite
			1100	12	Ca, Al	1:2:38	2:8:90	β-crist (α-crist)
			1100	12	Ca, Al	1:4:38	2:15:83	β-crist (α-crist)
			1100	4	Ca, Al	1:2:38	2:8:90	β-crist (α-crist)
			1100	4	Ca, Al	1:4:38	2:15:83	β-crist
Shinohara (1990)	silicic acid		1450	3	-			α-crist
			1100	?	-			α-crist
Thomas et al. (1994)	Ludox AM colloidal silica	sol/gel	1200	18-24	Na, Al	1:1:14	6:10:84	β-crist, amorphous
			1300	18-24	Na, Al	1:1:14	6:10:84	Amorphous, β-crist
			1000	18-24	Ca, Al	1:1:30	-	β-crist
			1000	18-24	Cu, Al	1:1:30	-	β-crist
			1000	18-24	Sr, Al	1:1:30	-	β-crist, feldspar-type
			1000	18-24	Ba, Al	1:1:30	-	α-crist, ?
			1000-1300	18-24	K, Al	1:1:14	-	Amorphous
			950	18-24	Li, Al	1:1:14	-	α-crist, stuffed quartz
			1000-1400	18-24	Na, Mg	1:1:14	-	Trid
			1050-1100	18-24	Na, Mg	1:1:1.5	-	$Na_4Mg_2Si_3O_{10}$, Na_2MgSiO_4
			1000	18-24	Mg, Al	1:1:9	-	β-crist, stuffed quartz, amorphous
			900	18-24	Mg, Al	1:1:14	-	Amorphous
			1000	18-24	Mg, Al	1:1:14	-	β-crist, stuffed quartz, amorphous, trid
			1100	18-24	Mg, Al	1:1:14	-	α-crist
			1000	18-24	Mg, Al	1:1:28	-	α-crist
			1100	18-24	Zn, Al	1:1:30	-	Quartz, α-crist
			1200	18-24	Ni, Al	1:1:30	-	α-crist

			1100	18-24	Co, Al	1:1:30	-	α-crist, quartz
			1000	18-24	Pb, Al	1:1:30	-	α-crist, $Pb_2Al_2O_5$
			1000	18-24	Ca, Fe	1:1:30	-	α-crist, $CaFe_4O_7$
			1000-1100	18-24	Pb, Fe	1:1:30	-	Trid
Venezia et al. (2001)	silica	incipient wetness	1000	4	Li			$LiSi_2O_5$, quartz
			800	4	Li			quartz, crist
			800	4	Na			Crist
			800-1000	4	K			trid, crist, amorphous
			1000	4	Cs			trid, crist, amorphous

References

ALCALÁ, M. D., REAL, C. & CRIADO, J. M. 1996. A New "Incipient-Wetness" Method for the Synthesis of Chemically Stabilized β-Cristobalite. *Journal of the American Ceramic Society,* 79**,** 1681-1684.

CHAO, C. H. & LU, H. Y. 2000. Crystallization of Na2O-doped colloidal gel-derived silica. *Materials Science and Engineering a-Structural Materials Properties Microstructure and Processing,* 282**,** 123-130.

CHAO, C. H. & LU, H. Y. 2002a. beta-cristobalite stabilization in (Na2O+Al2O3)-added silica. *Metallurgical and Materials Transactions a-Physical Metallurgy and Materials Science,* 33**,** 2703-2711.

CHAO, C. H. & LU, H. Y. 2002b. Stress-induced beta ->alpha-cristobalite phase transformation in (Na2O+Al2O3)-codoped silica. *Materials Science and Engineering a-Structural Materials Properties Microstructure and Processing,* 328**,** 267-276.

GAI-BOYES, P. L., SALTZBERG, M. A. & VEGA, A. 1993. Structures and Stabilization Mechanisms in Chemically Stabilized Ceramics. *Journal of Solid State Chemistry,* 106**,** 35-47.

PERROTTA, A. J., GRUBBS, D. K., MARTIN, E. S., DANDO, N. R., MCKINSTRY, H. A. & HUARG, C.-Y. 1989. Chemical Stabilization of β-Cristobalite. *Journal of the American Ceramic Society,* 72**,** 441-447.

SALTZBERG, M. A., BORS, S. L., BERGNA, H. & WINCHESTER, S. C. 1992. Synthesis of Chemically Stabilized Cristobalite. *Journal of the American Ceramic Society,* 75**,** 89-95.

ŞAN, O. & ÖZGÜR, C. 2009. Investigation of a high stable β-cristobalite ceramic powder from CaO–Al2O3–SiO2 system. *Journal of the European Ceramic Society,* 29**,** 2945-2949.

SHINOHARA, Y. 1990. Synthesis of well crystallized cristobalite as a reference mineral. *Industrial Health,* 28**,** 139-143.

THOMAS, E. S., THOMPSON, J. G., WITHERS, R. L., STERNS, M., XIAO, Y. & KIRKPATRICK, R. J. 1994. Further Investigation of the Stabilization of β-Cristobalite. *Journal of the American Ceramic Society,* 77**,** 49-56.

VENEZIA, A. M., LA PAROLA, V., LONGO, A. & MARTORANA, A. 2001. Effect of Alkali Ions on the Amorphous to Crystalline Phase Transition of Silica. *Journal of Solid State Chemistry,* 161**,** 373-378.

Chapter 3 - Grinding tests

Particle size distribution and BET surface area data for one non-doped (1600_4) and one doped (2Al+Na_1100_24) synthetic crystalline silica samples ground by cryogenic milling or hand grinding with an agate mortar and pestle is provided (Table AXX). Due to the use of these samples in toxicological experiments it was important to produce particles of a size fraction that would be able to penetrate into the lung (<100 µm inhalable, <10 µm thoracic and <4 µm respirable), but that had high enough surface area to enable differences in surface functionalities to be assessed.

Table A2: Mean particle diameter, particle size distribution (cumulative volume (c.v.) %) and BET surface area of 1600_4 and 2Al+Na_1100_24 ground by cryogenic milling or by hand with agate mortar and pestle. 1600_4 was tested by cryogenic grinding for 30 mins and 1 h.

	Cryogenically milled			**Hand ground**	
	1600_4_1h	**1600_4_30min**	**2Al+Na_1100_24_30min**	**1600_4_HG**	**2Al+Na_1100_24_HG**
Particle size					
Mean diameter (µm)	44.8	32.7	17.5	22.3	19.7
c.v. %					
<4 µm	12.5	19.3	30.8	13.6	17.8
<10 µm	25.8	36.6	51.6	27.7	35.6
<100 µm	89.8	94.1	100.0	100.0	100.0
Surface area					
m^2/g	-	6.5	6.2	0.4	0.9

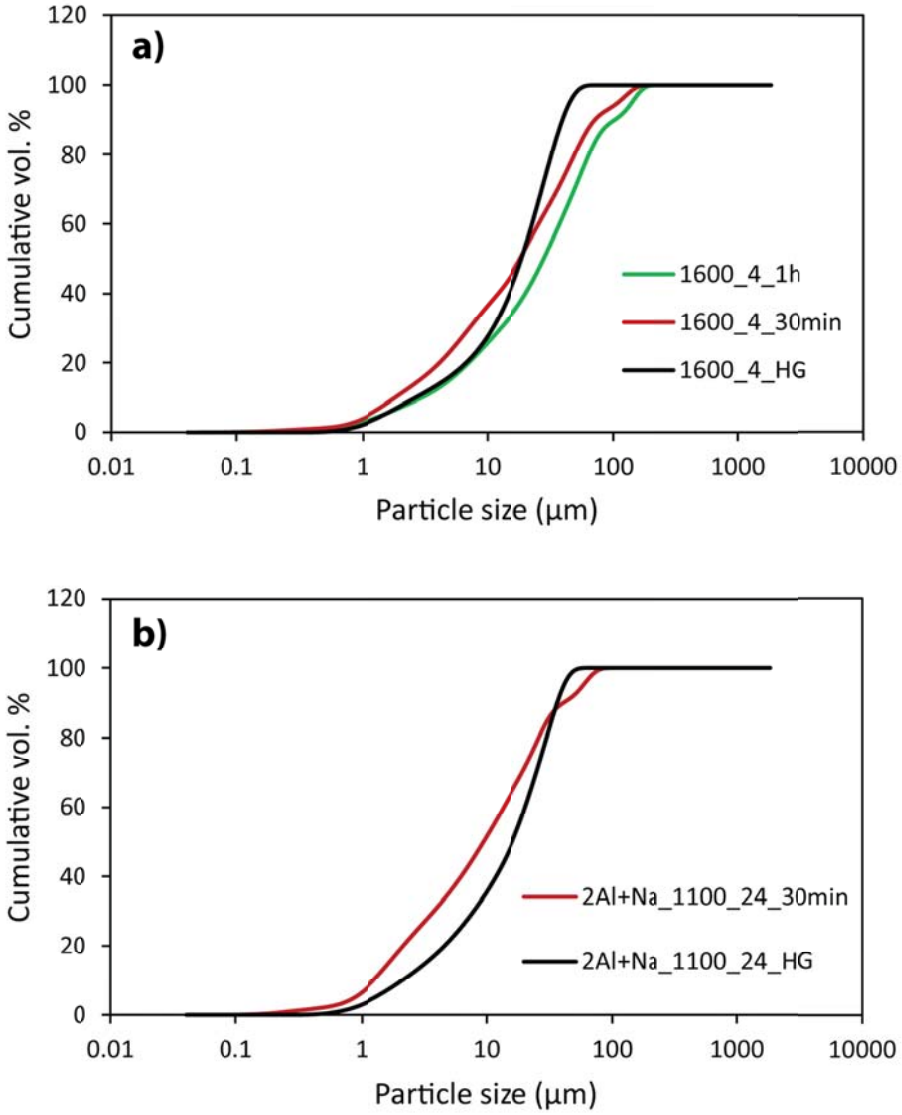

Figure A1: Particle size distributions of **a)** 1600_4 and **b)** 2Al+Na_1100_24 ground by cryogenic grinding for 30 minutes (red) or 1 h (green), or ground by hand with agate mortar and pestle.

Particles with a low surface area were produced by hand grinding, and cryogenic milling for 30 minutes produced a higher per cent of particles <10 and <4 µm. Therefore, cryogenic grinding for 30 minutes was used for the production of powders for toxicological experiments in Chapter 7.

Chapter 4 – data

All raw data for Chapter 4 are available in Appendix 2.

Chapter 5 – data

All raw data for Chapter 5 are available in Appendix 2. Here, graphical presentation of the haemolytic potential of the bulk and fine fraction of DE (Figure A2). There was no significant difference between the haemolytic potential of the bulk and fine fraction of any sample, analysed by ANOVA, and Tukey's post-hoc statistical tests. The haemolytic potency and cytotoxicity determined by the alamarBlue® assay of DE leachates is shown in Figures A3 and A4. There was no difference between leachate treatments and the untreated controls.

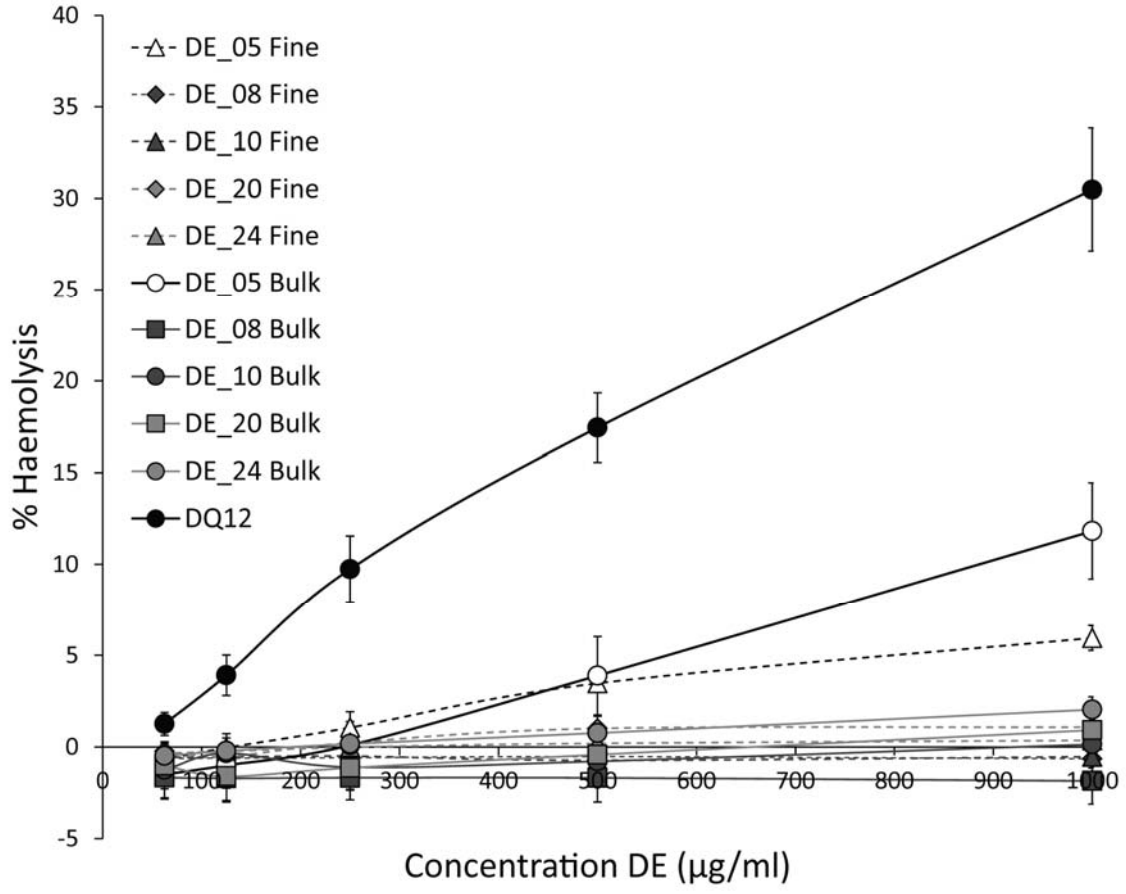

Figure A2: Haemolytic potential of the bulk and fine fractions of DE samples. Per cent haemolysis relative to an untreated control, of sheep red blood cells post-exposure to 1 mg/ml of unprocessed (white), calcined (light grey) and flux-calcined (dark grey) DE and positive (DQ12) standard (black). Error bars represent standard error (n=3).

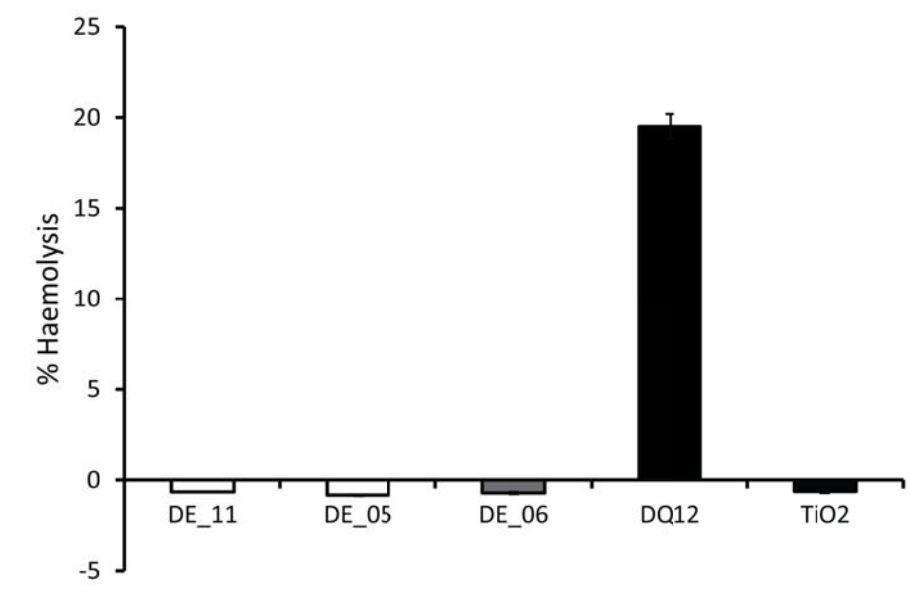

Figure A3: Haemolytic potential of leachates of DE samples. Per cent haemolysis relative to an untreated control, of sheep red blood cells post-exposure to 1 mg/ml of unprocessed (white), and flux-calcined (dark grey) DE leachate and positive (DQ12) and negative (TiO_2) particles standards (black). Error bars represent standard error (n=3).

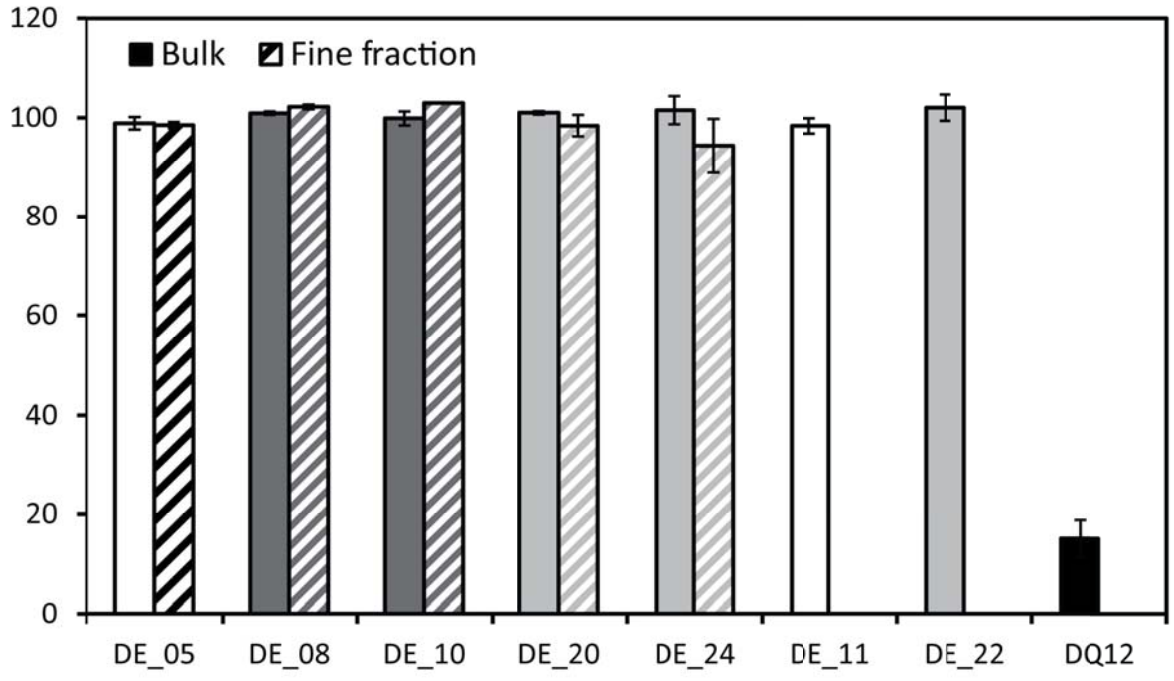

Figure A4: Cell viability of J774 macrophages exposed to DE leachates, measured by the alamarBlue® assay. Leachates from the fine fraction (hashed) and bulk (solid) of unprocessed (white), calcined (light grey) and flux-calcined (dark grey) DE, and positive (DQ12) and negative (TiO_2) standards (black) for 24 hours. Fine fractions of DE_11, DE_22 not separated so there are no data. Error bars represent standard error.

Chapter 6 – data

All raw data for Chapter 6 are available in Appendix 2.

Chapter 7 – data

All raw data for Chapter 7 are available in Appendix 2.

Appendix 2

Raw data

A digital version of all the raw data for the four research chapters are provided on the CD-ROM in the back cover of this thesis or can be provided by the author upon request.

Appendix 3

Publications

Journal of Occupational Medicine and Toxicology (2015) 10:23

The global variability of diatomaceous earth toxicity: a physicochemical and in vitro investigation

C. Nattrass, C. J. Horwell, D. E. Damby, A. Kermanizadeh, D. M. Brown and V. Stone

Nattrass et al. Journal of Occupational Medicine and Toxicology (2015) 10:23
DOI 10.1186/s12995-015-0064-7

JOURNAL OF OCCUPATIONAL MEDICINE AND TOXICOLOGY

RESEARCH Open Access

The global variability of diatomaceous earth toxicity: a physicochemical and in vitro investigation

C. Nattrass[1], C. J. Horwell[1*], D. E. Damby[2], A. Kermanizadeh[3,4], D. M. Brown[3] and V. Stone[3]

Abstract

Background: Diatomaceous earth (DE) is mined globally and is potentially of occupational respiratory health concern due to the high crystalline silica content in processed material. DE toxicity, in terms of variability related to global source and processing technique, is poorly understood. This study addresses this variability using physicochemical characterisation and in vitro toxicology assays.

Methods: Nineteen DE samples sourced from around the world, comprising unprocessed, calcined and flux-calcined DE, were analysed for chemical and mineral composition, particle size and morphology, and surface area. The potential toxicity of DE was assessed by its haemolytic capacity, and its ability to induce cytotoxicity or cytokine release by J774 macrophages.

Results: The potential toxicity of DE varied with source and processing technique, ranging from non-reactive to as cytotoxic and haemolytic as DQ12. Crystalline silica-rich, flux-calcined samples were all unreactive, regardless of source. The potential toxicity of unprocessed and calcined samples was variable, and did not correlate with crystalline silica content. Calcium-rich phases, iron content, amorphous material, particle size and morphology all appeared to play a role in sample reactivity. An increased surface area was linked to an increased reactivity in vitro for some sample types.

Conclusions: Overall, no single property of DE could be linked to its potential toxicity, but crystalline silica content was not a dominant factor. Occlusion of the potentially toxic crystalline silica surface by an amorphous matrix or other minerals and impurities in the crystal structure are suggested to pacify toxicity in these samples. In vivo verification is required, but these data suggest that crystalline silica content alone is not a sufficient indicator of the potential DE hazard.

Keywords: Diatomaceous earth, Cristobalite, Crystalline silica, Cytotoxicity, Haemolysis, Variability

Introduction

Diatomaceous earth (DE), a sedimentary deposit of silica-rich diatom frustules, is mined globally for a range of purposes, including its commercial value in the filler and filter aid industries [1, 2]. Diatomite deposits are mainly composed of amorphous silica or opal diatom skeletons – the dominant diatom species of which can vary among deposits [2] – and can be interspersed with contaminant minerals, such as clays or carbonates [1]. Extracted material is processed by a series of grinding, calcination and classification techniques to give a wide range of end products. During this process, the diatomite deposit (unprocessed DE) is treated at ~1000 °C with (flux-calcined) or without (calcined) the presence of a fluxing agent, usually sodium carbonate [1, 3]. During calcination, the amorphous silica is converted to crystalline silica, predominantly in the form of cristobalite [2, 3]. The potential for crystalline silica to cause silicosis is well established [4–6], and quartz and cristobalite are classified as Group 1 carcinogens [7, 8]; therefore, exposure to processed DE has the potential to cause chronic respiratory disease.

* Correspondence: claire.horwell@durham.ac.uk
[1]Institute of Hazard, Risk & Resilience, Department of Earth Sciences, Durham University, Durham DH1 3LE, UK
Full list of author information is available at the end of the article

A number of epidemiology studies assessing the respiratory DE hazard show increased mortality [9, 10], pneumoconiosis [11–14], increased risk of lung cancer [9, 10, 15] and other lung diseases [16] in DE workers, compared to unexposed populations. These findings are supported by radiographic evidence, which shows a strong relationship between exposure and the risk of opacities in chest X-rays indicative of silicosis [17]. However, these studies only focused on DE deposits from California, USA, and little is known about how the physicochemical characteristics of DE vary globally. As such, these data may not inform the health hazard of DE worldwide; the few studies at other locations are much less detailed. The largest of these studies, in Iceland, showed a non-significant increase in lung cancer for DE workers [18]. Beskow [19] and Ebina et al. [20] found signs of silicosis in DE workers in Sweden and Japan, but these were based on a small number of cases; whereas, Joma et al. [21] found no signs of pneumoconiosis in DE-exposed workers in the Netherlands, but airflow in the lung was reduced after exposure.

Some of the above studies include evidence of silicosis-type pathology [12, 19, 20, 22], or strong, positive correlations between crystalline silica content and level of observed disease [9, 17, 23]. However, other clinical and epidemiological studies have demonstrated no link between crystalline silica exposure and the pathogenicity observed in DE workers [14], and showed pathological changes in the lungs which differ from typical quartz-induced silicosis [22]. Generally, crystalline silica content is shown to be very low in unprocessed samples (0–4 wt.%), high in calcined samples (>10 wt.%), and highest in flux-calcined samples (>20 wt.%) (e.g. [9, 24]). It is often difficult to distinguish among these different types of DE exposures in epidemiological studies.

Toxicology studies allow differences between processed and unprocessed DE to be studied systematically. As with epidemiological studies, there is discrepancy among toxicological studies as to whether crystalline silica content is the determinant factor for disease. This knowledge is essential for the effective risk management of worker safety.

Many in vitro studies indicate that the cytotoxicity of DE does not correlate with crystalline silica content, as unprocessed and calcined DE exert a greater cytotoxic effect than cristobalite-rich flux-calcined DE in a number of in vitro assays on different cell lines [24–27]. However, work by Elias and co-workers has shown that cristobalite-rich DE samples (both flux-calcined and those calcined at high temperature) have increased procarcinogenic potential in Syrian hamster embryos compared to unprocessed DE and DE calcined at lower temperature [26, 28]. Exposure to both unprocessed and flux-calcined DE also resulted in an increase in abnormal nuclei formation (a marker of genotoxicity) in Chinese hamster ovary cells, with the damage more significant than quartz and cristobalite standards [24].

In vivo studies of unprocessed, amorphous DE show it has the potential to be pathogenic, causing acute/subacute inflammation in rats 60 days after a single intratracheal injection of 10 mg DE, an effect that decreased with time [29]. While inhalation of unprocessed DE (170 million particles per cubic foot (mppcf)) by guinea pigs for 39–44 h/week for 24 months resulted in fibrosis, calcined, cristobalite-rich DE was seen to cause more severe fibrosis more rapidly [30]. However, in a separate study, exposure via inhalation to 5–50 mppcf flux-calcined DE, consisting of 61 % cristobalite, for 30 h/week up to 30 months caused no body weight loss or pulmonary fibrosis in rats, guinea pigs or dogs [31].

Previous studies have focussed on few samples and single locations and, therefore, have not been able to investigate the source-dependent compositional and morphological variability of DE and the effect of this variability on toxicity endpoints. This study overcomes this limitation by determining the potential toxicity of DE sourced from seven quarries across the world, and investigating the physicochemical characteristics of the material to understand the properties that affect DE toxicity. Samples chosen cover a spectrum of deposit types, purities and processing techniques. Physicochemical analyses assessed sample composition, morphology, particle size and surface area. Haemolysis allowed for the assessment of particle-induced membrane damage, while cytotoxicity and cytokine release from macrophages were used to assess potential particle toxicity and the potential to induce inflammation.

Materials and methods

Nineteen DE samples were sourced from mines around the world to account for the global variability of DE deposits (Table 1). A range of DE products that encompass the spectrum of compositional characteristics and processing techniques available were selected using geochemical data obtained though the European Industrial Minerals Association (IMA-Europe). The sample set comprised unprocessed, calcined and flux-calcined samples, and included filler and filter aid grades of DE, which are determined by post-calcination size classification. Samples were chosen from a range of source deposits, including those with impurities (carbonates and clays). Unprocessed samples, and the equivalent sample post-processing, were sourced where possible in order to directly establish the effects of processing.

Separation of the fine fraction

Fine fractions (close to PM10) were separated from 5 bulk samples for toxicological assessment alongside their

Table 1 Information for diatomaceous earth samples, including: particle size distribution, surface area and chemical composition

Sample information				Particle size distribution (c.v. %)		BET surface area (m^2/g)		Chemical composition (wt.%)							
Sample ID	Source	Process	Grade	<4 μm	<10 μm	Mean	s.d.	SiO_2	TiO_2	Al_2O_3	Fe_2O_3	MgO	CaO	Na_2O	K_2O
DE_05[#a]	Spain	U	Filler	11.3	38.8	7.5	0.7	90.47	0.05	0.91	0.38	0.34	6.96	0.65	0.14
DE_11[b]	Spain	U	Filler	12.4	47.3	6.3	0.4	87.26	0.05	1.40	0.42	0.49	8.96	1.04	0.17
DE_13[c]	France	U	Filter aid	7.8	28.0	22.9	0.2	89.02	0.64	4.42	3.22	0.36	0.66	0.38	0.35
DE_15[d]	France	U	Filter aid	7.9	28.5	23.8	0.3	87.40	0.70	4.73	3.99	0.49	0.74	0.19	0.34
DE_16[d]	France	C	Filter aid	6.7	25.0	3.8	0.1	88.03	0.66	4.50	3.86	0.39	0.66	0.17	0.33
DE_18	China	C	Filter aid	7.3	28.1	3.1	0.1	93.49	0.15	3.71	1.67	0.35	0.08	−0.04	0.50
DE_20[#]	Mexico	C	Filter aid	6.8	25.3	4.0	0.1	92.00	0.24	5.07	1.95	0.34	0.30	−0.13	0.20
DE_21	USA-1[e]	C	Filter aid	6.2	21.7	5.7	0.2	87.83	0.32	6.57	1.81	1.02	0.54	0.51	1.02
DE_22	USA-1	C	Filler	25.4	71.5	10.6	0.2	93.24	0.17	3.82	1.15	0.65	0.17	0.03	0.59
DE_23	USA-1	C	Filter aid	21.8	65.5	6.8	0.2	93.88	0.15	3.03	1.05	0.69	0.30	0.21	0.47
DE_24[#]	Mexico	C	Filter aid	12.1	45.0	5.9	0.2	93.63	0.19	3.89	1.49	0.33	0.22	0.01	0.18
DE_06[a]	Spain	FC	Filler	8.5	34.4	1.1	0.1	91.27	0.03	0.67	0.35	0.27	6.25	1.00	0.09
DE_07	USA-1	FC	Filler	10.6	31.6	1.3	0.0	91.67	0.15	3.00	1.07	0.53	0.29	2.69	0.48
DE_08[#]	USA-2[e]	FC	Filler	9.2	28.7	1.3	0.1	93.07	0.06	1.12	1.99	0.51	0.30	2.89	0.03
DE_09	Chile	FC	Filler	9.8	33.4	1.5	0.1	93.04	0.10	1.82	0.95	0.23	1.29	2.15	0.34
DE_10[#]	Mexico	FC	Filler	8.7	35.3	1.7	0.1	93.64	0.10	2.05	0.80	0.14	0.32	2.59	0.12
DE_12[b]	Spain	FC	Filler	8.5	33.4	1.0	0.1	90.67	0.03	1.12	0.35	0.31	6.64	0.69	0.10
DE_14[c]	France	FC	Filter aid	6.4	17.0	1.1	0.1	87.36	0.58	4.10	2.61	0.40	0.62	3.17	0.39
DE_17	China	FC	Filter aid	4.6	11.4	1.0	0.0	91.68	0.13	3.12	1.44	0.27	0.11	2.22	0.51

Table sorted by process: *U* unprocessed, *C* calcined, *FC* flux-calcined, *c.v.* cumulative volume, *s.d.* standard deviation ($n = 3$). [#]The fine fractions of these samples were separated for use in toxicology assays. [e] Samples were sourced from two separate deposits in the USA and so are denoted as USA-1 and USA-2.[a–d] Unprocessed samples and their corresponding processed samples

bulk counterparts (Table 1). The samples, which comprise a range of crystalline silica contents, bulk impurities, and processing techniques, were separated by dry-resuspension as previously described by Moreno et al. [32]. Briefly, the sample was suspended in a horizontal rotating drum with a baffle (1.5 rpm). Airflow of 6 l/min was passed through this system, which carried suspended particles through a gravitational settling chamber, where coarser particles were deposited, and the fine fraction continued through a Negretti elutriation filter system and was collected on a polycarbonate filter. The particle size distribution of the separated fine fractions was determined by SEM image analysis.

Physicochemical characterisation

Physiochemical analyses were carried out on bulk samples (because of the mass required by some techniques). The crystalline silica polymorph and relative crystalline silica contents were measured by X-ray diffraction position sensitive detection (XRD-PSD; Bruker D8 Advance, Durham University) from 5 to 90° 2θ. Samples were ground to a fine powder and compacted into a well using the knife-edge of a spatula to ensure random crystal orientation [33]. The intensity of the primary peak (26.6 °2θ for quartz and 21.8 °2θ for cristobalite) was used as a proxy for the relative amounts of crystalline silica. To account for the different diffraction intensities of quartz and cristobalite, the peak heights of pure-phase quartz and cristobalite standards, run under the same conditions, were used to normalise the relative peak heights in the samples. This allowed the addition of peak intensities of quartz and cristobalite to give relative total crystalline silica contents amongst the samples. Bulk chemical compositions were measured by X-ray fluorescence (XRF; PANalytical Axios Advanced X-ray fluorescence spectrometer, University of Leicester). Particle sections were produced in polished resin blocks, coated with 25 nm carbon, and imaging and elemental analysis were performed by scanning electron microscopy (SEM) and energy dispersive X-ray spectroscopy (EDS) at 15 kV (Hitachi SU-70 FEG SEM, Durham University). The elemental composition of cristobalite in individual particles, and amorphous material in cristobalite-containing particles was measured in samples where these particles were clearly seen.

Particle size distributions were analysed by laser diffraction using a Coulter LS analyser (Durham University), with polarization intensity differentiation scattering (PIDS)

to analyse particles in the range of 0.04–2000 μm diameter (all samples fell within this range). Data are presented as cumulative volume (c.v.) % and are an average of two 90 s measurements, analysed by Fraunhofer theory.

Qualitative analysis of dominant diatom morphology was performed on all samples by mounting particles on polycarbonate discs, which were adhered to aluminium stubs by carbon pads. These were coated with 25 nm gold/palladium and imaged at 8 kV by SEM. Quantitative assessment (1000–2000 particles per sample) of particle size and the abundance of fibre-like particles (defined by an aspect ratio >3 [34]), was conducted on the five fine fractions used in toxicology experiments and their corresponding bulk samples (DE_05, DE_08, DE_10, DE_20 and DE_24).

Surface area was analysed by nitrogen adsorption measurements at 77 K using a TriStar 3000 instrument (Durham University). Samples were dried in nitrogen gas at 120 °C overnight. The Brunauer-Emmett-Teller (BET) theory was applied to measurements at relative pressures of 0.05–0.24, and the results are the mean of three repeated measurements.

In vitro toxicology

Haemolysis is a measure of the ability of particles to rupture cell membranes, and has been shown to be a good indicator of the pro-inflammatory potential of crystalline silica [35]. Haemolysis was performed on all 19 bulk samples and 5 separated fine fractions by treating red blood cells with 63–1000 μg/ml DE powder for 1 h. A volume of 1 ml of sheep blood in Alsever's solutions (Oxoid Ltd.) was centrifuged at 5000 rpm for 2 min and the supernatant removed. Isolated red blood cells were washed three times with saline and 100 μl of cells were added to 3.6 ml saline. Particle suspensions of 1 mg/ml particles in saline were sonicated for 20 min, serially diluted to final concentrations, and 150 μl of the particle suspensions added to 96 well plates in triplicate. Next, 75 μl of the prepared blood was added to each well, the plate covered and placed on an orbital shaker for 1 h. Post-exposure, the plate was centrifuged at 250 rcf for 5 min, 100 μl of the supernatant transferred to a new plate and absorbance measured at 540 nm (SpectraMax M5, Heriot-Watt University).

Cytotoxicity was measured using alamarBlue® (a measure of mitochondrial enzyme activity) and lactate dehydrogenase (LDH; a measure of membrane integrity) assays (Heriot-Watt University). These assays were performed on the five fine fractions, their corresponding bulk samples, two bulk samples chosen due to their haemolytic potential (DE_11 and DE_22), as well as a further unprocessed bulk sample (DE_15). The samples were suspended in RPMI medium containing 10 μl/ml L-glutamine, 10 μl/ml penicillin and streptomycin, and 10 % bovine foetal serum (complete medium), and sonicated for 20 min. J774 macrophages were seeded in a 96 well plate (5×10^4 cells per well) and exposed to 100 μl of DE suspension in concentrations of 8, 16, 31, 63, 125, 250, and 500 μg/ml for 24 h at 37 °C and 5 % CO_2. Following exposure, the supernatant was removed and stored at −80 °C for LDH and cytokine analysis. A solution of 1 mg/ml alamarBlue® reagent (resazurin sodium salt; Sigma) in saline was diluted 1:10 in complete medium and 100 μl added to the cells. The plate was incubated for 4 h and fluorescence measured at excitation at 560 nm and emission at 590 nm. LDH release from macrophages was measured by adding 10 μl of cell supernatant to 50 μl 1 mg/ml NADH in 0.75 mM sodium pyruvate, incubating for 30 min at 37 °C in 5 % CO_2, adding 50 μl of 2 mg/ml 2,4-dinitrophenylhydrazine in 1 M HCl and incubating for 20 min at room temperature in the dark, before adding 50 μl 4 M sodium hydroxide and measuring the absorbance at 550 nm.

Cytokine production was measured as a marker of inflammation using BD™ Cytometric Bead Array cytokine flex sets (bead based immunoassay; BD Biosciences, Heriot-Watt University). Flow cytometry was used to discriminate between different bead populations based on size and fluorescence, according to the manufacturer's instructions. Keratinocyte chemoattractant (KC), interleukin 1β (IL-1β), tumour necrosis factor alpha (TNF-α) and interleukin 10 (IL-10) were measured for cells treated with 125 μg/ml or lower of the fine fractions of DE only. TNF-α and IL-1β are pro-inflammatory cytokines associated with silica induced toxicity [36, 37], IL-10 is an anti-inflammatory cytokine providing information on the balance between pro- and anti-inflammatory signalling, and KC induces neutrophil and macrophage chemotaxis. For samples demonstrating cytotoxicity, the LC20 concentration, two times the LC20 and half the LC20 would generally be assessed to investigate cytokine production. However, in low toxicity samples, where an LC20 was not reached, only a concentration of 125 μg/ml was chosen to evaluate the inflammatory response.

Cells treated with the five fine fractions were imaged by light microscopy. J774 cells (2.5×10^5) were treated with 600 μl of 63 μg/ml DE in a 24 well plate. Cells were scraped from the plate and 50 μl of the cell suspension diluted in 300 μl saline and centrifuged onto a microscope slide at 1160 rcf for 5 min. The treated cells were dried and stained with Diff-Quik (Fisher Scientific). Briefly, slides were dipped in methanol, then Eosin G in phosphate buffer and Thiazine dye in phosphate buffer, rinsed with H_2O and air dried.

In all assays, Triton-X was used as a positive control and untreated cells as a negative control. DQ12 was used as a positive crystalline silica standard and TiO_2 as a negative particle standard. A calcite standard was also used in the alamarBlue® and haemolysis assays, due to a

high calcite content in some samples. Results are presented as the relative percentages of the positive and negative controls.

Statistical analysis

Student's *t*-test and ANOVA general linear model with a Tukey's post-hoc test were performed to determine the significance of differences among samples in the in vitro assays (Minitab 15). Pearson's correlation test was used to determine significant correlations amongst different physicochemical characteristics and toxicological results (* p <0.05, ** p <0.01, *** p <0.001).

Results

Physicochemical characterisation

Bulk chemical composition

The bulk chemical composition was variable across deposit sources and processing technique (Table 1). All samples were predominantly SiO_2, which ranged from 87 to 94 wt.%. Samples contained up to 7 and 4 wt.% Al_2O_3 and Fe_2O_3, respectively. Fe_2O_3 content was highest in French samples and Al_2O_3 contents were lower in Spanish samples compared to other locations. Samples from Spain had CaO contents up to 9 wt.%, substantially higher than from all other locations. On average, flux-calcined samples contained significantly more Na_2O than unprocessed and calcined samples from all locations (p <0.001), and contained less Al_2O_3 than calcined samples. Other elements comprised <1.3 wt.% in all samples.

Crystalline silica

Crystalline silica content varied amongst samples, but was the dominant mineral phase in flux-calcined and calcined samples (Fig. 1). Flux-calcined samples were predominantly cristobalite; though, samples from China and USA also contained small quantities of quartz (Fig. 1c). Conversely, calcined samples contained cristobalite as well as quartz, with the exception of cristobalite-only Mexican samples DE_20 and DE_24 (Fig. 1b). Quartz was the dominant crystalline silica polymorph in calcined samples DE_16 and DE_21, whereas cristobalite was the dominant phase in the other calcined samples. On average, cristobalite peak intensity was three times higher in flux-calcined samples than in calcined samples, as calcined samples retained more amorphous material and a proportion of the crystalline silica was quartz. These differences in abundance were substantiated by qualitative SEM imaging. Unprocessed samples were predominantly amorphous and only contained small amounts of cristobalite (Fig. 1a) or, rarely, quartz was observed in all four samples.

By backscatter SEM, crystalline silica appeared as dark grey patches within lighter grey matrices of amorphous material (Fig. 2). In samples that contained both quartz and cristobalite, cristobalite could often be identified by characteristic 'fish-scale' cracking, indicative of the particle having undergone the transition from the high-temperature beta form to the low-temperature alpha form [38]. By EDS analysis on cristobalite-only samples and 'fish-scale' patches in samples containing both polymorphs, Na, Al, Fe and Ca were detected in the cristobalite (Fig. 2). The amorphous matrix was enriched in impurities compared to the cristobalite, containing Na, Al, Fe, Ca, Mg, K, Ti and P (Fig. 2).

Contaminant phases

Spanish samples contained calcite (Figs. 1 and 3a); this was most prominent in the unprocessed samples (DE_05, DE_11), with only traces remaining in the corresponding flux-calcined samples (DE_06, DE_12). Calcium silicates were observed in abundance in all Spanish samples (Fig. 3b).

Clays were observed by SEM-EDS (texturally, and by their high Al contents) and were most prevalent in French samples (e.g. Fig. 3c), but were also observed in samples from USA-1, Mexico and China. Distinct clay

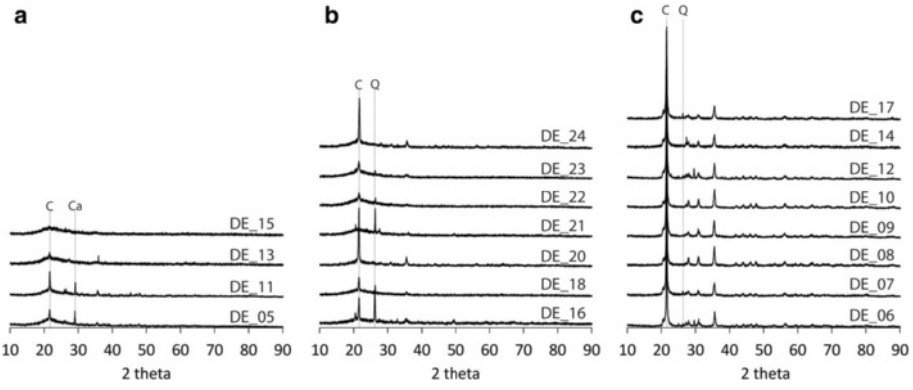

Fig. 1 XRD patterns of (**a**) unprocessed, (**b**) calcined and (**c**) flux-calcined DE. *C* cristobalite, *Q* quartz, *Ca* calcite. Only primary peaks are labelled for clarity. Quartz was not detected in unprocessed samples by XRD

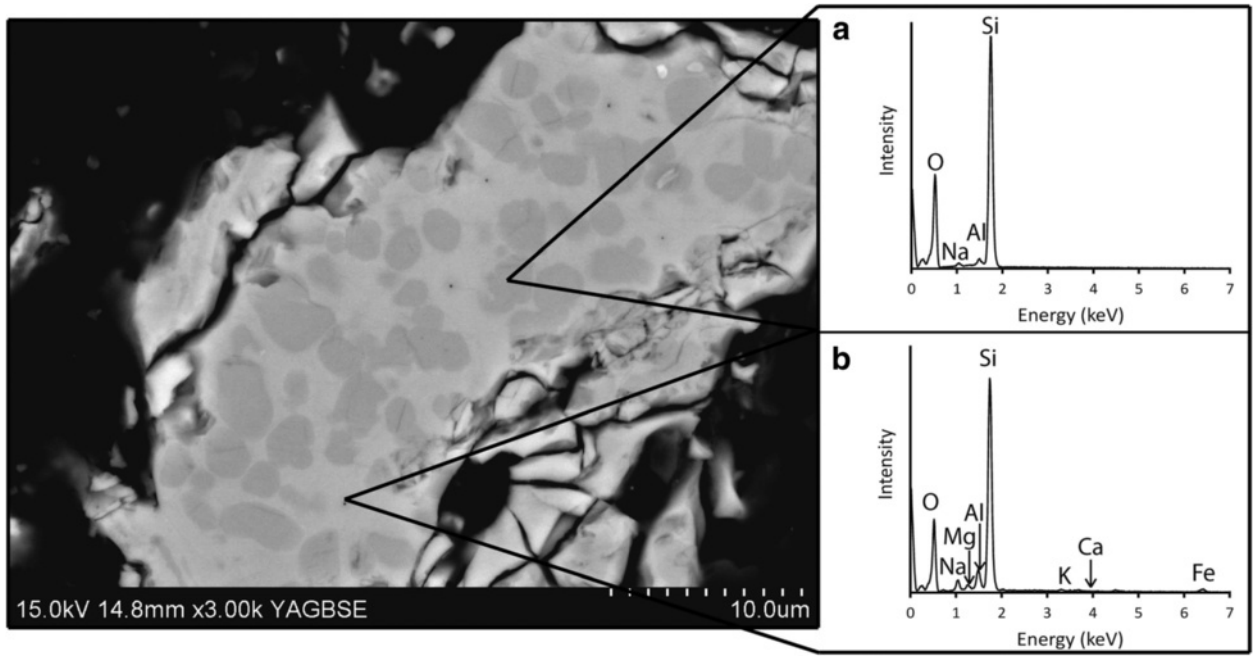

Fig. 2 Backscatter image and EDS spectra of flux-calcined DE particle. Backscatter image of DE particle in a flux-calcined sample with cristobalite patches (*dark grey*; identified by cracking and cristobalite is only crystalline phase in this sample by XRD) surrounded by an amorphous matrix (*light grey*). EDS spectra of (**a**) cristobalite patches showing Al and Na impurities and (**b**) amorphous matrix containing Na, Mg, Al, Ca, K and Fe impurities. These are representative spectra from ~800 spot analyses of cristobalite patches and amorphous matrices (400 of each). Some cristobalite patches also contained Ca and Fe, and some amorphous material also contained Ti and P

phases were not identifiable using textural features or chemical composition, and quantities were too low for detection by XRD.

In the French, unprocessed samples, iron-rich particles of up to 70 μm were observed and these were iron and titanium-rich or iron and phosphorus-rich particles (Fig. 3d). These larger particles were not observed in the calcined and flux-calcined samples from France; instead, small iron-rich patches were seen throughout particles and sometimes in cracks and pore spaces (Fig. 3e). Some of these deposits were iron and titanium-rich but were mostly iron and silicon. In calcined samples where the corresponding unprocessed samples were not available, iron-rich patches were seen throughout particles (Fig. 3f).

Physical properties

Bulk samples contained between 11 and 71 c.v. % particles <10 μm and between 5 and 25 c.v. % particles <4 μm in diameter (Table 1), analogous to the thoracic and respirable fractions, respectively [39]. Flux-calcined samples were coarser than unprocessed and calcined samples for both filler and filter aid grade samples. Calcined samples had a wide range of particle size distributions, containing between 22 and 71 c.v. % <10 μm material (Table 1). The maximum particle diameter observed in the separated fine fractions was 51 μm, reduced from 73 μm in the bulk fractions. Additionally, 83–99 % of particles, by number, in the fine fractions were <10 μm in diameter, compared to 73–96 % in the bulk samples (Table 2). The separated fraction of flux-calcined samples was coarser (median diameter 1.5–2.6 μm) than the fine fractions of calcined and unprocessed samples (median diameters 0.8 μm; Table 2). These data are not comparable to laser diffraction data, which present equivalent spherical diameter in volume % so are heavily mass-biased.

Particle morphology varied substantially amongst samples as the dominant diatom species qualitatively varied with sample source. Samples from Chile, China, Mexico and Spain contained predominantly disc-shaped diatoms, whereas samples from USA-2 and France consisted mainly of cylindrical diatoms (Fig. 4). Samples sourced from USA-1 contained a number of different diatom species and morphologies, including disc-shaped, and long, thin diatoms (Fig. 4c). Most particles were fragments of diatoms and, therefore, particle morphology varied substantially within individual samples. Processed samples contained some sintered

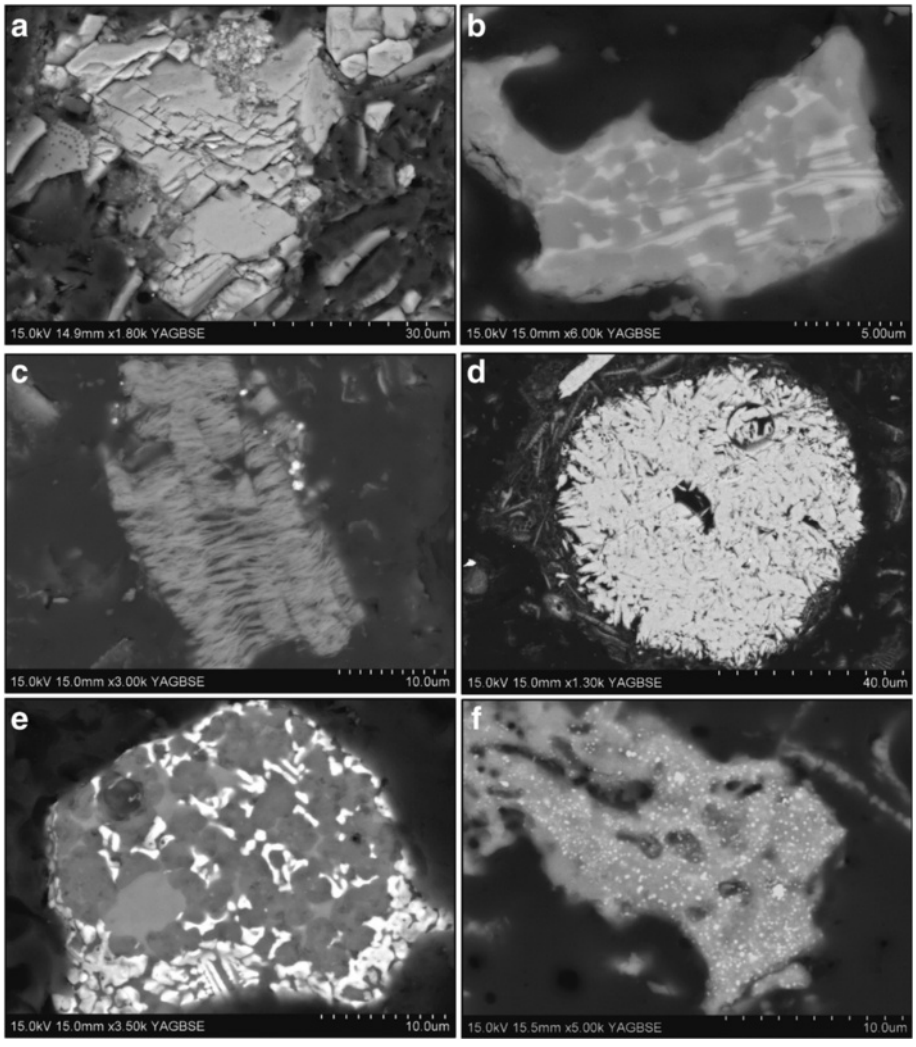

Fig. 3 Backscatter images of contaminant phases in DE. **a** a pure calcite particle in unprocessed DE from Spain (DE_05), **b** a particle containing calcium silicate (*very light grey*) and cristobalite patches (*dark grey*) in flux-calcined DE from Spain (DE_06), **c** a clay mineral particle in an unprocessed sample from France (DE_13), **d** a large iron phosphate particle in unprocessed DE from France (DE_13), and **e**-**f** iron-rich patches within particles in French (DE_16) and Mexican (DE_24) calcined samples

Table 2 Particle size measured by SEM image analysis

Sample	Maximum particle diameter (μm)		Median particle diameter (μm)		Particles <10 μm diameter (number %)		Fibre-like particles (%)	
	Bulk	Fine	Bulk	Fine	Bulk	Fine	Bulk	Fine
DE_05	26.9	18.5	1.7	0.8	96.6	99.2	17.9	15.4
DE_20	52.0	31.5	1.9	0.8	94.1	96.5	21.2	18.8
DE_24	47.0	17.3	1.8	0.8	96.5	99.0	17.8	16.4
DE_08	73.0	43.7	5.0	1.5	73.2	82.7	3.3	5.7
DE_10	46.2	51.3	4.1	2.6	77.9	83.0	4.9	9.8

Includes maximum particle diameter, median particle diameter, the number % of particles <10 μm, and the number % of fibre-like particles in five bulk samples and their corresponding fine fractions

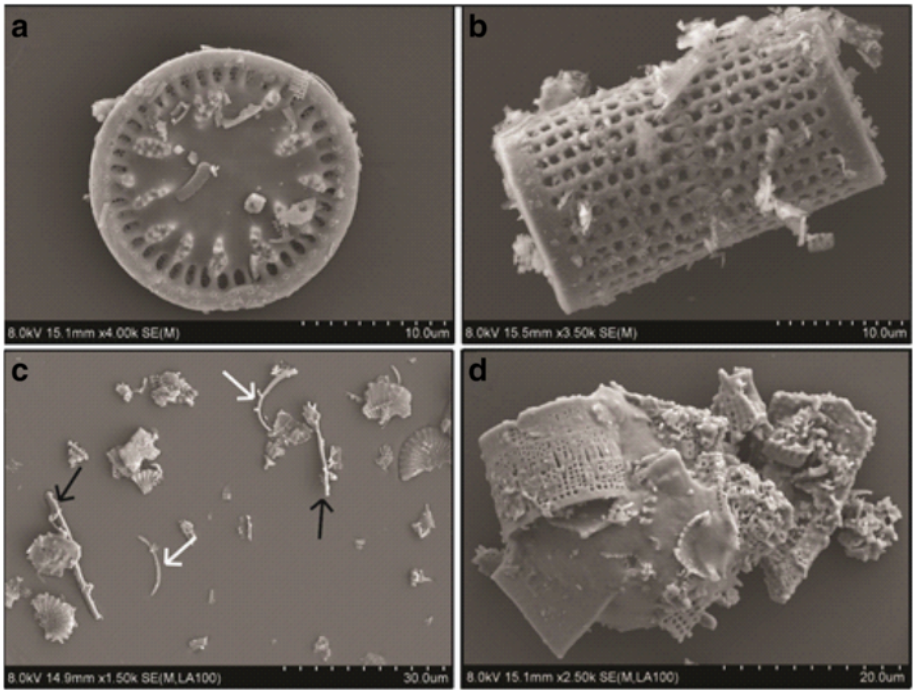

Fig. 4 SEM images of examples of DE morphologies. **a** disc-shaped DE found in Chilean, Chinese, Mexican and Spanish samples, **b** cylindrical diatoms found in French and USA-2 samples, **c** fibre-like rods (*black arrows*) and diatom rinds (*white arrows*), and **d** a large agglomeration of fused diatoms in a flux-calcined DE sample

particles and fused pores, and this was most evident in flux-calcined samples, where large agglomerates of diatoms were observed (Fig. 4d).

In the five bulk samples and equivalent fine fractions, between 3 and 21 % of particles, by number, were classified as fibre-like (Table 2). The total number of fibre-like particles was 2 to 6 times lower in flux-calcined samples than in unprocessed or calcined samples, for both bulk samples and fine fractions (Table 2).

Surface area did not vary much among flux-calcined samples and was always <1.7 m^2/g. However, in calcined and unprocessed samples, surface area varied

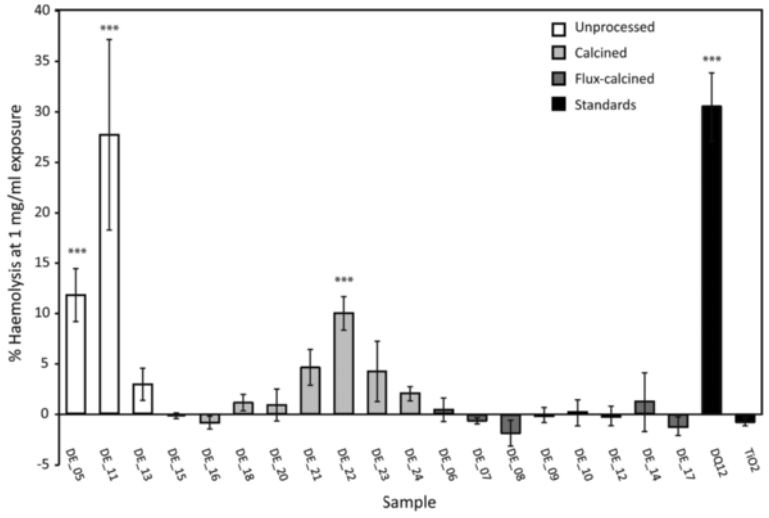

Fig. 5 Haemolytic potential of DE samples. Percent haemolysis relative to an untreated control, of sheep red blood cells post-exposure to 1 mg/ml of unprocessed (*white*), calcined (*light grey*) and flux-calcined (*dark grey*) DE and positive (DQ12) and negative (TiO_2) standards (*black*). *Error bars* represent standard error ($n = 3$), *** $p = <0.001$ difference from untreated control

substantially, ranging from 3.1 to 10.6 m^2/g in calcined samples and 6.3 to 23.8 m^2/g in unprocessed samples (Table 1).

In vitro toxicology

Haemolysis

Haemolysis results are shown in Fig. 5 for bulk samples. Haemolysis caused by the fine fractions did not differ significantly from their corresponding bulk samples and, hence, are not shown. Unprocessed samples from Spain (DE_05 and DE_11) were two of the most haemolytic samples, with DE_11 as haemolytic as DQ12. The most haemolytic calcined sample, DE_22, was one third as haemolytic as DQ12 at the highest concentration. All other samples were not significantly haemolytic at any concentration tested, including the calcite standard (data not shown).

Cytotoxicity

In the alamarBlue® assay (Fig. 6), there was no statistically significant difference in cytotoxicity of bulk DE samples and their separated fine fractions. Bulk flux-calcined samples, and DE_20 and DE_15, TiO_2 and calcite did not differ from the untreated control. All other samples exhibited a cytotoxic response and the cytotoxicity of DE_24 (bulk and fine), DE_22, DE_11 and the fine fraction of DE_05 did not differ significantly from DQ12 ($p > 0.2$). LDH release data were in broad agreement with cell viability measurements via the alamarBlue® assay, in that flux-calcined samples were less cytotoxic than unprocessed and calcined samples (Additional file 1).

Cytokine release

Only TNF-α was produced by macrophages in concentrations greater than untreated cells following exposure to the fine-fraction samples (Fig. 7, data for other cytokines given in Additional file 1). DE_05, DE_20 and DE_24 all increased TNF-α production, with DE_05 inducing the greatest TNF-α production at 125 μg/ml, which was 2.7 times greater than that released following treatment with DQ12. For the calcined samples (DE_20, DE_24), the induction of TNF-α production by treated cells was comparable to that induced by DQ12. In contrast, DE_10 and DE_08 did not enhance TNF-α production.

Cell imaging

Imaged cells treated with the fine fractions of DE and an untreated control are shown in Fig. 8. In the treated cells, there was some degree of frustrated phagocytosis, with instances of numerous cells attempting to phagocytose the same particle and particles not fully engulfed (Fig. 8b-d). Qualitatively, evidence of frustrated phagocytosis was more abundant in cells treated with calcined or unprocessed samples, compared to flux-calcined samples, but were observed in all cases.

Discussion

The variability of DE properties

DE deposits vary in composition and diatom species providing DE particles with a range of physical and chemical properties. Treatment of DE by calcination is used to optimise these properties for use in the filtration and filler industries, during which amorphous silica

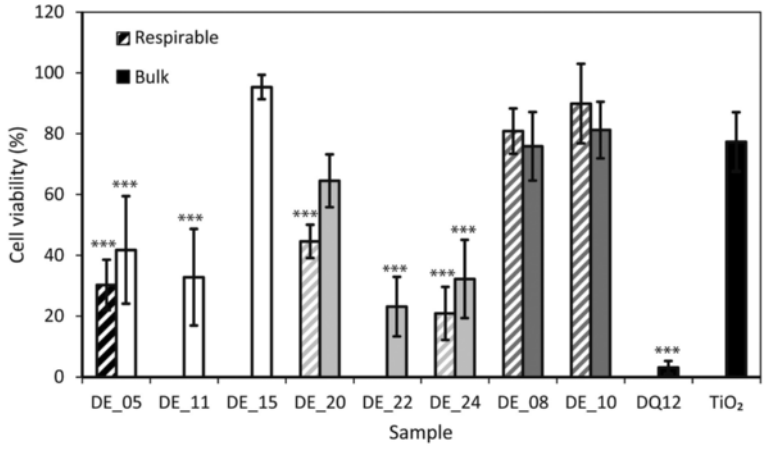

Fig. 6 Cell viability of J774 macrophages exposed to DE. Cell viability relative to an untreated control (% of untreated control–positive control), measured by the alamarBlue® assay, of J774 macrophages exposed to 500 μg/ml of bulk (*solid*) or the fine fraction (*hashed*) of unprocessed (*white*), calcined (*light grey*) and flux-calcined (*dark grey*) DE, and positive (DQ12) and negative (TiO_2) standards (*black*) for 24 h. No data for fine fractions of DE_11, DE_15 and DE_22. *Error bars* represent standard error ($n = 4$), *** $p = <0.001$ difference from untreated control

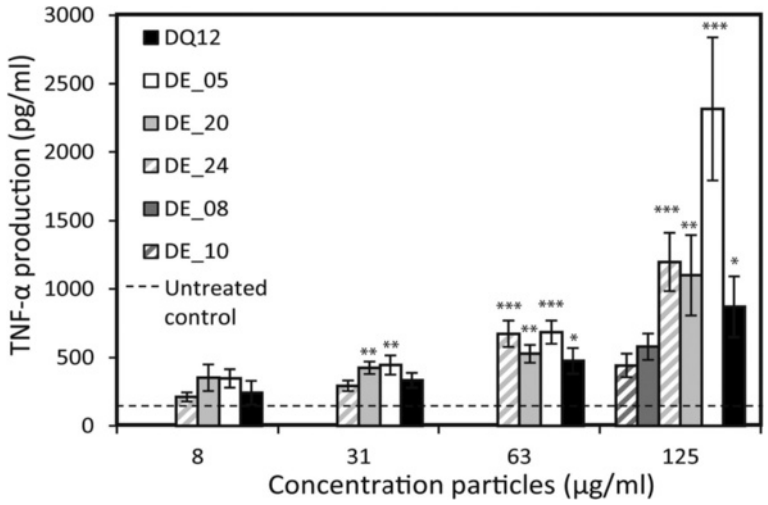

Fig. 7 TNF-α production by macrophages exposed to the fine fractions of DE. Exposure to unprocessed (*white*), calcined (*light grey*) and flux-calcined (*dark grey*) DE and a positive standard (DQ12) for 24 h. *Error bars* represent standard error ($n = 8$). * $p = <0.05$, ** $p = <0.01$, *** $p = <0.001$ compared to untreated control

crystallises [1, 2]. Here, crystalline silica contents and polymorphs varied substantially amongst DE samples from different locations, with processing playing a key role. Flux-calcined samples were the most crystalline silica-rich, and cristobalite was the dominant crystalline silica polymorph. Most calcined samples contained both cristobalite and quartz and there is some evidence that the quartz formed during calcination (based on data from the unprocessed DE_15 and calcined DE_16 samples). This distribution of crystalline silica polymorphs by processing technique has also been observed by Ghiazza et al. [27] and Elias et al. [28]. The preferential crystallisation of cristobalite in flux-calcined samples is likely due the addition of the fluxing agent: doping of

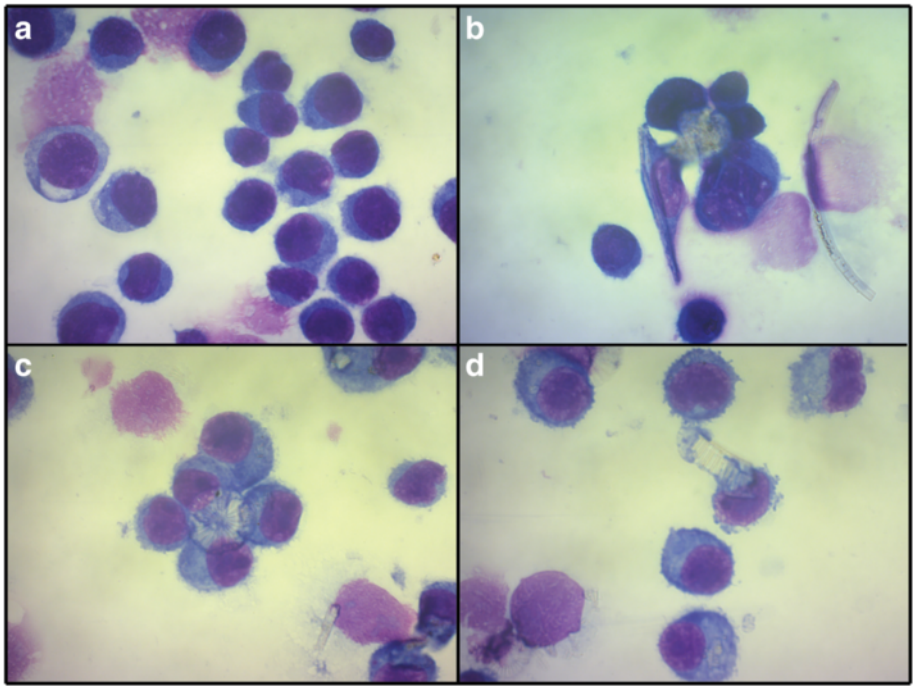

Fig. 8 Frustrated phagocytosis in macrophages treated with DE. Light microscopy image of (**a**) untreated macrophages, and (**b**-**d**) macrophages treated with DE showing indicators of frustrated phagocytosis

amorphous silica with sodium salts promotes cristobalite crystallisation instead of quartz at the temperatures used for calcination [40, 41]. It is unknown why quartz preferentially forms in some calcined samples, whereas in others only cristobalite was observed (Mexican samples DE_20 and DE_24). Unprocessed samples contained trace quantities of cristobalite and quartz; the cristobalite in unprocessed samples likely forms by diagenesis of amorphous silica over time, or is possibly from other sources, such as volcanic deposits [2].

Cristobalite formed in patches throughout particles, crystallising within a matrix of amorphous material (Fig. 2). The cristobalite patches in the samples analysed were impure, containing Al, Na, Ca and Fe (e.g. Fig. 2). Aluminium and Fe ions can substitute for Si in the silica tetrahedra, but require interstitial cations (e.g., Na or Ca) to charge balance the substitution [42], as has been discussed for volcanic cristobalite [43, 44].

Contaminant phases were observed in all samples. Spanish deposits contained calcite (DE_05, DE_11), which would thermally decompose at calcination temperatures (~1000 °C) [45], allowing Ca and Si to form calcium silicates, which were in abundance in flux-calcined samples from Spain. Clay minerals and iron-rich particles are also likely to be broken down during calcination as few individual clay mineral particles or large, iron-rich particles were seen in processed samples compared to unprocessed samples from France. As with Ca in Spanish samples, this frees Fe ions to react with Si, and precipitate in pores and cracks, which was seen in all calcined samples (Fig. 3e-f). The addition of a sodium carbonate flux leads to sodium silicate melt binding with Fe [2], which explains the lack of iron-rich particles in flux-calcined samples.

Physical properties varied substantially among the samples. Flux-calcined particles had complex morphologies, and were coarser and had lower surface area than calcined and unprocessed samples, due to sintering of particles into large agglomerates and the closure of pore spaces [3]. The morphology of diatom frustules varied with source (Fig. 4); however, the abundance of fragmented frustules in all samples meant diatom species, alone, could not be used as a good proxy for particle morphology.

The variability of the potential toxicity of DE

Previous studies of DE toxicity insufficiently constrain the respiratory hazard posed by exposure to DE deposits worldwide: epidemiology studies have mainly focussed on DE workers in a single location (California) (e.g. [9, 10, 14–17]), and are unable to distinguish between exposure to unprocessed or processed DE, while toxicology studies rarely state the sample source and investigate few samples. Therefore, variability among deposits and processing techniques has not been fully considered. Here, we show that DE is not a single entity, with a toxic potential that ranges from unreactive to as haemolytic or cytotoxic as the positive standard α-quartz (DQ12).

Unprocessed samples from Spain (DE_05 and DE_11) were haemolytic and induced significant cytotoxicity to macrophages. Furthermore, DE_05 induced a large increase in TNF-α release from treated macrophages relative to processed samples, indicating the potential for unprocessed DE to incite inflammation if inhaled. However, unprocessed samples from France did not induce any measurable haemolysis or cytotoxicity, suggesting that the potential toxicity of DE can vary by deposit source.

Flux-calcined samples all displayed low haemolytic potential, cytotoxicity and cytokine release from treated cells. This suggests that short-term exposure to flux-calcined samples may not result in toxicity or an inflammatory response. There was no variation in the reactivity of flux-calcined samples from different locations, suggesting that flux-calcination is key to dampening the adverse effects attributed to DE. This is likely due to alteration of the physicochemical properties of DE during flux-calcination and is discussed in detail below.

DE_22 from USA-1 was the only calcined sample that elicited a haemolytic response and was also one of the most cytotoxic samples analysed. This introduces the possibility that data in epidemiological studies from the USA may not be representative of likely disease outcomes worldwide. However, other calcined samples from USA-1 were non-haemolytic, emphasising the variable reactivity that exists amongst samples from a single deposit source. Calcined samples from Mexico were cytotoxic but not haemolytic. Therefore, as these assays assess different mechanisms of toxicity, and there is a disagreement in sample reactivities among the assays for samples from some locations but not others, different mechanisms may be responsible for the observed reactivity.

Factors affecting DE toxicity

Presence of crystalline silica

Here, total crystalline silica (quartz plus cristobalite) content alone did not control DE reactivity in vitro (Fig. 9), as has also been reported by other in vitro toxicity studies [24–27]. This contrasts with previous epidemiology studies that attribute observed pathologies to crystalline silica in processed DE [e.g. [9, 14]]. Some of these studies are referenced in reviews of crystalline silica toxicity [46, 47], and are used in determining safe exposure limits to crystalline silica [e.g. [48]].

The low reactivity of all flux-calcined samples agrees with previous reports on discrete samples [24, 25, 27, 31]. Ghiazza et al. [27] suggested that the low levels of cytotoxicity, lipid peroxidation and NO synthesis caused by crystalline silica-rich flux-calcined DE was due to the

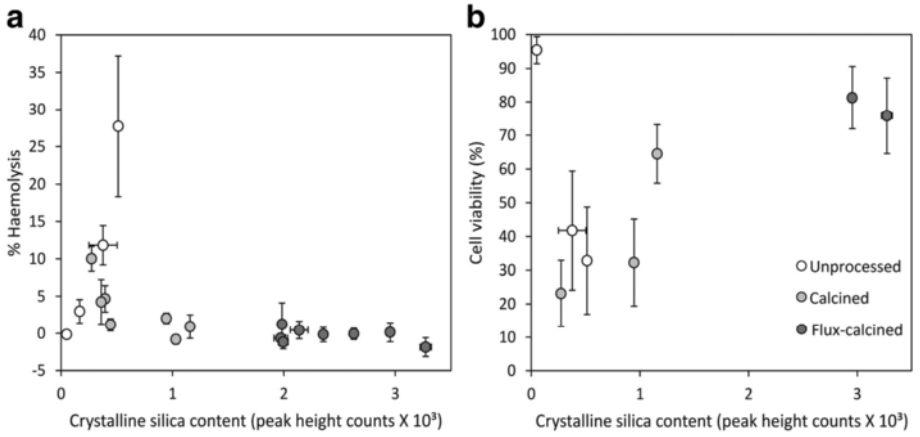

Fig. 9 Relationship between crystalline silica content and reactivity in vitro. Correlation of crystalline silica content of DE (measured by the addition of cristobalite and quartz peak heights, accounting for different diffraction power using standards) with (**a**) haemolysis post-exposure to 1 mg/ml bulk DE, and (**b**) cell viability post-exposure to 500 μg/ml bulk DE

formation of a vitreous rim during flux-calcination, which obscured cell exposure to cristobalite in these samples. No vitreous rim, per se, was observed in this study but the cristobalite is partly occluded, occurring in patches within the otherwise amorphous particles, resulting in a variable percentage of cristobalite at the particle surface. This may account for the lack of correlation between crystalline silica content and potential toxicity. The variable toxicity of crystalline-silica bearing dusts is well established [e.g. [36, 49, 50]], and the hosting of crystalline silica within heterogeneous particles has previously been suggested to explain variations in the toxic potential of quartz-rich coal dusts [49, 51], and to mask the toxicity of cristobalite in volcanic ash [44]. Here, exposure times for the cytotoxicity assays were short (24 h), and the amorphous matrix may have low bio-durability, thereby exposing more cristobalite at the surface of the particle over time. Therefore, future longer exposures and in vivo experiments may be necessary.

Toxicity of the limited surface cristobalite could be further dampened by the presence of cation substitutions (Fig. 2), as structural impurities have been hypothesised to decrease the toxic potential of cristobalite in volcanic ash [44]. Treating quartz with aluminium salts or clay extracts has also been shown to reduce its toxicity and haemolytic potential [52–55], and quartz in coal with clay mineral impurities had lower toxicity than pure, coal-sourced quartz [51]. Therefore, the production of aluminium ions via breakdown of aluminium-rich components of the DE samples could affect the cristobalite exposed at the surface of particles, decreasing the potential toxicity. Conversely, treating quartz with ferric or ferrous iron does not change its toxic potency in vivo [52] and can decrease its haemolytic potential [54]. However, Fubini et al. [56] showed iron may increase silica toxicity via production of free radicals. Therefore, the role of iron in determining DE crystalline silica toxicity remains unclear.

Reactivity of contaminant phases

Some samples with little to no crystalline silica were highly reactive, indicating contaminant phases may control the in vitro response in those samples. The presence of calcite could explain the high reactivity of Spanish (calcite-rich) unprocessed samples: Aladdin et al. [57] have shown exposure to calcite alone caused significant cytotoxic effects in human epithelial cells and inflammation in mice, and Diler and Ergene [58] showed that micronuclei and nuclei abnormalities were more common in calcite factory workers than control groups. However, as the calcite standard was non-reactive in both the haemolysis and alamarBlue® assays, it is unlikely that calcite content is solely responsible for the different reactivity of Spanish unprocessed and flux-calcined DE. The presence of clays may also have an effect, as some clays have been shown to be more haemolytic than crystalline silica [59, 60]. However, the lack of clay in processed DE samples and the low reactivity of French, unprocessed samples, suggests that clay minerals are not the cause of DE induced toxicity.

Iron has been hypothesised as a source for free radical generation in DE [26], and was measured in quantities of up to 4 wt.% here and, therefore, could be contributing to the potential toxicity. Bulk iron content did not correlate with either haemolysis or cytotoxicity (Additional file 1); however, further work would be required to determine the co-ordination of iron and its potential to produce free radicals. Calcined samples all contained iron-rich phases but had variable toxicity, suggesting total Fe does not control the reactivity of these samples. Also, previous studies have shown ferric

and ferrous oxides to have low cytotoxicity [61], although exposure to ultrafine iron oxide particles has been shown to lead to oxidative stress and a pro-inflammatory response in rats [62, 63]. Soluble iron oxide has also been shown to be cytotoxic to human mesothelioma MSTO-211H cells [64]. However, as soluble components of the DE were non-cytotoxic (see Additional file 1), this is unlikely to be the case here.

Amorphous silica is generally perceived as less toxic than crystalline silica [49] but can be reactive in vitro [65, 66]. The ability of amorphous, unprocessed DE to elicit a haemolytic or cytotoxic response, or induce abnormal nuclei growth in vitro [24, 25, 29], and cause fibrosis in vivo [30], has also previously been demonstrated. Unprocessed samples from Spain, the most haemolytic of all samples, were predominantly amorphous. The cytotoxic (DE_20, DE_22 and DE_24) and haemolytic (DE_22) calcined samples also contained a substantial amount of amorphous material. It is possible that the amorphous phases of these samples are linked to their reactivity, as certain vitreous silicas have been shown to be more haemolytic than quartz [66]. However, the lack of haemolysis caused by French, unprocessed samples, which were also predominantly amorphous, means that amorphous material is unlikely the predominant control on the observed reactivity. The high levels of impurities in processed amorphous material (Fig. 2) may also play a role in its biological reactivity at the surface of the particle, but further work is needed to determine this.

Therefore, although the mineralogical and chemical compositions are likely to play a role in DE toxicity, no definitive link can be made between individual characteristics considered here and the potential toxicity measured in this study.

Physical properties

Surface area has been related to pro-inflammatory responses [67, 68], and the surface area of processed DE may be a key factor controlling toxicity. Correlations between bulk surface area of processed samples (calcined and flux-calcined) and haemolysis or cell viability were observed (Fig. 10). In flux-calcined samples, up to 27 % of particles were >10 μm (Table 2), which may account for their low surface area (Table 1) and, accordingly, their low reactivity. However, the variable particle size distributions of unprocessed and calcined DE could not be correlated to their toxic potential (Additional file 1), and the correlation between surface area and reactivity could not be extended to unprocessed samples. This suggests that other parameters are responsible for their observed toxicity.

Fibres can cause frustrated phagocytosis, where macrophages struggle to fully engulf particles [69]. Fibre-like particles, up to 21 %, in calcined and unprocessed samples, were mainly in the form of diatom 'rinds' or small fragments of diatoms. The lower abundance in flux-calcined samples is likely due to sintering of fragments into large agglomerates. Previously, DE containing fibre-like particles (aspect ratio >3) was shown to be more potent in vitro than 'non-fibrous' DE [70], suggesting that particle morphology could play a role in the observed cytotoxicity. Particle morphology is important in phagocytosis [71] and, here, frustrated phagocytosis was observed and some fibre-like particles were not phagocytised. This was most evident for calcined and unprocessed samples (which had the highest % of fibre-like particles), where TNF-α production and LDH release, potential indicators of frustrated phagocytosis [72], were also elevated above flux-calcined samples. Frustrated phagocytosis was also observed as a number of cells attempted to engulf larger, disc-shaped diatoms. This was observed after treatment of cells with all of the fine fraction samples, suggesting that large, disc-shaped particles may play a role in DE toxicity, as platelets have been recently identified as a novel respiratory hazard [73], and DE particles with a diameter >7.5 μm have previously been suggested to determine DE toxicity [24].

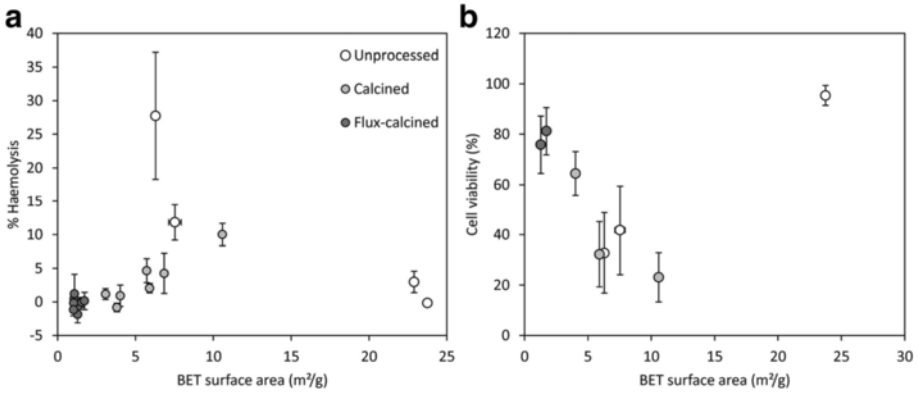

Fig. 10 Relationship between BET surface area and DE reactivity in vitro. Correlation between surface area and (**a**) haemolysis post-exposure to 1 mg/ml bulk DE, and (**b**) cell viability post-exposure to 500 μg/ml bulk DE

Conclusions

This study, the first to systematically characterise the physicochemical properties and potential toxicity of a range of globally sourced DE samples, shows that the toxic potential of DE varies by processing technique and source. Flux-calcined samples were unreactive, whereas unprocessed and calcined DE had variable reactivity.

No correlation was observed between crystalline silica content and DE's potential toxicity, despite previously being implicated in epidemiological studies of DE exposure. The dearth of crystalline silica at the particle surface, due to its crystallisation within an amorphous matrix, its presence in a heterogeneous dust, and impurities within the crystalline silica likely reduce the potential reactivity of these crystalline silica-bearing particles.

It is likely that a number of physicochemical properties play a role in DE toxicity. Calcium-rich phases may be important in the toxicity of some unprocessed samples, and iron or amorphous phases may be involved in calcined DE toxicity. Surface area, especially, was correlated to calcined and flux-calcined DE reactivity here, and the importance of surface reactivity and the unique particle morphologies of DE merits further investigation.

Although no single physicochemical property of DE considered here could be linked to its potential toxicity, a clear outcome of this study is that the crystalline silica content, alone, should not be used to determine the DE hazard, nor should it be assumed that it is the cause of disease observed in epidemiological or clinical studies without further investigation.

Additional file

Additional file 1: This document includes additional data including LDH and cytokine release data and correlations between and bulk Fe content and in vitro toxicity, and particle size and in vitro toxicity, which are all referred to in the main manuscript.

Abbreviations

DE: Diatomaceous earth; IMA: Industrial Minerals Association; XRD-PSD: X-ray diffraction position sensitive detection; XRF: X-ray fluorescence; SEM: Scanning electron microscopy; EDS: Energy dispersive X-ray spectroscopy; BET: Brunauer-Emmett-Teller; LDH: Lactate dehydrogenase; KC: Keratinocyte chemoattractant; IL-1β: Interleukin 1β; TNF-α: Tumour necrosis factor alpha; IL-10: Interleukin 10.

Competing interests

The research has been part-funded by IMA Europe, an umbrella organisation representing a number of diatomite companies in all non-commercial issues related to the properties and safe use of minerals. Samples were provided by one diatomite company. Neither IMA Europe nor the company had input to the experimental design or research conducted but have seen a draft version of this manuscript.

Authors' contributions

CN designed the study, performed physicochemical analyses at Durham University and in vitro toxicology assays at Heriot-Watt University, and drafted the manuscript. CJH conceived and designed the study, supervised CN, and participated in physicochemical characterisation. DED advised on study outcomes, and helped with physicochemical analyses. AK performed cytokine analysis and AK and DB participated in in vitro assays. VS and DB participated in the design of the study and VS supervised CN. All authors helped draft the manuscript, read and approved the final version.

Acknowledgements

The authors acknowledge IMA Europe and Durham University as the primary funders of this study and support provided by Horwell's NERC Postdoctoral Research Fellowship (Grant No. NE/C518081/2). Thanks to Nick Marsh, University of Leicester, for XRF analyses and to Leon Bowen, Durham GJ Russell Microscopy Facility, for assistance with SEM analyses. Thanks to Ian Chaplin for assistance with sample preparation, Kathryn Melvin, Gary Oswald and David Johnson for technical assistance with laser diffraction, XRD and BET analyses, respectively. Thanks to the Nano-Safety Group at Heriot-Watt University for technical advice regarding the toxicology assays.

Author details

[1]Institute of Hazard, Risk & Resilience, Department of Earth Sciences, Durham University, Durham DH1 3LE, UK. [2]Department of Earth and Environmental Sciences, Ludwig-Maximilians-Universität München, Munich 80333, Germany. [3]School of Life Sciences, Heriot-Watt University, Edinburgh EH14 4AS, UK. [4]Department of Public Health, Section of Occupational and Environmental Health, University of Copenhagen, Copenhagen DK-1014, Denmark.

Received: 15 December 2014 Accepted: 22 June 2015
Published online: 10 July 2015

References

1. Engh KR. Diatomite. In: Kirk-Othmer encyclopedia of chemical technology. 2000. http://onlinelibrary.wiley.com/doi/10.1002/0471238961.0409012005140708.a01/abstract; John Wiley & Sons, Inc.
2. Flörke OW, Graetsch HA, Brunk F, Benda L, Paschen S, Bergna HE, et al. Silica. In: Ullmann's encyclopedia of industrial chemistry. 2000. http://onlinelibrary.wiley.com/doi/10.1002/14356007.a23_583/abstract; Wiley-VCH Verlag GmbH & Co. KGaA.
3. Ediz N, Bentli İ, Tatar İ. Improvement in filtration characteristics of diatomite by calcination. Int J Miner Process. 2010;94(3–4):129–34.
4. Greenberg MI, Waksman J, Curtis J. Silicosis: a review. Dis Mon. 2007;53(8):394–416.
5. Leung CC, Yu ITS, Chen W. Silicosis. Lancet. 2012;379(9830):2008–18.
6. NIOSH. In: Services DoHaH, editor. Health effects of occupational exposure to respirable crystalline silica. Volume 2002–129. 2002.
7. IARC. Silica, some silicates, coal dust and para-aramid fibrils. International Agency for Research on Cancer: Lyon; 1997.
8. IARC. Arsenic, metals, fibres, and dusts. Volume 100C. Lyon: International Agency for Research on Cancer; 2012.
9. Checkoway H, Heyer NJ, Demers PA, Breslow NE. Mortality among workers in the diatomaceous earth industry. Br J Ind Med. 1993;50(7):586–97.
10. Seixas NS, Heyer NJ, Welp EAE, Checkoway H. Quantification of historical dust exposures in the diatomaceous earth industry. Ann Occup Hyg. 1997;41(5):591–604.
11. Cooper WC, Sargent EN. A 26-year radiographic follow-up of workers in a diatomite mine and mill. J Occup Environ Med. 1984;26(6):456–60.
12. Dutra FR. Diatomaceous earth pneumoconiosis. Arch Environ Health. 1965;11(5):613–9.
13. Smart RH, Anderson WM. Pneumoconiosis due to diatomaceous earth; clinical and x-ray aspects. Ind Med Surg. 1952;21(11):509–18.
14. Harber P, Dahlgren J, Bunn W, Lockey J, Chase G. Radiographic and spirometric findings in diatomaceous earth workers. J Occup Environ Med. 1998;40(1):22–8.
15. Rice FL, Park R, Stayner L, Smith R, Gilbert S, Checkoway H. Crystalline silica exposure and lung cancer mortality in diatomaceous earth industry workers: a quantitative risk assessment. Occup Environ Med. 2001;58(1):38–45.
16. Park R, Rice F, Stayner L, Smith R, Gilbert S, Checkoway H. Exposure to crystalline silica, silicosis, and lung disease other than cancer in diatomaceous earth industry workers: a quantitative risk assessment. Occup Environ Med. 2002;59(1):36–43.
17. Hughes J, Weill H, Checkoway H, Jones R, Henry M, Heyer N, et al. Radiographic evidence of silicosis risk in the diatomaceous earth industry. Am J Respir Crit Care Med. 1998;158(3):807–14.

18. Rafnsson V, Gunnarsdóttir H. Lung cancer incidence among an Icelandic cohort exposed to diatomaceous earth and cristobalite. Scand J Work Environ Health. 1997;23:187–92.
19. Beskow R. Silicosis in diatomaceous earth factory workers in Sweden. Scand J Respir Dis. 1978;59(4):216–21.
20. Ebina T, Takase Y, Inasawa Y, Horie K. Silicosis in the diatomaceous earth factories. Tohoku J Exp Med. 1952;56(3):214.
21. Joma THJM, Borm PJA, Koiter KD, Slangen JJM, Henderson PT, Wouters EFM. Respiratory effects and serum type III procollagen in potato sorters exposed to diatomaceous earth. Int Arch Occup Environ Health. 1994;66(4):217–22.
22. Vigliani EC, Mottura G. Diatomaceous earth silicosis. Br J Ind Med. 1948;5:148–60.
23. Checkoway H, Heyer NJ, Demers PA, Gibbs GW. Reanalysis of mortality from lung cancer among diatomaceous earth industry workers, with consideration of potential confounding by asbestos exposure. Occup Environ Med. 1996;53(9):645–7.
24. Hart GA, Hesterberg TM. *In vitro* toxicity of respirable-size particles of diatomaceous earth and crystalline silica compared with asbestos and titanium dioxide. 40th ed. Hagerstown, MD: ETATS-UNIS: Lippincott Williams & Wilkins; 1998.
25. Bye E, Davies R, Griffiths DM, Gylseth B, Moncrieff CB. *In vitro* cytotoxicity and quantitative silica analysis of diatomaceous earth products. Br J Ind Med. 1984;41(2):228–34.
26. Elias Z, Poirot O, Fenoglio I, Ghiazza M, Danière MC, Terzetti F, et al. Surface reactivity, cytotoxic, and morphological transforming effects of diatomaceous earth products in Syrian hamster embryo cells. Toxicol Sci. 2006;91(2):510–20.
27. Ghiazza M, Gazzano E, Bonelli B, Fenoglio I, Polimeni M, Ghigo D, et al. Formation of a vitreous phase at the surface of some commercial diatomaceous earth prevents the onset of oxidative stress effects. Chem Res Toxicol. 2009;22(1):136–45.
28. Elias Z, Poirot O, Danière MC, Terzetti F, Marande AM, Dzwigaj S, et al. Cytotoxic and transforming effects of silica particles with different surface properties in Syrian hamster embryo (SHE) cells. Toxicol In Vitro. 2000;14(5):409–22.
29. Adamis Z, Tátrai E, Honma K, Six É, Ungváry G. *In vitro* and *in vivo* tests for determination of the pathogenicity of quartz, diatomaceous earth, mordenite and clinoptilolite. Ann Occup Hyg. 2000;44(1):67–74.
30. Pratt PC. Lung dust content and response in guinea pigs inhaling three forms of silica. Arch Environ Health. 1983;38(4):197–204.
31. Wagner WD, Fraser DA, Wright PG, Dobrogorski OJ, Stokinger HE. Experimental evaluation of the threshold limit of cristobalite—calcined diatomaceous earth. Am Ind Hyg Assoc J. 1968;29(3):211–21.
32. Moreno T, Higueras P, Jones T, McDonald I, Gibbons W. Size fractionation in mercury-bearing airborne particles (HgPM10) at Almadén Spain: implications for inhalation hazards around old mines. Atmos Environ. 2005;39:6409–19.
33. Batchelder M, Cressey G. Rapid, accurate phase quantification of clay-bearing samples using a position-sensitive X-ray detector. Clay Clay Miner. 1998;46(2):183–94.
34. Ziemann C, Harrison PT, Bellmann B, Brown RC, Zoitos BK, Class P. Lack of marked cyto- and genotoxicity of cristobalite in devitrified (heated) alkaline earth silicate wools in short-term assays with cultured primary rat alveolar macrophages. Inhal Toxicol. 2014;26(2):113–27.
35. Pavan C, Rabolli V, Tomatis M, Fubini B, Lison D. Why does the hemolytic activity of silica predict its pro-inflammatory activity? Part Fibre Toxicol. 2014;11:76.
36. Mossman BT, Glenn RE. Bioreactivity of the crystalline silica polymorphs, quartz and cristobalite, and implications for occupational exposure limits (OELs). Crit Rev Toxicol. 2013;43(8):632–60.
37. Piguet PF, Collart MA, Grau GE, Sappino A-P, Vassalli P. Requirement of tumour necrosis factor for development of silica-induced pulmonary fibrosis. Nature. 1990;344(6263):245.
38. Carpenter MA, Salje EKH, Graeme-Barber A. Spontaneous strain as a determinant of thermodynamic properties for phase transitions in minerals. Eur J Mineral. 1998;10(4):621–91.
39. Quality of Urban Air Review Group. Airborne particulate matter in the United Kingdom. In: Department of the Environment, editor. Third report of the Quality of Urban Air Review Group. London, UK: Quality of Urban Air Review Group; 1996.
40. Chao CH, Lu HY. Crystallization of Na2O-doped colloidal gel-derived silica. Mater Sci Eng A-Struct Mater Prop Microstruct Process. 2000;282(1–2):123–30.
41. Venezia AM, La Parola V, Longo A, Martorana A. Effect of alkali ions on the amorphous to crystalline phase transition of silica. J Solid State Chem. 2001;161(2):373–8.
42. Deer WA, Howie RA, Zussman J. An introduction to the rock-forming minerals. 3rd ed. London, UK: Mineralogical Society of Great Britain & Ireland; 2013. p. 498.
43. Damby DE, Llewellin EW, Horwell CJ, Williamson BJ, Najorka J, Cressey G, et al. The [alpha]-[beta] phase transition in volcanic cristobalite. J Appl Crystallogr. 2014;47(4):1025–215.
44. Horwell C, Williamson B, Donaldson K, Le Blond J, Damby D, Bowen L. The structure of volcanic cristobalite in relation to its toxicity; relevance for the variable crystalline silica hazard. Part Fibre Toxicol. 2012;9(1):44.
45. Rodriguez-Navarro C, Ruiz-Agudo E, Luque A, Rodriguez-Navarro AB, Ortega-Huertas M. Thermal decomposition of calcite: mechanisms of formation and textural evolution of CaO nanocrystals. Am Mineral. 2009;94(4):578–93.
46. Borm PJA, Tran L, Donaldson K. The carcinogenic action of crystalline silica: a review of the evidence supporting secondary inflammation-driven genotoxicity as a principal mechanism. Crit Rev Toxicol. 2011;41(9):756–70.
47. Steenland K, Mannetje A, Boffetta P, Stayner L, Attfield M, Chen J, et al. Pooled exposure–response analyses and risk assessment for lung cancer in 10 cohorts of silica-exposed workers: an IARC multicentre study. Cancer Causes Control. 2001;12(9):773–84.
48. Collins JF, Salmon AG, Brown JP, Marty MA, Alexeeff GV. Development of a chronic inhalation reference level for respirable crystalline silica. Regul Toxicol Pharmacol. 2005;43(3):292–300.
49. Donaldson K, Borm PJA. The quartz hazard: a variable entity. Ann Occup Hyg. 1998;42(5):287–94.
50. Meldrum M, Howden P. Crystalline silica: variability in fibrogenic potency. Ann Occup Hyg. 2002;46 suppl 1:27–30.
51. Tourmann JL, Kaufmann R. Biopersistence of the mineral matter of coal mine dusts in silicotic human lungs: is there a preferential release of iron? Environ Health Perspect. 1994;102 Suppl 5:265–8.
52. Cullen RT, Vallyathan V, Hagen S, Donaldson K. Protection by iron against the toxic effects of quartz. Ann Occup Hyg. 1997;41:420–5. inhaled particles VIII.
53. Duffin R, Gilmour PS, Schins RPF, Clouter A, Guy K, Brown DM, et al. Aluminium lactate treatment of DQ12 quartz inhibits its ability to cause inflammation, chemokine expression, and nuclear factor-κB activation. Toxicol Appl Pharmacol. 2001;176(1):10–7.
54. Nolan RP, Langer AM, Harington JS, Oster G, Selikoff IJ. Quartz hemolysis as related to its surface functionalities. Environ Res. 1981;26(2):503–20.
55. Stone V, Jones R, Rollo K, Duffin R, Donaldson K, Brown DM. Effect of coal mine dust and clay extracts on the biological activity of the quartz surface. Toxicol Lett. 2004;149(1–3):255–9.
56. Fubini B, Bolis V, Cavenago A, Volante M. Physicochemical properties of crystalline silica dusts and their possible implication in various biological responses. Scand J Work Environ Health. 1995;21 suppl 2:9–14.
57. Aladdin M, Jian J, Yang Q, Chen L-C, Finkelman RB, Huang X. Laboratory studies of the impact of calcite on *in vitro* and *in vivo* effects of coal dust: a potential preventive agent for coal workers' pneumoconiosis? Am J Ind Med. 2013;56(3):292–9.
58. Diler SB, Ergene S. Nuclear anomalies in the buccal cells of calcite factory workers. Genet Mol Biol. 2010;33(2):374–8.
59. Oscarson DW, Van Scoyoc GE, Ahlrichs JL. Lysis of erythrocytes by silicate minerals. Clay Clay Miner. 1986;34(1):74–80.
60. Vallyathan V, Schwegler D, Reasor M, Stettler L, Clere J, Green FHY. Comparative *In vitro* cytotoxicity and relative pathogenicity of mineral dusts. Ann Occup Hyg. 1988;32(VI):279–89.
61. Karlsson HL, Gustafsson J, Cronholm P, Moller L. Size-dependent toxicity of metal oxide particles–a comparison between nano- and micrometer size. Toxicol Lett. 2009;188(2):112–8.
62. Zhou YM, Zhong CY, Kennedy IM, Pinkerton KE. Pulmonary responses of acute exposure to ultrafine iron particles in healthy adult rats. Environ Toxicol. 2003;18(4):227–35.
63. Zhu MT, Feng WY, Wang B, Wang TC, Gu YQ, Wang M, et al. Comparative study of pulmonary responses to nano- and submicron-sized ferric oxide in rats. Toxicology. 2008;247(2–3):102–11.
64. Brunner TJ, Wick P, Manser P, Spohn P, Grass RN, Limbach LK, et al. *In vitro* cytotoxicity of oxide nanoparticles: comparison to asbestos, silica, and the effect of particle solubility†. Environ Sci Technol. 2006;40(14):4374–81.

65. Costantini LM, Gilberti RM, Knecht DA. The phagocytosis and toxicity of amorphous silica. PLoS One. 2011;6(2):e14647.
66. Pavan C, Tomatis M, Ghiazza M, Rabolli V, Bolis V, Lison D, et al. In search of the chemical basis of the hemolytic potential of silicas. Chem Res Toxicol. 2013;26(8):1188–98.
67. Duffin R, Tran CL, Clouter A, Brown DM, MacNee W, Stone V, et al. The importance of surface area and specific reactivity in the acute pulmonary inflammatory response to particles. Ann Occup Hyg. 2002;46 suppl 1:242–5.
68. Duffin R, Tran L, Brown D, Stone V, Donaldson K. Proinflammogenic effects of low-toxicity and metal nanoparticles *in vivo* and *in vitro*: highlighting the role of particle surface area and surface reactivity. Inhal Toxicol. 2007;19(10):849–56.
69. Schinwald A, Donaldson K. Use of back-scatter electron signals to visualise cell/nanowires interactions *in vitro* and *in vivo*; frustrated phagocytosis of long fibres in macrophages and compartmentalisation in mesothelial cells *in vivo*. Part Fibre Toxicol. 2012;9(1):34.
70. Chamberlain M, Davies R, Brown RC, Griffiths DM. *In vitro* tests for the pathogenicity of mineral dusts. Ann Occup Hyg. 1982;26(1–4):583–92.
71. Champion JA, Mitragotri S. Role of target geometry in phagocytosis. Proc Natl Acad Sci U S A. 2006;103(13):4930–4.
72. Ye J, Shi X, Jones W, Rojanasakul Y, Cheng N, Schwegler-Berry D, et al. Critical role of glass fiber length in TNF-α production and transcription factor activation in macrophages. Am J Physiol Lung Cell Mol Physiol. 1999;276(3):L426–34.
73. Schinwald A, Murphy FA, Jones A, MacNee W, Donaldson K. Graphene-based nanoplatelets: a new risk to the respiratory system as a consequence of their unusual aerodynamic properties. ACS Nano. 2012;6(1):736–46.